

UNIVERSITY OF CALIFORNIA  
SANTA CRUZ

**SEARCH FOR WW AND WZ RESONANCES IN  $\ell\nu qq$  FINAL  
STATES IN  $pp$  COLLISIONS AT  $\sqrt{s} = 13$  TEV WITH THE ATLAS  
DETECTOR**

A dissertation submitted in partial satisfaction of the  
requirements for the degree of

DOCTOR OF PHILOSOPHY

in

PHYSICS

by

**Natasha Woods**

December 2019

The Dissertation of Natasha Woods  
is approved:

---

Abraham Seiden, Chair

---

Mike Hance

---

Bruce Schumm

---

Quentin Williams  
Vice Provost and Dean of Graduate Studies

Copyright © by

Natasha Woods

2019

# Table of Contents

List of Figures	vi
List of Tables	xvi
Abstract	xviii
Dedication	xix
Acknowledgments	xx
<b>I Introduction</b>	<b>1</b>
<b>1 Introduction</b>	<b>2</b>
<b>II Theoretical Motivation</b>	<b>6</b>
<b>2 The Standard Model of Particle Physics</b>	<b>7</b>
2.1 Introduction . . . . .	7
2.2 Quantum Field Theory . . . . .	7
2.3 $U(1)_{EM}$ Local Gauge Invariance . . . . .	8
2.4 Yang-Mills Gauge Theories . . . . .	11
2.5 Particles in the Standard Model . . . . .	12
2.6 Higgs Mechanism . . . . .	17
2.7 Electroweak Theory . . . . .	18
2.8 Quantum ChromoDynamics . . . . .	19
<b>3 Standard Model Successes and Limitations</b>	<b>24</b>
<b>4 New Physics Models with Diboson Resonances</b>	<b>27</b>
4.1 Randall Sundrum Bulk Model . . . . .	27
4.2 Simple Standard Model Extensions . . . . .	29

<b>III Experimental Setup</b>	<b>31</b>
<b>5 LHC</b>	<b>32</b>
5.1 LHC Layout and Design . . . . .	34
<b>6 The ATLAS Detector</b>	<b>39</b>
6.1 Coordinate System . . . . .	41
6.2 Inner Detector . . . . .	42
6.2.1 Pixel Detector . . . . .	45
6.2.2 Semiconductor Tracker . . . . .	45
6.2.3 Transition Radiation Tracker . . . . .	45
6.3 Calorimeters . . . . .	47
6.4 Muon Spectrometer . . . . .	51
6.5 Magnet System . . . . .	55
6.6 Trigger System . . . . .	56
<b>IV Method</b>	<b>58</b>
<b>7 Dataset and Simulated Samples</b>	<b>59</b>
7.1 Dataset . . . . .	59
7.2 Simulated Samples . . . . .	62
<b>8 Objects</b>	<b>63</b>
8.1 Electrons . . . . .	63
8.2 Muons . . . . .	64
8.3 Jets . . . . .	65
8.3.1 Small-R jets . . . . .	68
8.3.2 Large-R jets . . . . .	68
8.3.3 Variable Radius jets . . . . .	71
8.3.4 Jet Flavor Tagging . . . . .	72
8.4 MET/Neutrinos . . . . .	72
8.5 Overlap Removal . . . . .	72
8.6 Reconstructed Resonance Mass ( $m_{WV}$ ) . . . . .	73
<b>9 Event Selection and Categorization</b>	<b>75</b>
9.1 Pre-selection . . . . .	75
9.2 Trigger . . . . .	75
9.3 non-VBF/VBF RNN . . . . .	77
9.4 Signal Region Definitions . . . . .	84
9.5 Selection Acceptance times efficiency for Signal Events . . . . .	93
9.6 Background Estimate . . . . .	94
9.6.1 Control Regions . . . . .	94

9.6.2	Fake Lepton Backgrounds . . . . .	95
<b>10</b>	<b>Systematic Uncertainties</b>	<b>109</b>
10.1	Experimental Systematics . . . . .	109
10.2	Theory Systematics . . . . .	111
<b>11</b>	<b>Statistical Analysis</b>	<b>119</b>
11.1	Likelihood Function Definition . . . . .	119
11.2	Fit Configuration . . . . .	120
11.3	Best Fit $\mu$ . . . . .	122
11.4	Discovery Test . . . . .	123
11.5	Exclusion Limits . . . . .	124
<b>12</b>	<b>Results</b>	<b>126</b>
12.1	Discovery Tests . . . . .	126
12.2	Systematic Profiling and Correlations . . . . .	132
12.3	Expected and Measured Yields . . . . .	133
12.4	Limits . . . . .	147
<b>V</b>	<b>Quark and Gluon Tagging</b>	<b>149</b>
<b>13</b>	<b>Prospects</b>	<b>150</b>
<b>14</b>	<b><math>n_{trk}</math> Calibration</b>	<b>157</b>
<b>15</b>	<b>Application</b>	<b>163</b>
<b>VI</b>	<b>Conclusion</b>	<b>168</b>
<b>16</b>	<b>Conclusions</b>	<b>169</b>
	<b>Bibliography</b>	<b>170</b>

# List of Figures

2.1	The particles of the Standard Model. . . . .	14
2.2	Summary of how Standard Model particles interact with other Standard Model particles. . . . .	15
2.3	This figure shows the three dominant QCD interactions. From Ref. [17] . . . . .	21
2.4	Strength of the U(1), SU(2), and SU(3) gauge couplings as a function of the energy scale of the interaction ( $Q$ ). From Ref. [11] . . . . .	22
3.1	A comparison of cross section measurements at $\sqrt{s} = 7, 8, 13$ TeV from ATLAS compared to theoretical measurements. From Ref. [5]	26
4.1	Cartoon of RS Bulk Model . . . . .	28
5.1	Scaling of cross sections with $\sqrt{s}$ . Natasha: write more here . . . . .	33
5.2	LHC Layout. Natasha write more . . . . .	35
5.3	LHC Accelerator. Natasha write more . . . . .	37
6.1	Big picture layout of ATLAS detector. Natasha: write more . . . . .	40
6.2	Big picture layout of ATLAS detector. Natasha: write more . . . . .	40
6.3	A simplified schematic of how different particles interact and are detected within ATLAS. . . . .	41
6.4	Layout of ATLAS Inner Detector . . . . .	43
6.5	Layout of ATLAS ID Barrel System. . . . .	44
6.6	Overview of ATLAS electromagnetic and hadronic calorimeters. . . . .	48

6.7	Schematic of ECAL . . . . .	49
6.8	Schematic of HCAL . . . . .	50
6.9	Schematic of Muon Spectrometer [cite G35] . . . . .	53
6.10	Schematic of MDT chamber. [cite G35] . . . . .	54
6.11	Schematic of RPC chamber, which is used for triggering in the central region of the detector [cite G35]. . . . .	54
6.12	Schematic of TGC chamber, which is used for triggering in the muon end-cap region. [cite G35] . . . . .	55
6.13	Layout of ATLAS magnet systems. . . . .	56
7.1	Integrated luminosity for data collected from ATLAS from 2011 - 2018 . . . . .	60
7.2	Mean number of interactions per crossing for data collected from ATLAS from 2011 - 2018 . . . . .	61
8.1	This figure shows the breakdown of the muon reconstruction efficiency scale factor measured in $Z \rightarrow \mu\mu$ as a function of $p_T$ [4]. . . . .	65
8.2	[7] This diagram shows the calibration stages for EM jets. . . . .	67
8.3	The upper cut on $D_2$ (a) and jet mass window cut i.e. the upper and lower boundary of the mass (b) of the $W$ -tagger as a function of jet $p_T$ . Corresponding values for $Z$ -tagger are shown in (c) and (d). The optimal cut values for maximum significance are shown as solid markers and the fitted function as solid lines. Working points from $VV \rightarrow JJ$ [ATLAS-HDBS-2018-31-002] is also shown as dashed lines as a reference. Natasha reword? . . . . .	70
8.4	Natasha write caption . . . . .	71
9.1	RNN architecture. Natasha add caption . . . . .	79
9.2	This figure shows the embedded logic in LSTM cells. This image was taken from [22], where a more in depth discussion about LSTMs may be found. . . . .	80

9.3	RNN Score distribution for ggF and VBF signals and backgrounds.	81
9.4	ROC curve using k-fold validation for RNN. . . . .	82
9.5	Comparison of GGF Z' limits for different RNN score selections. The bottom panel shows the ratio of the upper limits set for different RNN cuts to the cut-based analysis. In this panel smaller numbers, indicate that the expected upper limit is smaller than the cut-based analysis, which is desired. . . . .	83
9.6	Event Categorization. Natasha write more. . . . .	86
9.7	Data MC comparison for the merged $WW$ HP TCR. The bottom panel shows the ratio of the difference between data and simulation to simulation. The red bands include the all systematic and statistical uncertainties on the background. . . . .	87
9.8	Data MC comparison for the merged $WW$ LP TCR. The bottom panel shows the ratio of the difference between data and simulation to simulation. The red bands include the all systematic and statistical uncertainties on the background. . . . .	88
9.9	Data MC comparison for the merged $WZ$ HP TCR. The bottom panel shows the ratio of the difference between data and simulation to simulation. The red bands include the all systematic and statistical uncertainties on the background. . . . .	89
9.10	Data MC comparison for the merged $WZ$ LP TCR. The bottom panel shows the ratio of the difference between data and simulation to simulation. The red bands include the all systematic and statistical uncertainties on the background. . . . .	90
9.11	Data MC comparison for the resolved $WW$ TCR. The bottom panel shows the ratio of the difference between data and simulation to simulation. The red bands include the all systematic and statistical uncertainties on the background. . . . .	91

9.12 Data MC comparison for the resolved $WZ$ TCR. The bottom panel shows the ratio of the difference between data and simulation to simulation. The red bands include the all systematic and statistical uncertainties on the background. . . . .	92
9.13 Selection acceptance times efficiency for the $W' \rightarrow WZ \rightarrow \ell\nu qq$ events from MC simulations as a function of the $W'$ mass for (a) Drell-Yan and (b) VBF production, combining the merged HP and LP signal regions of the $WW \rightarrow \ell\nu J$ selection and the resolved regions of the $WW \rightarrow \ell\nu jj$ selection. . . . .	93
9.14 Selection acceptance times efficiency for the $G \rightarrow WW \rightarrow \ell\nu qq$ events from MC simulations as a function of the $G$ mass for (a) Drell-Yan and (b) VBF production, combining the merged HP and LP signal regions of the $WW \rightarrow \ell\nu J$ selection and the resolved regions of the $WW \rightarrow \ell\nu jj$ selection. . . . .	94
9.15 The $E_T^{miss}$ distribution in MJCR for 2017 data in the electron channel(left), muon channel with W-boson pT < 150 GeV (center) and > 150 GeV (right). Multi-jet templates are calculated as remaining data components after excluding known MC . . . . .	97
9.16 Postfit Data/MC comparison of distributions of $E_T^{miss}$ , $m_T^W$ , lepton and neutrino $p_T$ , $m_{\ell\nu jj}$ , lepton- $\nu$ angular distance in the $WW$ electron channel. The MJ template is obtained from the pre-MJ-fit. . . . .	98
9.17 Postfit Data/MC comparison of distributions of $E_T^{miss}$ , $m_T^W$ , lepton and neutrino $p_T$ , $m_{\ell\nu jj}$ , lepton- $\nu$ angular distance in the $WW$ muon channel. The MJ template is obtained from the pre-MJ-fit. . . . .	99
9.18 Postfit Data/MC comparison of distributions of $E_T^{miss}$ , $m_T^W$ , lepton and neutrino $p_T$ , $m_{\ell\nu jj}$ , lepton- $\nu$ angular distance in the $WZ$ untag electron channel. The MJ template is obtained from the pre-MJ-fit. . . . .	100
9.19 Postfit Data/MC comparison of distributions of $E_T^{miss}$ , $m_T^W$ , lepton and neutrino $p_T$ , $m_{\ell\nu jj}$ , lepton- $\nu$ angular distance in the $WZ$ untag muon channel. The MJ template is obtained from the pre-MJ-fit. . . . .	101

9.20 Postfit Data/MC comparison of distributions of $E_T^{miss}$ , $m_T^W$ , lepton and neutrino $p_T$ , $m_{\ell\nu jj}$ , lepton- $\nu$ angular distance in the $WZ$ untag electron channel. The MJ template is obtained from the pre-MJ-fit.	102
9.21 Postfit Data/MC comparison of distributions of $E_T^{miss}$ , $m_T^W$ , lepton and neutrino $p_T$ , $m_{\ell\nu jj}$ , lepton- $\nu$ angular distance in the $WZ$ untag muon channel. The MJ template is obtained from the pre-MJ-fit.	103
9.22 Postfit Data/MC comparison of distributions of $E_T^{miss}$ , $m_T^W$ , lepton and neutrino $p_T$ , $m_{\ell\nu jj}$ , lepton- $\nu$ angular distance in the VBF $WW$ electron channel. The MJ template is obtained from the pre-MJ-fit.	104
9.23 Postfit Data/MC comparison of distributions of $E_T^{miss}$ , $m_T^W$ , lepton and neutrino $p_T$ , $m_{\ell\nu jj}$ , lepton- $\nu$ angular distance in the VBF $WW$ muon channel. The MJ template is obtained from the pre-MJ-fit.	105
9.24 Postfit Data/MC comparison of distributions of $E_T^{miss}$ , $m_T^W$ , lepton and neutrino $p_T$ , $m_{\ell\nu jj}$ , lepton- $\nu$ angular distance in the VBF $WZ$ electron channel. The MJ template is obtained from the pre-MJ-fit.	106
9.25 Postfit Data/MC comparison of distributions of $E_T^{miss}$ , $m_T^W$ , lepton and neutrino $p_T$ , $m_{\ell\nu jj}$ , lepton- $\nu$ angular distance in the VBF $WZ$ muon channel. The MJ template is obtained from the pre-MJ-fit.	107
 10.1 The $W/Z+jet$ systematics for the a) Merged ggF, b) Resolved ggF, c) Merged VBF, and d) Resolved VBF regions. The top subplot shows the nominal and variation distributions/bands, the middle shows the ratio of the two, and the final shows just the shape of the envelope (the final uncertainty).	113
10.2 The two-point generator comparison between Sherpa and MadGraph for the $W/Z+jet$ samples in the a) Merged ggF, b) Resolved ggF, c) Merged VBF, and d) Resolved VBF regions. The normalization of the Madgraph sample is set to the Sherpa value to consider only shape effects. The bottom inlet shows the ratio of the two.	114

10.3	Ratio between the variations of generator (red) and hadronization (blue) variations for the Merged regime for $t\bar{t}$ sample. . . . .	115
10.4	Ratio between the variations of generator (red) and hadronization (blue) variations for the Resolved regime for $t\bar{t}$ sample. . . . .	115
10.5	Ratio between the variations of ISR up (red) and down (blue) variations for the Merged regime for $t\bar{t}$ sample. . . . .	116
10.6	Ratio between the variations of ISR up (red) and down (blue) variations for the Resolved regime for $t\bar{t}$ sample. . . . .	117
10.7	Ratio between the variations of FSR up (red) and down (blue) variations for the Merged regime for $t\bar{t}$ sample. . . . .	118
10.8	Ratio between the variations of FSR up (red) and down (blue) variations for the Resolved regime for $t\bar{t}$ sample. . . . .	118
11.1	The HVT signal mass resolution as a function of mass fit with a straight line in the Resolved ggF region (left) and VBF (right) region. . . . .	122
11.2	The HVT signal mass resolution as a function of mass fit with a straight line in the Merged ggF region (left) and VBF (right) region. . . . .	122
12.1	These plots show the measured $p_0$ value as a function of resonance mass for HVT Z' DY production. . . . .	127
12.2	These plots show the measured $p_0$ value as a function of resonance mass for HVT Z' VBF production. . . . .	128
12.3	These plots show the measured $p_0$ value as a function of resonance mass for HVT W' DY production. . . . .	129
12.4	These plots show the measured $p_0$ value as a function of resonance mass for HVT W' VBF production. . . . .	130
12.5	These plots show the measured $p_0$ value as a function of resonance mass for the RS Graviton DY production. . . . .	131
12.6	Ranked systematics and their fitted values for WW DY (right) and VBF (left) selections. . . . .	132

12.7	Ranked systematics and their fitted values for $WZ$ DY (right) and VBF (left) selections. . . . .	133
12.8	Correlations between systematics for $WW$ DY (right) and VBF (left) selections. . . . .	133
12.9	This figure shows the distribution of $m_{\ell\nu qq}$ in the $DY$ $WW$ control regions. . . . .	141
12.10	This figure shows the distribution of $m_{\ell\nu qq}$ in the $DY$ $WZ$ control regions. . . . .	142
12.11	This figure shows the distribution of $m_{\ell\nu qq}$ in the VBF $WW$ control regions. . . . .	143
12.12	This figure shows the distribution of $m_{\ell\nu qq}$ in the VBF $WZ$ control regions. . . . .	144
12.13	This figure shows the distribution of $m_{\ell\nu qq}$ in the GGF $WW$ signal regions. . . . .	145
12.14	This figure shows the distribution of $m_{\ell\nu qq}$ in the GGF $WZ$ Untag signal regions. . . . .	145
12.15	This figure shows the distribution of $m_{\ell\nu qq}$ in the GGF $WZ$ Tag signal regions. . . . .	146
12.16	This figure shows the distribution of $m_{\ell\nu qq}$ in the VBF $WZ$ Tag signal regions. . . . .	146
12.17	This figure shows the distribution of $m_{\ell\nu qq}$ in the VBF $WZ$ Tag signal regions. . . . .	147
12.18	This figure shows theory, expected and observed limits for HVT $W'$ DY (left) and VBF (right) production. . . . .	147
12.19	This figure shows theory, expected and observed limits for HVT $Z'$ DY (left) and VBF (right) production. . . . .	148
12.20	This figure shows theory, expected and observed limits for RS Gravitons via DY production. . . . .	148

13.1	PDGID of the truth-level parton matched to the small-R jets passing the Resolved GGF WW Signal Region selections for the (a) Leading (b) Sub-Leading jets . These distributions are shown for 300, 500, and 700GeV Z' signals and the background. . . . .	152
13.2	The number of tracks in small-R jets in events passing the Resolved GGF WW Signal Region selections for the (a) Leading (b) Sub-Leading jets. These distributions are shown for 300, 500, and 700GeV Z' signals and the background. . . . .	152
13.3	The number of tracks in background small-R jets in events passing the Resolved GGF WW Signal region selection vs. $\ln(p_T)$ for (a)Leading (b) Sub-Leading jets. The best fit line for the distribution is also shown, as well as the percentage of jets that pass a cut of number of tracks $< 4 \times \ln(p_T) - 5$ . Note the number of total entries in these plots has been normalized to one. . . . .	153
13.4	The number of tracks in small-R jets in 300GeV Z' events passing the Resolved GGF WW Signal region selection vs. $\ln(p_T)$ for (a)Leading (b) Sub-Leading jets. The best fit line for the distribution is also shown, as well as the percentage of jets that pass a cut of number of tracks $< 4 \times \ln(p_T) - 5$ . Note the number of total entries in these plots has been normalized to one. . . . .	153
13.5	The number of tracks in small-R jets in 500GeV Z' events passing the Resolved GGF WW Signal region selection vs. $\ln(p_T)$ for (a)Leading (b) Sub-Leading jets. The best fit line for the distribution is also shown, as well as the percentage of jets that pass a cut of number of tracks $< 4 \times \ln(p_T) - 5$ . Note the number of total entries in these plots has been normalized to one. . . . .	154

13.6 The number of tracks in small-R jets in 700GeV Z' events passing the Resolved GGF WW Signal region selection vs. $\ln(p_T)$ for (a)Leading (b) Sub-Leading jets. The best fit line for the distribution is also shown, as well as the percentage of jets that pass a cut of number of tracks $< 4 \times \ln(p_T) - 5$ .Note the number of total entries in these plots has been normalized to one. . . . .	154
13.7 The number of tracks in leading small-R jets in background events passing the Resolved GGF WW Signal region selection vs. $\ln(p_T)$ for (a)Gluons (b) Quarks jets. The best fit line for the distribution is also shown, as well as the percentage of jets that pass a cut of number of tracks $< 4 \times \ln(p_T) - 5$ .Note the number of total entries in these plots has been normalized to one. . . . .	155
13.8 ROC Curve for Quark and Gluon Tagging with a cut on the number of tracks that depends on the $\ln(p_T)$ . . . . .	155
13.9 The top panel shows the distribution of $m_{lvqq}$ with and without quark gluon tagging. The middle panel shows the ratio of the signals and backgrounds with and without quark gluon tagging. The bottom panel shows the change in $S/\sqrt{B}$ with quark gluon tagging. . . . .	156
15.1 The top panel shows the distribution of $m_{lvqq}$ with and without requiring jets to be true quarks. The middle panel shows the ratio of the signals and backgrounds with and without requiring jets to be true quarks. The bottom panel shows the change in $S/\sqrt{B}$ when requiring jets to be true quarks. . . . .	164
15.2 Unfolded and extracted $n_C$ qg dstbs. . . . .	165
15.3 PDGID of the truth-level parton matched to the small-R jets passing the Resolved GGF WW Signal Region selections for the (a) Leading (b) Sub-Leading jets . These distributions are shown for 300, 500, and 700GeV Z' signals and the background. . . . .	166

15.4 These figures show the impact of the uncertainties on the number  
of tracks in the leading jet in the sum of the background sample  
in the Resolved GGF WW SR (a) tracking efficiency (b) fake (c)  
PDF (d) ME (e) unfolding uncertainties. 167

# List of Tables

2.1	Representations of the SM fermions under $SU(3)_C \times SU(2)_L \times U(1)_Y$ gauge symmetry group. $SU(2)_L$ gauge transformations allow one to go between rows and $SU(3)_C$ transformations allow one to go between columns in these fermion representations. [REWORD]	13
9.1	The list of triggers used in the analysis. . . . .	76
9.2	Summary of selection criteria used to define the signal region (SR), $W$ +jets control region ( $W$ CR) and $t\bar{t}$ control region ( $t\bar{t}$ CR) for merged 1-lepton channel. . . . .	85
9.3	The list of selection cuts in the resolved analysis for the $WW$ and $WZ$ signal regions (SR), $W$ +jets control region (WR) and $t\bar{t}$ control region (TR). . . . .	86
9.4	Definitions of “inverted” leptons used in multijet control region . .	96
9.5	Fit validation result in WCRs for 2015+16 data. The fit is done in various WCRs, in order to obtain the corresponding scale factors for MJ templates: ggF resolved WCR for the $WW \rightarrow lvqq$ selection, ggF resolved untagged WCR for the $WZ \rightarrow lvqq$ selection, ggF resolved tagged WCR for the $WZ \rightarrow lvqq$ selection, VBF resolved WCR for the $WW \rightarrow lvqq$ selection, and VBF resolved WCR for the $WZ \rightarrow lvqq$ selection. Post-fit event yields for electroweak processes and MJ contributions are shown. The SF column shows the corresponding normalization scale factors for electroweak processes from the fit. R.U. stands for relative uncertainty. . . . .	108

12.1	Expected and Measured for DY $WW$ $W+\text{jets}$ , $t\bar{t}$ control regions and signal regions. . . . .	134
12.2	Expected and Measured for DY $WZ$ $W+\text{jets}$ , $t\bar{t}$ tag and untag control regions. . . . .	135
12.3	Expected and Measured for DY $WZ$ $W+\text{jets}$ , $t\bar{t}$ tag and untag signal regions. . . . .	136
12.4	Expected and Measured for VBF $WW$ $W+\text{jets}$ , $t\bar{t}$ control regions and signal regions. . . . .	137
12.5	Expected and Measured for VBF $WZ$ $W+\text{jets}$ , $t\bar{t}$ control regions and signal regions. . . . .	138
12.6	Fitted background normalizations for $t\bar{t}$ and $W+\text{jets}$ backgrounds for the DY $WW$ analysis region. . . . .	139
12.7	Fitted background normalizations for $t\bar{t}$ and $W+\text{jets}$ backgrounds for the DY $WZ$ analysis region. . . . .	139
12.8	Fitted background normalizations for $t\bar{t}$ and $W+\text{jets}$ backgrounds for the VBF $WW$ analysis region. . . . .	139
12.9	Fitted background normalizations for $t\bar{t}$ and $W+\text{jets}$ backgrounds for the VBF $WZ$ analysis region. . . . .	140

## Abstract

Search for  $WW$  and  $WZ$  Resonances in  $\ell\nu qq$  final states in  $pp$  collisions at

$\sqrt{s} = 13$  TeV with the ATLAS detector

by

Natasha Woods

This thesis presents a search for  $WW$  and  $WZ$  resonances using data from  $pp$  collisions at  $\sqrt{s} = 13$  TeV using the ATLAS detector, corresponding to an integrated luminosity of  $139 \text{ fb}^{-1}$ . Diboson resonances are predicted in a number of Standard Model (SM) extensions, such as Extended Gauge Models, and Extra dimensional models. This search looks for resonances where one  $W$  boson decays leptonically and the other  $W$  or  $Z$  boson decays hadronically. This search is sensitive to diboson resonance production via vector-boson fusion as well as quark-antiquark annihilation and gluon-gluon fusion mechanisms. No significant excess of events is observed with respect to the Standard Model backgrounds, and constraints on the masses of new  $W'$ ,  $Z'$ , and bulk-RS Gravitons are extended to up to 3.3 TeV, depending on the model. As the dominant backgrounds in this search contain gluons, classifying jets as quark-initiated or gluon-initiated would make this analysis more sensitive to new physics. Towards this end, this thesis provides a calibrated quark-gluon tagger based on the multiplicity of charged particles within a jet.

Loving Dedication

å

xix

## **Acknowledgments**

Proper acknowledgments of everyone else who helped you graduate. Write later.

# **Part I**

## **Introduction**

# <sup>3</sup> Chapter 1

## <sup>4</sup> Introduction

<sup>5</sup> In general, humanity has continually strived to understand the structure and  
<sup>6</sup> dynamics of reality for widely varying reasons. Each academic field uses a spe-  
<sup>7</sup> cific set of concepts and models to describe nature. Physics is one such field,  
<sup>8</sup> that uses mathematical objects to systematically develop testable models about  
<sup>9</sup> the universe. Currently, the most fundamental types particles are fermions and  
<sup>10</sup> bosons. Fermions are the particles that make up the "ordinary" matter of the  
<sup>11</sup> universe, while bosons are the quanta of the fundamental forces. The Standard  
<sup>12</sup> Model (SM) of particle physics describes the quantum behavior of three of the  
<sup>13</sup> four fundamental forces: electromagnetic, strong, and weak forces.

<sup>14</sup> The Standard Model has consistently described much of reality to an extreme  
<sup>15</sup> degree of accuracy. It has predicted cross sections for strong and electroweak  
<sup>16</sup> processes that span over ten orders of magnitude [see Fig 3.1] and contains no  
<sup>17</sup> known logical inconsistencies. Despite the reality of the Standard Model, it still  
<sup>18</sup> fails to describe aspects of reality and suffers from aesthetic issues. The SM fails  
<sup>19</sup> to account for dark matter, dark energy, neutrino masses, the hierarchy of the  
<sup>20</sup> fundamental force strengths, and other issues that may have not been noticed  
<sup>21</sup> yet! This incompleteness may indicate that a more fundamental theory exists. It

22 is hoped that such a theory would address the aforementioned phenomena and  
23 the ad-hoc structure and parameter values of the SM. In particular the relative  
24 scales of the fundamental forces impose oddly fine-tuned SM parameters, unless  
25 there is additional structure at higher energies (e.g. between the electroweak and  
26 Planck scales). This and other theoretical arguments motivate the search for new  
27 physics at the TeV scale. The set of theories that hope to explain more of reality  
28 are known as Beyond the Standard Model theories (BSM). Many of these theories,  
29 if true, would revolutionize concepts of symmetry and space-time, which would  
30 be intrinsically meaningful.

31 To probe the physics at this high energy frontier, physicists often collide ener-  
32 getic particles that combine to produce massive particles, such as the Higgs boson  
33 and top quark. The more energetic the colliding particles are the more massive  
34 produced particles can be. Currently, the world's highest energy particle collider  
35 is the Large Hadron Collider (LHC) at the European Organization for Nuclear  
36 Research (CERN).

37 This thesis presents a search for  $WW$  and  $WZ$  resonances using data from  $pp$   
38 collisions at  $\sqrt{s} = 13$  TeV using the ATLAS detector at CERN, corresponding  
39 to an integrated luminosity of  $139 \text{ fb}^{-1}$ . Diboson resonances are predicted in a  
40 number of BSM theories, such as Extended Gauge Models and Extra dimensional  
41 models. This search looks for resonances where one  $W$  boson decays leptonically  
42 and the other  $W$  or  $Z$  boson decays hadronically. This search is sensitive to  
43 diboson resonance production via vector-boson fusion as well as quark-antiquark  
44 annihilation and gluon-gluon fusion mechanisms (which will be collectively called  
45 non-VBF modes).

46 To search for these new resonances, Monte-Carlo simulations are used to model  
47 SM backgrounds and BSM signals. In these simulations, a series of optimized cuts

48 are used to create signal regions (SR) to identify the leptonic and hadronic decay  
49 products of the resonance, maximize signal acceptance, and minimize background  
50 contamination. In these regions, the resonance mass is calculated as the combined  
51 system mass of the leptonic and hadronic system. The expected resonance mass  
52 distribution from the simulated backgrounds and anticipated signal are compared  
53 to data to search for the existence of these BSM signals (also known as a "bump  
54 hunt"). Control regions enriched in the dominant backgrounds,  $t\bar{t}$  and  $W+\text{jets}$   
55 (TCR and WCR, respectively) are constructed to be orthogonal to SRs and used  
56 to determine the normalization of the  $t\bar{t}$  and  $W+\text{jets}$  backgrounds in SRs.

57 The VBF  $W'$  and  $Z'$  and ggF  $W'$  and  $Z'$  resonances studied have unique  
58 SR and CR selections to maximize analysis sensitivity. RS Graviton signals are  
59 probed using the same selections as the ggF  $Z'$  signal. Additionally, more mas-  
60 sive resonances are more likely to have boosted  $W/Z$  bosons. As the boost of  
61 the hadronically decaying boson increases the separation of its hadronic decay  
62 products decreases. When the hadronically decaying boson has sufficient boost,  
63 the two quarks will overlap and not be identified separately. For this reason, a  
64 set of "resolved" selections are used when the hadronic decay products are recon-  
65 structed separately, and "merged" selections when the decay products overlap and  
66 identified as a single object in the event. A  $W/Z$  tagger identifies merged jets as  
67 originating from a  $W/Z$  bosons based on jet substructure and mass cuts. However,  
68 the more boosted the jet is the less likely it is to pass the jet substructure cut, due  
69 to track merging. Consequently, the merged selection uses a high purity region  
70 (HP), which requires that the jet pass both cuts, and low purity (LP) region where  
71 the jet can fail the jet substructure cut.

72 The aforementioned SR definitions veto events with  $b$ -jets to minimize  $t\bar{t}$  con-  
73 tamination. However,  $b$ -jets are anticipated from  $W'$  resonances from the hadron-

74 ically decaying  $Z$  boson. To increase the signal acceptance of these resonances,  
75 a  $Z \rightarrow bb$  tagger is used to construct additional SR and CRs called the "tagged"  
76 regions (and "un>tagged" if the event fails the  $Z \rightarrow bb$  tagger).

77 For each signal model, the simulated and measured resonance mass distribu-  
78 tions in the relevant SR and CRs are combined to construct a likelihood. This  
79 likelihood is parameterized by the signal strength parameter,  $\mu$  and systematic  
80 uncertainties of the resonance mass distribution. This likelihood is used to quan-  
81 tify the likelihood of a certain signal model given the anticipated backgrounds and  
82 measured data.

83 No significant excess of events is observed with respect to the Standard Model  
84 backgrounds, and constraints on the masses of new  $W'$ ,  $Z'$ , and bulk-RS Gravi-  
85 tons are extended to up to 3.3 TeV, depending on the model. As the dominant  
86 backgrounds in this search contain gluons, classifying jets as quark-initiated or  
87 gluon-initiated would improve the sensitivity of this analysis to new physics. To-  
88 wards this end, this thesis provides a calibrated quark-gluon tagger based on the  
89 multiplicity of charged particles within a jet.

90 Part II reviews the SM, its successes and shortcomings, and the aforemen-  
91 tioned BSM theories that address the incompleteness of the SM. The structure  
92 and performance of the ATLAS detector used is given in Part III. Part IV summa-  
93 rizes the search for the diboson resonances using ATLAS data from  $pp$  collisions  
94 at  $\sqrt{s} = 13$  TeV. Finally, Part V examines the prospects for a quark gluon tagger  
95 based on the track multiplicity of jets and details the calibration of this tagger.

**Part II**

96

**Theoretical Motivation**

97

<sub>98</sub> **Chapter 2**

<sub>99</sub> **The Standard Model of Particle**

<sub>100</sub> **Physics**

<sub>101</sub> **2.1 Introduction**

<sub>102</sub> By determining the dynamics of the most elementary degrees of freedom, par-  
<sub>103</sub> ticle physics hopes to uncover the fundamental laws of the universe. The definition  
<sub>104</sub> of elementary has evolved through time and currently refers to matter and force  
<sub>105</sub> mediating particles: fermions and bosons, respectively. The Standard Model of  
<sub>106</sub> Particle Physics (SM) describes the quantum behavior of three of the four funda-  
<sub>107</sub> mental forces: weak, strong, and electromagnetic, via boson and fermion interac-  
<sub>108</sub> tions. Gravity is not included in the SM and still under investigation.

<sub>109</sub> **2.2 Quantum Field Theory**

<sub>110</sub> In the SM, forces (and particles) are represented as fields. In this context,  
<sub>111</sub> fields are mathematical objects that define a tensor (e.g. scalar, vector, etc) at  
<sub>112</sub> every point on a manifold, here the manifold is space-time. These fields obey laws

<sub>113</sub> dictated by Quantum Field Theory (QFT). Particles arise naturally in QFT as  
<sub>114</sub> quantized field excitations localized in spacetime.

<sub>115</sub> According to Noether's theorem, symmetries of a field give rise to conserved  
<sub>116</sub> quantities (e.g. time-translation invariance leads to energy conservation). Often  
<sub>117</sub> in the history of physics, a conserved quantity of a field is found and then the  
<sub>118</sub> underlying symmetry of the field is inferred. Gauge symmetries are symmetries  
<sub>119</sub> among the internal degrees of freedom of the field (components of the tensor),  
<sub>120</sub> which give rise to quantities associated with fields. By specifying the symmetries  
<sub>121</sub> of a system the dynamics and conserved quantities of the system may be succinctly  
<sub>122</sub> defined.

## <sub>123</sub> 2.3 $U(1)_{EM}$ Local Gauge Invariance

<sub>124</sub> The Lagrangian of Quantum Electrodynamics (QED) describes the electro-  
<sub>125</sub> magnetic force. QED may be derived by requiring local  $U(1)_{EM}$  gauge invariance  
<sub>126</sub> of the free dirac fermion Lagrangian,  $\psi$ :

$$\mathcal{L} = i\bar{\psi}\gamma^\mu\partial_\mu\psi - m\bar{\psi}\psi \quad (2.1)$$

<sub>127</sub> This symmetry may be represented as a complex number with unit modulus,  
<sub>128</sub>  $e^{i\theta}$ .  $U(1)$  gauge invariance requires this gauge transformation of  $\psi$  will leave the  
<sub>129</sub> Lagrangian unchanged.

$$\psi(x) \rightarrow \psi'(x) = e^{i\theta(x)}\psi(x) \quad (2.2)$$

<sub>130</sub> NB: This transformation is a local gauge transformation as  $\theta$  depends on the  
<sub>131</sub> spacetime coordinate.

<sub>132</sub> By requiring this symmetry of the free Dirac fermion Lagrangian:

$$\mathcal{L} = i\bar{\psi}\gamma^\mu\partial_\mu\psi - m\bar{\psi}\psi \quad (2.3)$$

<sup>133</sup> The mass term is unaffected, but the kinetic term is modified due to  $\theta(x)$ .

$$\mathcal{L} \rightarrow \mathcal{L}' = i\bar{\psi}e^{-i\theta(x)}\gamma^\mu\partial_\mu\psi e^{i\theta(x)} - m\bar{\psi}e^{-i\theta(x)}\psi e^{i\theta(x)} \quad (2.4)$$

<sup>134</sup>

$$= i\bar{\psi}\gamma^\mu(\partial_\mu\psi + i\psi\partial_\mu\theta) - m\bar{\psi}\psi \quad (2.5)$$

<sup>135</sup> The  $\partial_\mu\theta$  terms breaks the gauge invariance of the Lagrangian. By introducing a  
<sup>136</sup> new field,  $A_\mu$  we can recover the gauge invariance of the derivative. Now redefining  
<sup>137</sup> the derivative as the covariant derivative:

$$D_\mu\psi \equiv (\partial_\mu - iqA_\mu)\psi \quad (2.6)$$

<sup>138</sup> And letting  $A_\mu$  transform under  $U(1)$  as:

$$A_\mu \rightarrow A_\mu + \delta A_\mu \quad (2.7)$$

<sup>139</sup> The transformed covariant derivative becomes:

$$D_\mu\psi \rightarrow D_\mu\psi' = (\partial_\mu - iqA_\mu)\psi' \quad (2.8)$$

<sup>140</sup>

$$= (\partial_\mu - iq(A_\mu + \delta A_\mu))\psi e^{i\theta} \quad (2.9)$$

<sup>141</sup>

$$= e^{i\theta}D_\mu + ie^{i\theta}\psi(\partial_\mu\theta - q\delta A_\mu) \quad (2.10)$$

<sup>142</sup> The covariant derivative can be made gauage invariant by setting the last term  
<sup>143</sup> to zero.

$$\delta A_\mu = \frac{1}{q} \partial_\mu \theta \quad (2.11)$$

<sup>144</sup> So now  $A_\mu$  transforms as:

$$A_\mu \rightarrow A_\mu + \frac{1}{q} \partial_\mu \theta \quad (2.12)$$

<sup>145</sup> Finally, replacing the derivative with the covariant derivative the Dirac La-  
<sup>146</sup> grangian we have:

$$\mathcal{L} = i\bar{\psi}\gamma^\mu D_\mu \psi - m\bar{\psi}\psi - \frac{1}{4}F_{\mu\nu}F^{\mu\nu} \quad (2.13)$$

<sup>147</sup>

$$= \mathcal{L}_{QED} \quad (2.14)$$

<sup>148</sup> Here  $F_{\mu\nu} \equiv \partial_\mu A_\nu - \partial_\nu A_\mu$ . This last term in the Lagrangian is the kinetic  
<sup>149</sup> energy of the gauge boson field.

<sup>150</sup> So we have derived the QED Lagrangian. By requiring the free Dirac La-  
<sup>151</sup> grangian to be invariant under U(1) transformations we have generated a new  
<sup>152</sup> gauge boson field,  $A_\mu$ , which describes the photon. As expected the photon inter-  
<sup>153</sup> acts with fermions.

<sup>154</sup> Stepping back, a global U(1) gauge symmetry of the free Dirac Lagrangian  
<sup>155</sup> implies we cannot measure the absolute phase of a charged particle. A local U(1)  
<sup>156</sup> gauge symmetry changes the phase of fields differently across space time. For this  
<sup>157</sup> type of transformation to leave the Lagrangian invariant, we had to introduce an  
<sup>158</sup> additional field,  $A_\mu$ , which "communicates" these phase changes across space-time.  
<sup>159</sup> In less formal language this effectively means: if the field at one location changes,  
<sup>160</sup> this change is conferred to other particles via  $A_\mu$ .

## <sup>161</sup> 2.4 Yang-Mills Gauge Theories

<sup>162</sup> Requiring  $U(1)_{EM}$  gauge invariance of the free Dirac Lagrangian gave us QED.

<sup>163</sup> Requiring different gauge symmetries we can derive the structure of other inter-

<sup>164</sup> actions. Any gauge symmetry may be written as:

$$\psi_i \rightarrow \exp(i\theta^a T_{ij}^a) \psi_j \quad (2.15)$$

<sup>165</sup> Here  $\theta$  is a dimensionless real parameter and  $T$  is the generator of the gauge

<sup>166</sup> symmetry group. With this the covariant derivative can be written as:

$$D_\mu \psi_i \equiv \partial_\mu \psi_i + ig A_\mu^a T_{ij}^a \psi_j \quad (2.16)$$

<sup>167</sup> Then the gauge field must transform as:

$$A_\mu^a \rightarrow A_\mu^a - \frac{1}{g} \partial_\mu \theta^a - f^{abc} \theta^b A_\mu^c \quad (2.17)$$

<sup>168</sup> Here  $f$  is the structure constant of the gauge group. The field strength tensor

<sup>169</sup> is given by:

$$F_{\mu\nu}^a \equiv \partial_\mu A_\nu^a - \partial_\nu A_\mu^a - g f^{abc} A_\mu^b A_\nu^c \quad (2.18)$$

<sup>170</sup>

$$F_{\mu\nu}^a \rightarrow F_{\mu\nu}^a - f^{abc} \theta^b F_{\mu\nu}^c \quad (2.19)$$

<sup>171</sup> This gives the Yang-Mills Lagrangian:

$$\mathcal{L}_{YM} = -\frac{1}{4} F_{\mu\nu}^{a\mu\nu} F_{\mu\nu}^a + i \bar{\psi}_i \gamma^\mu D_\mu \psi_i + m \bar{\psi}_i \psi_i \quad (2.20)$$

## <sup>172</sup> 2.5 Particles in the Standard Model

<sup>173</sup> The SM consists of fermions (half-integer spin matter constituents) and bosons  
<sup>174</sup> (integer spin force mediators). Fermions are spinor representations of the Poincare  
<sup>175</sup> group and can be further separated into leptons and quarks. Bosons are the result  
<sup>176</sup> of requiring a particular symmetry among the spinor fields:

$$SU(3)_C \times SU(2)_L \times U(1)_Y \quad (2.21)$$

<sup>177</sup>  $SU(3)_C$  is the symmetry group of the strong force and generates eight gluon  
<sup>178</sup> fields,  $G_\mu$ .  $SU(2)_L$  is the symmetry group of the Electroweak force and generates  
<sup>179</sup> three electroweak boson fields. The mixing of this  $SU(2)_L$  and  $U(1)_Y$  gives rise  
<sup>180</sup> to the photon field, where Y is the weak-hypercharge:

$$Y = 2(Q - T_3) \quad (2.22)$$

<sup>181</sup> Q is the electromagnetic charge, and  $T_3$  is the z-component of the weak isospin.  
<sup>182</sup> Weak isospin is the charge associated with the  $SU(2)_L$  symmetry. The correspond-  
<sup>183</sup> ing covariant derivative is then:

$$D_\mu \phi \equiv (\partial_\mu + ig_1 B_\mu Y_{L/R} + [ig_2 W_\mu^\alpha T^\alpha]_L + [ig_3 G_\mu^\alpha \tau^\alpha]_C) \psi \quad (2.23)$$

<sup>184</sup> It is important to note that the gauge symmetry of the SM yields a particular  
<sup>185</sup> structure of the fermion representations. So for a given fermion to interact with  
<sup>186</sup> a given gauge field it must have a non-zero corresponding Noether charge for  
<sup>187</sup> that gauge symmetry. If the corresponding Noether charge is zero, that fermion  
<sup>188</sup> transforms as a singlet and does not participate in that gauge interaction.

<sup>189</sup> Fermions are divided into quarks and leptons based on their transformations  
<sup>190</sup> under  $SU(3)_C$ . Quarks transform as color triplets. Leptons transform as color

singlets and consequently do not interact with gluons. Fermions may be further  
 classified by their  $SU(2)_L$  interactions. Only the left-chiral part of fermions (denoted by L here) transform as  $SU(2)_L$  doublets, the right-chiral part forms singlets under this gauge. Lastly, all these groups of particles come in three generations, each a heavier copy of the previous, but with differing flavor quantum numbers.  
 This is summarized in Table 2.1 and shown in Figures 2.1 and 2.2.

SM Fermion Gauge Group	First Generation	Second Generation	Third Generation	$(SU(3)_C, SU(2)_L, U(1)_Y)$ Representations
Left-handed quarks	$\begin{pmatrix} u_L^r & u_L^g & u_L^b \\ d_L^r & d_L^g & d_L^b \end{pmatrix}$	$\begin{pmatrix} c_L^r & c_L^g & c_L^b \\ s_L^r & s_L^g & s_L^b \end{pmatrix}$	$\begin{pmatrix} t_L^r & t_L^g & t_L^b \\ b_L^r & b_L^g & b_L^b \end{pmatrix}$	$(3, 2, \frac{1}{6})$
Right-handed quarks	$(u_R^r, u_R^g, u_R^b)$ $(d_R^r, d_R^g, d_R^b)$	$(c_R^r, c_R^g, c_R^b)$ $(s_R^r, s_R^g, s_R^b)$	$(t_R^r, t_R^g, t_R^b)$ $(b_R^r, b_R^g, b_R^b)$	$(3, 1, \frac{2}{3})$ $(3, 1, -\frac{1}{3})$
Left-handed leptons	$\begin{pmatrix} \nu_e^L \\ e_L \end{pmatrix}$	$\begin{pmatrix} \mu_e^L \\ \mu_L \end{pmatrix}$	$\begin{pmatrix} \tau_e^L \\ \tau_L \end{pmatrix}$	$(1, 2, -\frac{1}{2})$
Right-handed leptons	$e_R$	$\mu_R$	$\tau_R$	$(1, 1, -1)$

**Table 2.1:** Representations of the SM fermions under  $SU(3)_C \times SU(2)_L \times U(1)_Y$  gauge symmetry group.  $SU(2)_L$  gauge transformations allow one to go between rows and  $SU(3)_C$  transformations allow one to go between columns in these fermion representations. [REWORD]

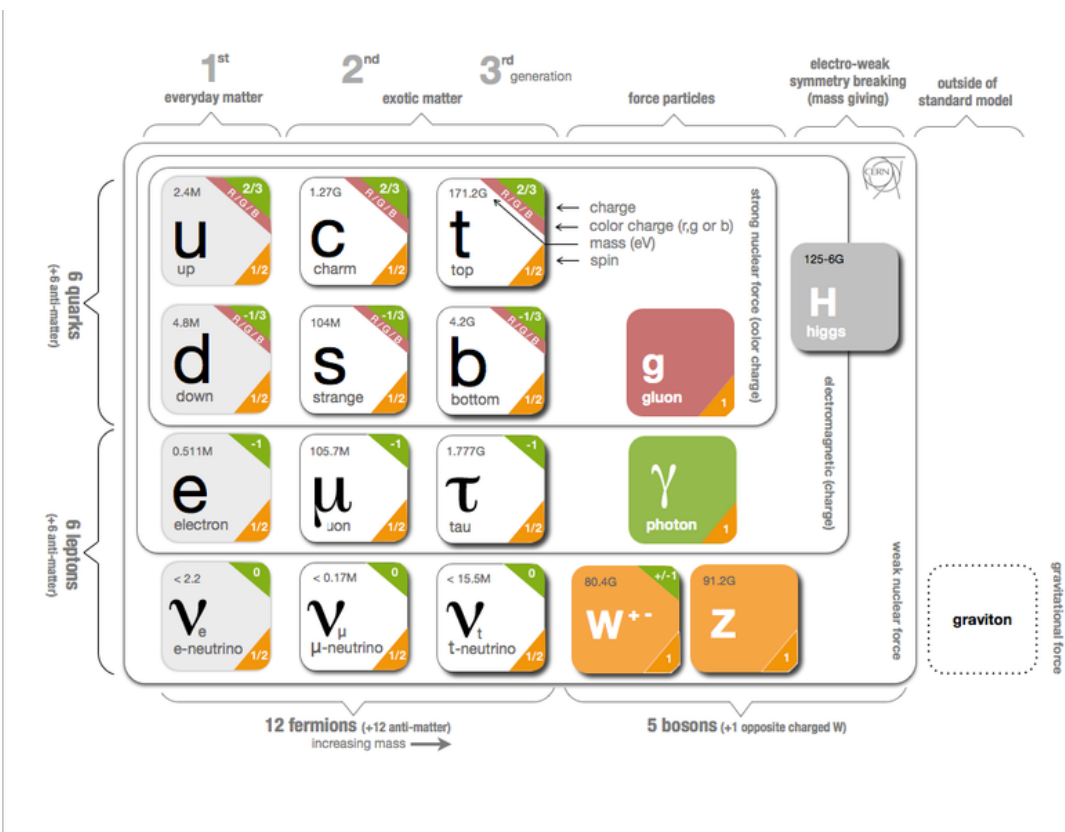


**Figure 2.1:** The particles of the Standard Model.



**Figure 2.2:** Summary of how Standard Model particles interact with other Standard Model particles.

197 Now we can understand the SM Lagrangian density as a Yang-Mills theory  
 198 with the gauge group:  $SU(3)_C \times SU(2)_L \times U(1)_Y$  with an additional  $SU(2)$  complex  
 199 scalar Higgs field doublet that will be discussed later.

$$\begin{aligned} \mathcal{L}_{SM} = & \underbrace{-\frac{1}{4}B_{\mu\nu}B^{\mu\nu} - \frac{1}{4}W_{\mu\nu}^a W^{a\mu\nu} - \frac{1}{4}G_{\mu\nu}^\alpha G^{\alpha\mu\nu}}_{\text{Kinetic Energies and Self-Interactions of Gauge Bosons}} \\ & + \underbrace{\bar{L}_i \gamma^\mu (i\partial_\mu - \frac{1}{2}g_1 Y_{iL} B_\mu - \frac{1}{2}g_2 \sigma^a W_\mu^a) L_i}_{\text{Kinetic Energies and EW Interactions of Left-handed Fermions}} \\ & + \underbrace{\bar{R}_i \gamma^\mu (i\partial_\mu - \frac{1}{2}g_1 Y_{iR} B_\mu) R_i}_{\text{Kinetic Energies and EW Interactions of Right-Handed Fermions}} \\ & + \underbrace{\frac{ig_3}{2} \bar{Q}_j \gamma^\mu \lambda^\alpha G_\mu^\alpha Q_j}_{\text{Strong Interactions between Quarks and Gluons}} \\ & + \underbrace{\frac{1}{2} |(i\partial_\mu - \frac{1}{2}g_1 B_\mu - \frac{1}{2}g_2 \sigma^a W_\mu^a)\Phi|^2 - V(\Phi)}_{\text{Electroweak Boson Masses and Higgs Couplings}} \\ & - (\underbrace{y_{kl}^d \bar{L}_k \Phi R_l + y_{kl}^u \bar{R}_k \tilde{\Phi} L_l + h.c.}_{\text{Fermion Mass terms and Higgs Couplings}}) \end{aligned}$$

200 Here several abstract spaces are being spanned:

- 201 – a spans the three  $SU(2)_L$  gauge fields with generators expanded in Pauli  
 202 matrices,  $T^\alpha = \frac{1}{2}\sigma^\alpha$
- 203 –  $\alpha$  spans the eight  $SU(3)_C$  gauge fields, with generators expanded in Gell-  
 204 Mann matrices,  $\tau^\alpha = \frac{1}{2}\lambda^\alpha$
- 205 – L/R represent left and right projections of Dirac fermion fields. The Strong  
 206 interaction is not chiral, so  $Q = L+R$

- 207 –  $\mu$  and  $\nu$  are four-vector indices
- 208 –  $i, j, k$  are summed over the three generations of SM particles.

## 209 2.6 Higgs Mechanism

210 The SM Lagrangian without the addition of a Higgs field does not allow for  
211 gauge boson and fermion mass terms:  $\frac{1}{2}m_A^2 A_\mu A_\mu$  and  $m(\bar{\psi}\psi)$ , as these terms are  
212 not gauge invariant. By introducing the Higgs field, mass terms for these particles  
213 may be included in a gauge invariant way. This field is a complex doublet with a  
214 potential  $V(\Phi)$ :

$$\Psi = \begin{pmatrix} \Phi^\dagger \\ \Phi^0 \end{pmatrix} \quad (2.24)$$

215

$$V(\Phi) = \mu^2 \Phi^\dagger \Phi + \lambda |\Phi^\dagger \Phi|^2 \quad (2.25)$$

216 The minima of this field occurs for  $|\Phi| = \sqrt{\frac{\mu^2}{2\lambda}} \equiv \frac{v}{2}$ . This yields degenerate  
217 minima, this symmetry is broken by choosing a specific minima (a.k.a. sponta-  
218 neous symmetry breaking). By convention  $\Phi_{min} = \frac{1}{\sqrt{2}} \begin{pmatrix} 0 \\ v \end{pmatrix}$  is chosen. This means  
219 the ground state of the Higgs field (Higgs vacuum) is non-zero,  $\sqrt{\frac{-\mu^2}{\lambda}}$ . The Higgs  
220 Field may now be expanded around this new ground state:

$$\Phi(x) = \frac{1}{\sqrt{2}} \begin{pmatrix} 0 \\ v + h(x) \end{pmatrix} \quad (2.26)$$

221 This non-zero Higgs vacuum now generates mass terms for the gauge bosons  
222 from the following term in the Lagrangian:

$$|(-\frac{1}{2}g_1B_\mu - \frac{1}{2}g_2\sigma^aW_\mu^a)\Phi|^2 = \frac{1}{2}m_W^2W_\mu^+W^{-\mu} + \frac{1}{2}m_Z^2Z_\mu Z^\mu \quad (2.27)$$

223 where:

$$W_\mu^\pm \equiv \frac{1}{\sqrt{2}}(W_\mu^1 \mp iW_\mu^2) \quad (2.28)$$

$$\begin{aligned} \text{224} \quad Z_\mu &\equiv \frac{1}{\sqrt{g_1^2 + g_2^2}}(g_2W_\mu^2 - g_1B_\mu) \end{aligned} \quad (2.29)$$

$$\begin{aligned} \text{225} \quad m_W &= \frac{vg_2}{\sqrt{2}} \end{aligned} \quad (2.30)$$

$$\begin{aligned} \text{226} \quad m_Z &= \frac{v}{\sqrt{2}}\sqrt{g_1^2 + g_2^2} \end{aligned} \quad (2.31)$$

227 The Higgs field also generates a mass term for the Higgs boson and self-  
228 interactions for the Higgs boson.

## 229 2.7 Electroweak Theory

230  $SU(2)_L$  generates  $W^\pm, W^0$  gauge bosons, which would be massless if  $SU(2)_L$   
231 was a perfect symmetry. These bosons are massive as this symmetry is broken.

232 The mass eigenstates,  $Z$  and  $\gamma$  given by:

$$\begin{pmatrix} Z_\mu \\ A_\mu \end{pmatrix} = \begin{pmatrix} \cos\theta_W & -\sin\theta_W \\ \sin\theta_W & \cos\theta_W \end{pmatrix} \begin{pmatrix} W_\mu^3 \\ B_\mu \end{pmatrix} \quad (2.32)$$

233 Here  $\theta_W$  is the Weinberg angle given by:

$$\cos\theta_W = \frac{g_2}{\sqrt{g_1^2 + g_2^2}} = \frac{m_W}{m_Z} \quad (2.33)$$

## <sup>234</sup> 2.8 Quantum ChromoDynamics

<sup>235</sup> As mentioned earlier the Strong Force, which binds the proton together, is  
<sup>236</sup> mediated by gluons. Quantum Chromodynamics is the QFT which describes the  
<sup>237</sup> interactions of quarks and gluons via  $SU(3)_C$  symmetry. QCD contains features  
<sup>238</sup> not present in Electroweak Interactions due to  $SU(3)_C$  generators not commuting  
<sup>239</sup> (a.k.a.  $SU(3)_C$  is a non-abelian group). For example, in QCD there is color  
<sup>240</sup> confinement and asymptotic freedom due to the structure constants being non-  
<sup>241</sup> zero. Requiring  $SU(3)_C$  local gauge invariance implies:

$$\psi(x) \rightarrow \psi(x)' = \exp[i g_S \alpha(x) \cdot \hat{T}] \psi(x) \quad (2.34)$$

<sup>242</sup> where  $\alpha(x)$  is the local phase function,  $g_S$  is the strong coupling constant, and  
<sup>243</sup>  $\hat{T}$  are the eight generators of  $SU(3)$  (note  $\hat{T}^a = \frac{1}{2}\lambda^a a$ , where  $\lambda^a$  are the Gell-Mann  
<sup>244</sup> matrices). As the Gell-Mann matrices are 3x3, this means  $\psi$  has three degrees of  
<sup>245</sup> freedom under these  $SU(3)$  rotations. So we represent  $\psi$  under  $SU(3)$  rotations  
<sup>246</sup> as:

$$\psi = \begin{pmatrix} \psi_{red} \\ \psi_{green} \\ \psi_{blue} \end{pmatrix} \quad (2.35)$$

<sup>247</sup> Consequently, particle fields transforming under  $SU(3)$  rotations have three  
<sup>248</sup> components which physicists describe as color components (red, green, and blue).  
<sup>249</sup> A particle's corresponding antiparticle has the corresponding anticolor. This color  
<sup>250</sup> is the "charge" of QCD and is conserved under  $SU(3)$  rotations. Combining colors,  
<sup>251</sup> color neutral states (e.g. red and antired, or red, green and blue) may be created.  
<sup>252</sup> For the Free Dirac Lagrangian to remain invariant under  $SU(3)$  transformations,  
<sup>253</sup> we must again postulate a boson field that modifies the derivative. The gluon

254 field tensor is given by ( $\alpha = 1, \dots, 8$ ):

$$G_{\mu\nu}^k = \partial^\mu G_\alpha^\nu - \partial^\nu G_\alpha^\mu - g_S f^{\alpha\beta\gamma} G_\beta^\mu G_\gamma^\nu \quad (2.36)$$

255 Here  $f^{\alpha\beta\gamma}$  are the structure constants of  $SU(3)$ . Combining all this gives the  
256 QCD Lagrangian:

$$\mathcal{L}_{QCD} = \bar{\psi}_q i\gamma^\mu (D_\mu)_{ij} \psi^{qj} - m \bar{\psi}^{qi} \psi_{qi} - \frac{1}{4} G_{\mu\nu}^\alpha G^{\alpha\mu\nu} \quad (2.37)$$

257 Here  $i$  are the color indices, and  $q$  are the quark flavors. It is important to  
258 note that quarks transform under the fundamental representation of  $SU(3)$ , while  
259 gluons transform under the adjoint representation. This means quarks carry a  
260 single color charge (red, green, blue, antired, antigreen, antiblue) and gluons carry  
261 a color and anticolor charge.

262 Figure 2.3 shows the three dominant QCD interactions. Since gluons carry  
263 color charge, they interact with one another. This does not occur in QED, as  
264 photons do not have electric charge and therefore do not interact with each other.  
265 In QED, a bare electron's effective charge is largest closest to the electron and  
266 decreases as a function of distance. This is because the QED vacuum fills with  
267 particle antiparticle pairs spontaneously, which screen the charge of the bare elec-  
268 tron. The larger the distance from the electron, the smaller the effective charge  
269 and therefore the weaker the force. So for a pair of electrons, as the distance  
270 between them increases the repulsive force decreases and they may be observed  
271 separately.

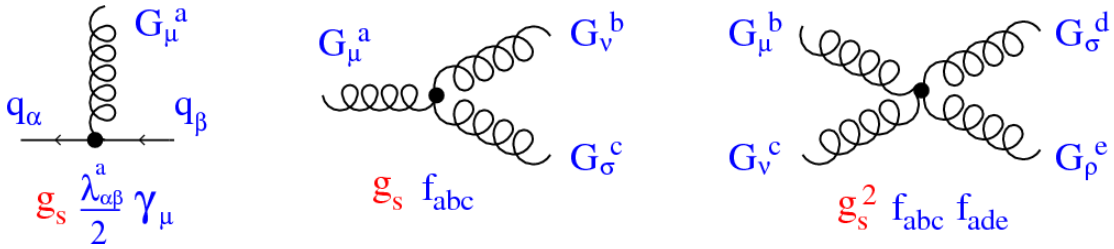


**Figure 2.3:** This figure shows the three dominant QCD interactions. From Ref. [17]

272        As the distance from a quark increases it's effective color charge increases due  
 273        to the vacuum polarization in QCD. Color charge grows as the distance from  
 274        the source increases (a.k.a. color is anti-screened in QCD). In this way, strong  
 275        interactions become stronger at large distances (low momenta interactions). At  
 276        small distances (large momenta interactions) strong interactions are significantly  
 277        weaker and considered nearly free. This effect of referred to as asymptotic freedom.  
 278        At large distances, a quark's effective charge is large and the strong force is more  
 279        significant. This force becomes so strong that quarks form colorless bound states  
 280        instead of remaining free particles. This effect is known as color confinement.  
 281        This running of all SM fields is shown in Figure 2.4.



**Figure 2.4:** Strength of the U(1), SU(2), and SU(3) gauge couplings as a function of the energy scale of the interaction ( $Q$ ). From Ref. [11]

Commonly the change in a particle's effective charge under a given force is quantified with  $\beta(r) \equiv -\frac{de(r)}{d\ln r}$ , where  $e(r)$  is the effective charge of a given particle under a force. In QED this function is positive but in QCD this function is negative leading to confinement and asymptotic freedom. Moreover, one can calculate how the coupling ( $\alpha$ ) of a force varies with energies. (More deeply this amounts to incorporating renormalization and vacuum polarization in the boson propagators).

For QCD this is:

$$\alpha_S(x) = \frac{\alpha_S(\mu^2)}{1 + \beta_0 \alpha_S(\mu^2) \ln(Q^2/\mu^2)} \quad (2.38)$$

289

$$\beta_0 = \frac{11N_c - 2n_f}{12\pi} \quad (2.39)$$

290 where  $Q$  is the momentum of the the force is probed at,  $\mu^2$  is the renormalization scale.

292 As stated previously, quarks and gluons have not been observed in isolation.  
 293 Instead they form bound colorless states. Hadronization is the process by which  
 294 quarks and gluons form hadrons. The process of hadronization is still an active  
 295 area of research. One qualitative description is show in Figure [Natasha add  
 296 figure]. In this figure, as two quarks separate the color field between them is  
 297 restricted to a tube with energy density of 1GeV/fm. As they separate further,  
 298 the energy in the color field increases, until there is enough energy to produce  
 299  $q\bar{q}$  pairs, which breaks the color field. This process repeats until quarks and  
 300 antiquarks have low enough energy to form colorless hadrons. The resulting spray  
 301 of hadrons is called a jet.

302 Since quarks and gluons carry different color charges, their respective jets have  
 303 different properties. As quarks carry only a single color charge (vs. gluons which  
 304 have color and anticolor charge), so their jets have less constituent particles. More  
 305 precisely, the Altarelli-Parisi splitting functions [3] contain a factor  $C_A$  for gluon  
 306 radiation off a gluon and  $C_F$  for gluon radiation off a quark ( $C_A/C_F = 9/4$ ). These  
 307 color factors are the prefactor in the Feynman diagrams for these processes [1],  
 308 which leads to gluon jets having more constituents and therefore more tracks than  
 309 quark jets. Gluon jets also tend to have a larger radius with lower momentum  
 310 constituents than quarks. There are many novel techniques to distinguish quarks  
 311 from gluons. For this study the number of charged particles will be focused on.

<sup>312</sup> **Chapter 3**

<sup>313</sup> **Standard Model Successes and  
<sup>314</sup> Limitations**

<sup>315</sup> The Standard Model has consistently described much of reality to an extreme  
<sup>316</sup> degree of accuracy. It has predicted cross sections for strong and electroweak pro-  
<sup>317</sup> cesses that span over ten order of magnitude correctly [see Fig. 3.1] and contains  
<sup>318</sup> no known logical inconsistencies. Despite the strength and reality of the Stan-  
<sup>319</sup> dard Model, it still fails to describe aspects of reality and suffers from aesthetic  
<sup>320</sup> issues. To date, dark matter and energy comprise 95% of the universe, but are  
<sup>321</sup> not accounted for in the SM. Additionally, neutrinos are known to have mass but  
<sup>322</sup> are massless in the SM. There are mechanisms for introducing massive neutrinos  
<sup>323</sup> in the SM, but these mechanisms create hierarchy problems.

<sup>324</sup> Possibly the most significant aesthetic issue is the hierarchy between the elec-  
<sup>325</sup> troweak and Planck scales. The electroweak scale is the scale of electroweak  
<sup>326</sup> symmetry breaking. The Planck scale is the scale where the gravitational force  
<sup>327</sup> is comparable in strength to the other forces. The Planck scale is where the SM  
<sup>328</sup> breaks down, as there is not an experimentally verified theory of quantum gravity,  
<sup>329</sup> and at this scale gravity cannot be ignored (like it can at the electro-weak scale).

330 These scales differ by  $\sim 30$  orders of magnitude. Understanding the difference  
331 in these energy scales, may help explain the weakness of gravity at electroweak  
332 scales, and possibly a QFT for gravity. (NB: This hierarchy can also be framed in  
333 terms of the corrections to the Higgs mass, which depend on the UV cutoff scale -  
334 where the SM is suppose to break, which is taken at the Planck scale. This leads  
335 the quantum corrections to the Higgs mass to force the Higgs mass to  $10^{18}$  TeV.)

336 These stark contrasts in scales may indicate that a more fundamental theory  
337 exists. It is hoped that such a theory would explain and motivate some of the ad-  
338 hoc features of the SM. In particular, there currently are no experimentally verified  
339 explanations of why there are three generations of fermions, the values of the 19  
340 SM parameters (6 quark masses, 3 charged lepton masses, 3 gauge couplings,  
341 Higgs parameters  $(\mu^2, \lambda)$ ), the structure of the fermion representations, etc.

### Standard Model Production Cross Section Measurements

Status: July 2018

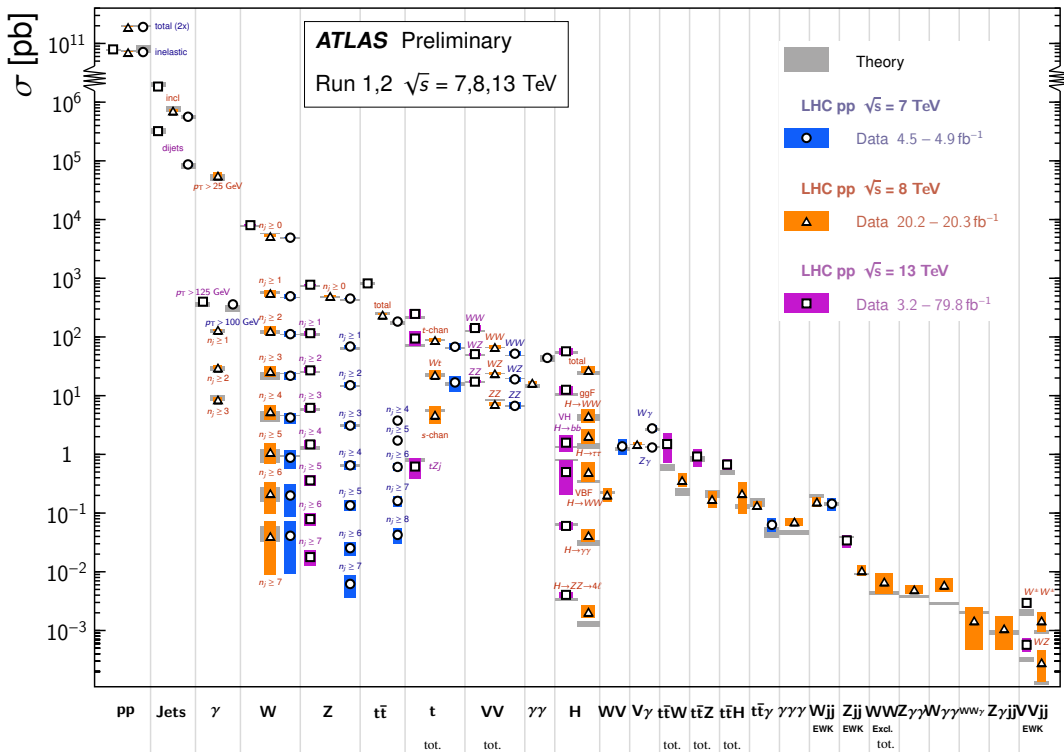


**Figure 3.1:** A comparison of cross section measurements at  $\sqrt{s} = 7, 8, 13$  TeV from ATLAS compared to theoretical measurements. From Ref. [5]

<sup>342</sup> **Chapter 4**

<sup>343</sup> **New Physics Models with**

<sup>344</sup> **Diboson Resonances**

<sup>345</sup> **4.1 Randall Sundrum Bulk Model**

<sup>346</sup> The electroweak-planck hierarchy may be explained by the existence of extra  
<sup>347</sup> dimensions, like the 5D Randall Sundrum Bulk Model ([18], [2]). In this model,  
<sup>348</sup> there is one extra warped spatial dimension,  $y$ , with a metric:

$$ds^2 = e^{-2k|y|} \eta_{\mu\nu} dx^\mu dx^\nu + dy^2 \quad (4.1)$$

<sup>349</sup> where  $e^{-k|y|}$  is the warp factor of the extra dimension, which is compactified on  
<sup>350</sup> a  $S^1/Z_2$  orbifold (a.k.a. a circle where  $y \rightarrow -y$ ). This can be visualized as every  
<sup>351</sup> point in space time having a line extending from it a distance  $L$ , representing  
<sup>352</sup> this fifth dimension. At the end of this line is the Planck brane. This fourth  
<sup>353</sup> spatial dimension separates two 4-D branes: Planck brane and TeV brane. We  
<sup>354</sup> live on the TeV brane, as shown in Figure 4.1. The Higgs field (and to a lesser  
<sup>355</sup> degree the top quark and graviton fields) is localized near the TeV Brane, while

356 the light fermion fields are localized more near the Planck brane. Fundamental  
 357 parameters are set on the Planck brane. The warp factor may be scaled away from  
 358 all dimensionless SM terms by field redefinitions. However, the only dimensionful  
 359 parameter,  $m_H^2 = v^2$  is rescaled by  $\tilde{v} \sim e^{-kL} M_{Pl} \sim 1\text{TeV}$  for  $kL \sim 35$ , explaining  
 360 why gravity is so weak on the TeV brane. Also, by localizing the light fermion  
 361 fields near the Planck brane and top and graviton fields near the TeV brane, the  
 362 light quarks will have smaller masses.

363 The two free parameters of this theory are  $M_{Pl}$  and  $k$ . Based on this RS Bulk  
 364 model, all SM particles should have Kaluza-Klein (KK) excitations. In particular,  
 365 the graviton would have KK excitations that prefer to decay to WW or ZZ, which  
 366 is why this analysis searches for RS Gravitons.

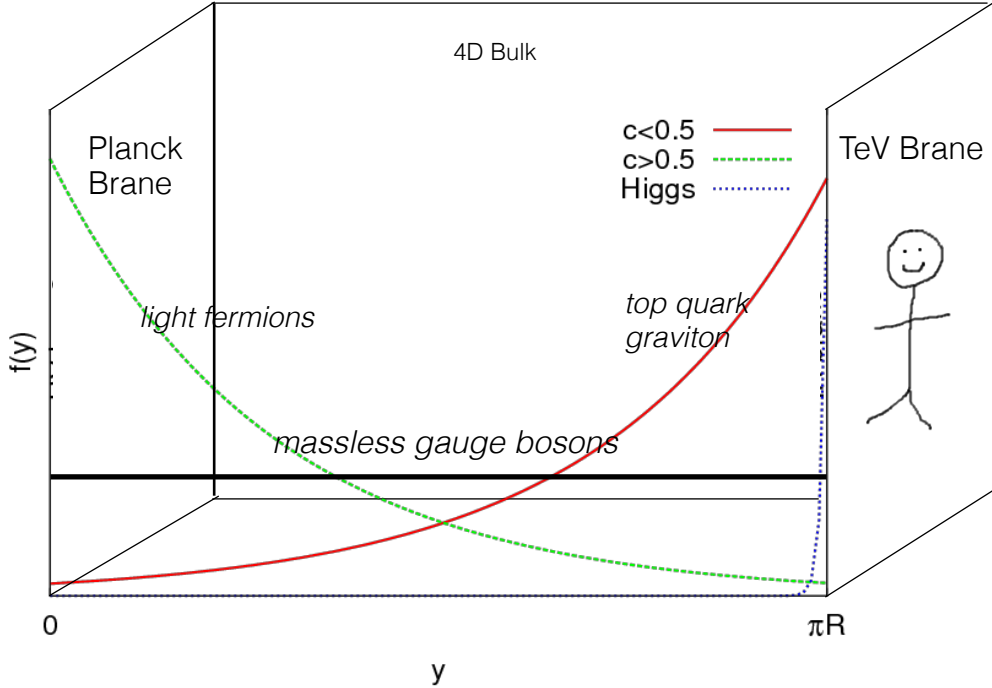


**Figure 4.1:** Cartoon of RS Bulk Model

## <sup>367</sup> 4.2 Simple Standard Model Extensions

<sup>368</sup>      The RS Bulk model is motivated by resolving the hierarchy problem. Ex-  
<sup>369</sup> tending the Scalar sector is a natural space to look for new physics due to the  
<sup>370</sup> complexity of fermion and boson groups. There are many other interesting and  
<sup>371</sup> well motivated frameworks, but there is a lack of completely predictive models,  
<sup>372</sup> due to model flexibility (free parameters). Therefore it is hard for experimentalists  
<sup>373</sup> to know which theories to search for in data. However, as seen in [16], a "Simpli-  
<sup>374</sup> fied Model" approach may be taken. In the search for reasonably narrow width  
<sup>375</sup> particles, as in this search, the search is not sensitive to all the details and free  
<sup>376</sup> parameters of the theory. Generally such searches are only sensitive to the reso-  
<sup>377</sup> nance mass and its interactions. Therefore, a theory's Lagrangian may be reduced  
<sup>378</sup> to only retain this information (mass parameters and couplings). Experimental  
<sup>379</sup> results using this framework may then be reinterpreted in a given theory.

<sup>380</sup>      In the simplified approach, the new resonance searched for is represented as  
<sup>381</sup> a real vector field in the adjoint representation of  $SU(2)_L$  with vanishing hyper-  
<sup>382</sup> charge. This results in one neutral and two charged bosons. Defined as:

$$V^\pm = \frac{V_\mu^1 \mp i V_\mu^2}{\sqrt{2}} \quad (4.2)$$

<sup>383</sup>       $V_\mu^0 = V_\mu^3 \quad (4.3)$

<sup>384</sup>      The SM Lagrangian is then augmented with the additional terms:

$$\mathcal{L} \supset -\frac{1}{4} D_{[\mu} V_{\nu]}^a D^{[\mu} V^{\mu]a} + \frac{m_V^2}{2} V_\mu^a V^{a\mu} + ig_V c_H V_\mu^a H^\dagger \tau^a \overset{\leftrightarrow}{D}{}^\mu H + \frac{g^2}{g_V} c_F V_\mu^a J_F^{\mu a} \quad (4.4)$$

<sup>385</sup>      In order the terms represent: the kinetic,  $V$  mass, Higgs- $V$  interaction, and  
<sup>386</sup>  $V$ -left-handed fermion interaction terms. Phenomenologically the three physical

387 particles this predicts are degenerate, where  $V$  couples most strongly to  $VV$ , via  
388 the  $g_V$  coupling factor. The dominant production modes are DY and VBF.

389 Two versions of HVT are considered, Model A and B. Model A is a weakly  
390 coupled model where  $g_V \sim 1$ , like the extended gauge symmetry discussed in Ref  
391 . [16]. Model B is a strongly coupled model, where  $1 < g_V < 4\pi$ . The width  
392 of the resonance grows with  $g_V$  so for this narrow resonance search only  $g_V$  is  
393 chosen to be less than 6 (so  $\Gamma/M < 10\%$ ). More precisely, the coupling of these  
394 resonances to fermions scales as  $g_f = g^2 c_F/g_V$ , where  $g$  is the SM  $SU(2)_L$  gauge  
395 coupling and  $c_F$  is the free parameter (expected to be of order 1 for Model A and  
396 B). This then means that for Model B the coupling to fermions is more suppressed  
397 than for Model A, leading to a smaller DY production rate and BR to fermionic  
398 final states. The coupling of  $V$  to SM bosons scales as  $g_H = g_V c_H$ , where  $c_H$  is  
399 a free parameter on the order of 1 for Model A and B. So for small values of  $g_V$   
400 (i.e. Model A - weakly coupled theories) the BR to gauge bosons is smaller than  
401 for Model B. So weakly coupled vectors have large production cross sections and  
402 decay prominently to leptons or jets, while strongly coupled vectors are produced  
403 less and decay predominantly to gauge bosons.

404 Vectors in Model A and B are generally produced via quark-anti-quark annihi-  
405 lation. The more rare production via vector-boson-fusion is considered by setting  
406  $g_H = 1$  and  $g_F = 0$ . In Model B diboson final states are enhanced as stated  
407 previously due to  $g_H$  and moreover the BR to  $WZ$ ,  $WH$ ,  $WW$ , and  $ZH$  are the  
408 same.

409 In summary,  $V$  couples most strongly to left-handed fermions and  $VV$  depen-  
410 dent on  $g_V$ .

411

## Part III

412

## Experimental Setup

<sup>413</sup> **Chapter 5**

<sup>414</sup> **LHC**

<sup>415</sup> The Large Hadron Collider (LHC) is the highest-energy particle collider in the  
<sup>416</sup> world. It was designed to expand the frontier of high energy particle collisions in  
<sup>417</sup> energy and luminosity. This enables LHC experiments to test the Standard Model  
<sup>418</sup> and search for new physics at higher energies than tested with previous colliders.  
<sup>419</sup> Collisions at higher energies not only produce more massive particles but also  
<sup>420</sup> more weakly interacting particles. Fig 5.1 shows production cross sections for  
<sup>421</sup> various processes at hadron colliders. The rate for electroweak physics processes  
<sup>422</sup> including  $W$  and  $Z$  scale with the center-of-momentum energy,  $\sqrt{s}$ .

<sup>423</sup> The LHC consists of a 26.7 km (17 miles) ring, approximately 100 m un-  
<sup>424</sup> derground, outside Geneva, Switzerland. Counter-circulating proton (and occa-  
<sup>425</sup> sionally heavy ions) beams collide inside four experiments along the beam line:  
<sup>426</sup> ATLAS, CMS, LHCb, ALICE. ATLAS and CMS are general purpose detectors de-  
<sup>427</sup> signed to explore the high energy frontier. LHCb is designed to study the physics  
<sup>428</sup> of  $b$ -quarks. ALICE specializes in studying heavy ion collisions.

## proton - (anti)proton cross sections

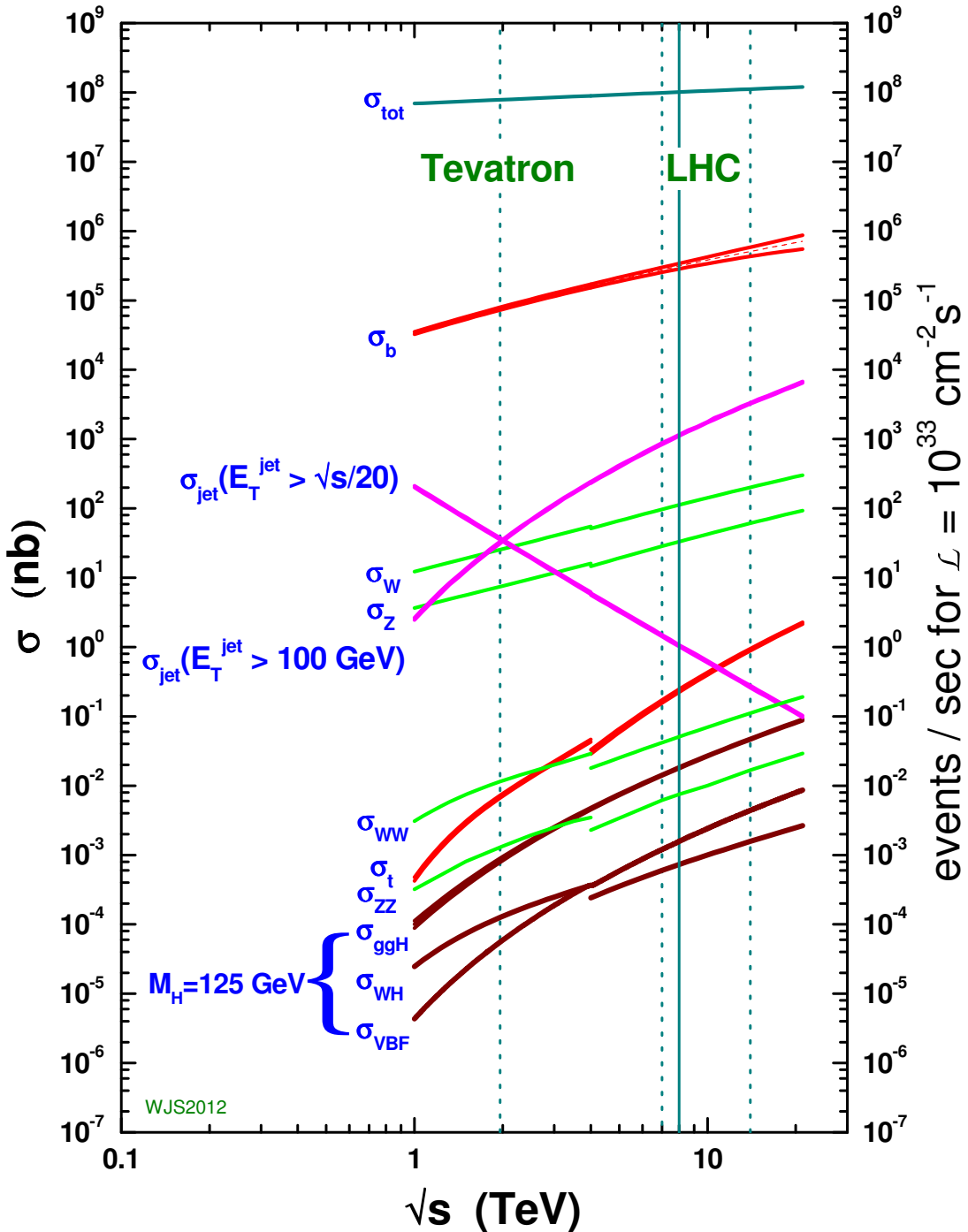
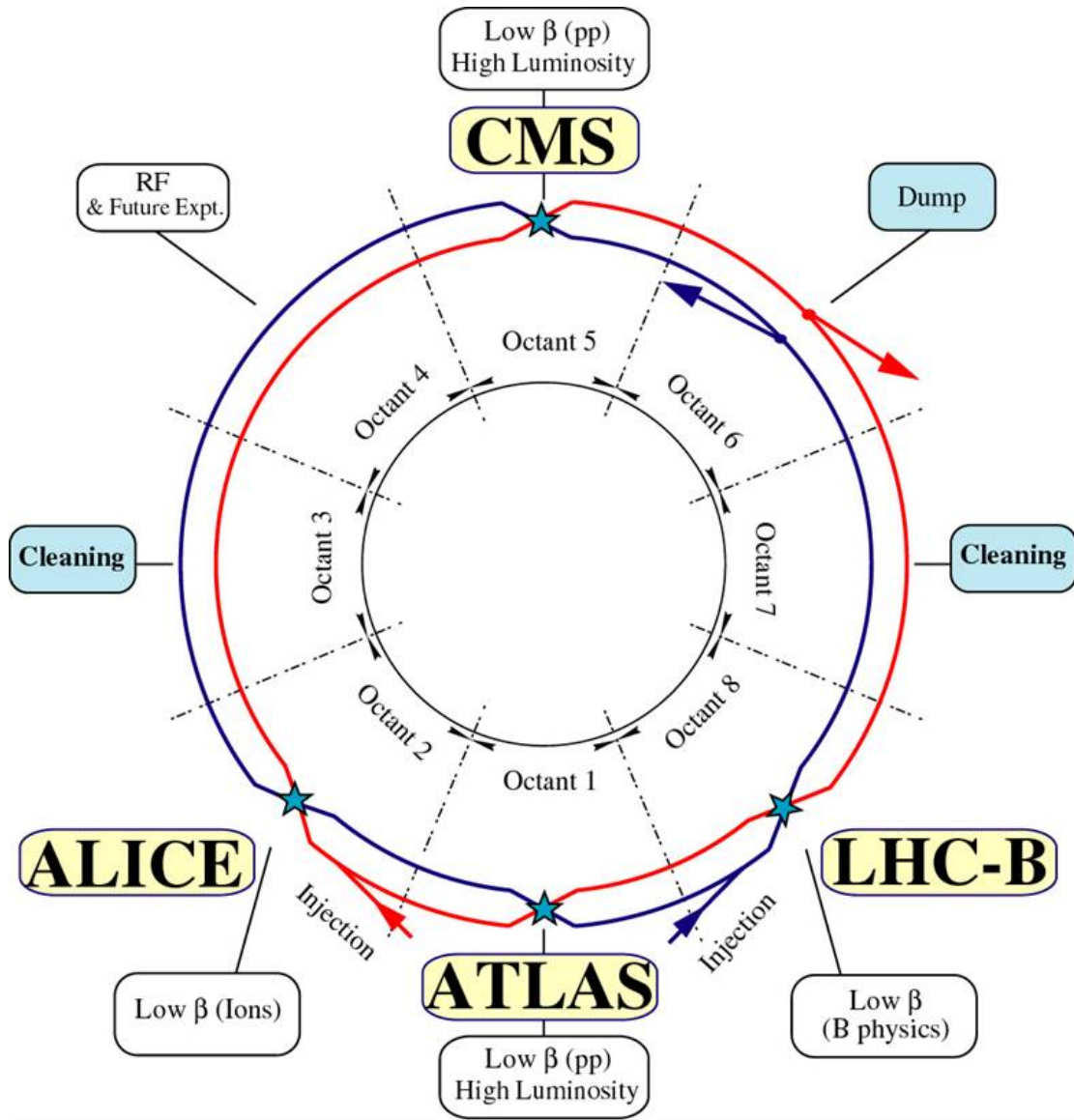


Figure 5.1: Scaling of cross sections with  $\sqrt{s}$ . Natasha: write more here

429        The first proton beams circulated in September, 2008. Nine days later an elec-  
430        trical fault lead to mechanical damage and liquid helium leaks in the collider. This  
431        incident delayed further operation until November 2009, when the LHC became  
432        the world's highest energy particle collider, at 1.18TeV per beam. This first oper-  
433        ational run continued until 2013, reaching 7 and 8 TeV collision energies. During  
434        this run a particle with properties consistent with the Standard Model Higgs bo-  
435        son was discovered. The next run began after a two year shutdown after upgrades  
436        to the LHC and experiments. This run lasted from 2013 to 2018 reaching 13 TeV  
437        collision energies. This analysis uses data from the second operational run.

## 438        5.1 LHC Layout and Design

439        The layout of the LHC is shown in Figure 5.2. The red and blue lines in the  
440        figure represent the counter-circulating proton beams. The LHC is divided into  
441        eight octants. Octant 4 contains the RF cavities that accelerate the protons and  
442        octant 6 contains the beam dump system. Octants 3 and 7 house the collimation  
443        systems for beam cleaning. The beams collide inside the four aforementioned  
444        experiments. Each octant contains a curved and straight section. The LHC  
445        magnets are built with NbTi superconductors cooled with super-fluid Helium to  
446        2K, creating a 8.3T magnetic field to bend the proton beams.

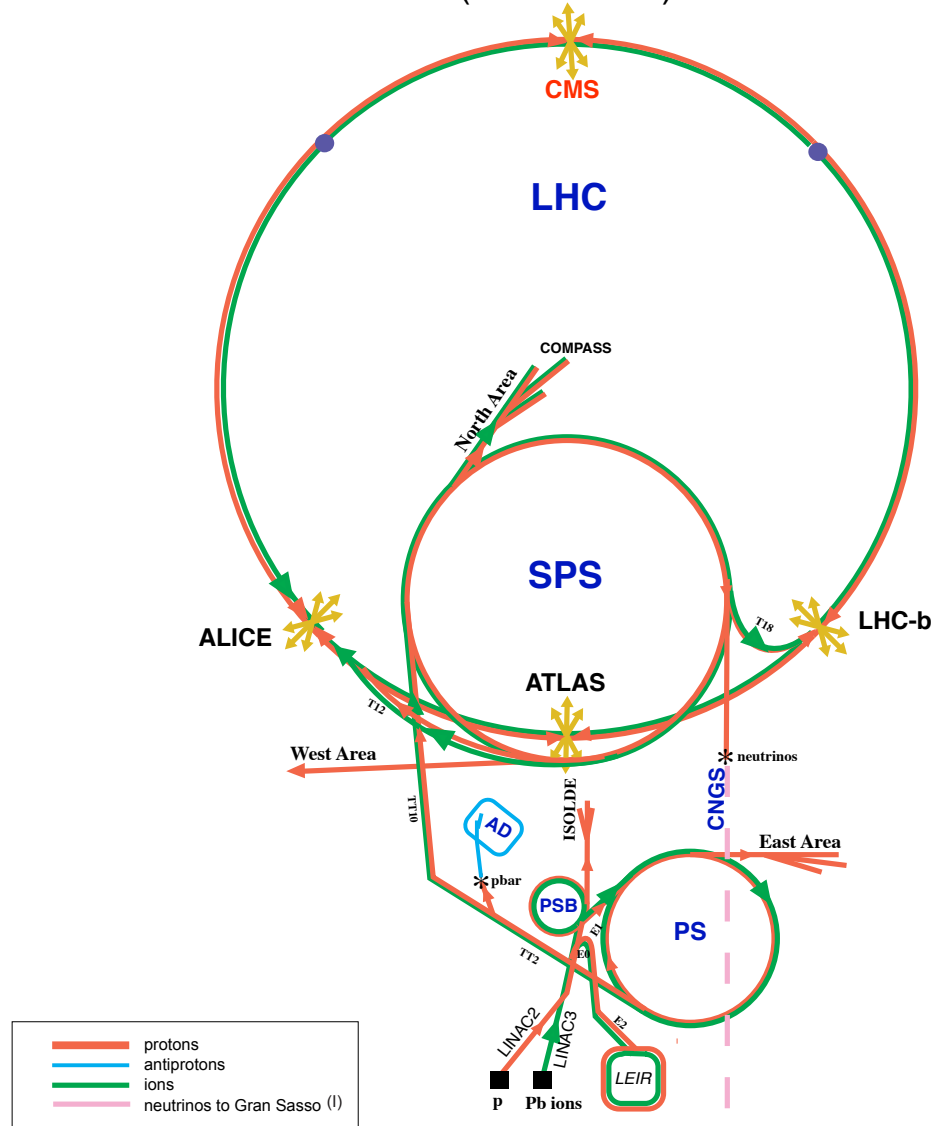


**Figure 5.2:** LHC Layout. Natasha write more

447     Four sequential particle accelerators are used to accelerate protons from rest  
 448    as shown in Figure 5.3. First, Hydrogen gas is ionized to produce protons which  
 449    are then accelerated to 50 MeV using Linac 2, a linear accelerator. The result-  
 450    ing proton beam is then passed to three circular particle accelerators: Proton  
 451    Synchrotron Booster, Proton Synchrotron, and Super Proton Synchrotron (SPS),

452 accelerating protons to 1.4, 25, and 450 GeV, respectively. Once the protons exit  
453 the SPS, they are injected into the LHC at octant 2 and 8. Each proton bunch  
454 contains  $\sim 10^{11}$  protons. The spacing between bunches is 25 ns, which means  
455 each beam contains 3564 bunches. However, some bunches are left empty due  
456 to injection and safety requirements, yielding 2808 bunches per beam. Once the  
457 proton beams are injected they are accelerated to 13 TeV.

## CERN Accelerators (not to scale)



LHC: Large Hadron Collider

SPS: Super Proton Synchrotron

AD: Antiproton Decelerator

ISOLDE: Isotope Separator OnLine DEvice

PSB: Proton Synchrotron Booster

PS: Proton Synchrotron

LINAC: LINear ACcelerator

LEIR: Low Energy Ion Ring

CNGS: Cern Neutrinos to Gran Sasso

Rudolf LEY, PS Division, CERN, 02.09.96  
Revised and adapted by Antonella Del Rosso, ETT Div.,  
in collaboration with B. Desforges, SL Div., and  
D. Manglunki, PS Div. CERN, 23.05.01

**Figure 5.3:** LHC Accelerator. Natasha write more

458        As many new physics models predict cross-sections below the weak scale it was  
459        important to design the LHC to be capable of collecting enough data, by running  
460        in high luminosity conditions. The machine luminosity depends only on beam  
461        parameters:

$$L = \frac{N_p^2 f}{4\epsilon\beta^*} F \quad (5.1)$$

462        where  $N_p$  is the number of protons per bunch,  $f$  is the bunch crossing frequency,  
463         $\epsilon$  is the transverse beam emittance,  $\beta^*$  is the amplitude function at the collision  
464        point, and  $F$  is the geometric luminosity reduction factor due to the beams crossing  
465        at an angle (rather than head-on).

466 **Chapter 6**

467 **The ATLAS Detector**

468 The ATLAS detector measures the position, momentum and energy of parti-  
469 cles produced in the proton collisions by using magnetic fields, silicon detectors,  
470 sampling calorimeters, and gaseous wire detectors. It is located approximately  
471 100 m underground at Point-1 around the LHC beam line and weighs 7000 metric  
472 tons. The detector is 46 m long, 25 m high, 25 m wide as shown in Figure 6.2.  
473 The detector can be divided into three subsystems: the Inner Detector (ID), the  
474 Calorimeters, and the Muon Spectrometer (MS). Figure 6.3 shows an overview of  
475 how different particles interact in the detector.

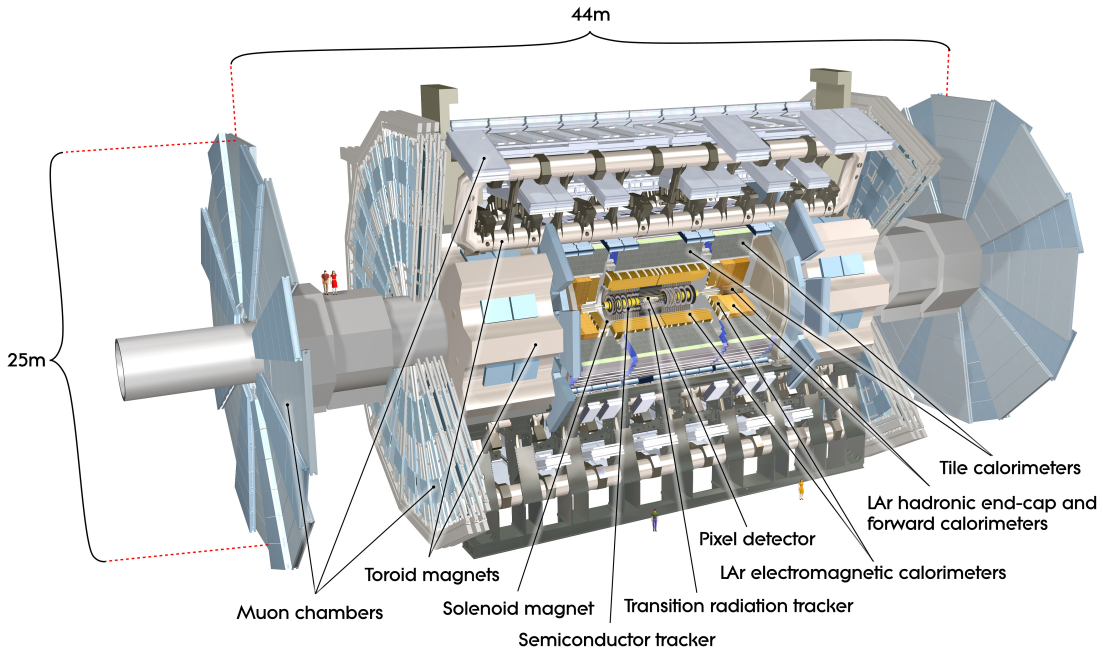


**Figure 6.1:** Big picture layout of ATLAS detector. Natasha: write more

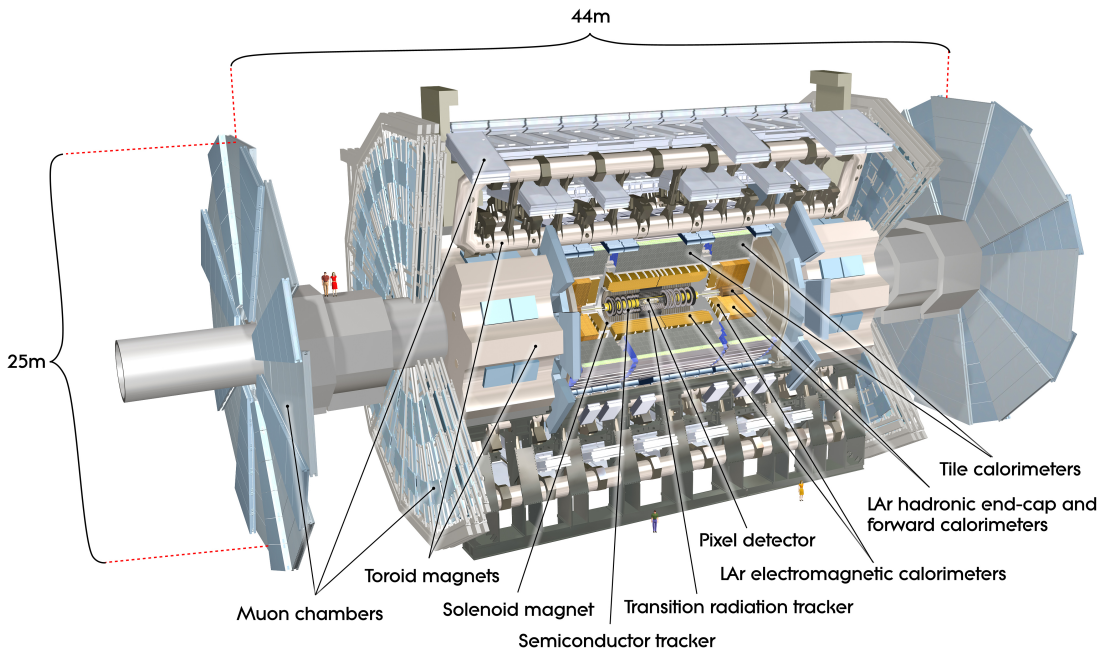


**Figure 6.2:** Big picture layout of ATLAS detector. Natasha: write more

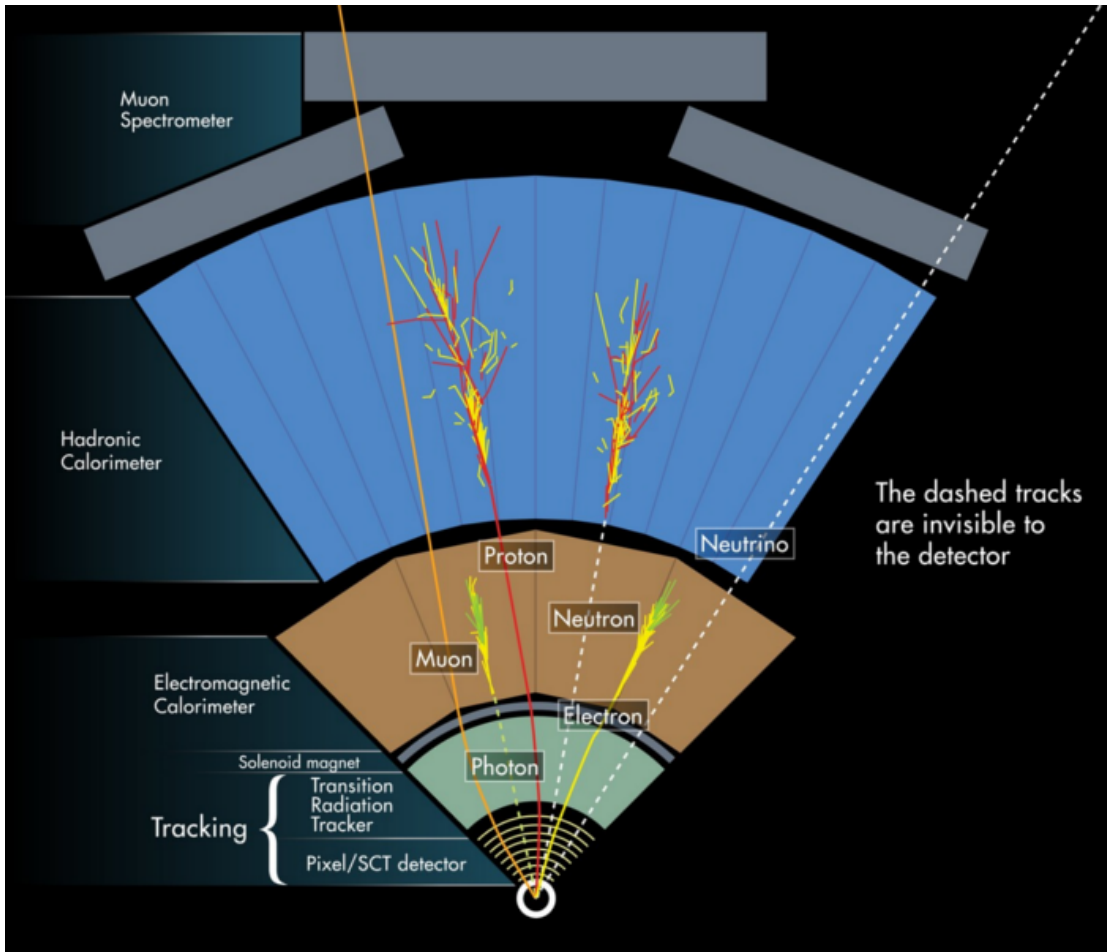


**Figure 6.3:** A simplified schematic of how different particles interact and are detected within ATLAS.

## 476 6.1 Coordinate System

477     The trajectory of particles within ATLAS is measured relative to the nominal  
 478 interaction point. The  $z$ -axis points along the beam line, such that when the  
 479 LHC is viewed from above, the counter-clockwise circulating beam points along  
 480 the positive- $z$  direction. The  $x - y$  plane is transverse to the beam line, with the  
 481 positive  $x$ -axis pointing towards the center of the LHC ring. The positive  $y$ -axis  
 482 points vertically upward. The azimuthal angle,  $\phi$ , is the angular distance about

483 the  $z$ -axis, with  $\phi = 0$  along the  $x$ -axis. The polar angle from the  $z$ -axis is denoted  
484 as  $\theta$ . However, this quantity is not Lorentz invariant, like rapidity,  $y = \frac{1}{2} \ln \frac{E+p_z}{E-p_z}$ ,  
485 where  $E$  is the energy of the particle considered, and  $p_z$ , is it's momentum along  
486 the  $z$ -axis. Pseudo-rapidity is preferred as  $\Delta\eta$  is invariant under boosts along  $z$   
487 and particle production is approximately invariant under  $\eta$ . For massless particles,  
488 rapidity and a related quantity, pseudorapidity, are the identical. The pseudora-  
489 pidity is defined as:  $\eta = -\ln \tan(\frac{\theta}{2})$ . This quantity is preferred as it is purely a  
490 geometric quantity, independent of particle energy. Angular separation between  
491 particles in ATLAS are given by  $\Delta R = \sqrt{\Delta\eta^2 + \Delta\phi^2}$ . The distance from the  
492 beamline is given by  $r = \sqrt{x^2 + y^2}$

## 493 6.2 Inner Detector

494 The Inner Detector (ID) was designed to identify and reconstruct vertices,  
495 distinguish pions from electrons, and measure the momentum of charged particles.  
496 The ID uses three different technologies for particle reconstruction: the Pixel  
497 Detector, Semiconductor Tracker (SCT), and the Transition Radiation Tracker  
498 (TRT), shown in Figure 6.4 and 6.5. The entire ID is immersed in a 2T solenoidal  
499 magnetic field parallel to the  $+z$ -axis, causing charged particles to bend in the  
500 transverse-plane, allowing particle momentum measurements.

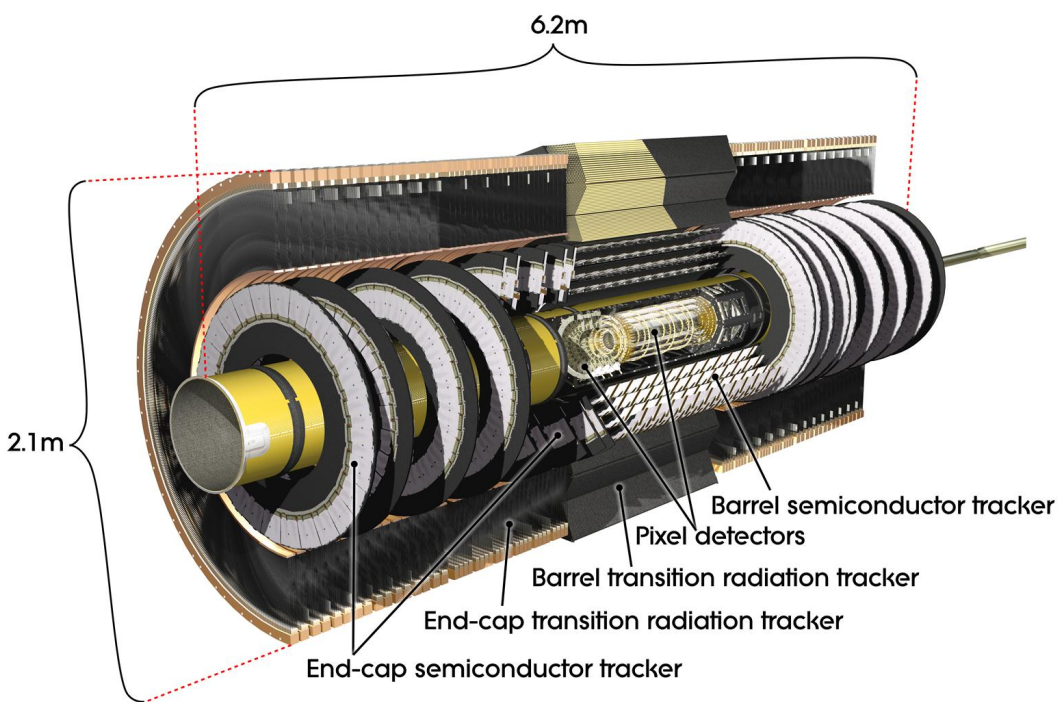


**Figure 6.4:** Layout of ATLAS Inner Detector

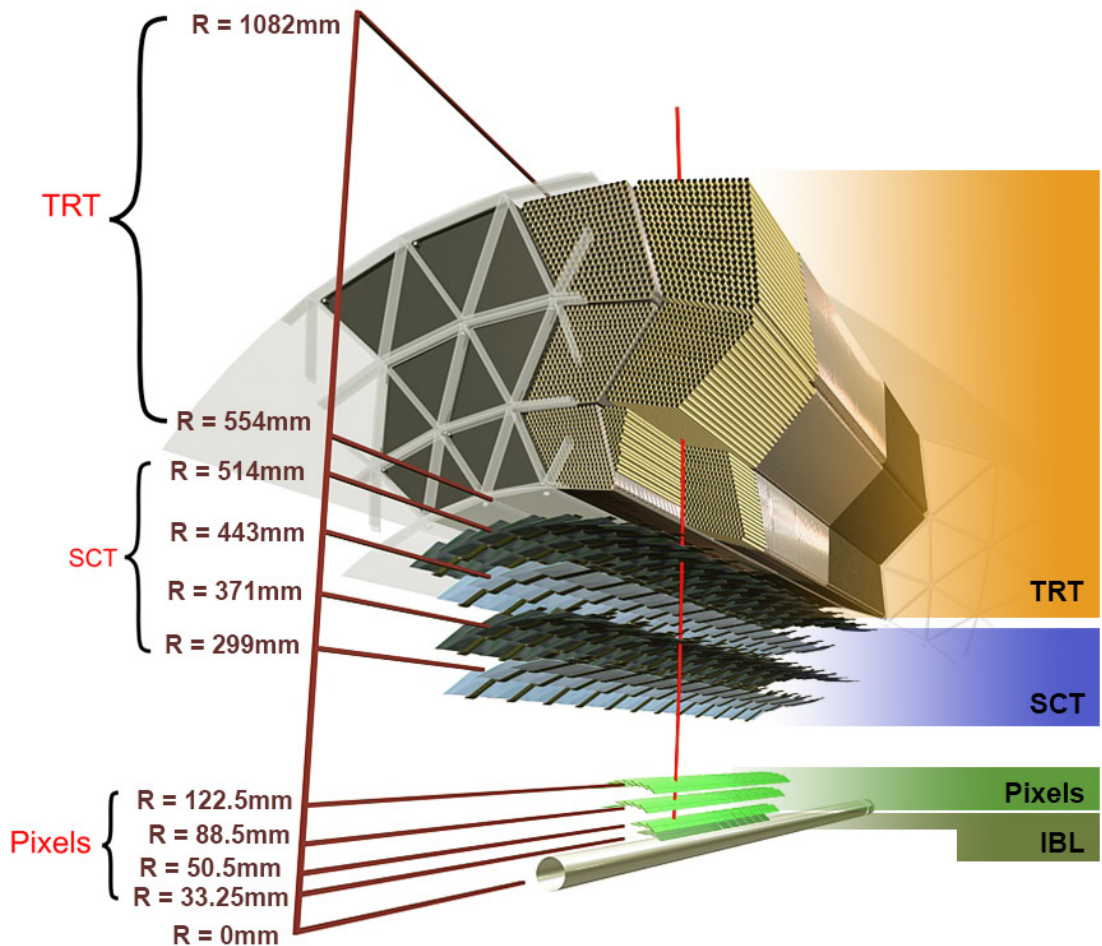


Figure 6.5: Layout of ATLAS ID Barrel System.

501 **6.2.1 Pixel Detector**

502 The pixel detector consists of four barrel layers between  $r = 32.7$  and  $122.5$   
503 mm, extending to  $|z| = 400.5$  mm. The remaining detectors are arranged in bar-  
504 rels and forward and backward rings. The innermost pixel barrel, the Insertable  
505 b-Layer (IBL), only extends to  $|z| = 332$  mm. The pixel detectors closer to the  
506 beam line (larger  $\eta$  values) consists of six parallel cylindrical rings of pixel de-  
507 tectors transverse to the beam line. The entire pixel detector consists of 1744  
508 identical pixel sensors each with 46080 readout channels, totaling about 80 mil-  
509 lion individual pixels. Most of the pixel sensors are  $50 \times 400 \mu\text{m}^2$ . Each pixel has  
510 a position resolution of  $14 \mu\text{m}$  in  $\phi$  and  $115 \mu\text{m}$  in the  $z$  direction.

511 **6.2.2 Semiconductor Tracker**

512 The SCT is located outside the pixel detector and has the same barrel and  
513 endcap geometry as the pixel detector. SCT sensors are  $80 \mu\text{m} \times 12$  cm with  
514 a  $80 \mu\text{m}$  strip pitch. In the barrel the strips are parallel to the  $z$ -axis and are  
515 segmented in  $\phi$ . In the endcaps, the strips extend radially. Sensors are grouped in  
516 modules containing two layers of strips rotated 40 mrad with respect to each other.  
517 This offset allows for the two-dimensional position of a track to be determined by  
518 identifying the crossing point of the strips that registered a hit. SCT modules  
519 measure tracks with an accuracy of  $17 \mu\text{m}$  in  $r - \phi$  and  $580 \mu\text{m}$  in  $z(r)$  in the  
520 barrel (end-cap) region.

521 **6.2.3 Transition Radiation Tracker**

522 The transition radiation tracker (TRT), enveloping the SCT, is a gaseous  
523 straw-tube tracker mainly used for electron/pion track separation. Each straw  
524 is 4 mm in diameter and filled with a Xe- $\text{CO}_2$ - $\text{O}_2$  gas mixture. An anode wire at

525 the center of the straw is held at ground potential, while the walls of the straw  
526 are kept at -1.4kV. When a charged particle passing through the TRT ionizes the  
527 gaseous mixture, the resulting ions form an avalanche on the anode wire with a  
528 gain of  $\sim 10^4$ . The signal from the anode wire is then digitized and discriminated.  
529 Signals passing a low threshold cutoff are used to distinguish noise from tracks.  
530 Signals passing a high threshold cutoff are sensitive to transition radiation (TR).  
531 TR photons are emitted when charged particles pass between materials with dif-  
532 ferent dielectric constants. The probability that a charged particle with energy  $E$   
533 and mass  $m$  passing between two materials emits a TR photon in the keV range  
534 is proportional to  $\gamma = E/m$ . In the TRT straws these often then convert via the  
535 photoelectric effect, causing a large avalanche triggering the high-threshold. Since  
536 electrons have a smaller mass than pions, electron tracks are more likely to trig-  
537 ger the high threshold. This then provides discrimination between electrons and  
538 charged hadrons.

539 The barrel region of the TRT extends from  $r = 563\text{-}1066$  mm and  $|z| < 712$   
540 mm. Barrel Straws are 144 cm long (divided  $\sim \eta \approx 0$ ) and orientated parallel to  
541 the beam direction. End-cap straws extend radially and are 37 cm long. There  
542 are 53,544 straws in the barrel and 160,000 straws in the end-caps. Radiator mats  
543 of polypropylene/polyethylene fibers in the barrel are aligned perpendicular to the  
544 barrel straws (with holes for the straws to pass through). In the end-cap region,  
545 radiator foils are layered between the radial TRT straws.

546 The arrival time of the signal pulse is sensitive to the distance between the  
547 charged particle track and the anode wire and allows for a hit resolution of  $130\mu\text{m}$ .  
548 The TRT extends to  $|\eta| = 2.0$  and provides about 36 hits per track.

## 549 6.3 Calorimeters

550 The ATLAS electromagnetic and hadronic calorimeters (EMC and HCAL,  
551 respectively) absorb and measure the energy of high energy hadrons, photons,  
552 and electrons with  $|\eta| < 4.9$ . Both systems use sampling calorimeters which  
553 consist of alternating layers of dense absorbing and active layers. In the absorbing  
554 layer particles interact and lose energy, creating showers. These showers are then  
555 detected and measured in the active layer. The amount of charge measured in the  
556 active material scales with the energy of the incident particle, and thus provides a  
557 measurement of the particle's energy. An overview of the layout of the calorimeter  
558 system is shown in Figure 6.6.

559 The EMC measures and contains the energy of electromagnetically interacting  
560 particles. It consists of layered accordion-shaped Lead absorber plates and elec-  
561 trodes immersed in liquid Argon with 170k channels.. Using accordion-shaped  
562 electrode and absorbers ensures  $\phi$  symmetry and coverage. The EMC is com-  
563 posed of a barrel part ( $|\eta| < 1.475$ ), two end-caps ( $1.375 < |\eta| < 3.2$ ), and a  
564 presampler ( $|\eta| < 1.8$ ). The presampler, containing only liquid Argon, corrects  
565 for upstream energy losses of electrons and photons. The EMC barrel is segmented  
566 into three layers. The first layer has finest segmentation with readout cells ex-  
567 tending  $\Delta\eta \times \Delta\phi = 0.025/8 \times 0.1$ . This provides a precise shower measurements  
568 used to separate prompt photons from  $\pi^0 \rightarrow \gamma\gamma$  decays. The second layer has  
569 coarser segmentation and is approximately 16 radiation lengths long. A radiation  
570 length is the average distance an electron travels before losing all but  $1/e$  of its  
571 energy to bremsstrahlung. The last layer is the most coarse and measures the tail  
572 of the electromagnetic shower. A schematic of the ECAL is shown in Figure 6.7.

573 The hadronic calorimeter located outside the EMC and is used to contain  
574 and measure the energy of hadronically interacting particles. It consists of a tile

575 calorimeter (TileCal), hadronic end-cap calorimeter (HEC), and liquid Argon for-  
 576 ward calorimeter (FCAL). TileCal is located behind the LAr EMC and uses steel  
 577 absorbers and liquid Argon as the active material. TileCal consists of three barrel  
 578 layers in the central and forward regions, extending up to  $|\eta| < 1.7$ . Photons  
 579 generated from hadronic interactions are collected via wavelength-shifting fibers  
 580 connected to photomultiplier tubes, as shown in Figure 6.8. The HEC lies behind  
 581 the EMC endcap wheels. It uses copper absorbers and liquid Argon as the active  
 582 material and covers  $1.5 < |\eta| < 3.2$ . Finally, the FCAL covers  $3.1 < |\eta| < 4.9$   
 583 and consists of three modules all using liquid Argon as the active material. The  
 584 first module uses copper absorber and was designed for electromagnetic measure-  
 585 ments. The second and third modules consist of tungsten absorber and are used  
 586 to measure the kinematics of hadronically interacting particles. A schematic of  
 587 the HCAL is shown in Figure 6.8.

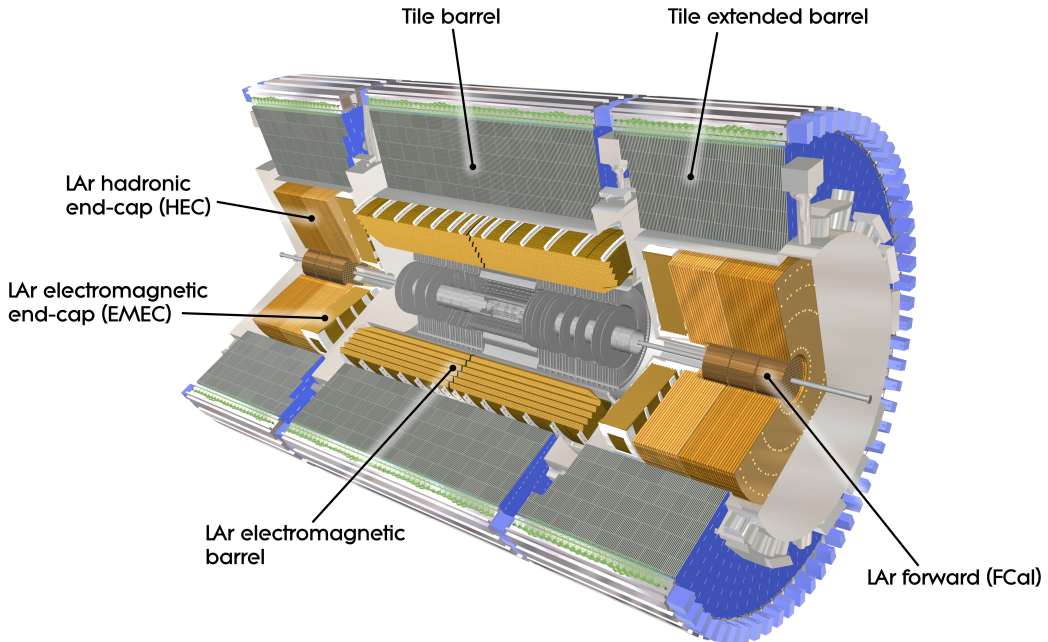


**Figure 6.6:** Overview of ATLAS electromagnetic and hadronic calorimeters.

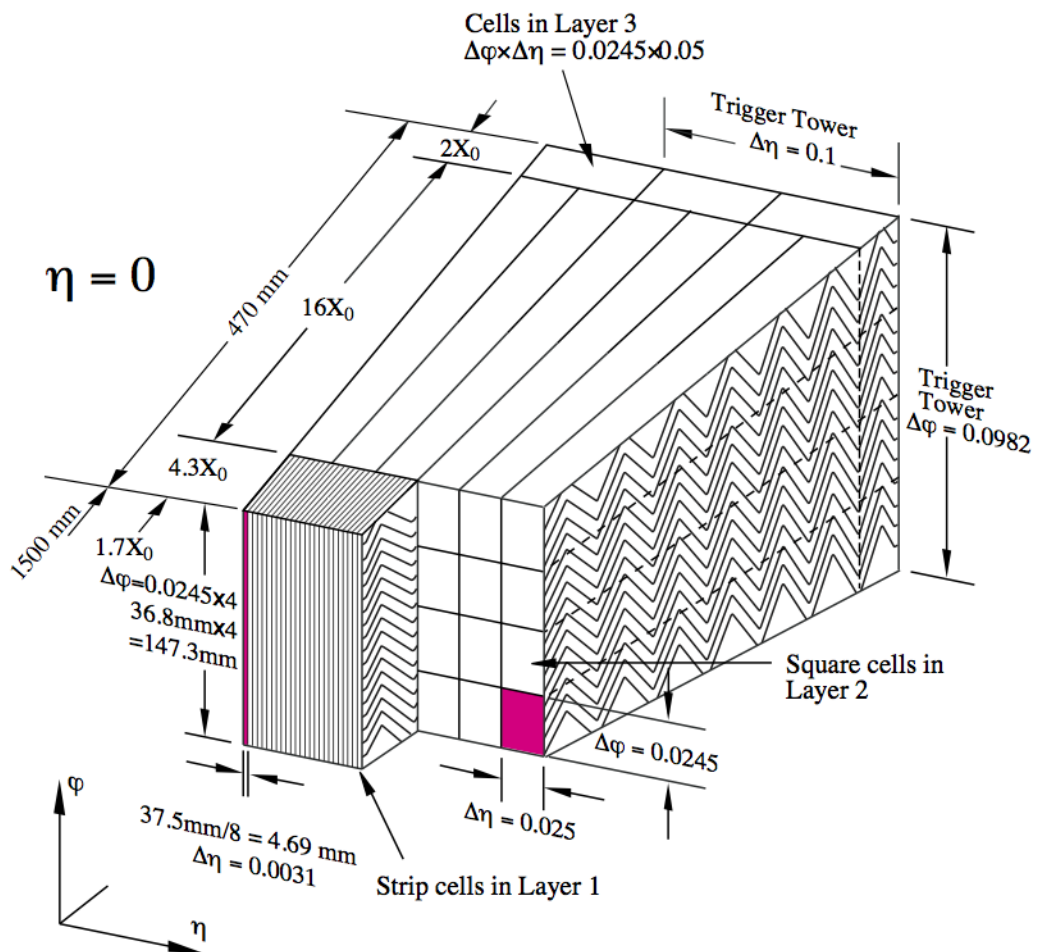


Figure 6.7: Schematic of ECAL.

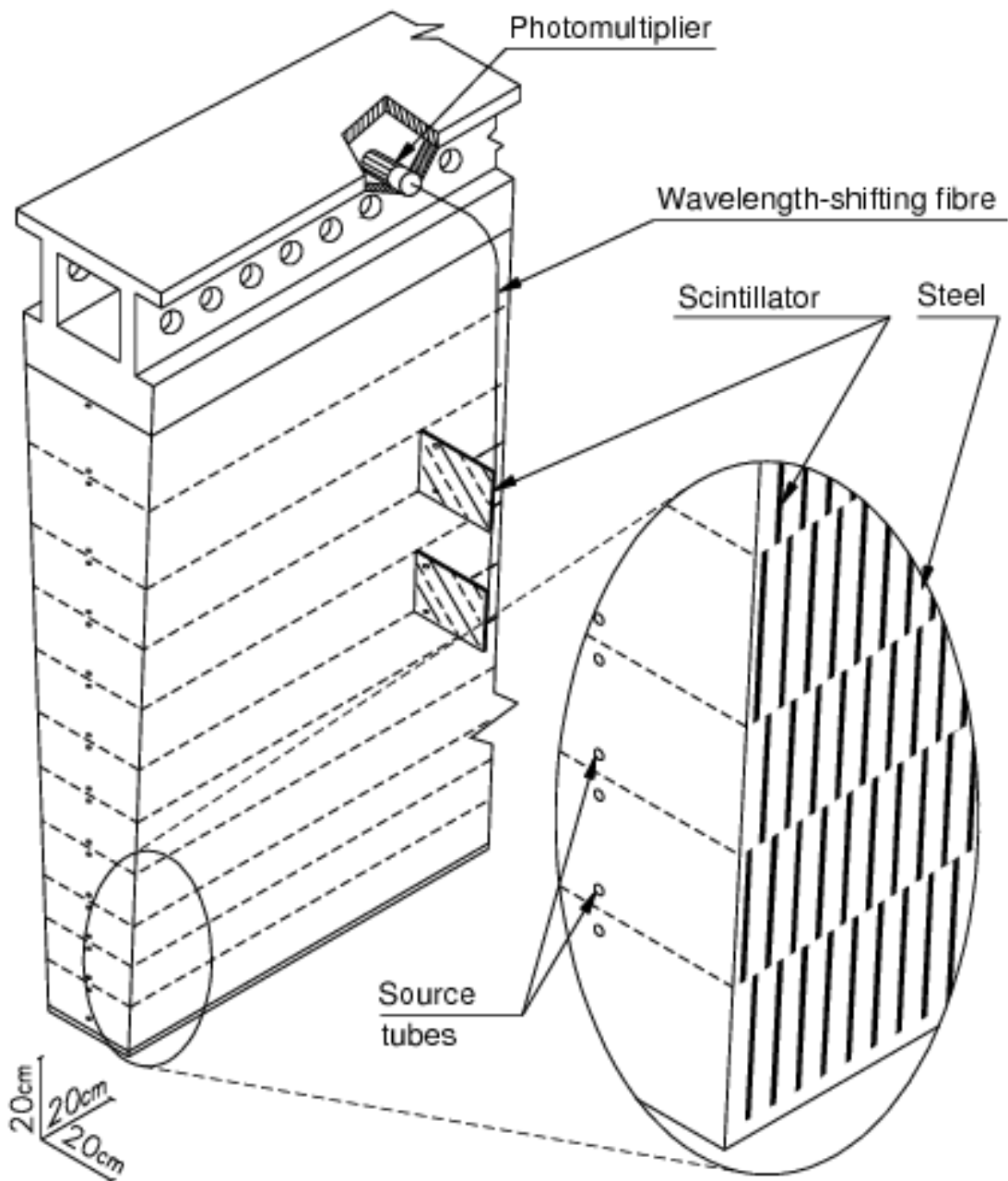


Figure 6.8: Schematic of HCAL.

588        The energy resolution of the calorimeter subsystems are:

589         $\frac{\sigma_E}{E} = \frac{10\%}{\sqrt{E}} \oplus 0.7\% \text{ EMC}$

590         $\frac{\sigma_E}{E} = \frac{50\%}{\sqrt{E}} \oplus 3\% \text{ hadronic barrel}$

591         $\frac{\sigma_E}{E} = \frac{100\%}{\sqrt{E}} \oplus 10\% \text{ hadronic end-cap}$

592        

## 6.4 Muon Spectrometer

593        The muon spectrometer (MS) is the outermost detector system in ATLAS.

594        Muons with a  $p_T > 4$  GeV are energetic enough to reach the MS. To measure the  
595        momentum of these muons barrel and end-cap toroid magnets are used covering  
596         $|\eta| < 1.4$  and  $1.6 < |\eta| < 2.7$ . For  $1.4 < |\eta| < 1.6$ , a combination of the barrel  
597        and end-cap toroidal magnetic fields bend muon trajectories. The detector in the  
598        barrel region form three concentric rings at  $R = 5, 7.5, 10$ m and are segmented  
599        in  $\phi$  to accommodate the magnets. The end-cap region consists of three circular  
600        planes perpendicular to  $z$  and located at  $|z| = 7.4, 14, 21.5$ m from the interaction  
601        region. An additional detector at  $|z| = 10.8$ m covers the transition region between  
602        the barrel and end-cap.

603        The MS readout consists of four subsystems: Monitored Drift Tubes (MDT),  
604        Cathode Strip Chambers (CSC), Resistive Plate Chambers (RPC), and Thin Gap  
605        Chambers (TGC). The first two subsystems are used primarily for measuring  
606        muon track parameters, while the RPC and TGC subsystems are used for muon  
607        triggering. A schematic of this system is shown in Figure 6.9.

608        The MDT subsystem consists of precision tracking chambers for  $|\eta| < 2.7$ ,  
609        except for the inner most end-cap layer ( $2.0 < |\eta| < 2.7$ ), where CSCs are used.  
610        The basic unit of MDT chambers are thin walled Aluminum tubes with a diameter  
611        of 3 cm and length of 0.9-6.2 m. These tubes are filled with a mixture of Ar-CO<sub>2</sub>  
612        gas with a 50μm W-Rn wire running down the center of the tube, which is kept at

613 3080 V. Since the maximum drift time of these chambers is  $\sim 700$  ns, they are not  
614 used for triggering. MDT chambers consist of 3-4 layers of tubes mounted on a  
615 rectangular support system, as seen in Figure 6.10, orientated along  $\phi$  to measure  
616 the coordinate in the bending plane of the magnetic field with a resolution of 35  
617  $\mu\text{m}$ .

618 The MDT subsystem can only handle hit rates below  $150\text{Hz}/\text{cm}^2$ . For this  
619 reason, CSCs are used in the innermost end-cap layer where hit rates are larger.  
620 CSCs can handle hit rates up to  $1000\text{Hz}/\text{cm}^2$ . CSC are multiwire proportional  
621 chambers. These chambers are filled with a Ar- $\text{CO}_2$  gas mixture and evenly spaced  
622 wires kept at 1900 V. These wires are orientated in the radial direction but not  
623 read out. Instead on one side of the cathode are copper strips parallel to the wires,  
624 measuring  $\eta$ , while on the other side of the cathode are strips parallel to the wires  
625 measuring  $\phi$ . The width between strips is approximately 1.5 mm providing a  
626 resolution of 60  $\mu\text{m}$  in the bending-plane and 5 mm in the non-bending plane.

627 Since the CSC and MDT systems do not have prompt timing signals, the RPC  
628 and TGC systems are used for triggering. The RPC system is used in the barrel  
629 region ( $|\eta| < 1.05$ ). RPC consist of two parallel resistive plates separated by a 2  
630 mm insulated spacer with 100 mm spacing kept at 9.8 kV, as shown in Figure 6.11.  
631 A gaseous mixture of  $\text{C}_2\text{H}_2\text{F}_4$ ,  $\text{C}_4\text{H}_{10}$ , and  $\text{SF}_6$  fills the space between the two  
632 plates. Metallic strips on the outer faces of the plates are used to read out signals  
633 produced by the gas ionizing. The middle barrel layer consists of two layers of  
634 RPCs on either side of the MDT layer and one layer on the outermost MDT  
635 layer. Each layer contains two orthogonal sets of metallic strips providing  $\eta$  and  
636  $\phi$  measurements. The timing resolution of RPCs is 1.5 ns, and therefore may be  
637 used to identify bunch crossings.

638 Finally, the TGCs are used in the end-cap regions and are primarily used to

639 provide L1 trigger decisions and  $\phi$  measurements. TGCs are multi-wire propor-  
 640 tional chambers consisting of arrays of gold-coated tungsten wires placed between  
 641 two cathode planes. These wires are separated by 1.8 mm and cathodes are 1.4 mm  
 642 from the wires. Orthogonal to the wires, on the opposite side of the cathode plane  
 643 are copper strips held at 2900 V. The chambers are filled with a mixture of  $CO_2$   
 644 and n-pentane gas, the latter acts as a quenching gas to prevent avalanches initi-  
 645 ated by secondary  $\gamma$ -rays from the primary avalanche. Figure 6.12 is a schematic  
 646 of a TGC. The timing resolution of TGCs is less than 25 ns and therefore they  
 647 are used for bunch crossing measurements.

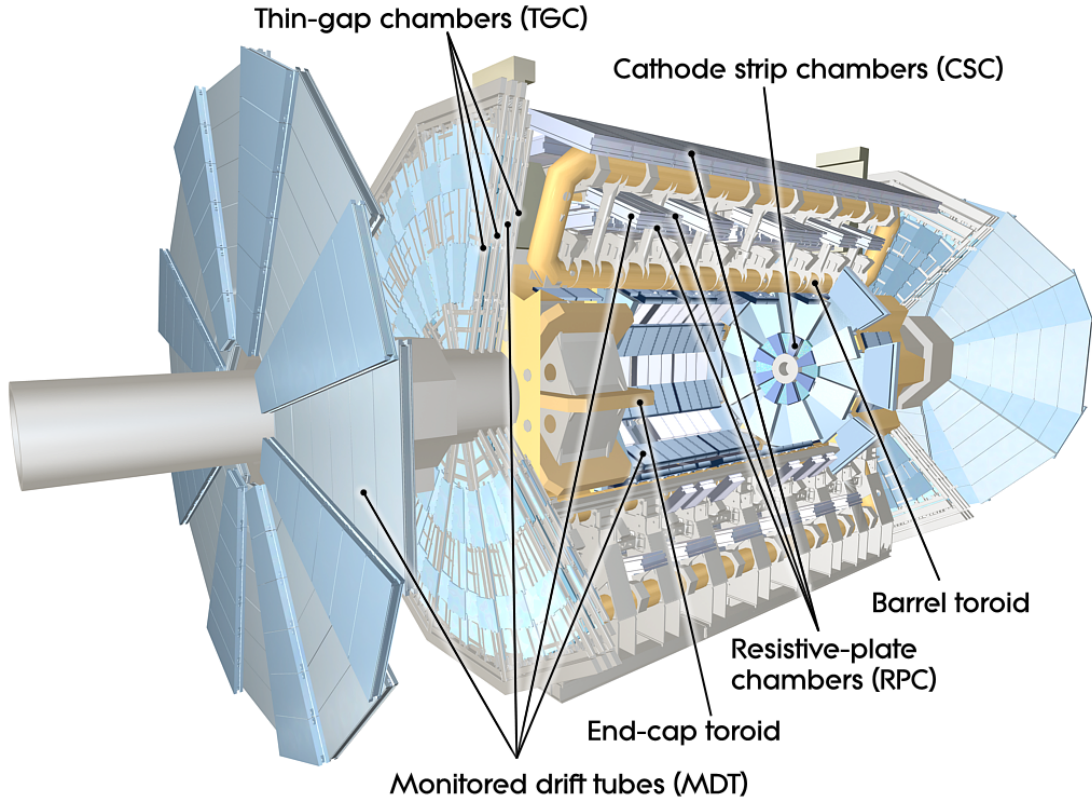


**Figure 6.9:** Schematic of Muon Spectrometer [cite G35]

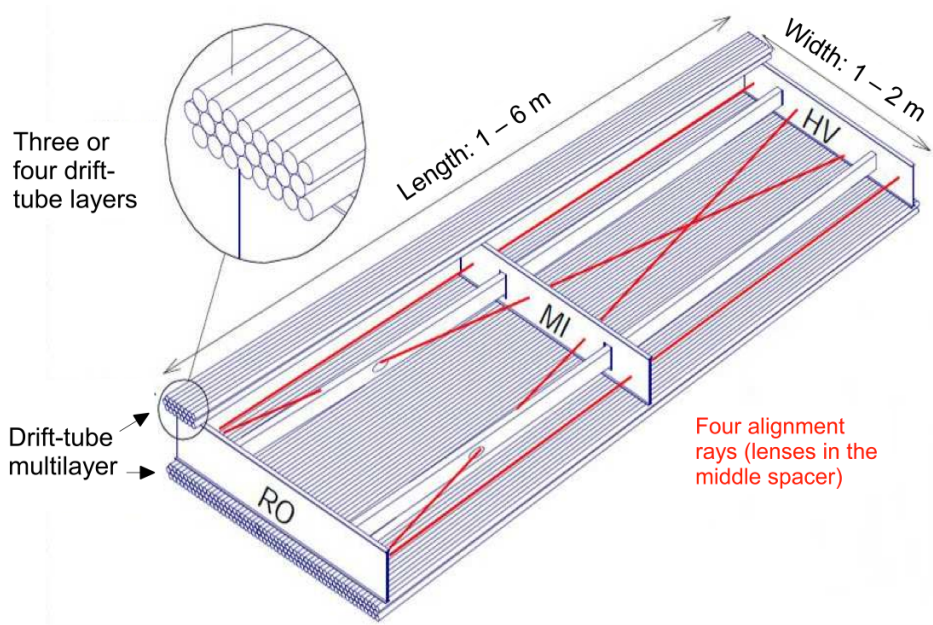


**Figure 6.10:** Schematic of MDT chamber. [cite G35]

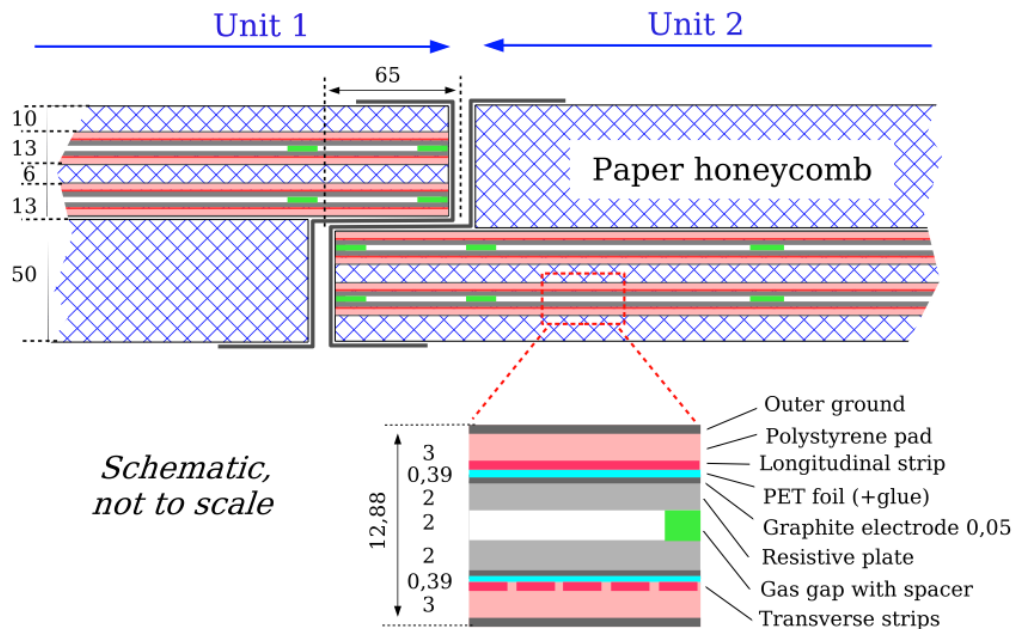


**Figure 6.11:** Schematic of RPC chamber, which is used for triggering in the central region of the detector [cite G35].

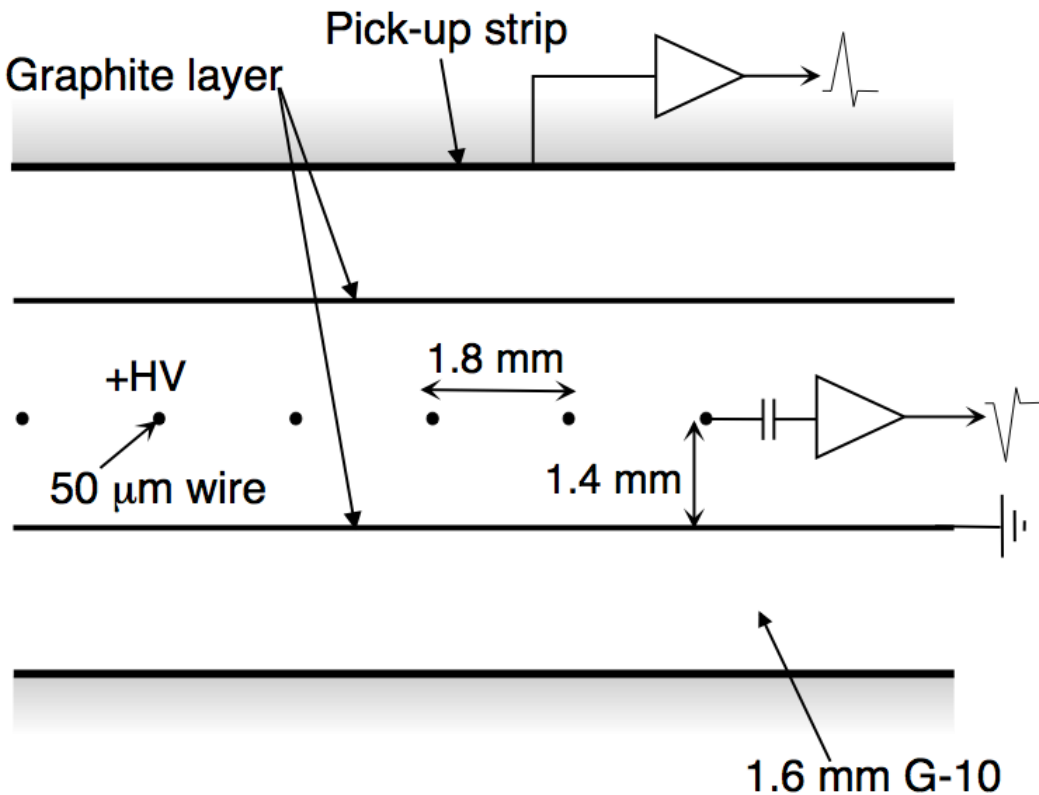


**Figure 6.12:** Schematic of TGC chamber, which is used for triggering in the muon end-cap region. [cite G35]

## 648    6.5 Magnet System

649    A particles with charge,  $q$ , and velocity  $v$ , moving in magnetic field,  $B$ , ex-  
 650    periences a force,  $F = qv \times B$ . This force can cause charged particles to have a  
 651    curved trajectory in magnetic fields, which the ID and MS use to determine the  
 652    particles  $p_T$ . The central solenoid provides the magnetic field for the ID and the  
 653    toroidal magnets provide the magnetic field for the MS.

654    The layout of the magnet system is shown in Figure 6.13. The central solenoid  
 655    consists of a single-layer Al-stabilized NbTi conductor coil wound inside an Al

656 support cylinder. The solenoid is 5.8 m long, 50 cm thick and has an inner radius  
657 of 1.23 m. It is cooled to 4.5 K to reach superconducting temperatures and shares  
658 the liquid argon calorimeter vacuum vessel to minimize material in the detector.  
659 A current of 7.730kA produces a 1.998 T solenoidal magnetic field, pointing in  
660 the  $+z$  direction.

661 The toroidal magnet system consists of a barrel and two end-cap toroidal  
662 magnets used to create a magnetic field outside the calorimeters that is orientated  
663 along  $\phi$ . Each barrel toroid is 25.3 m long with an inner and outer diameter of 9.4  
664 and 20.1 m and weighs 830 tonnes. Endcap toroids are 5 m long with an inner and  
665 outer radius of 1.65 and 10.7 m. Both toroid systems use Al-stabilized Nb/Ti/Cu  
666 conductors. The magnetic field strength in the barrel and endcap regions are 0.5  
667 and 1 T, respectively.

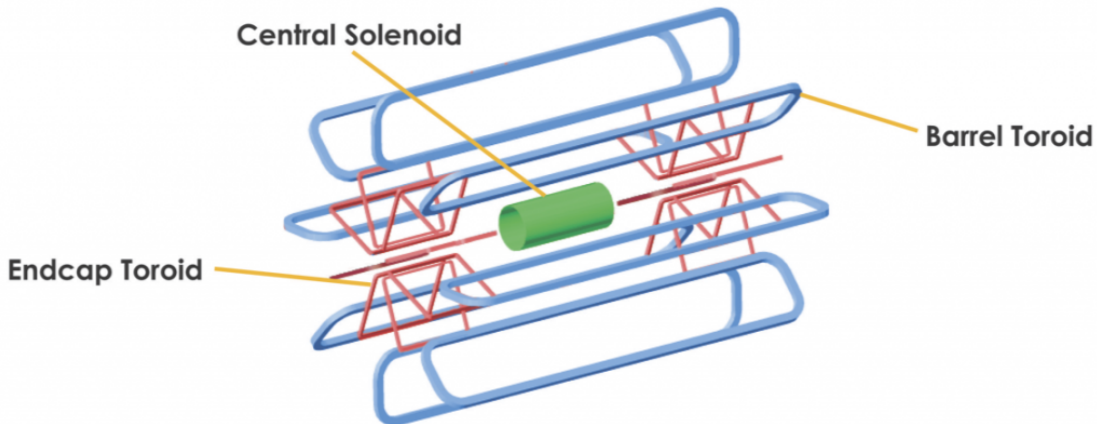


**Figure 6.13:** Layout of ATLAS magnet systems.

## 668 **6.6 Trigger System**

669 Since collisions occur every 25 ns and reading out all detector channels and  
670 storing that information is not currently feasible (would require saving 60 million  
671 megabytes per second), the majority of events are not kept for analysis. ATLAS

672 uses a multi-stage trigger system to select approximately 1,000 of the 1.7 billion  
673 collisions that occur each second (corresponding to a rate of 1 kHz from the 40  
674 MHz proton collision rate). The first stage of the trigger system is the hardware  
675 level (L1) trigger. This trigger reduces the event rate to  $\sim$ 100 kHz by identifying  
676 Regions-of-Interest (ROIs) containing high  $p_T$  leptons, photons, jets, or  $E_T^{miss}$  by  
677 using information from RPCs, TGCs, and calorimeters to make a  $2.5 \mu\text{s}$  decision.  
678 This information is then passed to a high-level trigger (HLT) which further de-  
679 creases event rates to  $\sim$  1 kHz. The HLT uses finer granularity measurements  
680 from the MS and ID to perform simplified offline reconstruction to decide which  
681 events to keep.

## **Part IV**

682

## **Method**

683

684 **Chapter 7**

685 **Dataset and Simulated Samples**

686 **7.1 Dataset**

687 This analysis uses  $pp$  collision data collected from 2015 to 2018 at  $\sqrt{s} = 13$   
688 TeV, corresponding to 139/fb of data as shown in Figure 7.1 and 7.2. From this  
689 dataset, only those events in which the tracker, calorimeters, and muon spectrom-  
690 eter have good data quality are used. For a given event, the solenoid and toroidal  
691 magnets must also be operating at their nominal field strengths. In addition to  
692 this, events must pass further quality checks to reject events where detector sub-  
693 systems may have failed. These selections reject events that containing LAr noise  
694 bursts, saturation in the electromagnetic calorimeter, TileCal errors, and failures  
695 in event recovery due to tracker failures. Events with information missing from  
696 subsystems (usually due to busy detector conditions) are rejected. Events must  
697 also contain a primary vertex with at least two associated tracks, where the pri-  
698 mary vertex is selected as the vertex with the largest  $\sum p_T^2$  over tracks associated  
699 with the vertex and  $p_T > 0.5$  GeV.

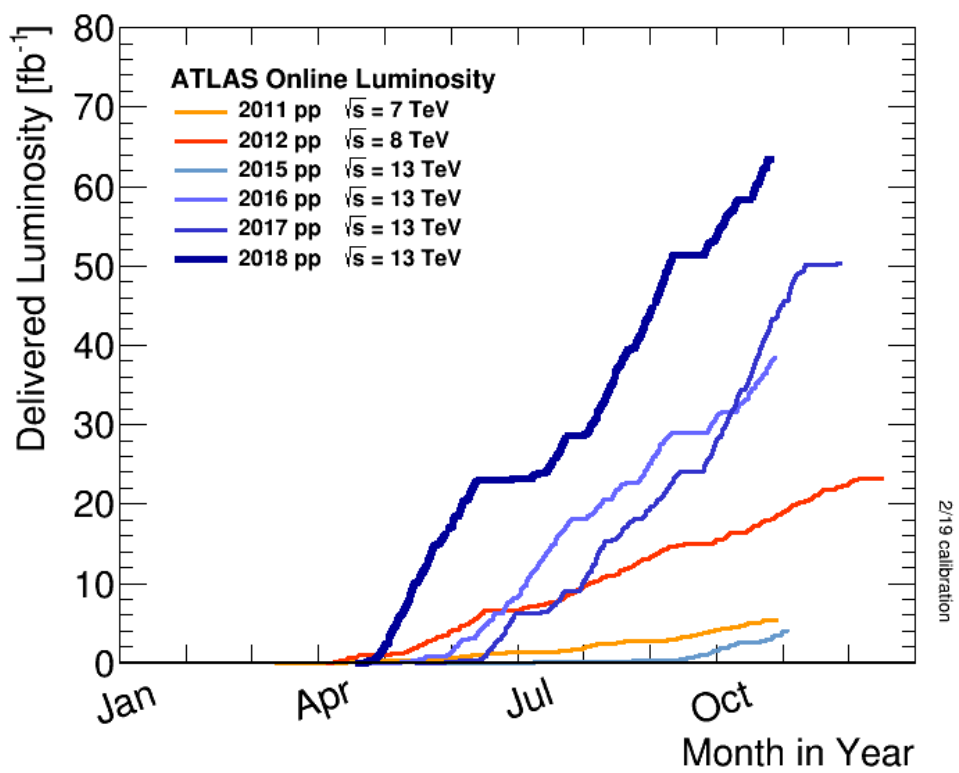


**Figure 7.1:** Integrated luminosity for data collected from ATLAS from 2011 - 2018

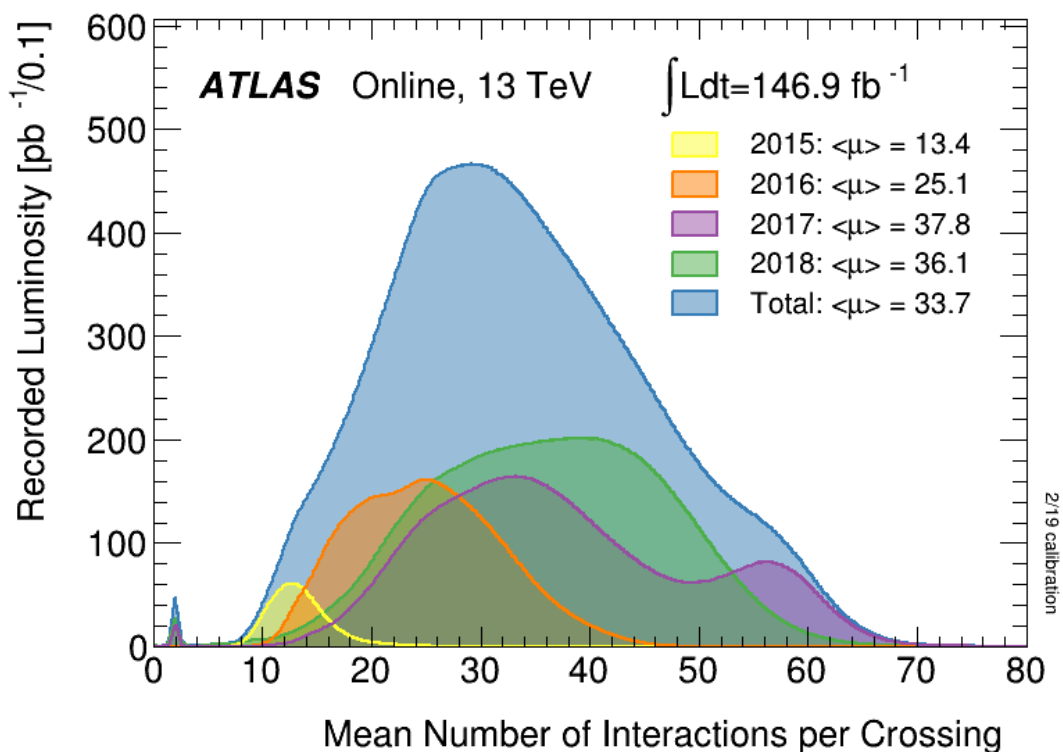


**Figure 7.2:** Mean number of interactions per crossing for data collected from ATLAS from 2011 - 2018

700 **7.2 Simulated Samples**

701 Samples are simulated in order to model backgrounds, evaluate signal ac-  
702 ceptance, optimize event selection and estimate systematic and statistical uncer-  
703 tainties. The dominant backgrounds for this analysis are  $W/Z + \text{jets}$ , diboson  
704 ( $WZ/WW$ ),  $t\bar{t}$ , single top and multijet production.

705  $W/Z+\text{jet}$  events are simulated using Sherpa 2.2.1 at NLO [cite [29]] and merged  
706 with the Sherpa parton shower using the ME+PS@NLO prescription [12]. These  
707 events are then normalized to NNLO cross sections. The  $t\bar{t}$  and single-top back-  
708 grounds are generated with Powheg-Box with NNPDF3.0NLO PDF sets in the  
709 matrix element calculation [cite[35]]. For all processes, the parton shower, frag-  
710 mentation, and underlying event are simulated using Pythia 8.320 with the A14  
711 tune set[cite[ATL-PHYS-PUB-2014-02]]. Diboson processes are generated using  
712 Sherpa 2.2.1.

713 Signal samples are simulated using MadGraph 5-2.2.2 [cite 42] and Pythia  
714 8.186 with NNPDF230LO. RS Graviton samples are generated with  $k/M_{PL}=1$ .  
715 HVT Model A (B) samples are simulated with  $g_V = 1(3)$ , as the difference in the  
716 width of the samples is smaller than detector resolution. Model C is generated by  
717 setting  $g_H = 1$  and  $g_f = 0$  to model VBF production of HVT bosons. Signals are  
718 generated for masses between 300 GeV and 5 TeV.

719 **Chapter 8**

720 **Objects**

721 **8.1 Electrons**

722 Electrons are reconstructed from electromagnetic showers in the LAr EM  
723 calorimeter. During reconstruction cells of  $\Delta\eta \times \Delta\phi = 0.025 \times 0.025$  are grouped  
724 into  $3 \times 5$  clusters. These clusters are then scanned for local maxima that seed  
725 electron clusters. These clusters must then be matched to ID track from the PV.  
726 This requirement minimizes non-prompt electron and fake electron backgrounds.  
727 Electrons must pass identification and isolation requirements. Electron identifica-  
728 tion (loose, medium, tight) classification is based on a multivariate discriminant  
729 that identifies electrons using a likelihood based method. For this analysis, events  
730 are required to have one tight electron and no additional loose electrons. Elec-  
731 trons are also required to be isolated. The electrons are considered isolated if the  
732 quotient of the sum of the transverse momentum (of calorimeter energy deposits)  
733 in a cone around the electron of size  $\Delta R = 0.2$  and the transverse momentum  
734 of the electron to be less than  $0.015 * p_T$  or 3.5 GeV, whichever is smaller. This  
735 requirement rejects non-prompt photons and other fake leptons. Electrons in this  
736 analysis are also required to have  $p_T > 30$  GeV and  $|\eta| < 2.47$ . Electrons are also

737 required to have  $p_T > 30$  GeV.

738 Electrons are calibrated to determine data-driven scale factors using  $J/\Psi \rightarrow$   
739  $ee$ ,  $Z \rightarrow ee$ ,  $Z \rightarrow \ell\ell\gamma$  processes. These corrections account for the non-uniform  
740 response of the detector which introduces modeling and reconstruction uncertain-  
741 ties.

## 742 8.2 Muons

743 As muons traverse the entire detector, they are reconstructed from ID and  
744 MS tracks. For this analysis the muon identification and isolation working points  
745 are chosen to minimize the contributions from non-prompt muons. Towards this  
746 end, each selected event must contain exactly one muon that passes the medium  
747 identification working point, and no additional muons (that pass the loose working  
748 point). For the medium working point, two types of reconstructed muons are  
749 used: combined and extrapolated muons (CB and ME, respectively). For CB  
750 muons, ID and MS tracks are reconstructed independently and a combined track  
751 fit is performed by adding or removing MS tracks to improve the fit quality.  
752 ME muons are reconstructed from only MS tracks with hits in at least two layers,  
753 which ensures the track originates from the PV. ME muons extend the acceptance  
754 for muon reconstruction outside the ID from  $2.5 < |\eta| < 2.7$ . The medium  
755 identification working point uses CB and ME tracks. CB tracks must have at  
756 least 3 hits in two MDT layers. ME tracks are required to have at least three  
757 MDT/CSC hits. To further minimize contributions from fake muons, the selected  
758 muons are required to be isolated from other tracks, as muons from  $W, Z$  decays are  
759 often isolated from other particles. To insure the selected muons are isolated, the  
760 scalar sum of the transverse momentum of tracks in a cone of  $\Delta R = 0.3$  compared  
761 to the transverse momentum of the muon must be less than 0.06. Muons are also

762 required to have  $p_T > 30$  GeV.

763 Muons are calibrated using well-studied resonances  $J/\Psi \rightarrow \mu\mu$  (low- $p_T$ ),  $Z \rightarrow$   
764  $\mu\mu$  (high- $p_T$ ). Figure 8.1 shows the combined muon  $p_T$  uncertainty from this  
765 calibration. The total systematic uncertainty is less than 1% for all  $p_T$  ranges  
766 considered in this analysis.

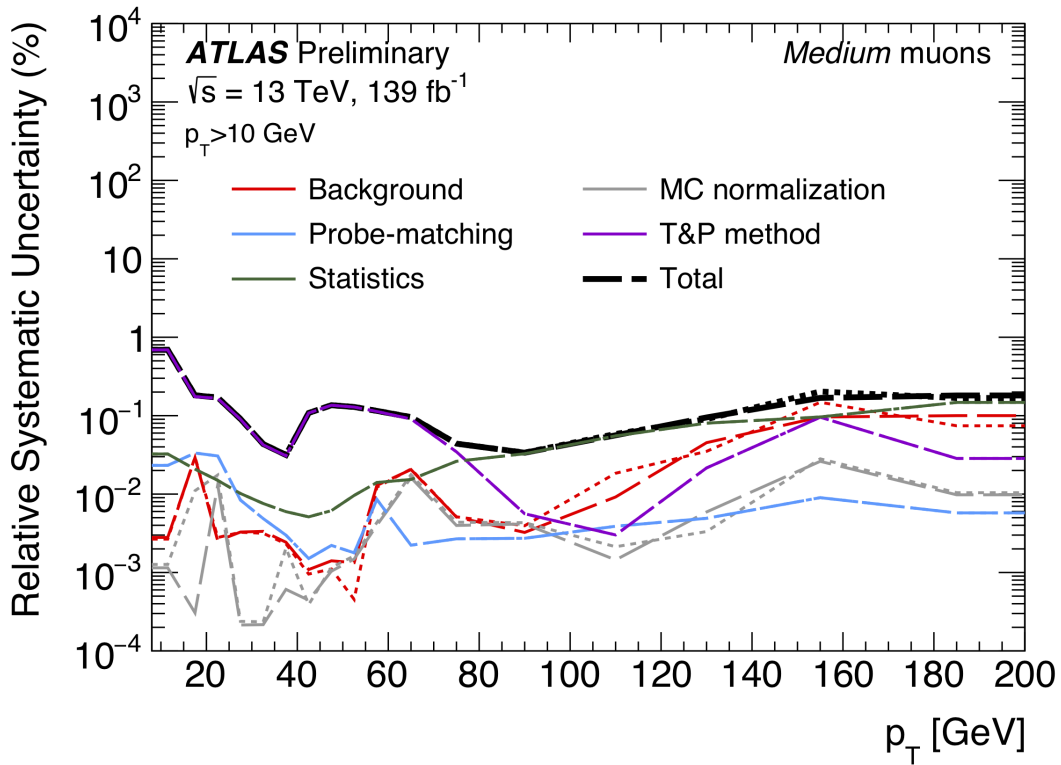


**Figure 8.1:** This figure shows the breakdown of the muon reconstruction efficiency scale factor measured in  $Z \rightarrow \mu\mu$  as a function of  $p_T$  [4].

### 767 8.3 Jets

768 Three types of jets are used in this analysis: variable radius, small-R and  
769 large-R jets. Variable radius jets are used to reconstruct  $Z$  bosons decaying to  
770 two  $b$ -jets in the jet catchment area of large-R jet in the Merged regime. Small-R

771 jets are used to reconstruct the hadronically decaying  $W/Z$  candidates in the  
772 resolved analysis and the forward jets from resonances produced through vector  
773 boson fusion. Large-R jets are used to reconstruct the hadronically decaying boson  
774 in the merged regime.

775 For all of these jet collections, the jet energy is calibrated sequentially as shown  
776 in Figure 8.2. After the jet direction is corrected to point to the PV, the energy  
777 of the jet is corrected. First, the jet energy is corrected to account for pileup  
778 contributions based on the  $p_T$  and area of the jet (these corrections are extracted  
779 from a  $pp \rightarrow jj$  sample). Following this, another pileup correction is applied that  
780 scales with  $\mu$  and  $N_{PV}$ .

781 MC-based corrections are then applied that are meant to transform the jet  
782 energy and  $\eta$  back to truth level. Therefore, these corrections account for the  
783 non-compensating nature of the ATLAS calorimeters and inhomogeneity of the  
784 detector. Following this, the Global Sequential Calibration is applied that re-  
785 duces flavor dependence of jet calibrations and accounts for energy leakage of jets  
786 outside the calorimeters. Finally, in-situ corrections are applied that account for  
787 differences in jet responses between data and simulation ( $\gamma/Z + \text{jet}$  and fake lep-  
788 ton samples are used). These differences can be due to mismodelling of the hard  
789 scatter event, pile-up, jet formation, etc.

790 To further reject fake jets, jets must pass quality requirements based on the  
791 following variables ([cite P42]):

- 792 -  $f_Q^{LAr}$ : fraction of energy of jet's LAr cells with poor signal shape
- 793 -  $f_Q^{HEC}$ : fraction of energy of jet's HEC cells with poor signal shape
- 794 -  $E_{neg}$ : sum of cells with negative energy
- 795 -  $f_{EM}$ : fraction of jet's energy deposited in EM calorimeter

- 796     -  $f_{HEC}$ : fraction of jet's energy deposited in HEC calorimeter
- 797     -  $f_{max}$ : maximum energy fraction in any single calorimeter layer
- 798     -  $f_{ch}$ : ratio of the scalar sum of the  $p_T$  of a jet's charged tracks to the jet's  $p_T$
- 799     Jets selected for the resolved analysis must pass one of the following criteria:
- 800     -  $f_{HEC} > 0.5$  and  $|f_Q^{HEC}| > 0.5$  and  $\langle Q \rangle > 0.8$
- 801     -  $|E_{neg}| > 60$  GeV
- 802     -  $f_{EM} > 0.95$  and  $f_Q^{LAr} > 0.8$  and  $\langle Q \rangle > 0.8$  and  $|\eta| < 2.8$
- 803     -  $f_{max} > 0.99$  and  $|\eta| < 2$
- 804     -  $f_{EM} < 0.05$  and  $f_{ch} < 0.05$  and  $|\eta| < 2$
- 805     -  $f_{EM} < 0.05$  and  $|\eta| > 2$

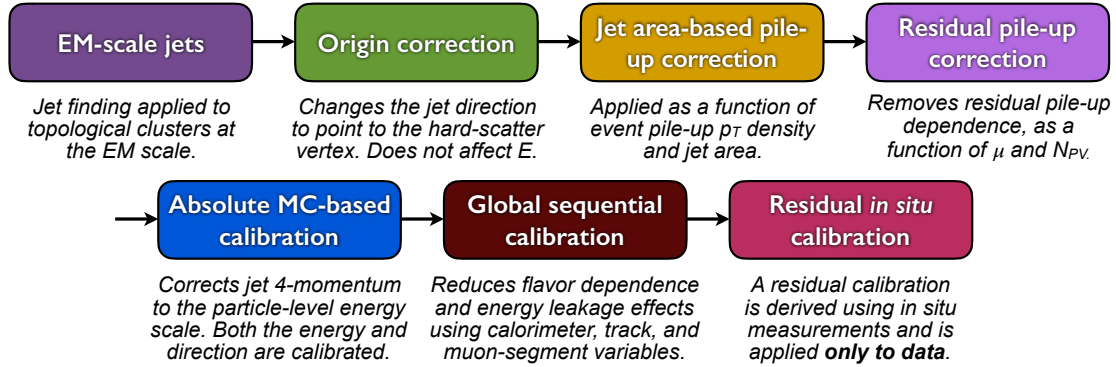


**Figure 8.2:** [7] This diagram shows the calibration stages for EM jets.

806    **8.3.1 Small-R jets**

807    Small-R jets are used to reconstruct the hadronically decaying  $W/Z$  candi-  
808    date when the two resulting jets are well-separated in  $\eta\text{-}\phi$  space. Small-R jets  
809    are also used to identify forward jets from resonances produced through vector  
810    boson fusion. Small-R jets are constructed from topologically connected clusters  
811    of calorimeter cells (topoclusters), seeded from calorimeter cells with energy de-  
812    posits significantly above the noise threshold. These cells are then used as inputs  
813    to the  $anti-k_t$  algorithm [15] with a radius parameter,  $R = 0.4$ .

814    Jets used in this analysis must have  $p_T > 30$  GeV and  $|\eta| < 2.5$ . To further  
815    reduce fake jets the jet-vertex-tagger (JVT) is used to reject pile-up jets [6]. The  
816    JVT uses two track-based variables, corrJVF and  $R_{p_T}$  to calculate the likelihood  
817    that the jet originated from the PV. The corrJVF compares the scalar sum of the  
818     $p_T$  of tracks associated with the jet and PV to the scalar sum of the  $p_T$  of tracks  
819    associated with the jet. This variable also includes a correction that reduces the  
820    dependency of corrJVF with the number of reconstructed vertices in the event.  
821    The other discriminant,  $R_{p_T}$ , is given by the ratio of the scalar sum of the  $p_T$  of  
822    tracks associated with the jet and PV to the  $p_T$  of the jet. Both of these variables  
823    peak around zero for pileup jets, as these jets are unlikely to have tracks associated  
824    with the PV. JVT cuts are applied to all jets with  $p_T > 120$  GeV. Central jets  
825    ( $|\eta| < 2.4$ ) are required to have a  $JVT > 0.59$  and forward jets ( $2.4 < |\eta| < 2.5$ )  
826    are required to have  $JVT > 0.11$ .

827    **8.3.2 Large-R jets**

828    Large-R ( $R = 1.0$ ) jets are used to reconstruct the hadronically decaying  $W/Z$   
829    candidate when the resulting jets are not well-separated in  $\eta\text{-}\phi$  space, and overlap  
830    forming one large-R jet. Track-Calorimeter Clusters (TCCs) are used to reconstruct these

jets [cite ANA 50]. These jets are constructed using a pseudo particle flow method  
 using ID tracks matched to calorimeter clusters. The angular resolution of the  
 calorimeter degrades sharply with jet  $p_T$ , but the jet energy resolution improves.  
 The tracker has excellent angular resolution which improves with  $p_T$ . Therefore,  
 by matching tracks to jets, TCCs have more precise energy and angular resolution  
 than jets constructed from calorimeter information only. These jets are required  
 to have  $p_T > 200$  GeV,  $|\eta| < 2.0$  and  $m_J > 50$  GeV.

TCC jets are trimmed as detailed in [cite ANA 45], which suppresses pileup  
 and soft radiation in the jet, the jet mass is calculated as the four-vector sum  
 of the jet's constituents (assuming massless constituents). The jet mass peaks  
 around the  $W/Z$  boson mass for  $W/Z \rightarrow qq$  jets, and more broadly for quark and  
 gluon induced jets.

These jets are then tagged as  $W$  jet if it passes optimized jet mass and  $D_2$   
 cuts for  $W$  bosons, and a  $Z$  jet if it passes the optimized cuts for the  $Z$  boson.  
 The jet substructure variable  $D_2$  is given by the ratio of energy correlation func-  
 tions. These fuctions are derived from the energies and pair-wise angles of a jet's  
 constituents [cite ANA 46, 47]:

$$D_2^{\beta=1} = E_{CF3} \left( \frac{E_{CF1}}{E_{CF2}} \right)^3 \quad (8.1)$$

Where the energy correlation functions are defined as:

$$E_{CF1} = \sum_i p_{T,i} \quad (8.2)$$

$$E_{CF2} = \sum_{ij} p_{T,i} p_{T,j} \Delta R_{ij} \quad (8.3)$$

$$E_{CF3} = \sum_{ijk} p_{T,i} p_{T,j} p_{T,k} \Delta R_{ij} \Delta R_{jk} \Delta R_{ki} \quad (8.4)$$

A two-dimensional optimization of the jet mass and  $D_2$  thresholds was performed to provide maximum sensitivity for this analysis. This optimization was done by maximizing the signal sensitivity (using HVT  $W'$  and  $G_{KK}$  samples) against the single quark and gluon jet backgrounds in bins of jet  $p_T$ . Figure 8.3 shows the optimized thresholds on  $D_2$  and jet mass as a function of jet  $p_T$ . Figure 8.4 shows the efficiency of the optimized  $W/Z$  taggers as a function of jet  $p_T$ .

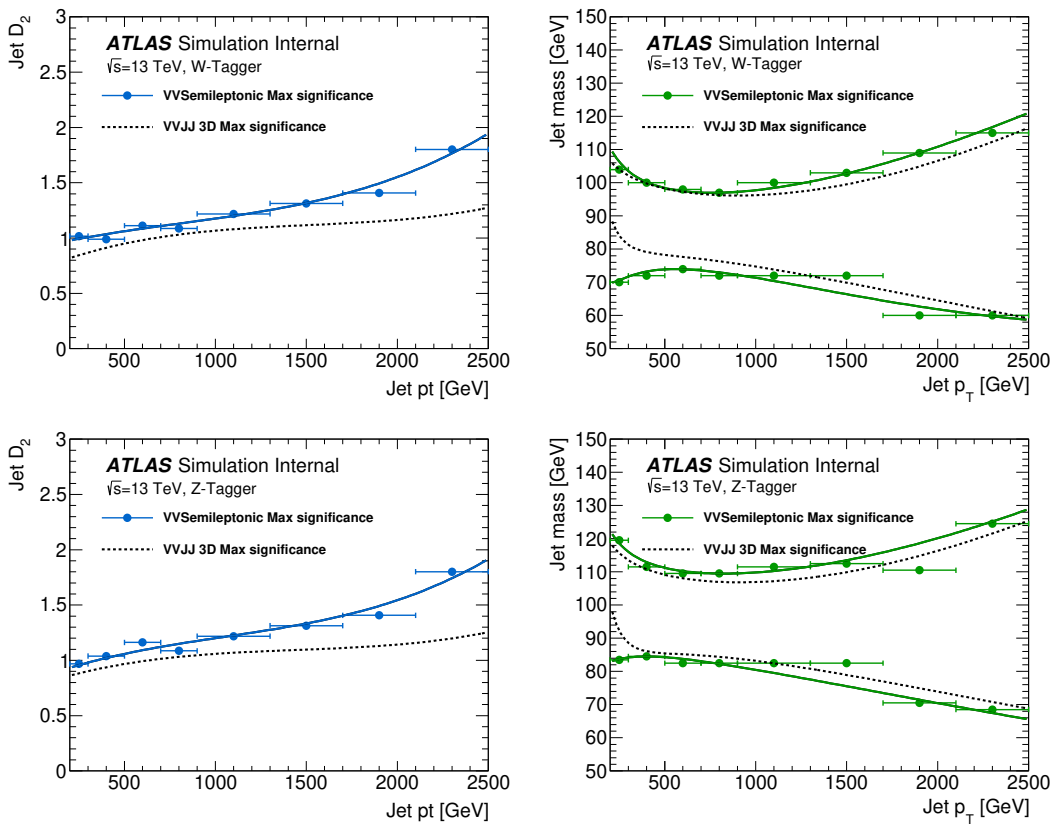


**Figure 8.3:** The upper cut on  $D_2$  (a) and jet mass window cut i.e. the upper and lower boundary of the mass (b) of the  $W$ -tagger as a function of jet  $p_T$ . Corresponding values for  $Z$ -tagger are shown in (c) and (d). The optimal cut values for maximum significance are shown as solid markers and the fitted function as solid lines. Working points from  $VV \rightarrow JJ$ [ATLAS-HDBS-2018-31-002] is also shown as dashed lines as a reference. Natasha reword?

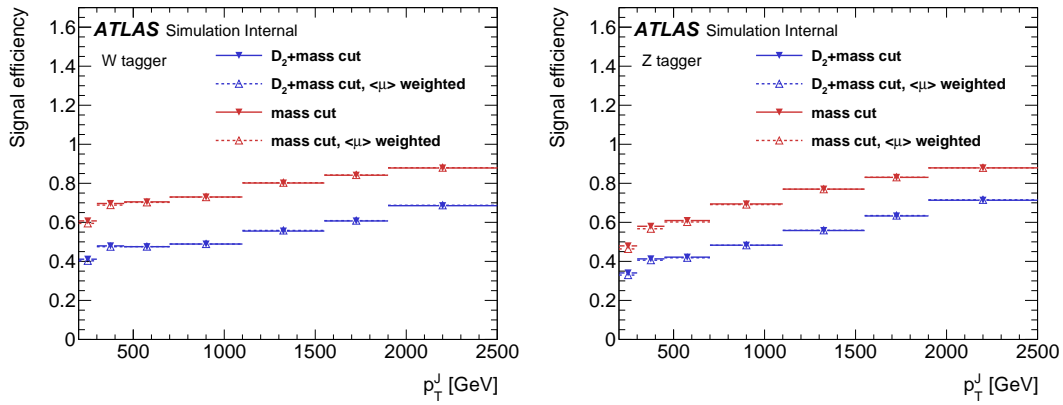


**Figure 8.4:** Natasha write caption

### 857 8.3.3 Variable Radius jets

858 To more accept more boosted  $Z$  bosons decaying to  $b\bar{b}$  that would normally be  
 859 rejected due to topological cuts discussed ?? variable radius (VR) track jets are  
 860 used to identify  $b$ -jets within the catchment area of large- $R$  jets [14]. VR jets are  
 861 constructed from ID tracks using the anti- $k_t$  algorithm with a radius parameter  
 862 that depends on the  $p_T$  of the track, shown in Equation 8.5.

$$R_{eff}(p_{T,i}) = \frac{\rho}{p_{T,i}} \quad (8.5)$$

863 For this search  $\rho = 30$  GeV and an upper and lower limit on cone size are set  
 864 to 0.02 and 0.4, respectively, to prevent unphysical asymptotic behavior of  $\rho$ .  
 865 Collinear VR jets are possible, so track jets that are not separated by the the  
 866 smaller jet's cone size are not used. Additionally, VR jets are required to have  
 867  $p_T > 10$  GeV and  $|\eta| < 2.5$ .

868 **8.3.4 Jet Flavor Tagging**

869 To further classify events, the small-R and VR jets originating from a b-quark  
870 are classified using a multivariate  $b$ -tagging algorithm (BDT), MV2c10 [cite G 210  
871 199]. This algorithm uses the impact parameters of the jet's ID tracks, secondary  
872 vertices (if they exist), and reconstructed flight paths of  $b$  and  $c$  hadrons in the  
873 jet to determine if the jet was induced by a  $b$ -quark. For this analysis the 85%  
874 efficient working point of this algorithm is used giving  $c$ ,  $\tau$ , and light-flavor jet  
875 rejection of 3, 8, and 34 respectively in simulated  $t\bar{t}$  samples.

876 **8.4 MET/Neutrinos**

877 As neutrinos are uncharged and colorless they do not leave tracks or jets in the  
878 detector. For this reason, neutrinos are reconstructed calculated the  $E_T^{miss}$ , the  
879 negative vector sum of  $p_T$  all the physics objects and an extra "soft" term. The  
880 "soft" term accounts for energy deposits not associated with any of the objects in  
881 the event. For this analysis the soft term is given by the sum  $p_T$  of all ID tracks  
882 not associated with objects in the event. The selected tracks must be matched to  
883 the primary vertex, which decreases pile-up contamination [cite G 217 218]. The  
884 tight working point is used [Natasha look up what this means].

885 **8.5 Overlap Removal**

886 Reconstructed jets and leptons in this analysis can arise from the same energy  
887 deposits. For instance, a cluster of energy from an electron can also be a valid  
888 calorimeter seed for a jet. To mitigate this confusion of multiple objects originating  
889 from a single jet or lepton overlapping objects are removed via a procedure referred  
890 to a overlap removal. In this procedure the separation of the two objects,  $\Delta(R) =$

891  $\sqrt{(\Delta\eta)^2 + (\Delta\phi)^2}$  determines which object is removed from the event.

892 The overlap selections used in this analysis are:

- 893 - when an electron shares a track with another electron with the lower  $p_T$   
894     electron is rejected, as it is more likely to be a fake electron
- 895 - when a muon and electron share a track the muon is rejected if it is a  
896     calo-muon, otherwise the electron is rejected
- 897 - when  $\Delta R < 0.2$  for an electron and jet, the jet is rejected to maximize signal  
898     acceptance
- 899 - when  $\Delta R > 0.2$  for an electron and jet, the electron is rejected as likely  
900     originated from decays within the jet
- 901 - when  $\Delta R < \min(0.4, 0.04 + 10\text{GeV}/p_T^\mu)$  the muon is rejected, again maximiz-  
902     ing signal acceptance, otherwise the jet is rejected
- 903 - when  $\Delta R < 1.0$  for the a large-R jet and electron, the jet is rejected

## 904 8.6 Reconstructed Resonance Mass ( $m_{WV}$ )

905 The  $WV$  system mass,  $m_{WV}$  is reconstructed from the lepton, neutrino, and  
906 hadronically-decaying boson candidate. The momentum of the neutrino along the  
907  $z$ -direction is obtained by constraining the  $W$  boson mass of the lepton neutrino  
908 system to be  $80.3 \text{ GeV}/c^2$ . For complex solutions to this constraint,  $p_Z$  is taken  
909 as the real component of the solution. For real solutions, the one with the smaller  
910 absolute value is used. For the resolved analysis,  $m_{WV}$  is reconstructed by con-  
911 straining the  $W(Z)$  dijet system in the SRs, which improves the mass resolution:

$$p_{T,jj}^{corr} = p_{T,jj} \times \frac{m_{W/Z}}{m_{jj}} \quad (8.6)$$

$$m_{jj}^{corr} = m_{W/Z} \quad (8.7)$$

912 where  $m_{jj}$  and  $m_{W/Z}$  are the reconstructed invariant mass of the hadronically-  
913 decaying W/Z boson and the PDG values of the  $W/Z$  boson masses, respectively.  
914 The reconstructed resonance mass is the final discriminating variable in this anal-  
915 ysis. The distribution of this variable in the CR and SRs are used in the final  
916 likelihood fit to search for evidence of an excess of events due to BSM resonances.  
917 The distribution of  $m_{WV}$  are shown in Figures 12.9-12.17.

918 **Chapter 9**

919 **Event Selection and**  
920 **Categorization**

921 **9.1 Pre-selection**

922 Before applying topological cuts to suppress backgrounds and reduce data  
923 size in this search, preselection cuts are applied which include trigger and event  
924 requirements. Events must contain exactly one tight lepton (no additional loose  
925 leptons), the  $p_T^{\ell\nu} > 75$  GeV, and there must be at least two small-R jets or one  
926 large-R jet.

927 **9.2 Trigger**

928 The data were collected using the lowest unprescaled single-lepton or  $E_T^{miss}$   
929 triggers, as summarized in Table 9.1. Since the muon term is not considered in the  
930 trigger  $E_T^{miss}$  calculation, the  $E_T^{miss}$  trigger is fully efficient to events with high- $p_T$   
931 muons. For this reason, the  $E_T^{miss}$  trigger is used for events where  $p_T^\mu > 150$  GeV, to  
932 compensate for the poor efficiency of the single muon trigger above  $p_T^\mu > 150$  GeV.

**Table 9.1:** The list of triggers used in the analysis.

Data-taking period	$e\nu qq$ channel	$\mu\nu qq$ ( $p_T(\mu\nu) < 150$ GeV) channel	$\mu\nu qq$ ( $p_T(\mu\nu) > 150$ GeV) channel
2015	HLT_e24_lhmedium_L1EM20 OR HLT_e60_lhmedium OR HLT_e120_lhloose	HLT_mu20_iloose_L1MU15 OR HLT_mu50	HLT_xe70
2016a (run $< 302919$ ) $(L < 1.0 \times 10^{34} \text{ cm}^{-2} \text{ s}^{-1})$	HLT_e26_lhtight_nod0_ivarloose OR HLT_e60_lhmedium_nod0 OR HLT_e140_lhloose_nod0 HLT_e300_etcut	HLT_mu26_ivarmedium OR HLT_mu50	HLT_xe90_mht_L1XE50
2016b (run $\geq 302919$ ) $(L < 1.7 \times 10^{34} \text{ cm}^{-2} \text{ s}^{-1})$	same as above	same as above	HLT_xe110_mht_L1XE50
2017	same as above	same as above	HLT_xe110_pufit_L1XE55
2018	same as above	same as above	HLT_xe110_pufit_xe70_L1XE50

933 **9.3 non-VBF/VBF RNN**

934 To classify events as originating from non-VBF or VBF production a recursive  
935 neural network (RNN [21]) is used. This approach is more powerful than a cut-  
936 based classification as it improves signal efficiency and analysis sensitivity by  
937 exploiting correlations between variables that the RNN learns. In particular, a  
938 RNN architecture is ideal as it can handle variable numbers of jets in the events.

939 The RNN uses the four-momentum of candidate VBF jets to classify events  
940 as VBF or non-VBF topologies. Sometimes jets are incorrectly reconstructed,  
941 so the number of jets in the event is expected to vary across the input samples.  
942 VBF candidate jets are identified by removing jets from the event that are likely  
943 from  $W/Z \rightarrow qq$ . For the resolved regime this means removing the two leading  
944 small-R jets from the VBF candidate jet list. For the merged regime this means  
945 removing small-R jets separated by less than 1.0 in  $dR$  from the large-R jet. VBF  
946 candidate jets are also required to be within  $|\eta| < 4.5$ . From the list of remaining  
947 VBF candidate jets, the two highest- $p_T$  jets are chosen.

948 The architecture of the RNN is shown in Figure 9.2. The RNN is composed  
949 of Long Short Term Memory Cells (LSTM) that extract meaningful information  
950 and retains<sup>3</sup> it. The logic embedded in the LSTM is shown in Figure ???. LSTMs  
951 are useful for VBF event classification for events with two jets, where using the  
952 kinematic properties of both jets (and their correlations) will lead to more efficient  
953 event classification.

954 In this RNN architecture, the VBF candidates are first passed to a masking  
955 layer which checks the number of jets in the event. If there is only one jet, only one  
956 vertical LSTM layer is used. The output of masking is then passed to a LSTM,  
957 with a tanh activation function. The output of the LSTM is then passed to a  
958 second horizontal LSTM layer (and vertical LSTM layer if there are two jets in

959 the event). Finally the output of the last LSTM cell is passed to a dense layer  
960 and then to a sigmoid activation layer, leading to an overall RNN score.

961 The weights and other parameters of the network are learned by training the  
962 network with VBF and non-VBF signals over 200 epochs with an Adam Optimizer  
963 [13]. To prevent overfitting during training, dropout is applied to RNN weights  
964 and training is truncated if the network parameters are unchanged after ten it-  
965 erations [23]. Figure 9.4 shows the ROC curve for the RNN using k-fold cross  
966 validation [19].

967 Figure 9.3 shows the RNN discriminant for backgrounds, non-VBF signals,  
968 and VBF signals. The RNN score is  $\sim 0$  for non-VBF signals and background  
969 processes and  $\sim 1$  for VBF processes. Figure 9.5 shows the limits for various signal  
970 processes based on the RNN cut applied. Requiring the RNN score to be  $> 0.8$   
971 was chosen as it provided the best significance (and signal efficiency) for this final  
972 state and the  $\nu\nu qq$  and  $\ell\ell qq$  channels, which this channel will be combined with  
973 for future publications.

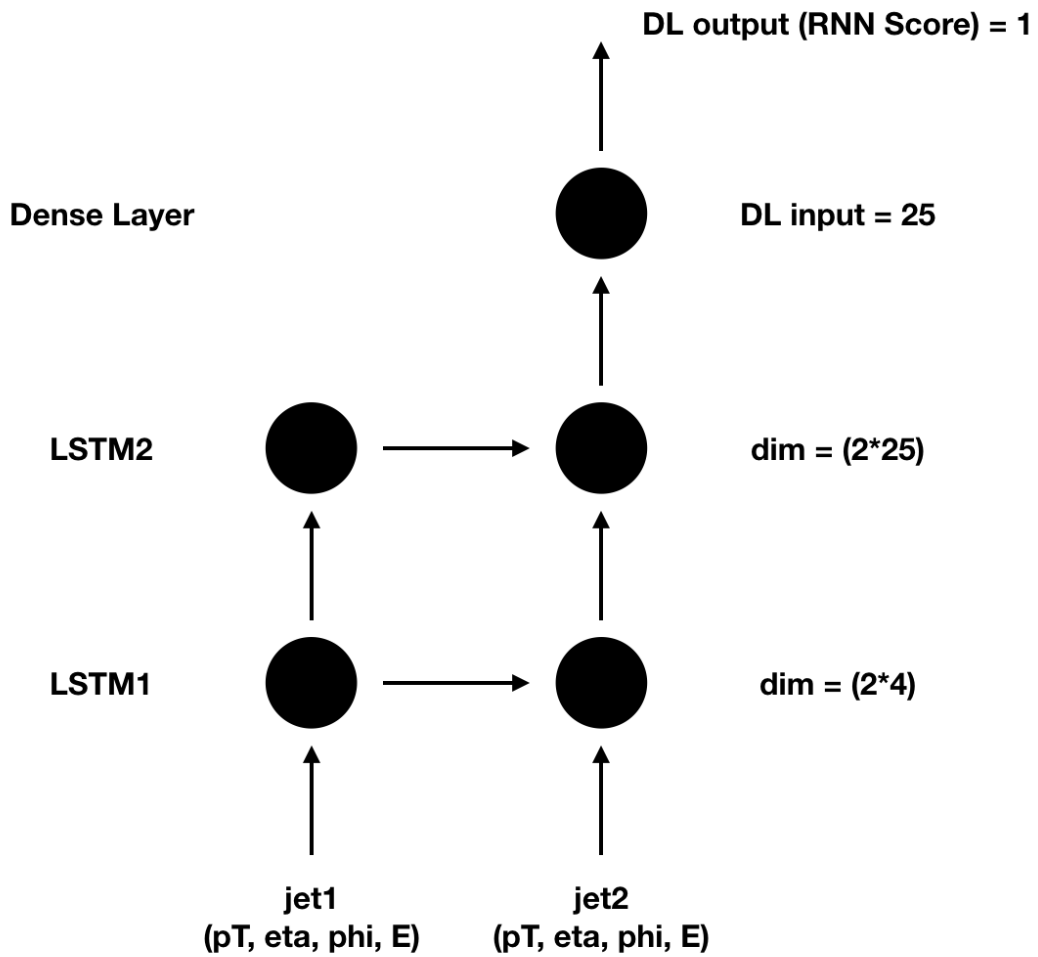


**Figure 9.1:** RNN architecture. Natasha add caption

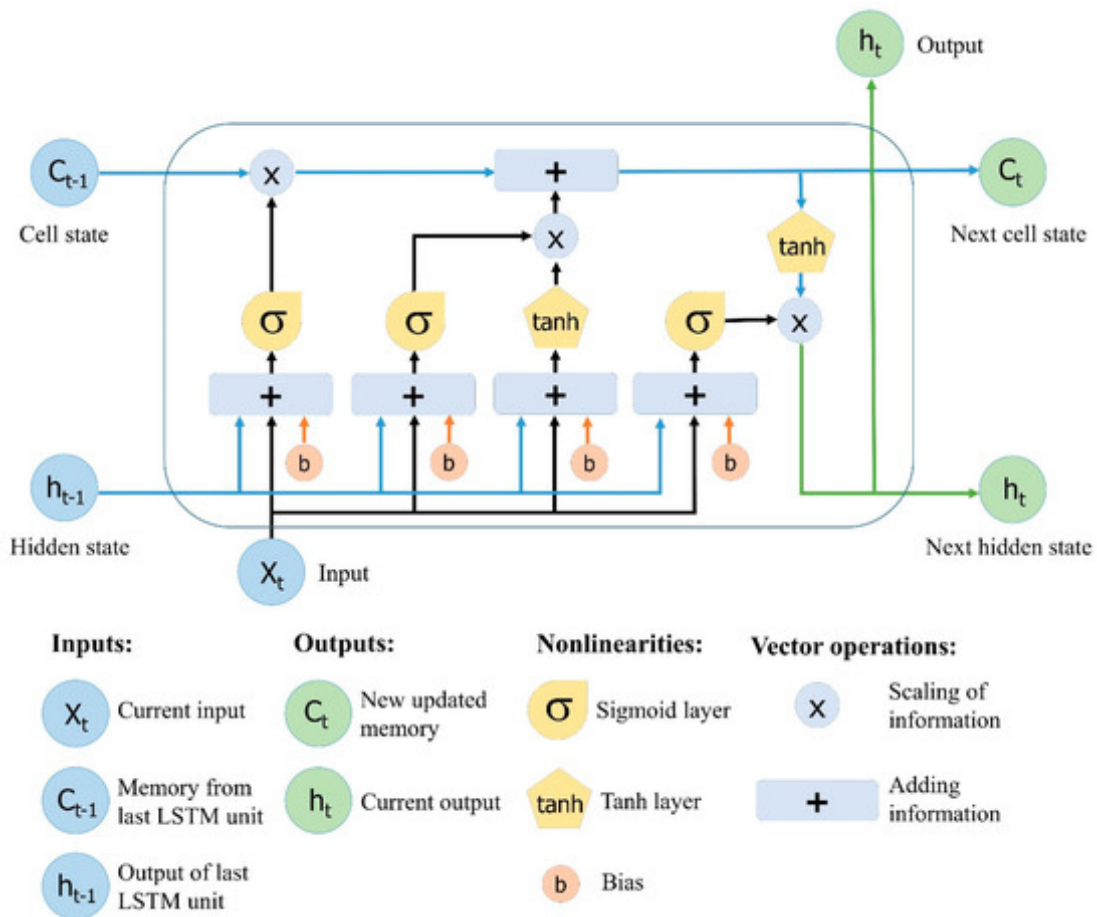


**Figure 9.2:** This figure shows the embedded logic in LSTM cells. This image was taken from [22], where a more in depth discussion about LSTMs may be found.

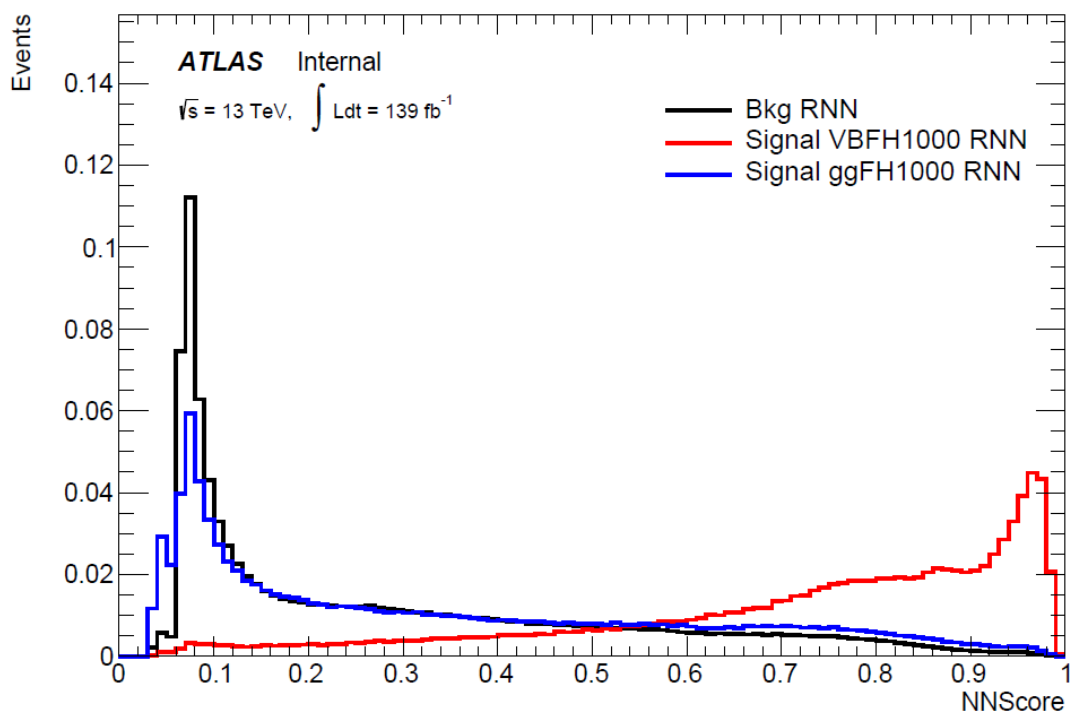


**Figure 9.3:** RNN Score distribution for ggF and VBF signals and backgrounds.

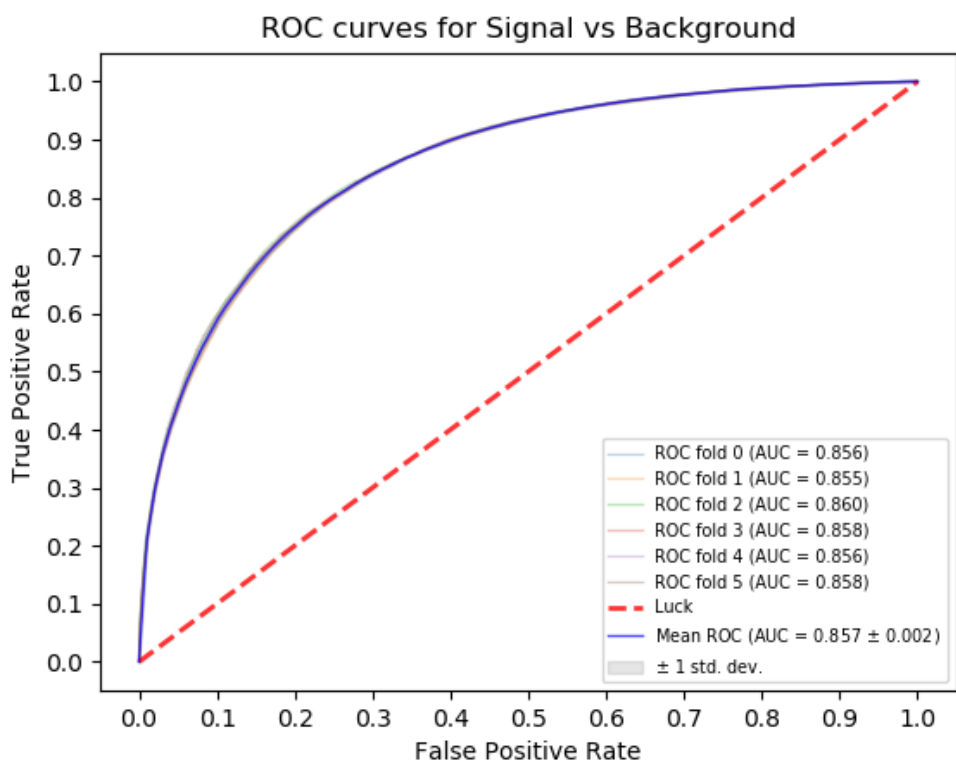


**Figure 9.4:** ROC curve using k-fold validation for RNN.

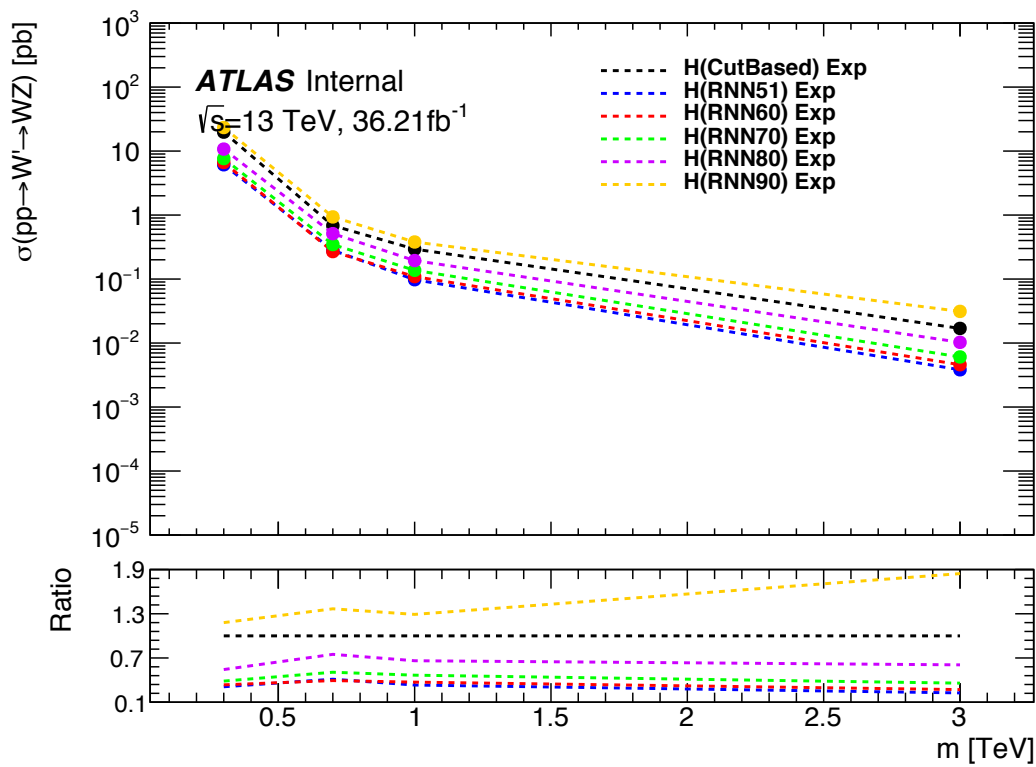


**Figure 9.5:** Comparison of GGF Z' limits for different RNN score selections. The bottom panel shows the ratio of the upper limits set for different RNN cuts to the cut-based analysis. In this panel smaller numbers, indicate that the expected upper limit is smaller than the cut-based analysis, which is desired.

## 974 9.4 Signal Region Definitions

975     Signal regions are constructed to be dominated by signal and used in the final  
976 likelihood fit to look for a bump in the reconstructed resonance mass distribution.  
977     Once an event is classified by the RNN, it must pass topological cuts that maximize  
978  $S/\sqrt{B}$ . To efficiently select events with a  $W \rightarrow \ell\nu$  candidate exactly one tight  
979 lepton is required and  $E_T^{miss} > 100(60)$  GeV and  $p_{T,\ell\nu} > 200(75)$  GeV in the  
980 merged (resolved) analysis to suppress the fake lepton backgrounds.

981     For the merged analysis, in addition to the  $W \rightarrow \ell\nu$  and  $W/Z \rightarrow J$  selections  
982 above, the  $\min(p_{T,\ell\nu}, p_{T,J})/m_{WV} > 0.35(0.25)$  for the non-VBF (VBF) category.  
983     To reduce  $t\bar{t}$  contamination, events with at least one b jet with  $\Delta R > 1.0$  from  
984 the large-R jet are excluded. High purity signal regions require the  $D_2$  and  $W/Z$   
985 mass window cut to be passed, whereas the low purity region only requires the  
986  $W/Z$  mass window cut to be passed.

987     For the HVT  $W'$  resonance search tagged and untagged regions are used to  
988 increase signal acceptance. For events to be classified as tagged the large-R jet  
989 must contain exactly two b-tagged jets. Untagged events must have no more than  
990 one b-tagged jet matched to the large-R jet. These selections are shown in Table  
991 9.2.

992     Events failing the merged selection are then re-analyzed in the resolved cat-  
993 egory. To enhance resolved signals, the event should contain two high- $p_T$  boson  
994 candidates that are back-to-back in the  $\phi$  as shown by the cuts in Table 9.3.  
995     Again, to suppress the  $t\bar{t}$  backgrounds, events are required to have no additional  
996 b-jets. A summary of the resolved selections is shown in Table 9.3.

997     The analysis cutflow is shows in Figure 9.6. Events classified as VBF events  
998 are classified as Merged High purity, low purity or resolved signal region selections  
999 sequentially. If the event does not pass any of these selections but passes a VBF

**Table 9.2:** Summary of selection criteria used to define the signal region (SR),  $W$ +jets control region ( $W$  CR) and  $t\bar{t}$  control region ( $t\bar{t}$  CR) for merged 1-lepton channel.

Selection		SR		W CR (WR)		$t\bar{t}$ CR (TR1)	
		HP	LP	HP	LP	HP	LP
$W \rightarrow \ell\nu$	Num of Tight leptons	1					
	Num of Loose leptons	0					
	$E_T^{\text{miss}}$	$> 100 \text{ GeV}$					
	$p_T(\ell\nu)$	$> 200 \text{ GeV}$					
$W/Z \rightarrow J$	Num of large- $R$ jets	$\geq 1$					
	$D_2$ cut	pass	fail	pass	fail	pass	fail
	$W/Z$ mass window cut	pass	pass	fail	fail	pass	pass
	Numb. of associated VR track jets $b$ -tagged	For $Z \rightarrow J$ : $\leq 1$ ( $= 2$ ) for untagged (tagged) category					
	$\min(p_{T,\ell\nu}, p_{T,J}) / m_{WV}$	$> 0.35(0.25)$ for DY/ggF (VBF) category					
	Top-quark veto	Num of $b$ -tagged jets outside of large- $R$ jet	0			$\geq 1$	
Pass VBF selection			no (yes) for DY/ggF (VBF) category				

control region selection it is classified as a VBF CR event. If the event fails the VBF selection it is then checked if it passes the Merged High purity, Low purity or resolved signal region selections (NB: for the  $WZ$  decay modes all the regions have tagged and untagged categories). If the event fails all the GGF signal region selections, it is then kept for GGF control region selections, if it passes those selections.

**Table 9.3:** The list of selection cuts in the resolved analysis for the  $WW$  and  $WZ$  signal regions (SR),  $W+\text{jets}$  control region (WR) and  $t\bar{t}$  control region (TR).

cuts	SR	$W$ CR (WR)	$t\bar{t}$ CR (TR1)
$W \rightarrow \ell\nu$	Number of Tight leptons	1	
	Number of Loose leptons	0	
	$E_T^{\text{miss}}$	$> 60 \text{ GeV}$	
	$\cancel{p}_T(\ell\nu)$	$> 75 \text{ GeV}$	
$W/Z \rightarrow jj$	Number of small-R jets	$\geq 2$	
	Leading jet $p_T$	$> 60 \text{ GeV}$	
	Subleading jet $p_T$	$> 45 \text{ GeV}$	
	$Z \rightarrow q\bar{q}$ $W \rightarrow q\bar{q}$	$78 < m_{jj} < 105 \text{ GeV}$ $68 < m_{jj} < 98 \text{ GeV}$	$50 < m_{jj} < 68 \text{ GeV}$ or $105 < m_{jj} < 150 \text{ GeV}$
Topology cuts	Num. of $b$ -tagged jets	For $Z \rightarrow jj$ : $\leq 1$ ( $= 2$ ) for untagged (tagged) category	
	$\Delta\phi(j, \ell)$	$> 1.0$	
	$\Delta\phi(j, E_T^{\text{miss}})$	$> 1.0$	
	$\Delta\phi(j, j)$	$< 1.5$	
	$\Delta\phi(\ell, E_T^{\text{miss}})$	$< 1.5$	
Top vetos	$\min(p_{T,\ell\nu}, p_{T,jj}) / m_{WW}$	$> 0.35(0.25)$ for DY/ggF (VBF) category	
	Number of additional $b$ -tagged jets	0	$\geq 1$
Pass VBF selection		no (yes) for DY/ggF (VBF) category	

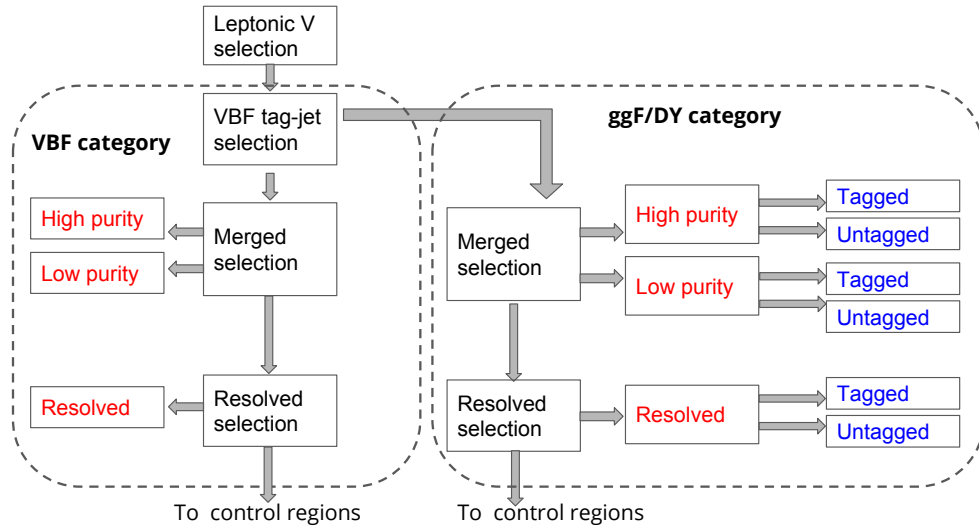


**Figure 9.6:** Event Categorization. Natasha write more.

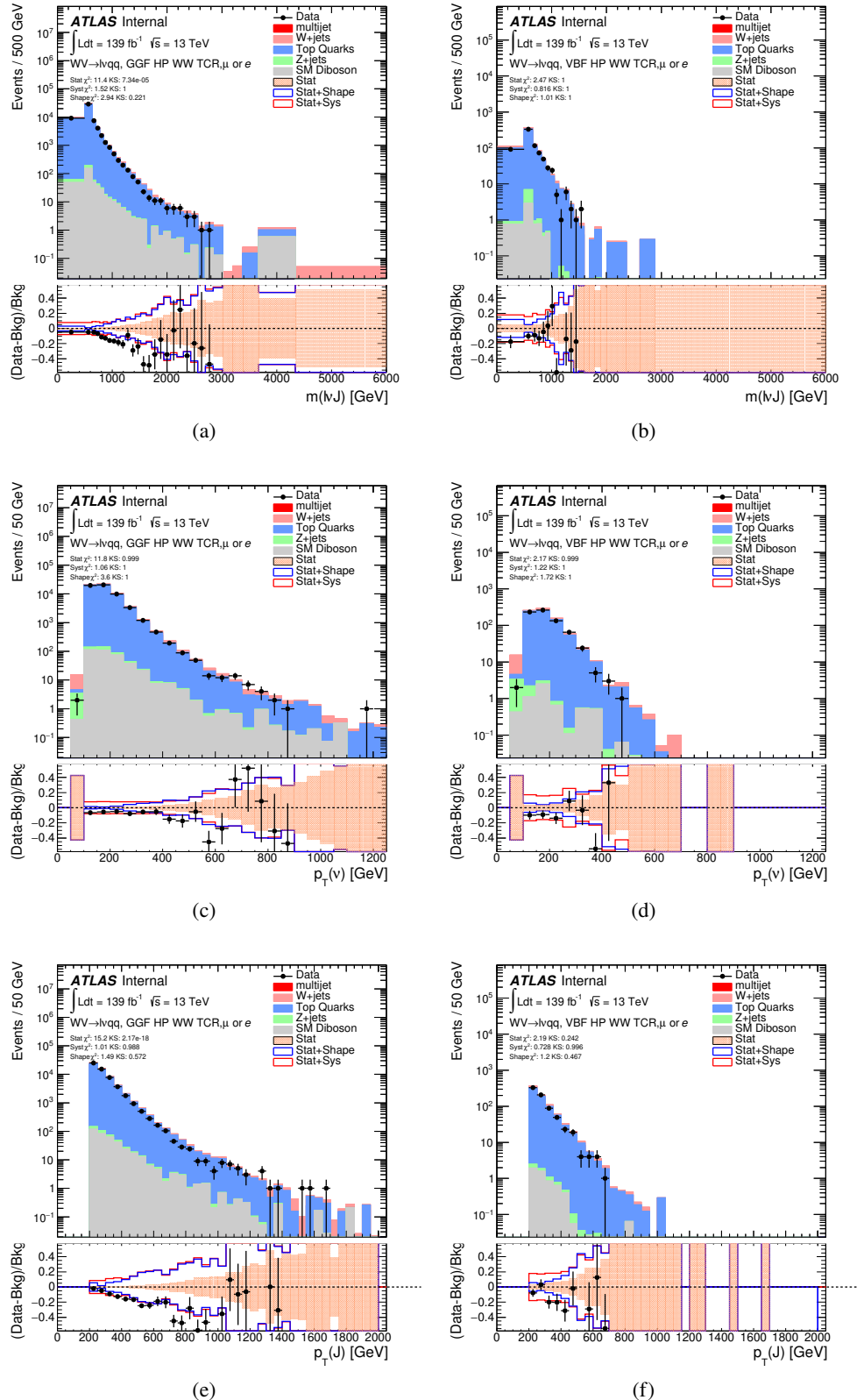


**Figure 9.7:** Data MC comparison for the merged  $WW$  HP TCR. The bottom panel shows the ratio of the difference<sup>87</sup> between data and simulation to simulation. The red bands include the all systematic and statistical uncertainties on the background.

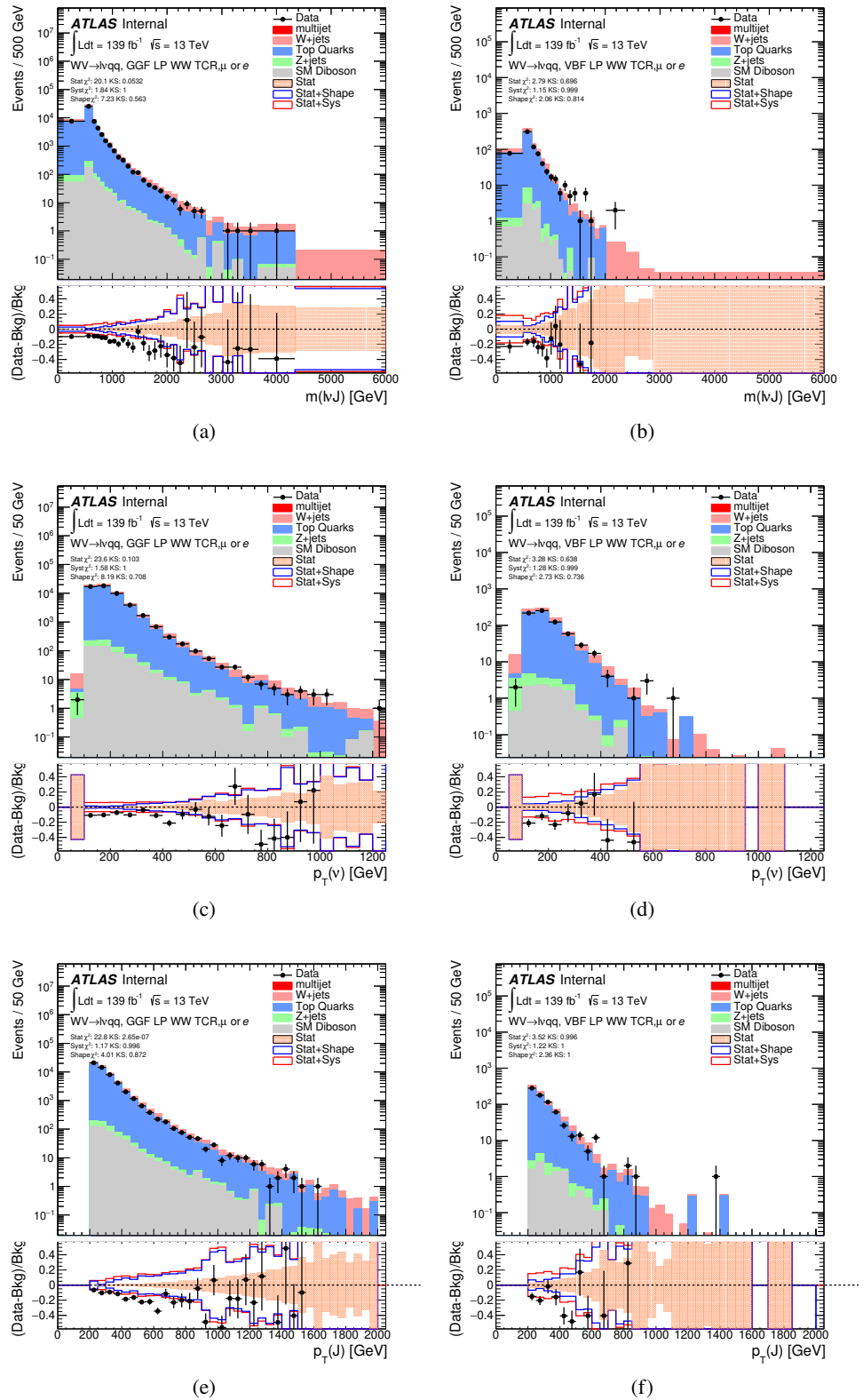


**Figure 9.8:** Data MC comparison for the merged  $WW$  LP TCR. The bottom panel shows the ratio of the difference between data and simulation to simulation. The red bands include the all systematic and statistical uncertainties on the background.<sup>88</sup>

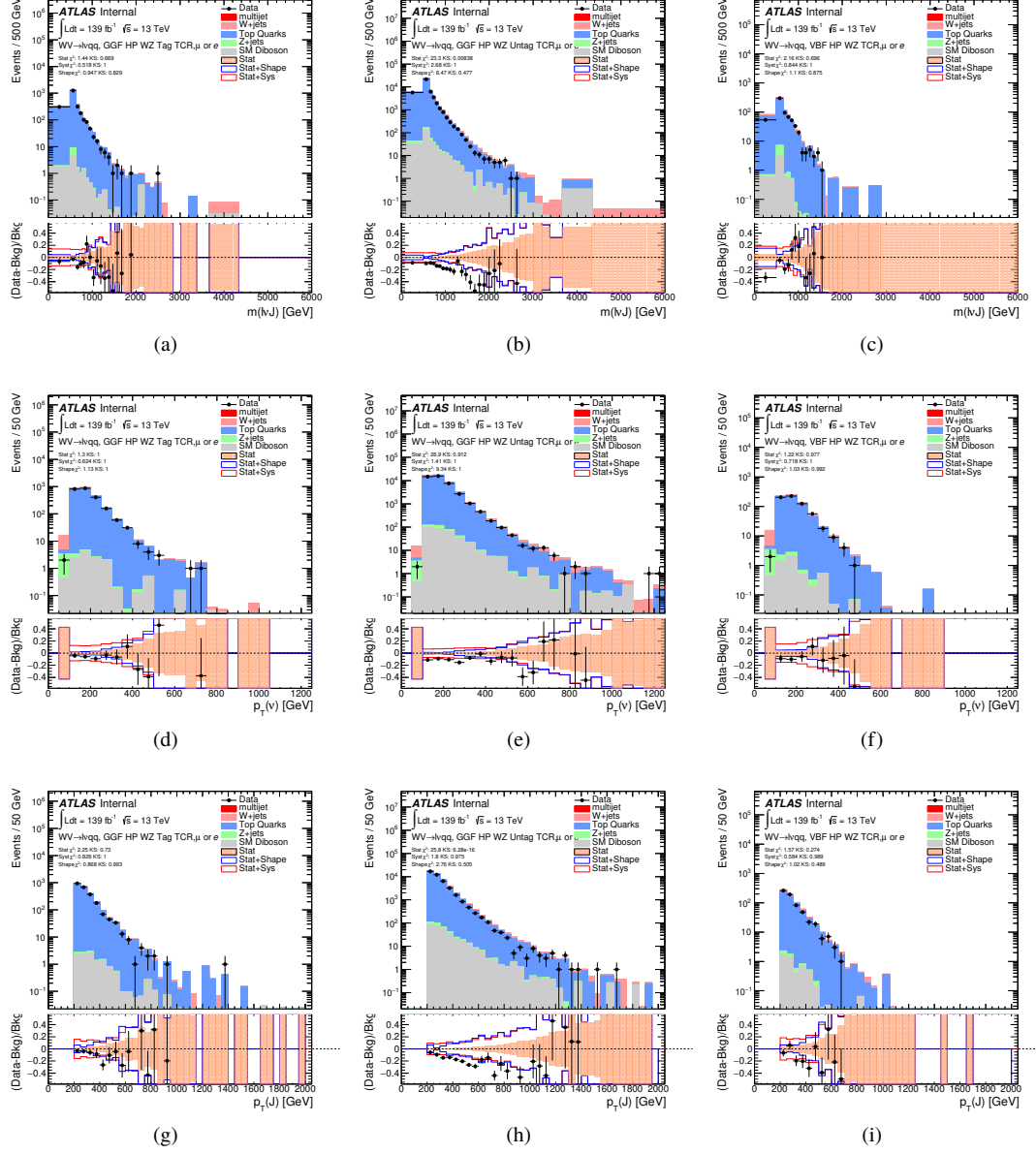


**Figure 9.9:** Data MC comparison for the merged  $WZ$  HP TCR. The bottom panel shows the ratio of the difference between data and simulation to simulation. The red bands include the all systematic and statistical uncertainties on the background.

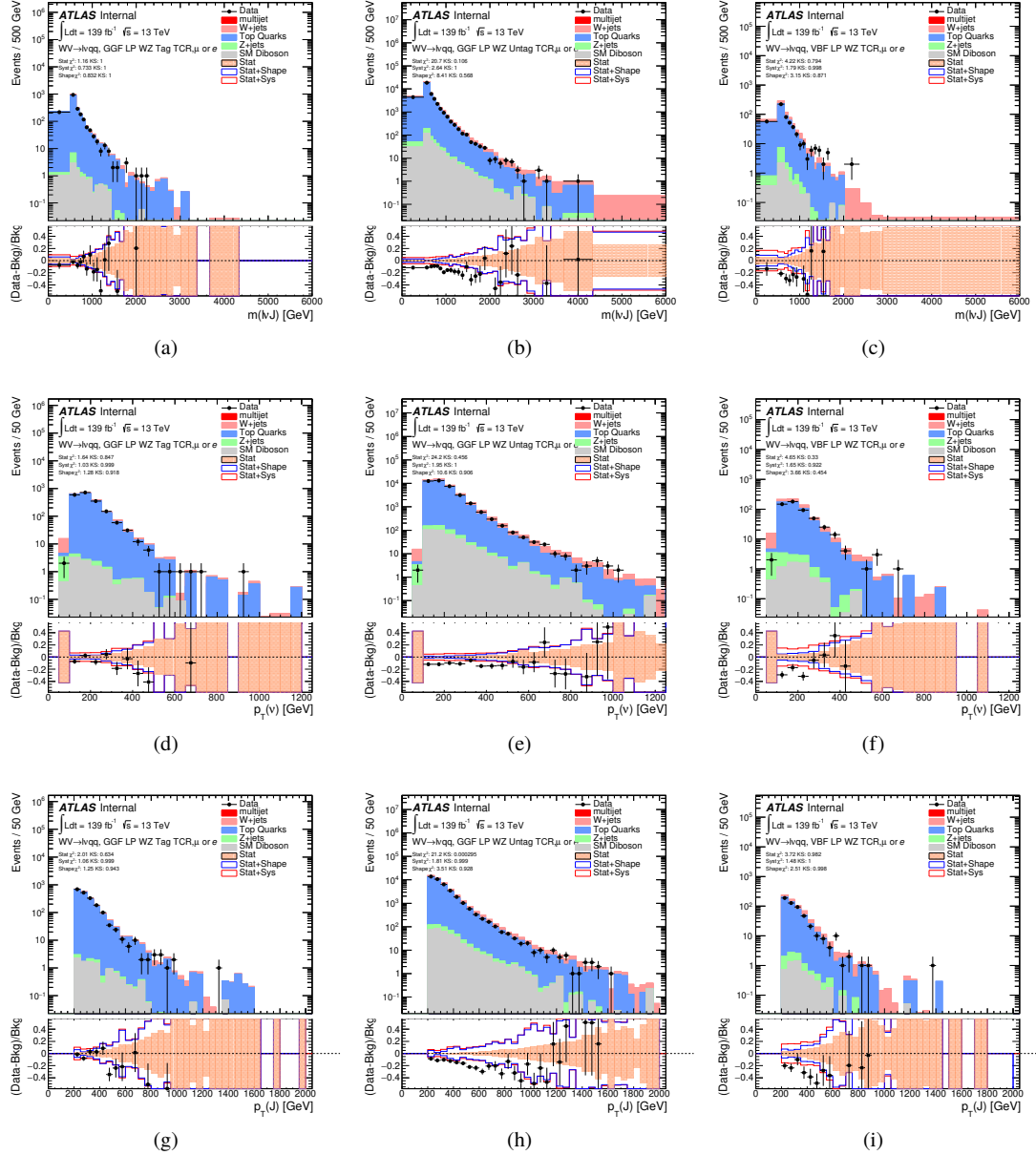


**Figure 9.10:** Data MC comparison for the merged  $WZ$  LP TCR. The bottom panel shows the ratio of the difference between data and simulation to simulation. The red bands include the all systematic and statistical uncertainties on the background.

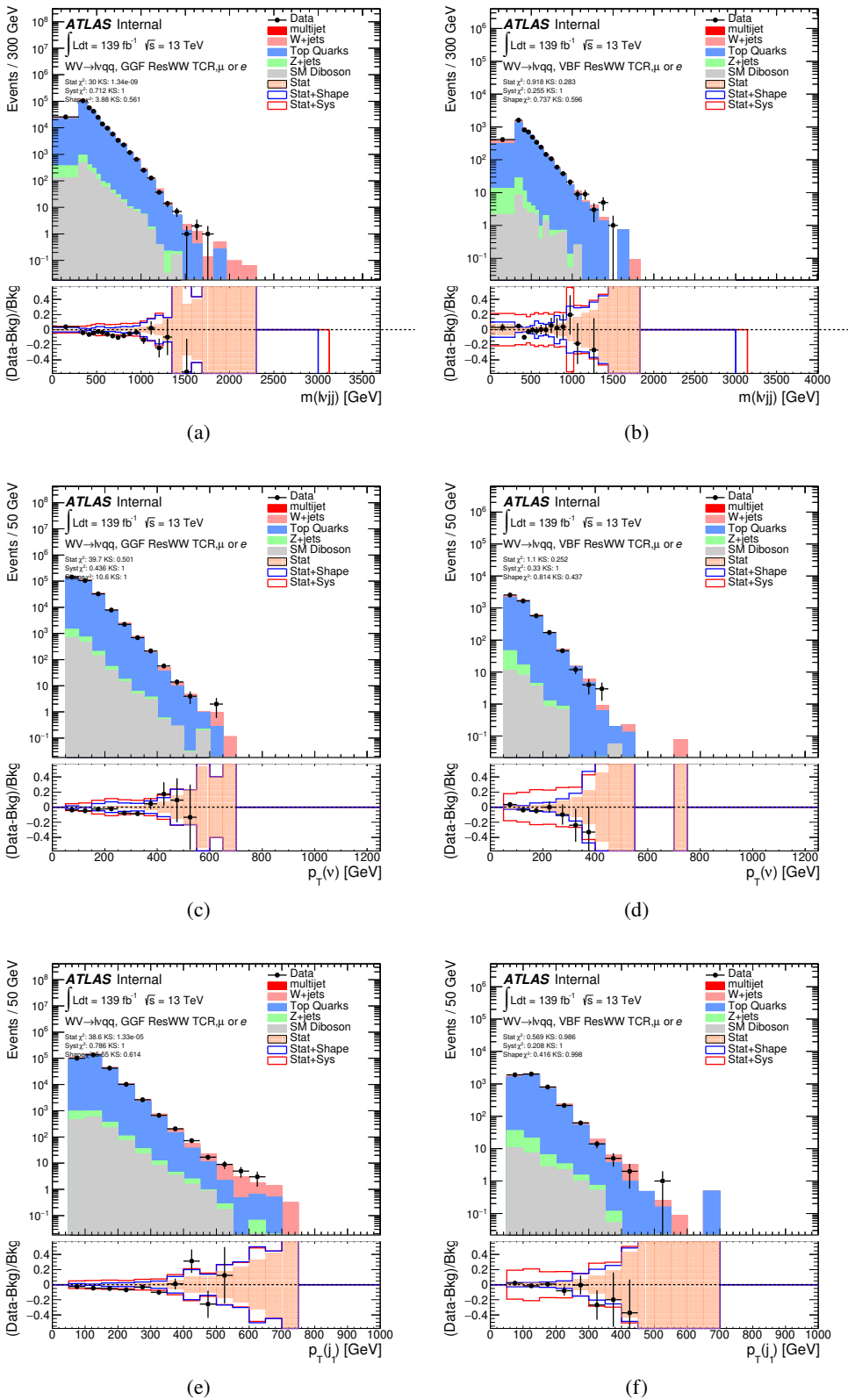


**Figure 9.11:** Data MC comparison for the resolved  $WW$  TCR. The bottom panel shows the ratio of the difference between data and simulation to simulation. The red bands include the all systematic and statistical uncertainties on the background.

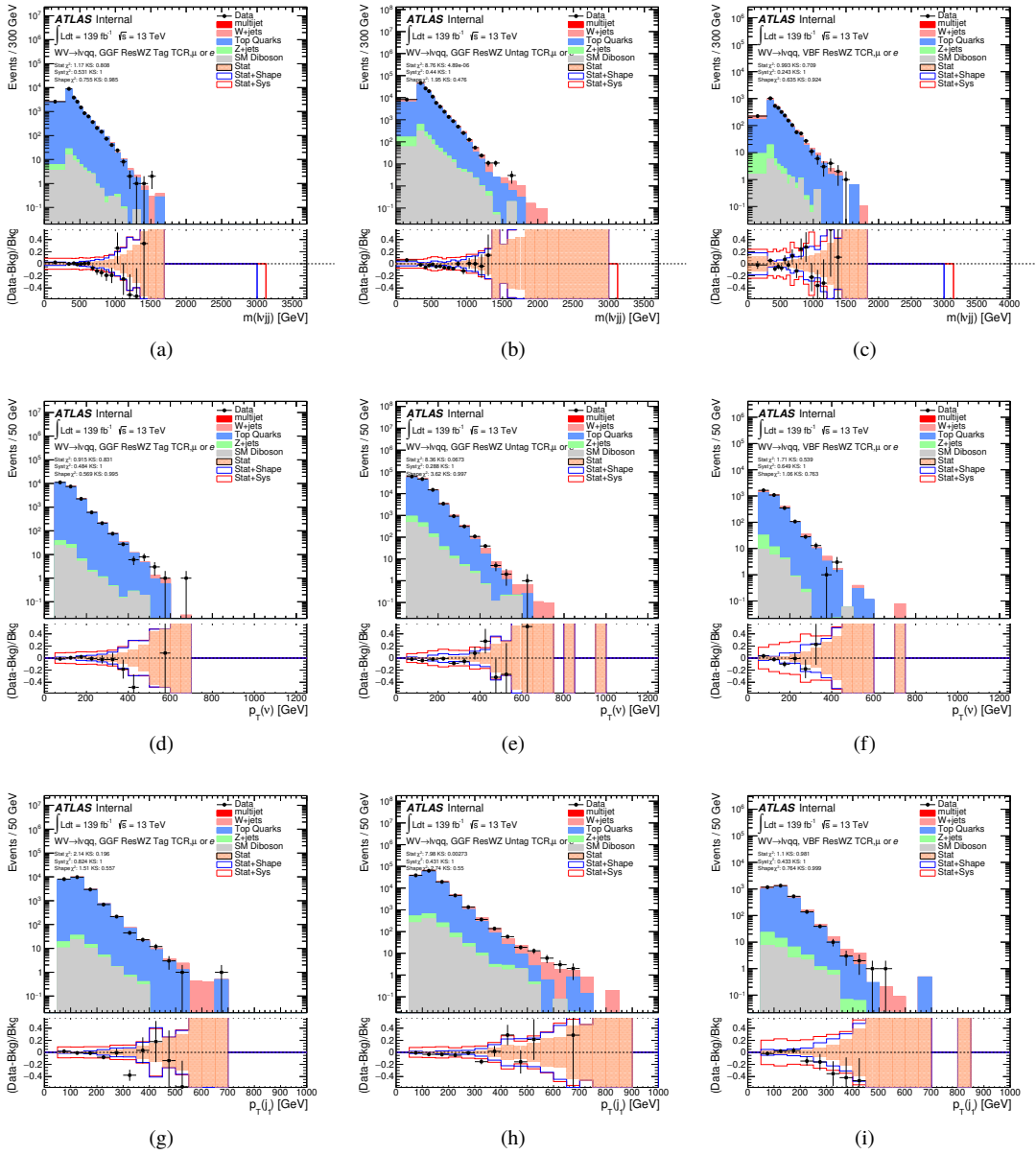


**Figure 9.12:** Data MC comparison for the resolved  $WZ$  TCR. The bottom panel shows the ratio of the difference between data and simulation to simulation. The red bands include the all systematic and statistical uncertainties on the background.

## 1006 9.5 Selection Acceptance times efficiency for Sig- 1007 nal Events

1008 The acceptance times efficiency for the signal region selection is defined as:

$$A \cdot \epsilon = \frac{N_{\text{events selected}}^{\text{truth}}}{N_{\text{events generated}}^{\text{truth}}} \cdot \frac{N_{\text{events selected}}^{\text{reco}}}{N_{\text{events selected}}^{\text{truth}}} = \frac{N_{\text{events selected}}^{\text{reco}}}{N_{\text{events generated}}^{\text{truth}}} \quad (9.1)$$

1009 The distributions of  $A \cdot \epsilon$  as a function of the resonance mass for the different spin  
1010 models are shown in Figures 9.14 - ??.

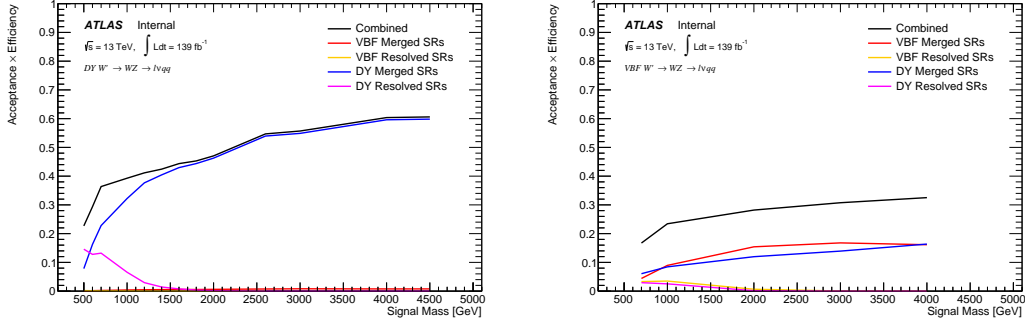


**Figure 9.13:** Selection acceptance times efficiency for the  $W' \rightarrow WZ \rightarrow \ell\nu qq$  events from MC simulations as a function of the  $W'$  mass for (a) Drell-Yan and (b) VBF production, combining the merged HP and LP signal regions of the  $WW \rightarrow \ell\nu J$  selection and the resolved regions of the  $WW \rightarrow \ell\nu jj$  selection.

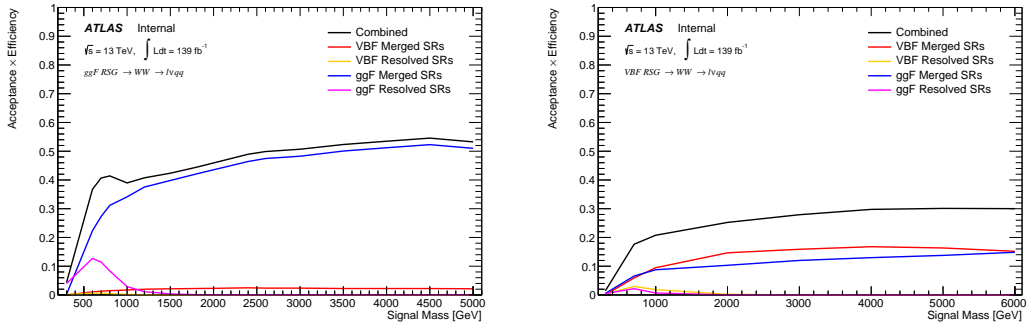


**Figure 9.14:** Selection acceptance times efficiency for the  $G \rightarrow WW \rightarrow \ell\nu qq$  events from MC simulations as a function of the  $G$  mass for (a) Drell-Yan and (b) VBF production, combining the merged HP and LP signal regions of the  $WW \rightarrow \ell\nu J$  selection and the resolved regions of the  $WW \rightarrow \ell\nu jj$  selection.

## 1011 9.6 Background Estimate

### 1012 9.6.1 Control Regions

1013 The distributions for the variables used in merged analysis for top control  
1014 regions are shown in Figure 9.7-9.10.

1015 The distributions for the variables used in the resolved analysis in the TCR  
1016 are shown in Figure 9.11, 9.12.

1017 To more accurately model the two dominant backgrounds in this analysis,  
1018  $W+jets$  and  $t\bar{t}$ , control regions are constructed for each. These control regions  
1019 are dominated by these processes and used to extract normalization factors in  
1020 the final likelihood fit that are then used in the signal region estimates. For the  
1021  $t\bar{t}$  control region the event must contain at least one such b jet. The WCR is  
1022 constructed using the  $m_{jj/J}$  mass window sidebands. All other backgrounds are  
1023 estimated using simulation, except fake lepton backgrounds, which are derived  
1024 using a data-driven method.

1025    **9.6.2 Fake Lepton Backgrounds**

1026    Backgrounds in this analysis containing real leptons (e.g.  $W/Z + \text{jets}$ , diboson,  
1027     $t\bar{t}$ , single- $t$ ) are well-modeled with simulated samples and constrained with data  
1028    from CRs. However, the fake lepton background (also referred to as the multijet  
1029    background) is not well-modeled with simulation. For this reason, the multijet  
1030    background is extracted from data. Heavy flavor decay products, jets, and con-  
1031    verted photons can be mistakenly reconstructed as electrons. Fake electrons often  
1032    arise from jet fakes while non-prompt muons usually arise from heavy flavor decay.  
1033    For this analysis, these fake electrons generally fail the electron ID criteria and  
1034    fake muons fail the muon isolation requirement. Therefore, to derive the multijet  
1035    template shape the SR and CR selections and inverted lepton requirements are  
1036    used as seen in Table 9.4. NB: by inverting the lepton isolation/identification  
1037    criteria the SRs and CRs are orthogonal.

1038    The template shape of the MJ background is determined by using a multijet  
1039    validation region (MJVR) that requires the inverted lepton isolation/identification  
1040    requirement and the two signal jets to satisfy the  $m_{jj}$  requirement used in the  
1041     $W + \text{jets}$  CRs. The  $E_T^{\text{miss}}$  distribution in MJCR is shown in Figure 9.15 for 2017  
1042    data. The template is then extracted by subtracting the data in the MJVR from  
1043    the electroweak background processes. The resulting template and electroweak  
1044    backgrounds are then fit to data. In this fit, the  $E_T^{\text{miss}}$  distribution compared to  
1045    data to extract electroweak background, multijet electron and muon background  
1046    normalizations. The fitted scale factors from this MJVR template are then applied  
1047    in the MJCR template. The electron and muon background normalizations in the  
1048    MJCR template are parameters in the final simultaneous fit. Technically, there  
1049    should be a separate template for every CR and SR, but some MJ regions have  
1050    insufficient statistics to do this. Additionally, the shapes for the MJ templates for

1051 VBF and ggF regions are found to be compatible within statistical uncertainty.  
 1052 Therefore, the sample MJ template used for VBF and ggF CR/SRs, but with  
 1053 different pre-MJ-fit scale factors.

1054 This template method was validated using WCR and full Run 2 data. The  
 1055 results of the fit are shown in Table 9.5. The multijet contribution in the muon  
 1056 channel for  $p_T^W > 150$  GeV is consistent with zero, and therefore neglected in  
 1057 the final fit. Applying the extracted normalization factor to MJVR in WCRs for  
 1058 various kinematic variables such as  $E_T^{miss}$ ,  $W$  transverse mass, lepton  $p_T$ , and the  
 1059 invariant mass as show in Figures 9.16 -9.25. These figures show good agreement  
 1060 between the data and background estimate.

**Table 9.4:** Definitions of “inverted” leptons used in multijet control region

	Criterion	signal lepton	inverted lepton
Electron	ID	TightLH	MediumLH !TightLH
	Calo Isolation	FixedCutHighPtCaloOnlyIso	FixedCutHighPtCaloOnlyIso
Muon	ID	WHSignalMuon	WHSignalMuon
	Track Isolation	FixedCutTightTrackOnlyIso	!FixedCutTightTrackOnlyIso $ptvarcone30/pt < 0.07^*$
*Only applied to events with $pTW < 150GeV$			

1061

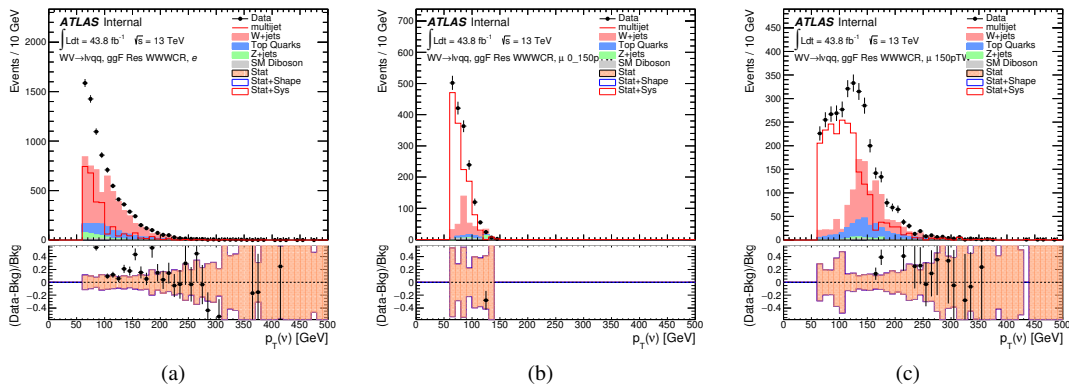


**Figure 9.15:** The  $E_T^{miss}$  distribution in MJCR for 2017 data in the electron channel(left), muon channel with  $W$ -boson  $pT < 150$  GeV (center) and  $> 150$  GeV (right). Multi-jet templates are calculated as remaining data components after excluding known MC

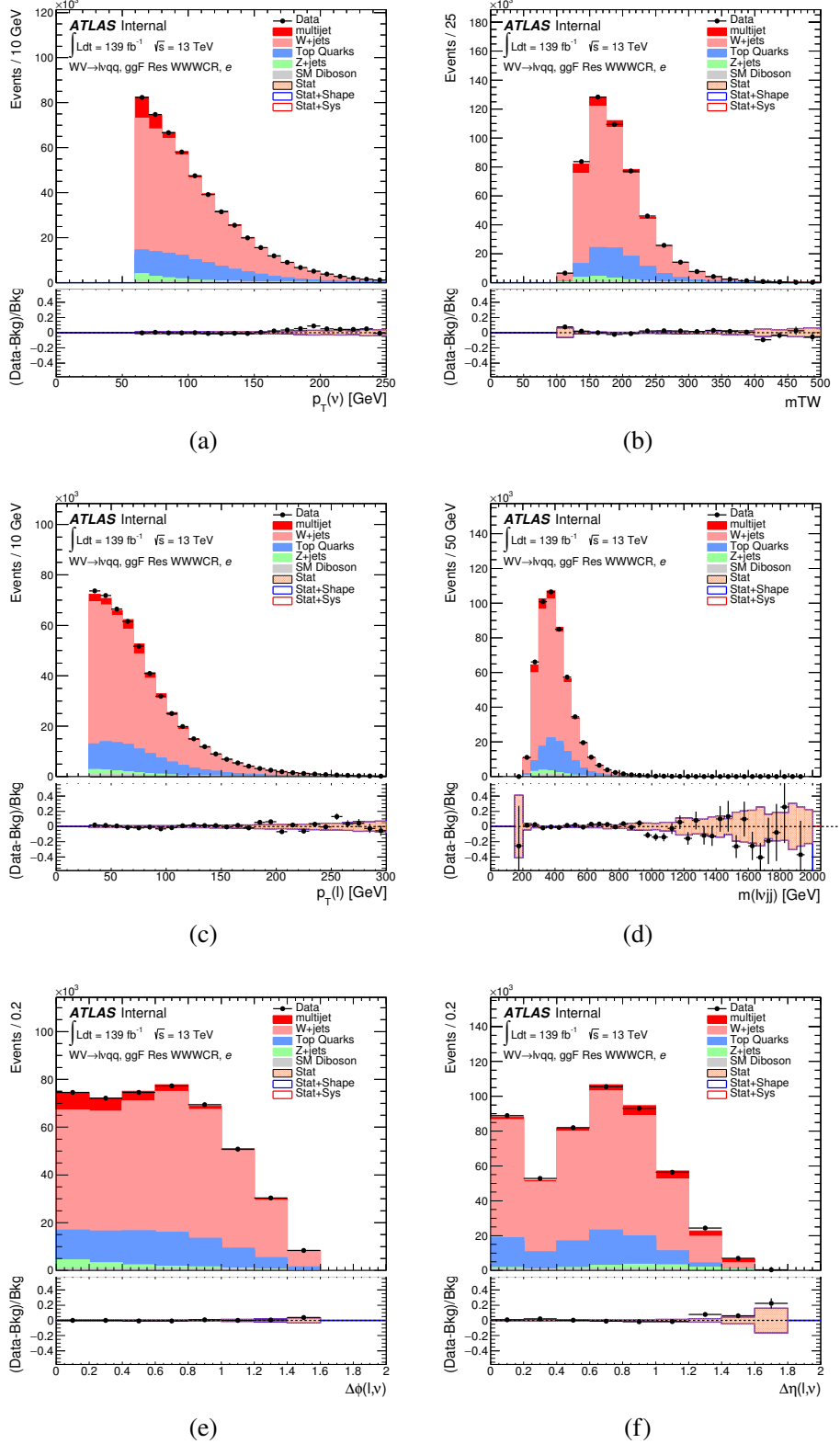


**Figure 9.16:** Postfit Data/MC comparison of distributions of  $E_T^{miss}$ ,  $m_T^W$ , lepton and neutrino  $p_T$ ,  $m_{l\nu jj}$ , lepton- $\nu$  angular distance in the  $WW$  electron channel. The MJ template is obtained from the pre-MJ-fit.

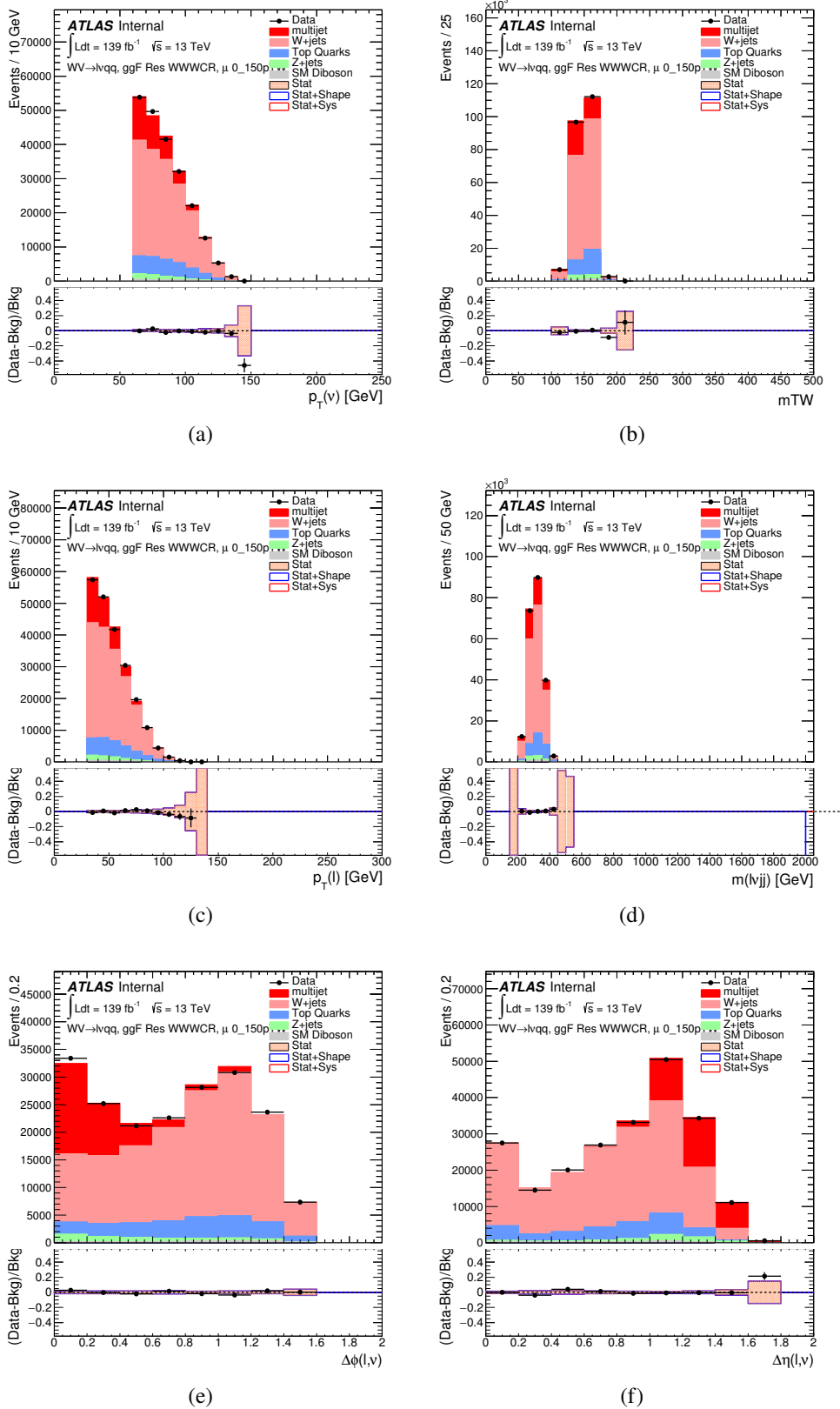


**Figure 9.17:** Postfit Data/MC comparison of distributions of  $E_T^{miss}$ ,  $m_T^W$ , lepton and neutrino  $p_T$ ,  $m_{ljj}$ , lepton- $\nu$  angular distance in the  $WW$  muon channel. The MJ template is obtained from the pre-MJ-fit.

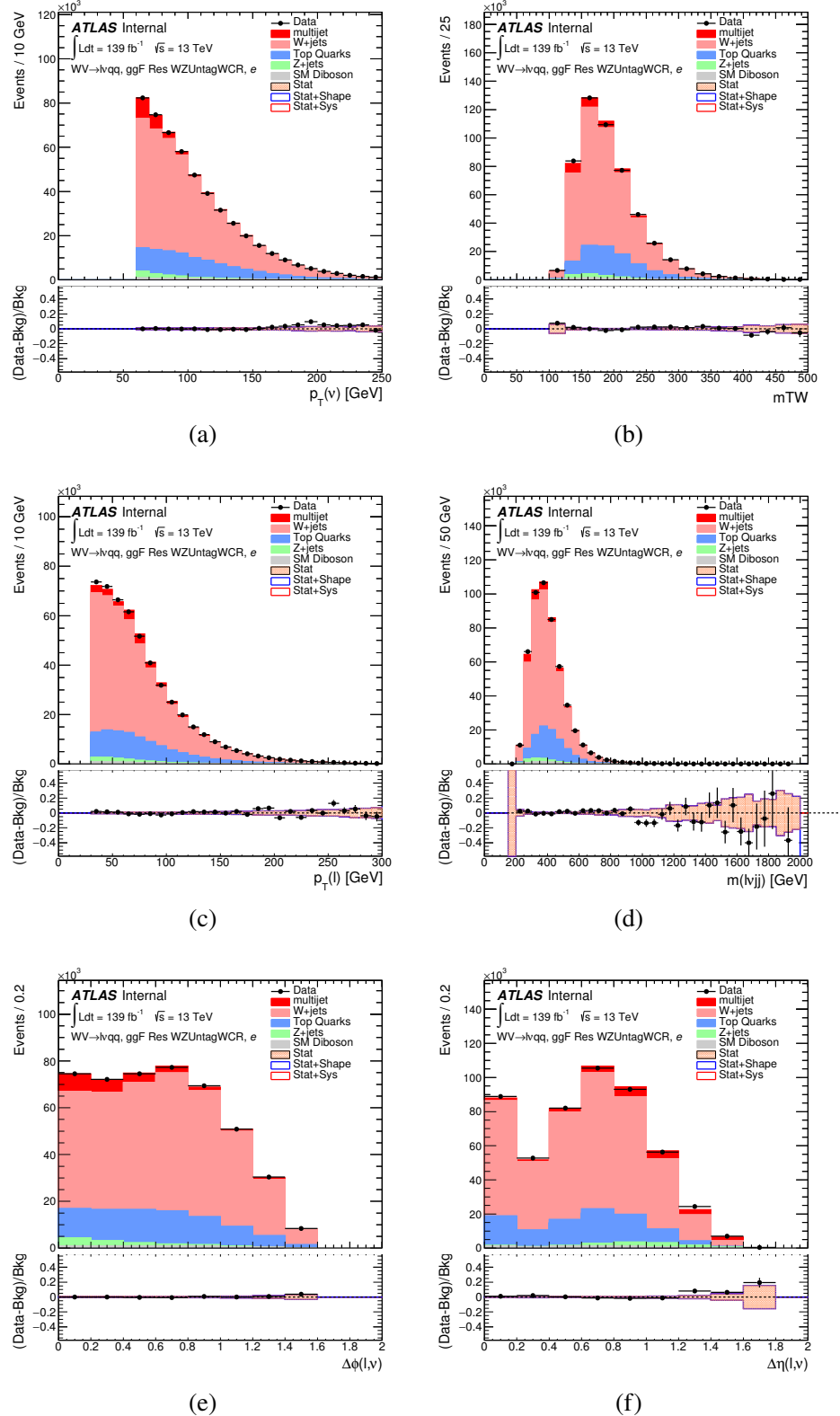


**Figure 9.18:** Postfit Data/MC comparison of distributions of  $E_T^{miss}$ ,  $m_T^W$ , lepton and neutrino  $p_T$ ,  $m_{l\nu jj}$ , lepton- $\nu$  angular distance in the  $WZ$  untag electron channel. The MJ template is obtained from the pre-MJ-fit.

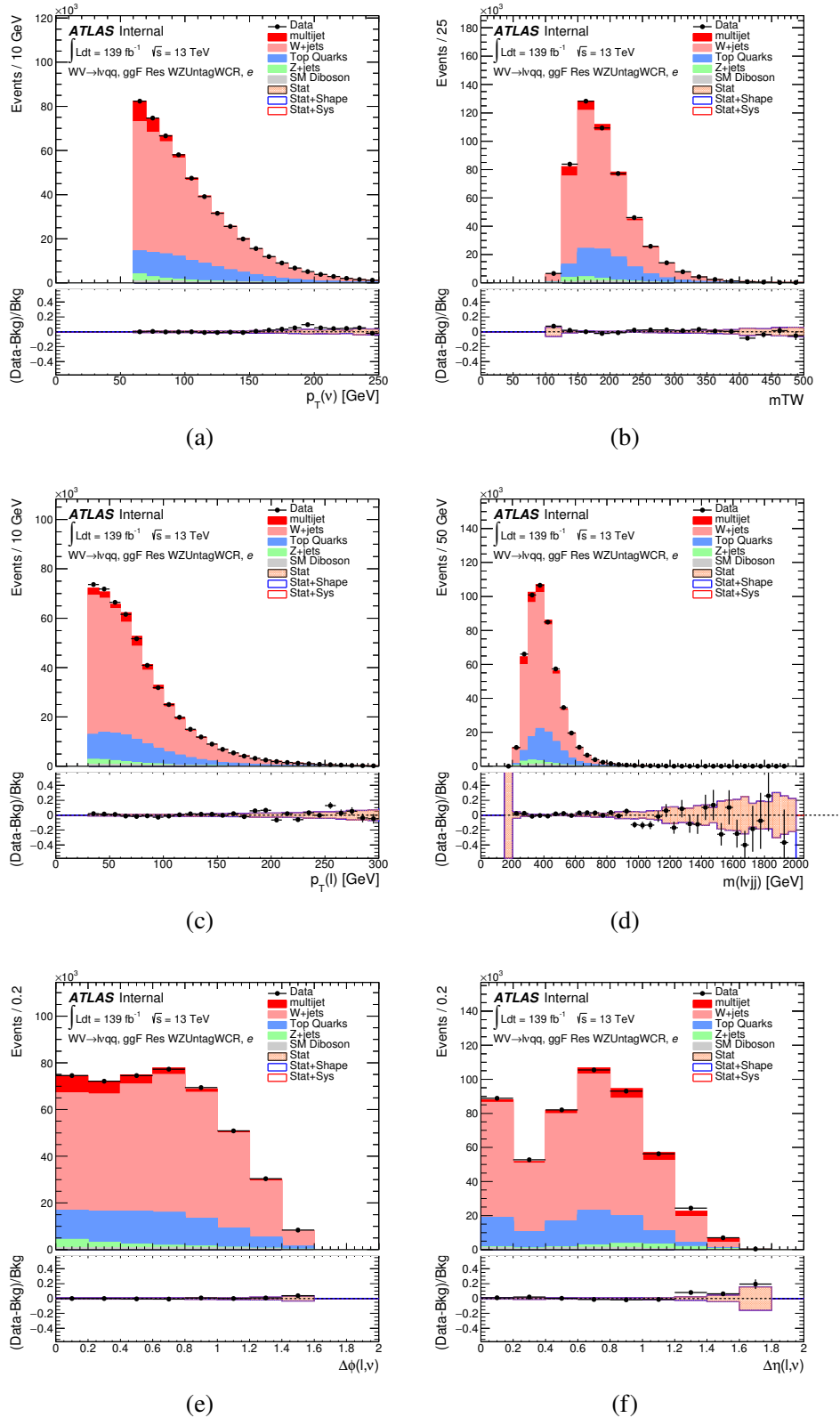


**Figure 9.19:** Postfit Data/MC comparison of distributions of  $E_T^{miss}$ ,  $m_T^W$ , lepton and neutrino  $p_T$ ,  $m_{l\nu jj}$ , lepton- $\nu$  angular distance in the  $WZ$  untag muon channel. The MJ template is obtained from the pre-MJ-fit.

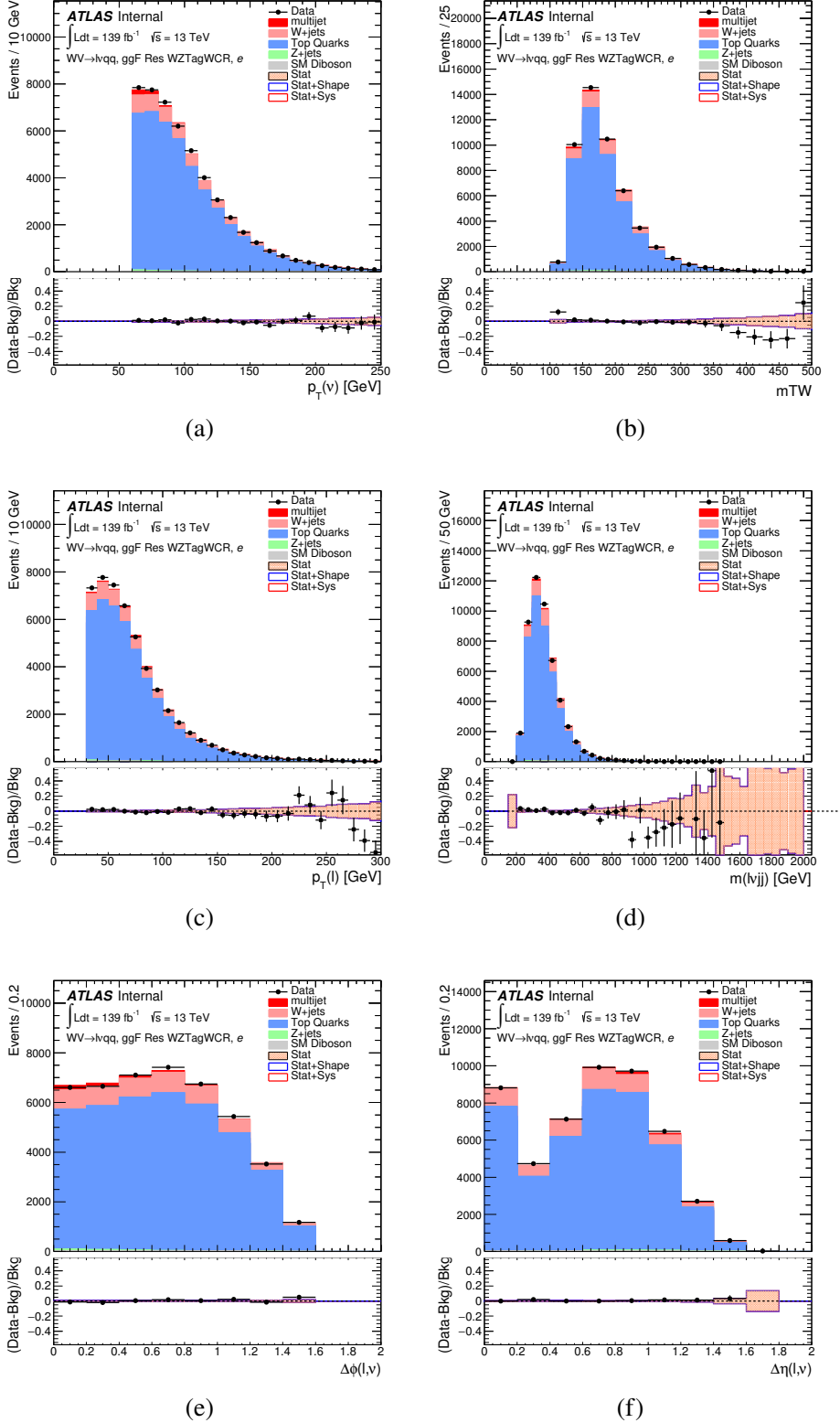


**Figure 9.20:** Postfit Data/MC comparison of distributions of  $E_T^{miss}$ ,  $m_T^W$ , lepton and neutrino  $p_T$ ,  $m_{l\nu jj}$ , lepton- $\nu$  angular distance in the  $WZ$  untag electron channel. The MJ template is obtained from the pre-MJ-fit.

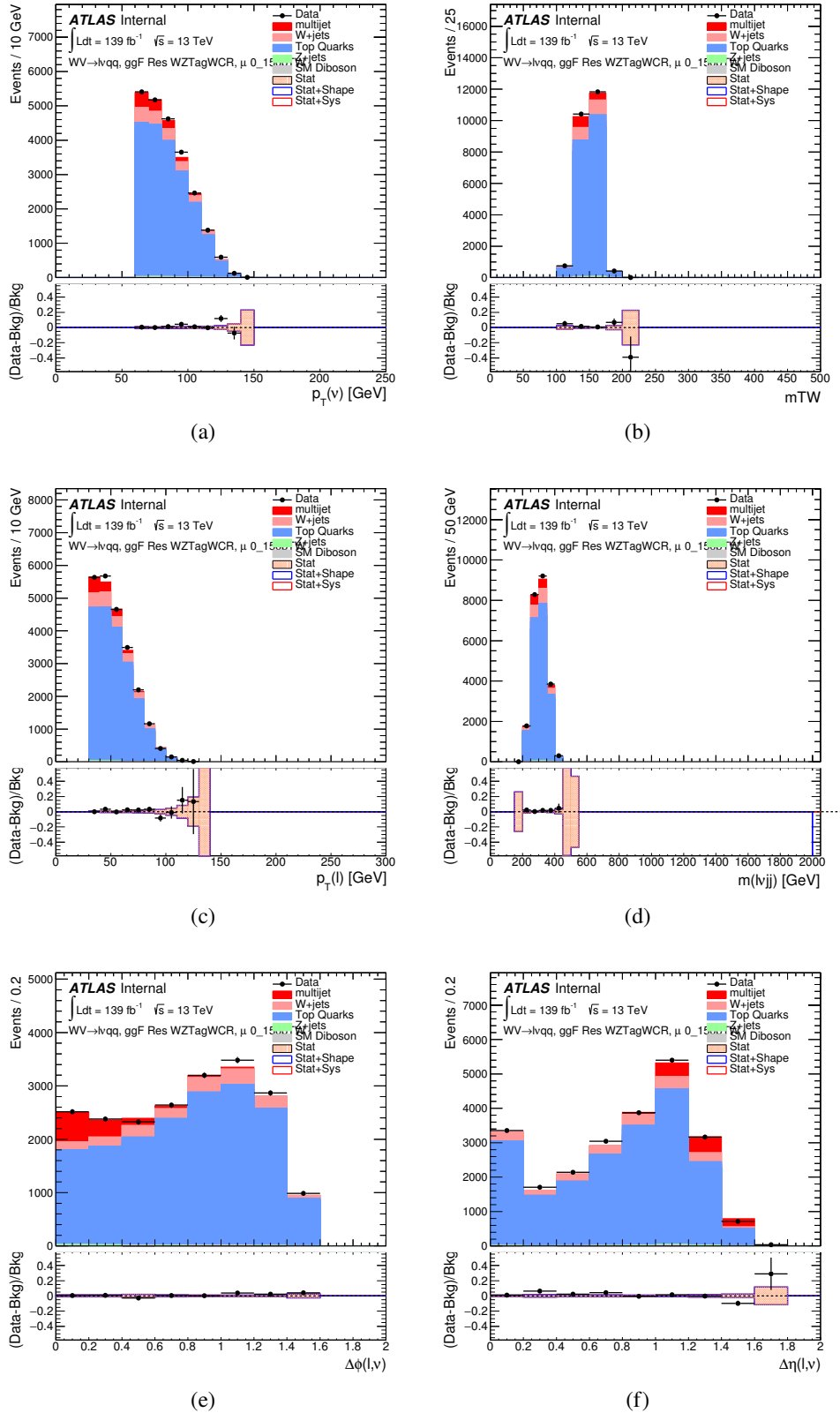


**Figure 9.21:** Postfit Data/MC comparison of distributions of  $E_T^{miss}$ ,  $m_T^W$ , lepton and neutrino  $p_T$ ,  $m_{l\nu jj}$ , lepton- $\nu$  angular distance in the  $WZ$  untag muon channel. The MJ template is obtained from the pre-MJ-fit.

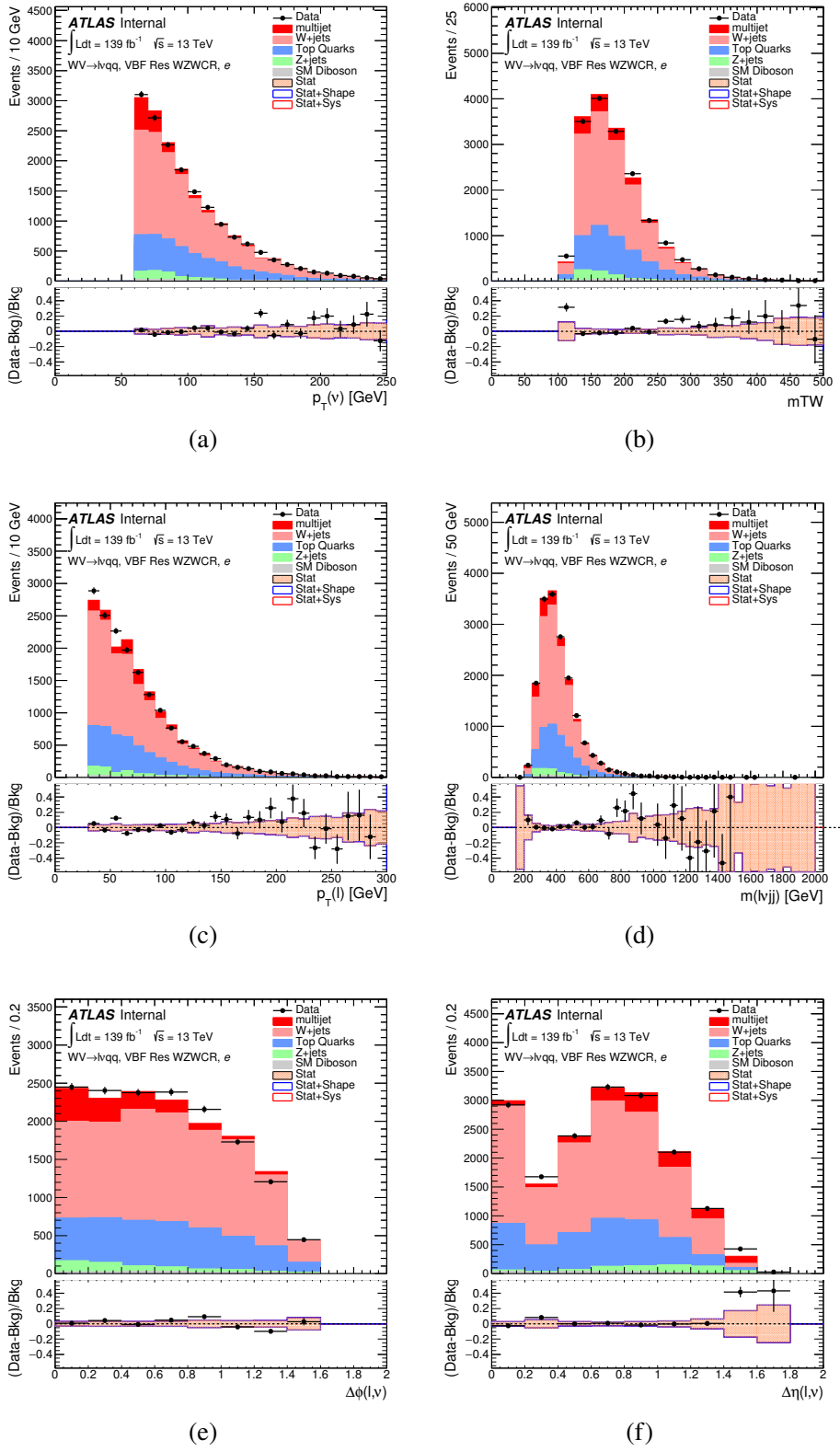


**Figure 9.22:** Postfit Data/MC comparison of distributions of  $E_T^{\text{miss}}$ ,  $m_T^W$ , lepton and neutrino  $p_T$ ,  $m_{l\nu jj}$ , lepton- $\nu$  angular distance in the VBF  $WW$  electron channel. The MJ template is obtained from the pre-MJ-fit.

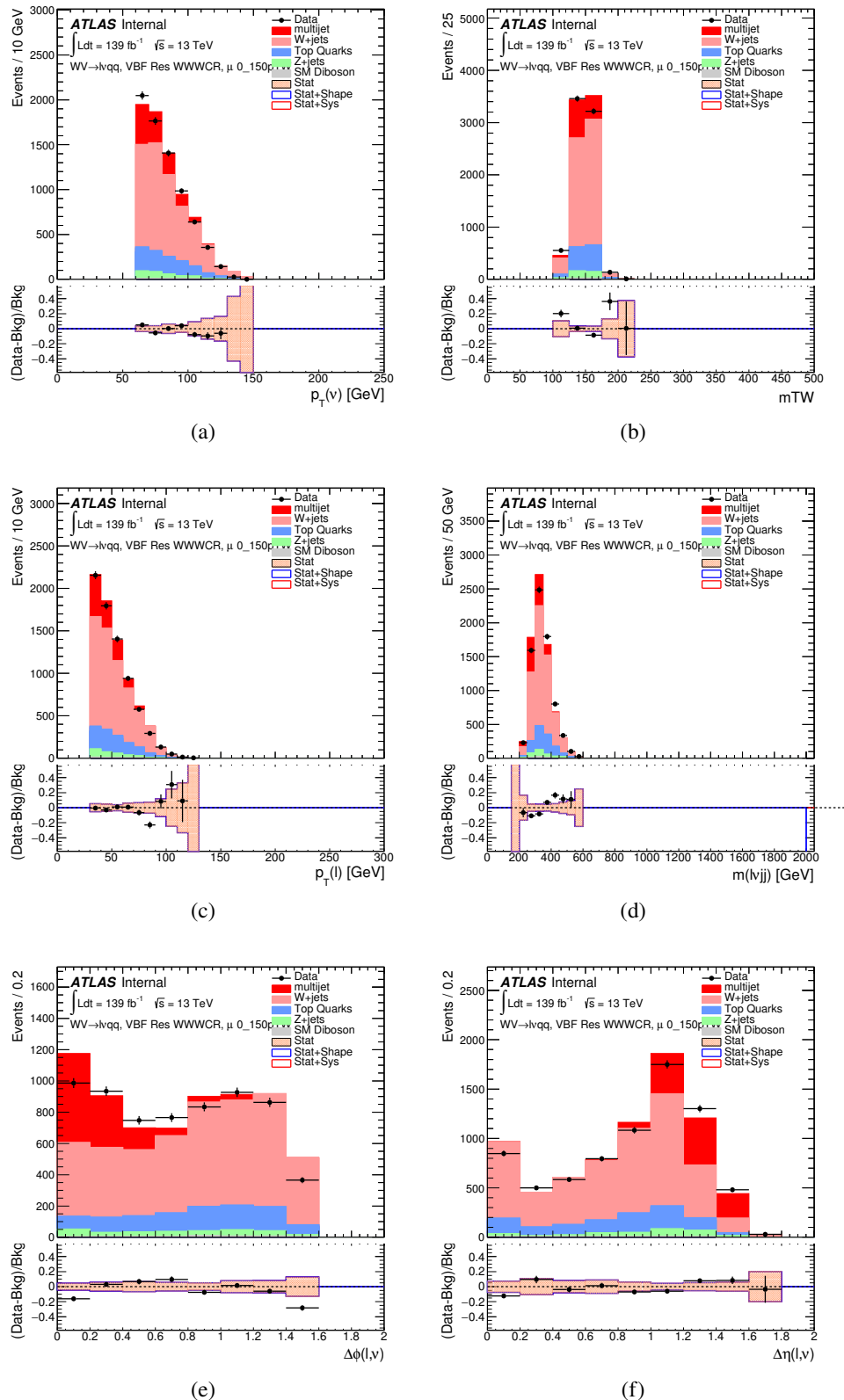


**Figure 9.23:** Postfit Data/MC comparison of distributions of  $E_T^{miss}$ ,  $m_T^W$ , lepton and neutrino  $p_T$ ,  $m_{\ell\nu jj}$ , lepton- $\nu$  angular distance in the VBF  $WW$  muon channel. The MJ template is obtained from the pre-MJ-fit.

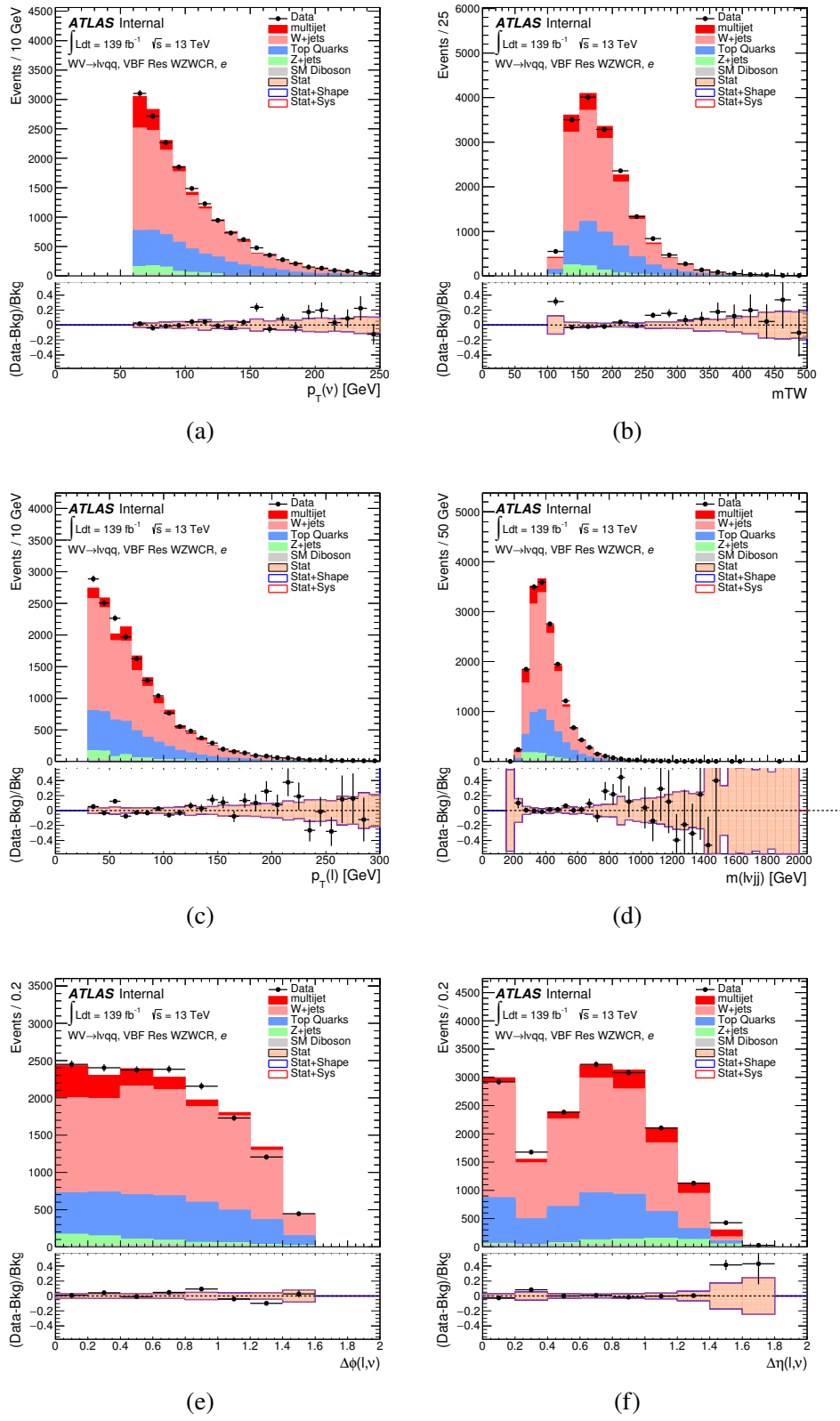


**Figure 9.24:** Postfit Data/MC comparison of distributions of  $E_T^{miss}$ ,  $m_T^W$ , lepton and neutrino  $p_T$ ,  $m_{l\nu jj}$ , lepton- $\nu$  angular distance in the VBF  $WZ$  electron channel. The MJ template is obtained from the pre-MJ-fit.

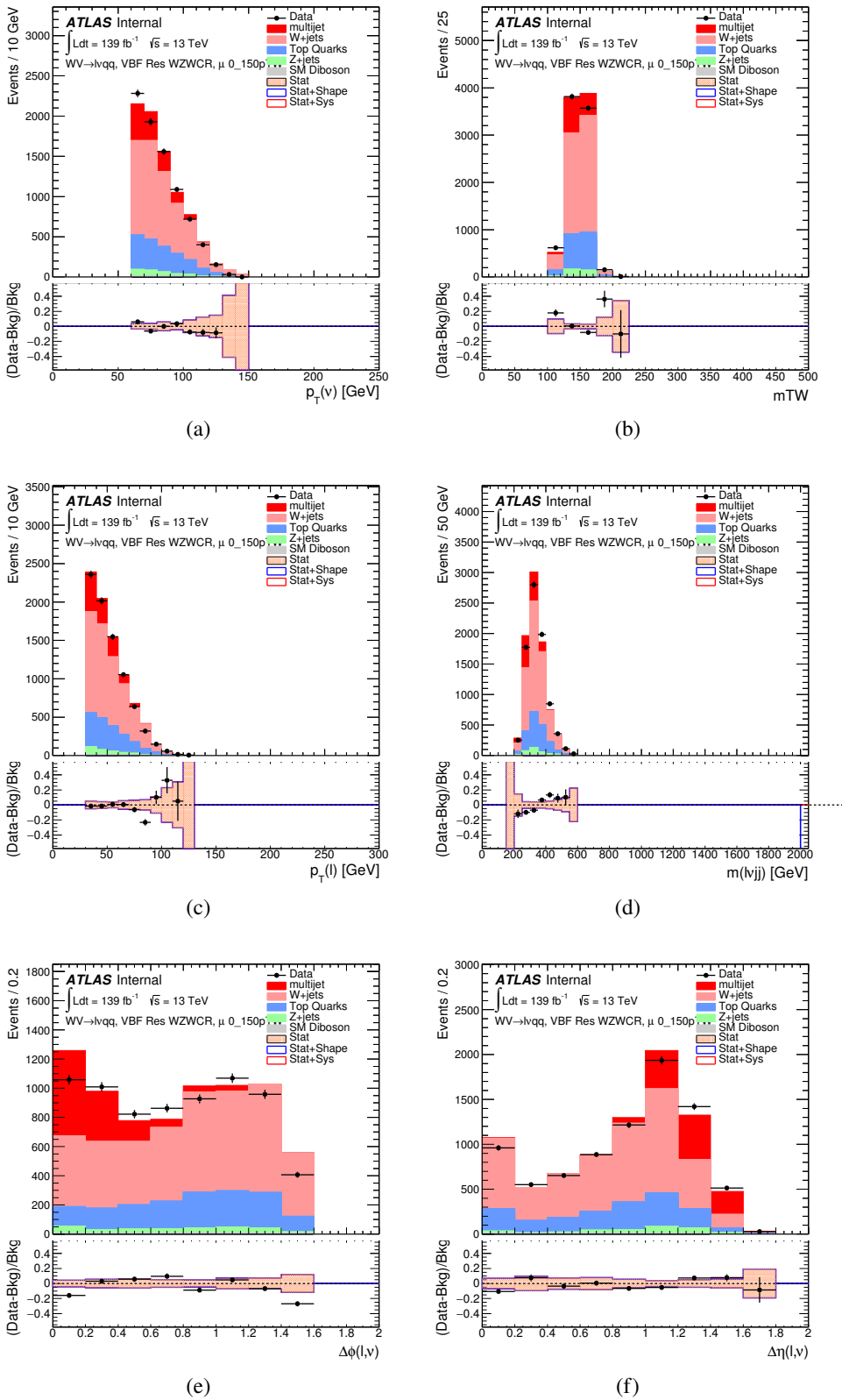


**Figure 9.25:** Postfit Data/MC comparison of distributions of  $E_T^{miss}$ ,  $m_T^W$ , lepton and neutrino  $p_T$ ,  $m_{l\nu jj}$ , lepton- $\nu$  angular distance in the VBF  $WZ$  muon channel. The MJ template is obtained from the pre-MJ-fit.

Full Run 2  
ggF Res WWWCR

Sample	Yield	R.U.	SF
Top&W	$645040 \pm 1971.68$	0.31%	0.998
Z&VV	24075.9		fixed
MJ_el	$24156.3 \pm 1224.62$	5.06%	3.973
MJ_mu	$35528.5 \pm 923.94$	2.60%	9.019

ggF Res WZ01bWCR

Sample	Yield	R.U.	SF
Top&W	$644690 \pm 1981.4$	0.31%	0.997
Z&VV	24075.9		fixed
MJ_el	$24366.5 \pm 1232.69$	5.05%	3.874
MJ_mu	$35528.5 \pm 921.27$	2.58%	8.746

ggF Res WZ2bWCR

Sample	Yield	R.U.	SF
Top&W	$71236.5 \pm 688.74$	0.97%	1.031
Z&VV	518.5		fixed
MJ_el	$595.63 \pm 449.34$	75.44%	0.094
MJ_mu	$1196.9 \pm 222.13$	18.56%	0.294

VBF Res WWWCR

Sample	Yield	R.U.	SF
Top&W	$19032.3 \pm 364.43$	1.91%	0.928
Z&VV	1091.63		fixed
MJ_el	$1425.73 \pm 214.42$	15.03%	0.235
MJ_mu	$1281.36 \pm 157.21$	11.83%	0.314

VBF Res WZWCR

Sample	Yield	R.U.	SF
Top&W	$21341.8 \pm 392.21$	1.84%	0.942
Z&VV	1111.75		fixed
MJ_el	$1413.76 \pm 230.36$	16.29%	0.225
MJ_mu	$1281.36 \pm 157.21$	12.27%	0.314

**Table 9.5:** Fit validation result in WCRs for 2015+16 data. The fit is done in various WCRs, in order to obtain the corresponding scale factors for MJ templates: ggF resolved WCR for the  $WW \rightarrow lvqq$  selection, ggF resolved untagged WCR for the  $WZ \rightarrow lvqq$  selection, ggF resolved tagged WCR for the  $WZ \rightarrow lvqq$  selection, VBF resolved WCR for the  $WW \rightarrow lvqq$  selection, and VBF resolved WCR for the  $WZ \rightarrow lvqq$  selection. Post-fit event yields for electroweak processes and MJ contributions are shown. The SF column shows the corresponding normalization scale factors for electroweak processes from the fit. R.U. stands for relative uncertainty.

1062 **Chapter 10**

1063 **Systematic Uncertainties**

1064 This section describes the sources of systematic uncertainties considered in  
1065 this analysis. These uncertainties are divided into three categories: experimental  
1066 uncertainties, background modeling uncertainties, and theoretical uncertainties on  
1067 signal processes. In the statistical analysis each systematic uncertainty is treated  
1068 as a nuisance parameter estimated on the  $m_{VV}$  distribution.

1069 **10.1 Experimental Systematics**

1070 The uncertainty on the integrated luminosity of the dataset used is 1.7% and  
1071 a systematic in the final fit. This uncertainty was calculated using  $x - y$  beam  
1072 separation scans [ref P55].

1073 An additional source of systematic uncertainty is assigned to the pileup mod-  
1074eling in MC samples. This ensures simulated detector response and particle re-  
1075construction conditions are as similar as possible. The distribution of the average  
1076 number of interactions per bunch crossing applied to simulation is called the  $\mu$  pro-  
1077file. The pileup modeling uncertainty is accounted for by re-weighting simulated  
1078events so the average number of interactions per bunch crossing varies within its

1079 uncertainty due to systematics from vertex reconstruction [ref ATL-COM-SOFT-  
1080 2015-119]. The associated re-weighting factors are propagated through the entire  
1081 analysis chain to construct a systematic uncertainty on  $m_{VV}$ .

1082 The single-lepton and  $E_T^{miss}$  triggers used are not fully efficient, so scale factors  
1083 are applied to simulation to more accurately model the data. These scale factors  
1084 are given by the ratio of the distribution of offline objects before trigger selection  
1085 and after trigger selection. The associated uncertainty on these scale factors are  
1086 used in the final fit.

1087 Uncertainties on small-R jet energy scale and resolution are measured in-situ  
1088 by calculating the response between data and simulation. This analysis uses a  
1089 reduced set of JES and JER uncertainties (totaling 30 and 8 systematics, re-  
1090 spectively). These reduced sets of systematics are calculated using a principal  
1091 component analysis, yield largely uncorrelated independent systematics. These  
1092 uncertainties on JES and JER account for the dependence on  $p_T$ ,  $\eta$ ,  $\mu$ , flavor re-  
1093 sponse and global sequential corrections. Systematic uncertainties associated with  
1094  $b$ -tagging are also considered. These systematics are evaluated as uncertainties on  
1095 the scale factor which account for the difference in  $b$ -tagging efficiencies in data  
1096 and MC, and the flavor dependence (between b, c, and light jets).

1097 The uncertainty on the  $p_T$  scale of the large-R jets is determined by comparing  
1098 the jet's  $p_T^{calo}$  to  $p_T^{track}$  in di-jet simulation and data. In addition to this uncertain-  
1099 ties from tracking, modeling (Pythia vs Herwig), and statistical constraints are  
1100 also calculated. The large-R jet  $p_T$  resolution is given by smearing the jet  $p_T$  with  
1101 a Gaussian with a 2% width.

1102 The  $W/Z$  tagging efficiency SF is estimated by comparing the tagging effi-  
1103 ciency in simulation with that in data for four regions of the  $W/Z$  tagger ( $D_2$  fail,  
1104  $m_J$  fail;  $D_2$  pass,  $m_J$  fail;  $D_2$  fail,  $m_J$  pass;  $D_2$  pass,  $m_J$  pass). (Additionally,

1105 separate scale factors are determined for events with large-R jets from  $W$  bosons  
 1106 and top backgrounds.) A simultaneous template fit is used to fit the signal jets  
 1107 (jets initiated by  $W/Z$  bosons or top quarks) and background jets (all other jets  
 1108 from the simulated backgrounds) to the data in the four regions. using the  $m_J$   
 1109 distributions. The SF for a given region is then given by:

$$SF = \frac{\epsilon_{data} = \frac{N_{fitted-signals}^{region}}{N_{all-regions}^{fitted-signals}}}{\epsilon_{MC} = \frac{N_{signal}^{region}}{N_{signal}^{all-regions}}} \quad (10.1)$$

1110 The effects of experimental and theoretical uncertainties on the efficiency scale  
 1111 factor are determined by taking the ratio of efficiencies in data and simulation.  
 1112 By taking this ratio the uncertainties not arising for jet mass and  $D_2$  cancel.

1113 Lepton identification, reconstruction, isolation systematic uncertainties are de-  
 1114 termined by reconstructing the  $Z$  mass peak with a tag and probe method. The  
 1115 lepton energy and momentum scales are also measured with the  $Z$  mass peak.

1116 As  $E_T^{miss}$  is calculated using all the physics objects in the event, all those objects  
 1117 associated errors result in an uncertainty on  $E_T^{miss}$ . Additionally, the unassociated  
 1118 tracks used to construct  $E_T^{miss}$  contribute to the uncertainty on  $E_T^{miss}$ .

## 1119 10.2 Theory Systematics

1120 Theoretical uncertainties for signal and background processes arise from un-  
 1121 certainties in the parameters used in Monte Carlo simulation. In particular for  
 1122 the  $t\bar{t}$ ,  $W/Z+jets$ , diboson backgrounds and signal samples, the QCD scale, PDF,  
 1123 generator and hadronization uncertainties were evaluated. To assess the QCD  
 1124 scale uncertainty the renormalization and factorization scales were scaled up and  
 1125 down by a factor of two at the event generation stage of sample production. Un-

certainties due to the choice of the parton distribution functions were evaluated by re-weighting samples from the nominal PDF to a set of error PDFs which account for the uncertainty of the fits used to produce the PDF set. In addition to this, samples are re-weighted to different PDF sets to account for the arbitrariness of the PDF choice. The difference between the  $m_{WV}$  distributions using different event generators is assessed by comparing samples generated with different generators. Similarly, the uncertainty in hadronization models is accounted for by comparing samples created using different hadronization models (e.g.  $t\bar{t}$  Powheg is compared to AMC@NLO,  $W + jets$  compares Sherpa and MadGraph+Pythia samples). Figures 10.2 - 10.8 show the impact of these uncertainties on the  $t\bar{t}$  and  $W/Z + jets$  backgrounds. Additionally, contributions to the diboson background for the VBF analysis were found to be small and were accounted for by including a 5(10)% systematic in the diboson normalization in the final fit.

The normalization of the  $t\bar{t}$  and  $W+jets$  processes impact the multijet template shape. The impact of these normalizations was assessed by including a shape systematic on the multijet background from varying the  $t\bar{t}$  and  $W+jets$  normalization factors.

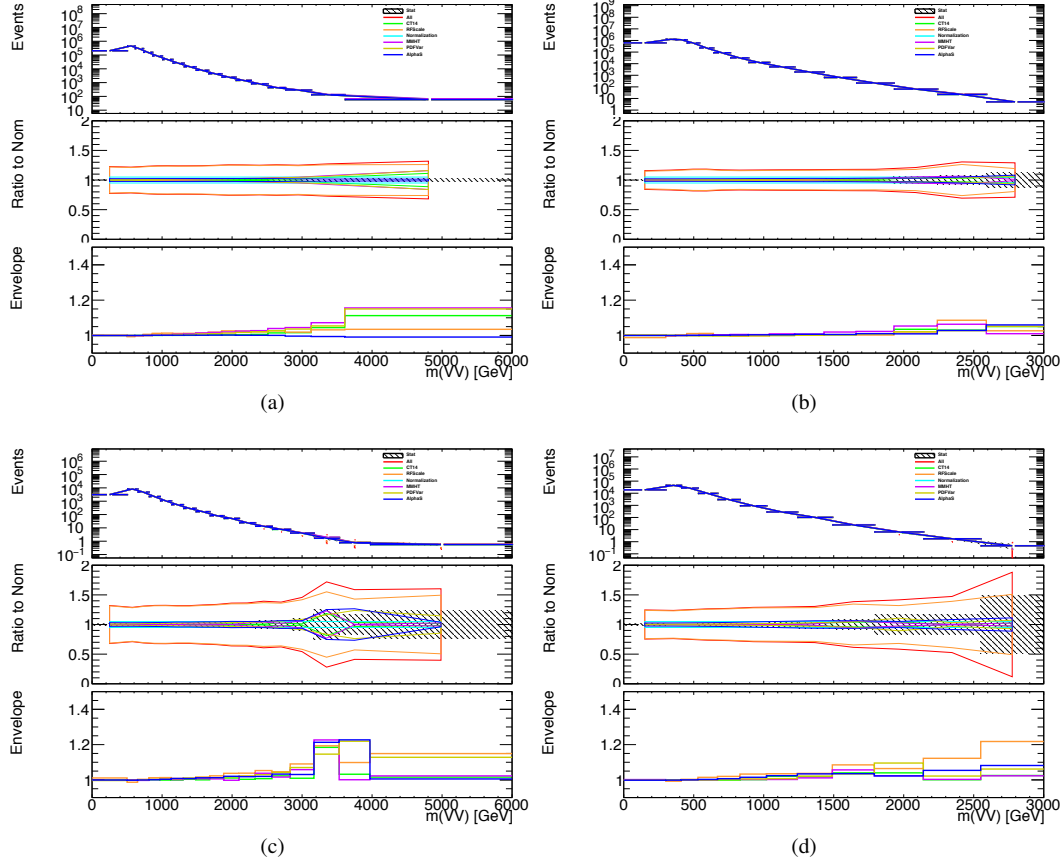


**Figure 10.1:** The  $W/Z + \text{jet}$  systematics for the a) Merged ggF, b) Resolved ggF, c) Merged VBF, and d) Resolved VBF regions. The top subplot shows the nominal and variation distributions/bands, the middle shows the ratio of the two, and the final shows just the shape of the envelope (the final uncertainty).

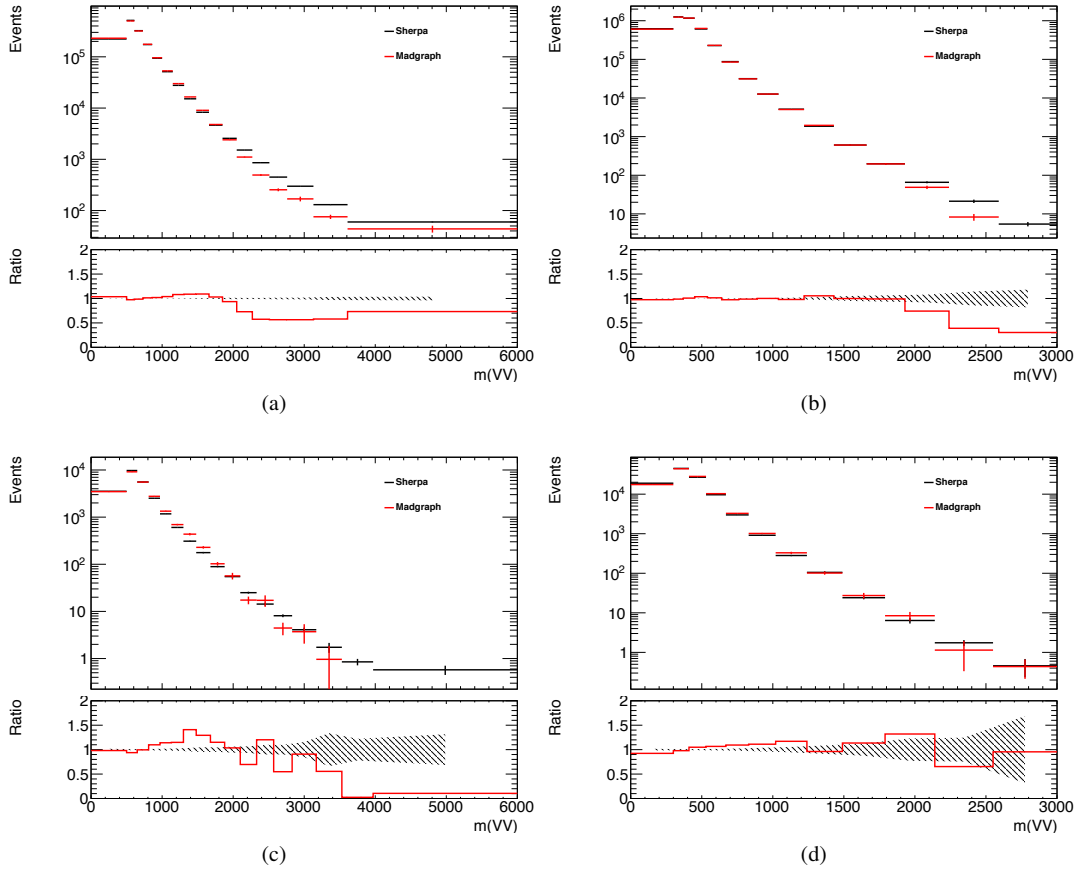


**Figure 10.2:** The two-point generator comparison between Sherpa and MadGraph for the  $W/Z + \text{jet}$  samples in the a) Merged ggF, b) Resolved ggF, c) Merged VBF, and d) Resolved VBF regions. The normalization of the Madgraph sample is set to the Sherpa value to consider only shape effects. The bottom inset shows the ratio of the two.

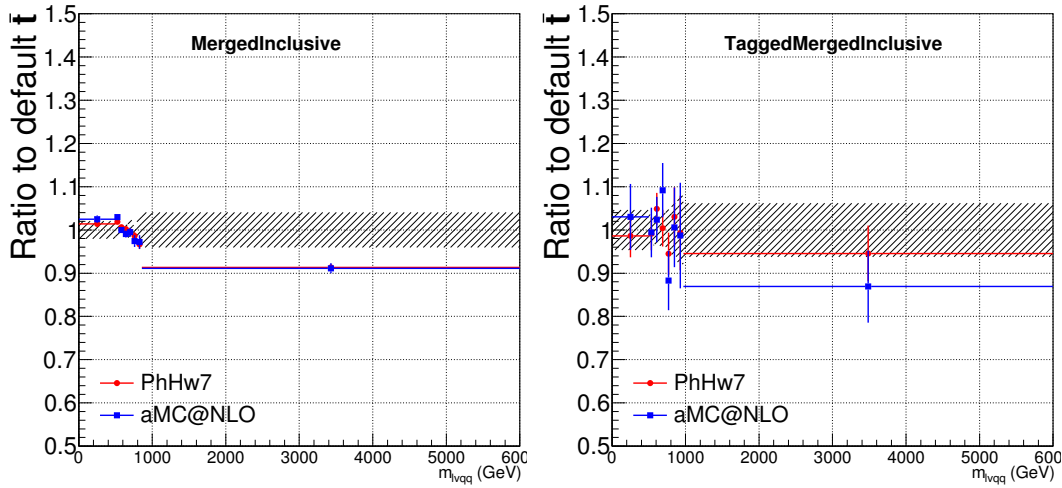


**Figure 10.3:** Ratio between the variations of generator (red) and hadronization (blue) variations for the Merged regime for  $t\bar{t}$  sample.

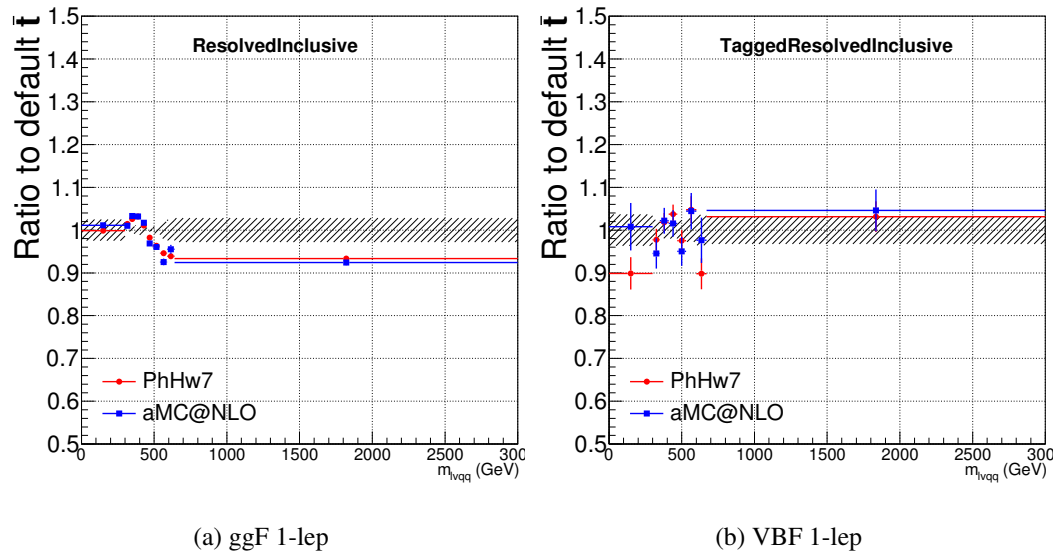


**Figure 10.4:** Ratio between the variations of generator (red) and hadronization (blue) variations for the Resolved regime for  $t\bar{t}$  sample.

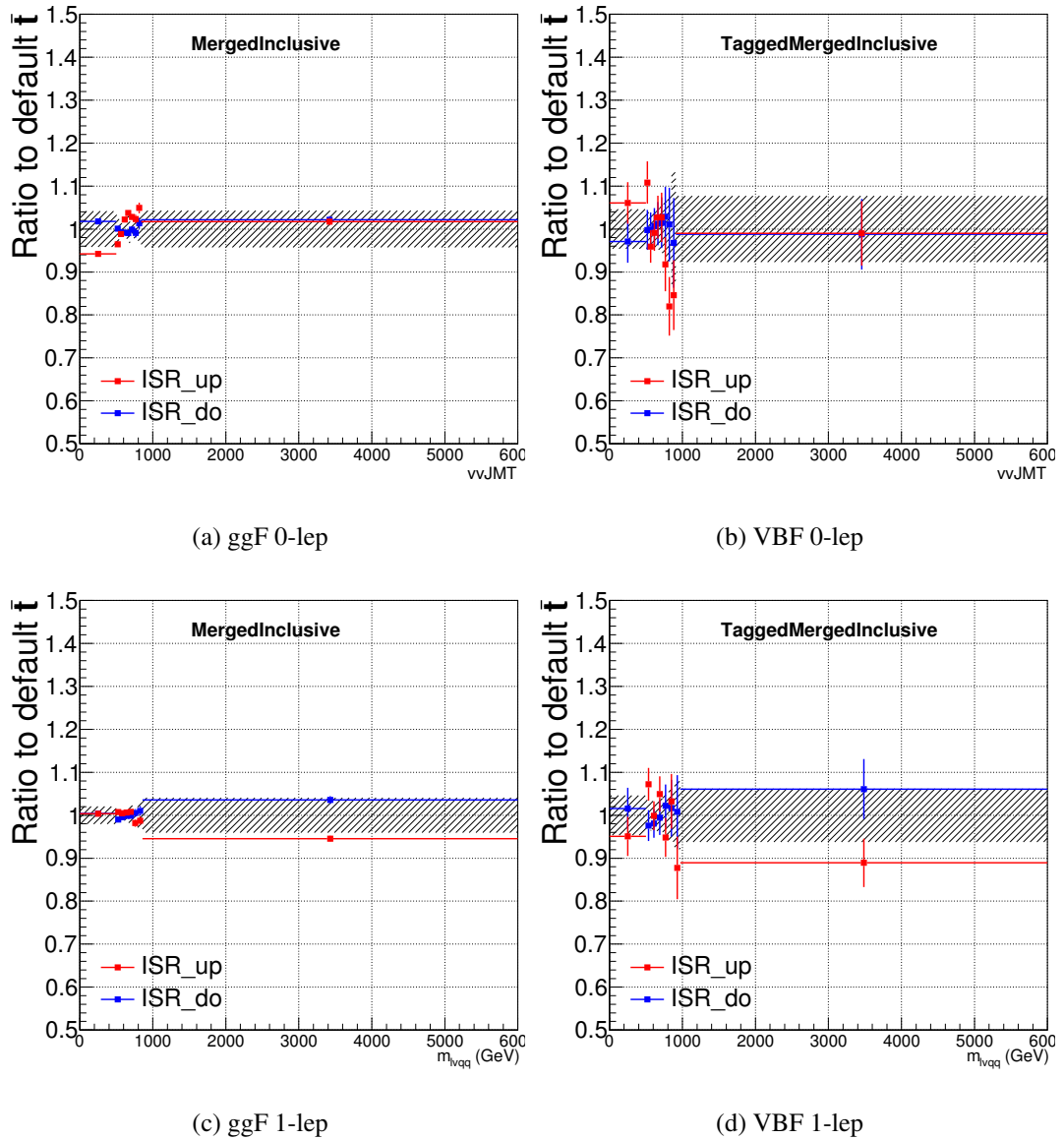


**Figure 10.5:** Ratio between the variations of ISR up (red) and down (blue) variations for the Merged regime for  $t\bar{t}$  sample.

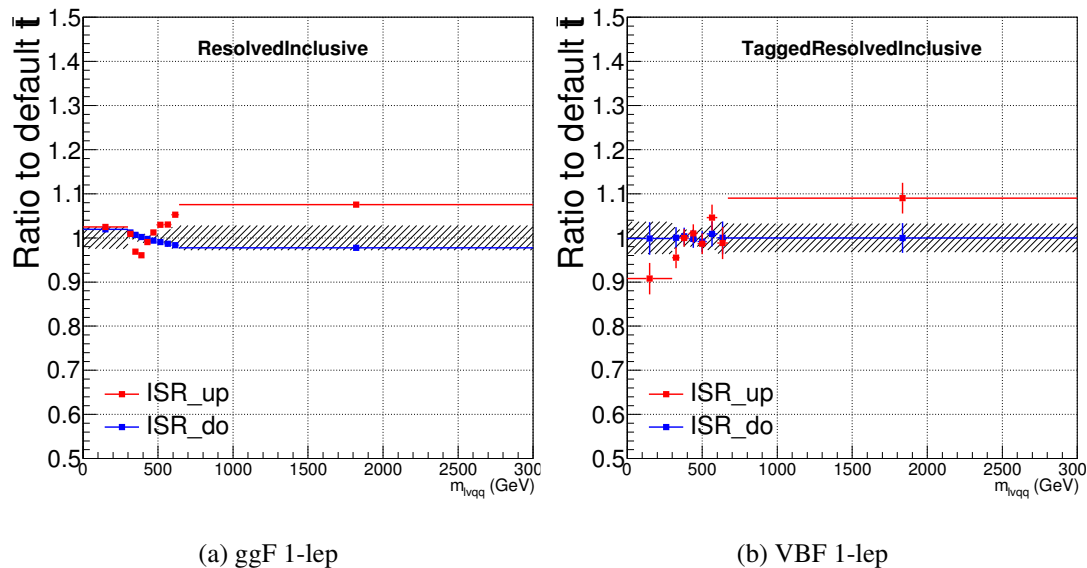


**Figure 10.6:** Ratio between the variations of ISR up (red) and down (blue) variations for the Resolved regime for  $t\bar{t}$  sample.

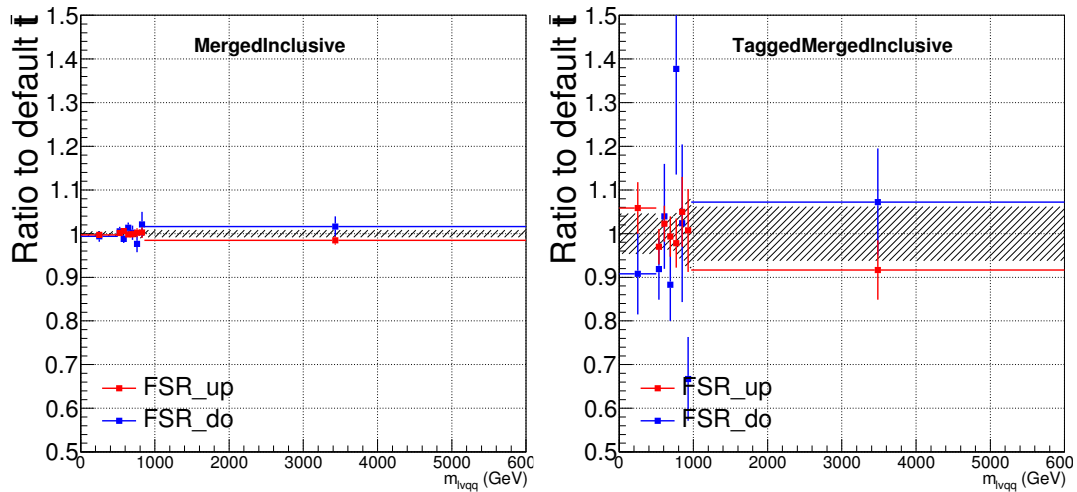


**Figure 10.7:** Ratio between the variations of FSR up (red) and down (blue) variations for the Merged regime for  $t\bar{t}$  sample.

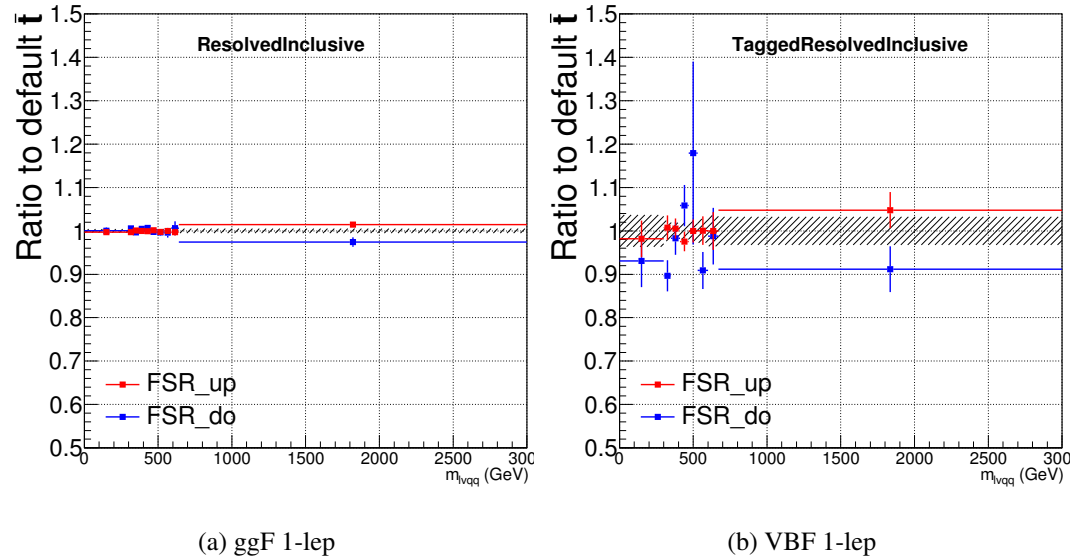


**Figure 10.8:** Ratio between the variations of FSR up (red) and down (blue) variations for the Resolved regime for  $t\bar{t}$  sample.

<sub>1143</sub> **Chapter 11**

<sub>1144</sub> **Statistical Analysis**

<sub>1145</sub> To determine the compatibility of the data collected with the proposed reso-  
<sub>1146</sub> nances a statistical procedure based on a likelihood function is used. A discovery  
<sub>1147</sub> test is used to measure the compatibility of the observed data with the back-  
<sub>1148</sub> ground only hypothesis. If the observed data is sufficiently incompatible with the  
<sub>1149</sub> background only hypothesis, this could indicate a discovery. In the absence of  
<sub>1150</sub> discovery, upper limits on the signal strength parameter,  $\mu$ , are assessed using the  
<sub>1151</sub> CLs method.

<sub>1152</sub> **11.1 Likelihood Function Definition**

<sub>1153</sub> The likelihood function is product of Poisson probabilities for all analysis bins  
<sub>1154</sub> and systematic constraints:

$$\mathcal{L}(\mu, \boldsymbol{\theta}) = \prod_c \prod_i \frac{(\mu s_{ci}(\boldsymbol{\theta}) + b_{ci}(\boldsymbol{\theta}))^{n_{ci}}}{n_{ci}!} e^{-(\mu s_{ci}(\boldsymbol{\theta}) + b_{ci}(\boldsymbol{\theta}))} \prod_k (\theta'_k | \theta_k) \quad (11.1)$$

<sub>1155</sub> Here  $c$  are the analysis channels considered and  $i$  runs over all the  $m_{\ell\nu qq}$  bins

1156 used in the fit. The signal strength parameter,  $\mu$ , multiplies the expected signal  
1157 yield in each analysis bin,  $s_{ci}$ . The background content for channel  $c$  and bin  $i$  is  
1158 given by  $b_{ci}$ . The dependence of signal and background predictions on system-  
1159 atic uncertainties is described by the aforementioned set of nuisance parameters  
1160  $\boldsymbol{\theta}$ , which are parameterized by Gaussian or log-normal priors denoted here as  
1161  $\theta_k$ . Statistical uncertainties of the simulated bin contents are also included as  
1162 systematic uncertainties. Most systematics are correlated among all the analysis  
1163 regions and considered to be independent from each other. The validity of this  
1164 assumption is checked by evaluating the covariance of nuisance parameters.

## 1165 11.2 Fit Configuration

1166 The binning of  $m_{\ell\nu qq}$  in signal regions for likelihood fit is determined by the  
1167 statistical uncertainty of signal mass width. For each signal mass point, the signal  
1168 mass resolution is given by the fitted Gaussian width of the  $m_{\ell\nu qq}$ . The fitted  
1169 signal widths are then fit to a line to give a parameterized signal mass width, as  
1170 shown in Figures 11.1 and 11.2. Bin widths are set first to this parameterized  
1171 signal mass resolution. Then if the statistical uncertainty of the data or simulated  
1172 background is more than 50%, bins are merged until the statistical uncertainty is  
1173 less than 50%. All control regions contain only a single bin.

1174 For this analysis, each signal model is fit in the Merged and Resolved chan-  
1175 nels for the relevant signal production mode simultaneously. The  $W + \text{jets}$  and  $t\bar{t}$   
1176 normalizations are given by the best fit values in the overall fit and these fitted  
1177 normalizations are then applied to those backgrounds in the SRs.

1178 Systematics may be affected by low statistics, leading to unsmooth  $m_{VV}$  dis-  
1179 tributions with unphysically large fluctuations. This can lead to artificial pulls  
1180 and constraints in the fit. To remove such issues a multi-step smoothing pro-

1181 cedure is applied to all systematic variation distributions in all regions. First,  
1182 distributions are rebinned until the statistical error per bin is at least 5%. Next  
1183 all local extrema are identified. The bins around smallest extrema are iteratively  
1184 merged until only four local extrema remain. Then distributions are rebinned so  
1185 that statistical uncertainties in each bin are  $< 5\%$ .

1186 For some systematics, up and down variations may be in the same direction  
1187 with respect to the nominal distributions. This causes the variations to not cover  
1188 the nominal choice, and the interpretation of the confidence interval is skewed as  
1189 the nominal distribution should be bracketed by the up and down variations. This  
1190 asymmetry may also lead to unconstrained systematics in the fit. To handle such  
1191 asymmetric systematics, if the up and down variation for a given systematic are in  
1192 the same direction for at least three  $m_{VV}$  bins the variation is averaged for those  
1193 bins. The averaging procedure replaces bin-by-bin the up and down variation bins  
1194 by  $b_{\pm}^{new} = b_{nom} \pm \frac{|b_+ - b_-|}{2}$ , where  $b_{nom}$  is the nominal bin content and  $b_{\pm}$  are the  
1195 original up and down variation bin content. The same procedure is also applied to  
1196 any variations where the integral of the difference between the up/down variation  
1197 and the nominal distribution is twice that of the other down/up variation, further  
1198 ensuring variations are symmetric around the nominal distribution.

1199 Finally, systematics that have a negligible effect on the  $m_{VV}$  distribution are  
1200 not considered in the fit. Shape systematics where no bin in the variational dis-  
1201 tribution deviates more than 1% from the nominal distribution (after normalizing  
1202 all histograms to the nominal) are not included in the fit. Also, statistical bin  
1203 uncertainties  $< 1\%$  are ignored.

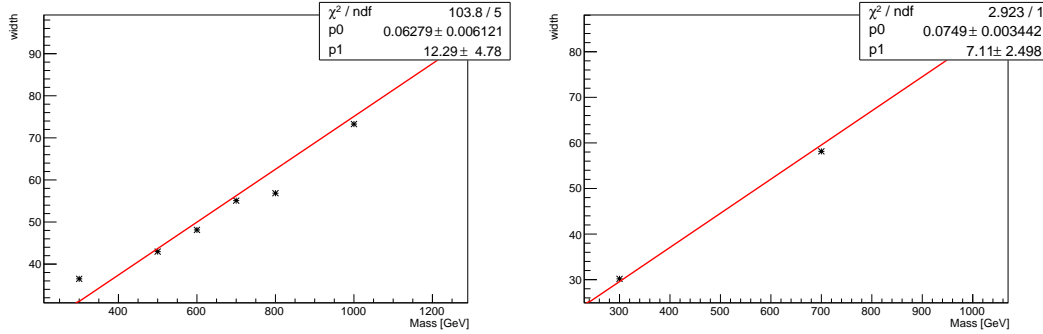


**Figure 11.1:** The HVT signal mass resolution as a function of mass fit with a straight line in the Resolved ggF region (left) and VBF (right) region.

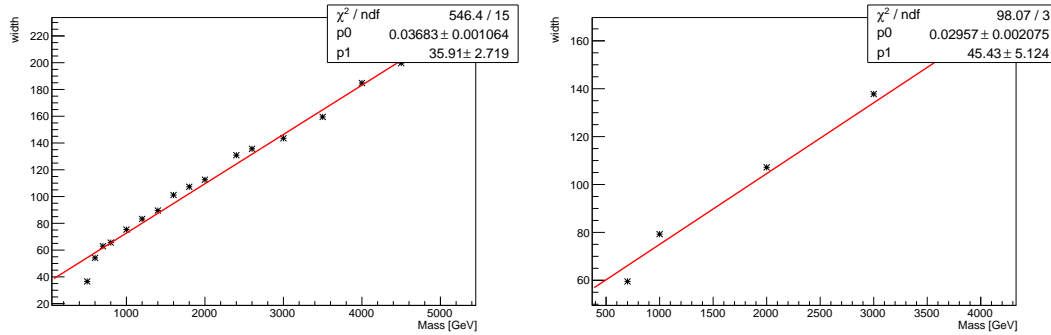


**Figure 11.2:** The HVT signal mass resolution as a function of mass fit with a straight line in the Merged ggF region (left) and VBF (right) region.

### 1204    11.3 Best Fit $\mu$

1205       The best fit signal strength parameter is denoted by  $\hat{\mu}$  and calculated by  
 1206       maximizing the likelihood function with respect to all systematics and  $\mu$ . The  
 1207       corresponding set of systematics that maximize the likelihood are given by  $\hat{\mu}$ .  
 1208       The first term in the likelihood is maximized when the expected number of signal  
 1209       and background events is equal to the number of events in data ( $n_{ci} = \mu s_{ci} +$   
 1210        $b_{ci}$ ). Thus, by maximizing the likelihood, the fit determines values of  $\mu$  and  $\theta$   
 1211       that give the best agreement between expected and measured event yields. The

1212 second term in the likelihood is a penalty term which decreases the likelihood  
1213 when systematics are shifted from their nominal values. This prevents the fit  
1214 from profiling systematics in unphysical ways to maximize the likelihood. The  
1215 uncertainty on  $\mu$  is calculated by varying  $\mu$  up and down until the natural log of  
1216 the likelihood function shifts by one-half.

## 1217 11.4 Discovery Test

1218 To determine if the observed dataset is consistent with tested signal model a  
1219 likelihood ratio is constructed:

$$\lambda(\mu) = \frac{\mathcal{L}(\mu, \hat{\theta}_\mu)}{\mathcal{L}(\hat{\mu}, \hat{\theta})} \quad (11.2)$$

1220 The denominator in this equation is the maximized value of  $\mathcal{L}$  over all system-  
1221 atics and  $\mu$ . The numerator is the maximized likelihood over all systematics for  
1222 a given  $\mu$  value, where the maximized systematics are given by  $\hat{\mu}_\mu$ . To test for  
1223 the existence of signal the observed dataset the null hypothesis ( $H_0$ ) is defined as  
1224 the background only hypothesis and the alternate hypothesis includes signal and  
1225 background ( $H_1$ ). This test quantifies the compatibility of observed data with  
1226  $H_0$  by calculating a p-value representing the probability of observing data as dis-  
1227 crepant or more than the observed data under the  $H_0$ . The test statistic used to  
1228 calculate this p-value is given by ( $r_0$ ):

$$r_0 = \begin{cases} -2 \ln \lambda(0), \hat{\mu} > 0 \\ +2 \ln \lambda(0), \hat{\mu} < 0 \end{cases} \quad (11.3)$$

1229 The expected distribution of the the test statistic under  $H_0$  ( $f(r_0|0)$ ) is used to  
1230 calculate the p-value:

$$p_0 = \int_{r_0, obs}^{\infty} f(r_0 | 0) dr_0 \quad (11.4)$$

1231        Small p-values indicate the observed data is poorly described by  $H_0$ . This  
 1232   equivalent Z-score of a given p-value is usually used to further quantify the agree-  
 1233   ment between the observed data and  $H_0$ . The Z-score is given by the number of  
 1234   standard deviations away from the mean of a Gaussian distribution, the integral  
 1235   of the upper tail of the distribution would equal the p-value. Mathematically:

$$Z = \Phi^{-1}(1 - p_0) \quad (11.5)$$

1236        where  $\Phi$  is the Gaussian cumulative distribution function. The statistical  
 1237   significance of these tests are expressed as the  $Z$ -score. In particle physics,  $3\sigma$  is  
 1238   considered evidence for new phenomena and  $5\sigma$  is the threshold for discovery.

## 1239        11.5 Exclusion Limits

1240        In the absence of discovery, upper limits on the signal strength,  $\mu$  are set using  
 1241   the CLs method [cite P60]. The test statistic for this test,  $q_\mu$ , is constructed as:

$$\tilde{\lambda}_\mu = \begin{cases} \frac{\mathcal{L}(\mu, \hat{\theta}_\mu)}{\mathcal{L}(\hat{\mu}, \hat{\theta})}, \hat{\mu} > 0 \\ \frac{\mathcal{L}(\mu, \hat{\theta}_\mu)}{\mathcal{L}(0, \hat{\theta}_0)}, \hat{\mu} < 0 \end{cases} \quad (11.6)$$

$$\tilde{q}_\mu = \begin{cases} -2 \ln \tilde{\lambda}(\mu), \hat{\mu} < \mu \\ +2 \ln \tilde{\lambda}(\mu), \hat{\mu} > \mu \end{cases} \quad (11.7)$$

1242        As defined, larger values of  $q_\mu$  correspond to increasing incompatibility between  
 1243   the observed data and the background + signal hypothesis. The observed value  
 1244   of the test statistic,  $q_{\mu, obs}$ , is then compared to its expected distribution,  $f$ , to

1245 calculate p-values to assess the likelihood of the background+signal hypothesis.

1246 Using these distributions,  $CL_s$  values are computed as:

$$CL_{s+b} = \int_{q_{\mu,obs}}^{\infty} f(q_{\mu}|\mu) dq_{\mu} \quad (11.8)$$

1247

$$CL_b = \int_{q_0^{obs}}^{\infty} f(q_{\mu}|\mu = 0) dq_{\mu} \quad (11.9)$$

1248

$$CL_s = \frac{CL_{s+b}}{CL_b} \quad (11.10)$$

1249  $CL_{s+b}$  is the p-value for the signal + background hypothesis and  $CL_b$  is the  
1250 p-value for the background only hypothesis. The  $CL_s$  value is interpreted as  
1251 the probability to observe the background + signal hypothesis normalized to the  
1252 probability of background-only hypothesis. Normalizing by  $CL_b$  prevents setting  
1253 artificially strong exclusion limits due to downward fluctuations in data.

1254 For a given signal hypothesis,  $\mu$  values are scanned simultaneously over all  
1255  $m_{WV}$  bins to find the  $\mu$  value that yields  $CL_s=0.05$ , meaning the likelihood of  
1256 finding data more incompatible with the signal+background hypothesis (relative  
1257 to the background only hypothesis) is 5%. The 95% upper limit on the cross  
1258 section is then calculated as the product of the  $\mu$  value found, branching ratio,  
1259 and theory cross section.

<sub>1260</sub> **Chapter 12**

<sub>1261</sub> **Results**

<sub>1262</sub> **12.1 Discovery Tests**

<sub>1263</sub> To test for the existence of signal in the observed dataset, the discovery tests  
<sub>1264</sub> discussed earlier are used to calculate p-values as a function of resonance mass.  
<sub>1265</sub> The results of these tests are shown in Figures 12.1 - 12.5. Across the different  
<sub>1266</sub> DY signals the largest excesses are  $\sim 2.2\sigma$  at 600 GeV and  $1.8\sigma$  at 2 TeV. The  
<sub>1267</sub> largest excesses for VBF signals are  $< 2.5\sigma$  at for 1 TeV resonances. As these  
<sub>1268</sub> deviations do not constitute discoveries, upper limits on  $\mu$  are calculated.

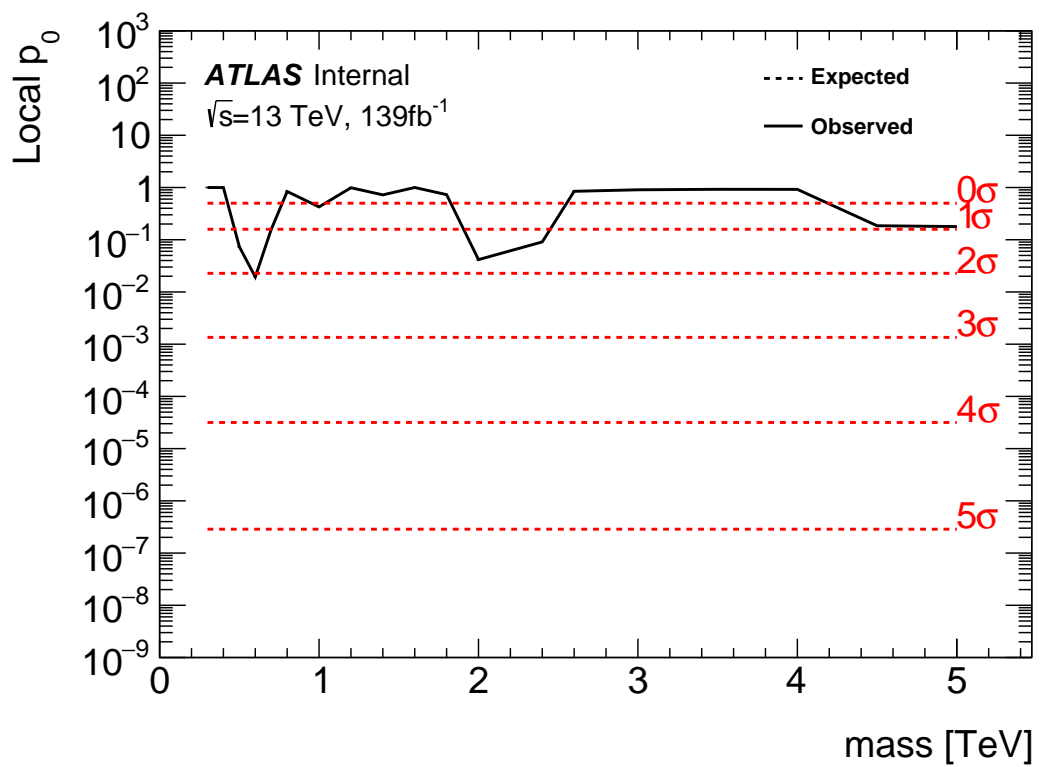


**Figure 12.1:** These plots show the measured  $p_0$  value as a function of resonance mass for HVT Z' DY production.

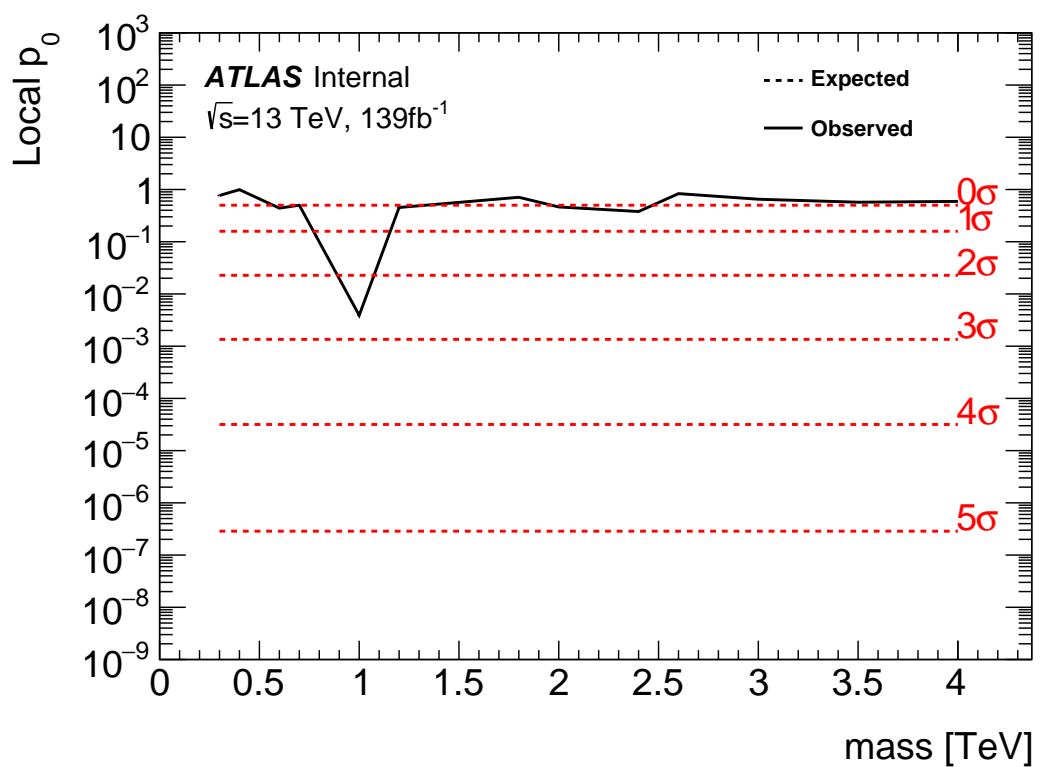


**Figure 12.2:** These plots show the measured  $p_0$  value as a function of resonance mass for HVT Z' VBF production.

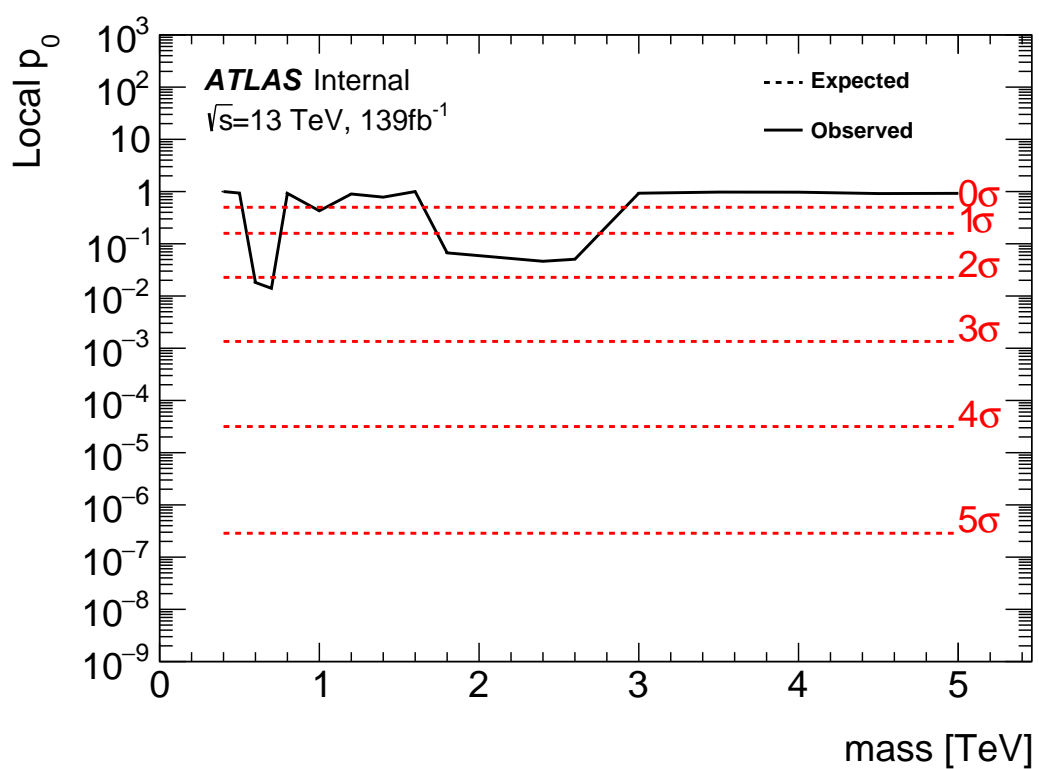


**Figure 12.3:** These plots show the measured  $p_0$  value as a function of resonance mass for HVT W' DY production.

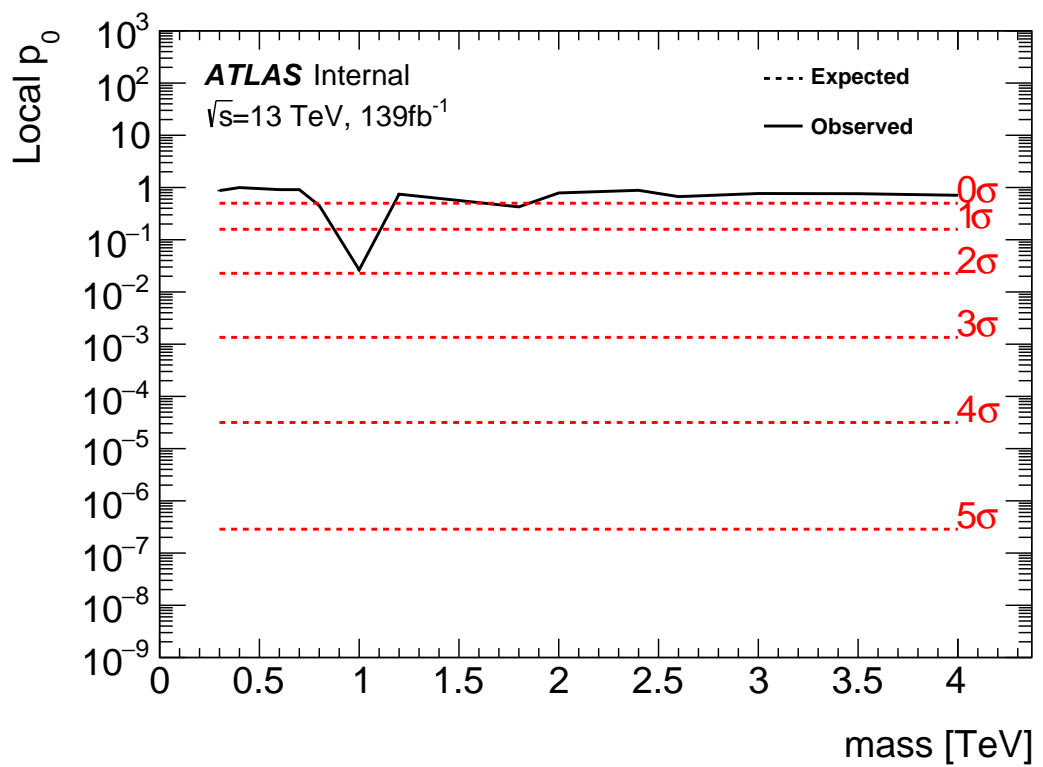


**Figure 12.4:** These plots show the measured  $p_0$  value as a function of resonance mass for HVT W' VBF production.

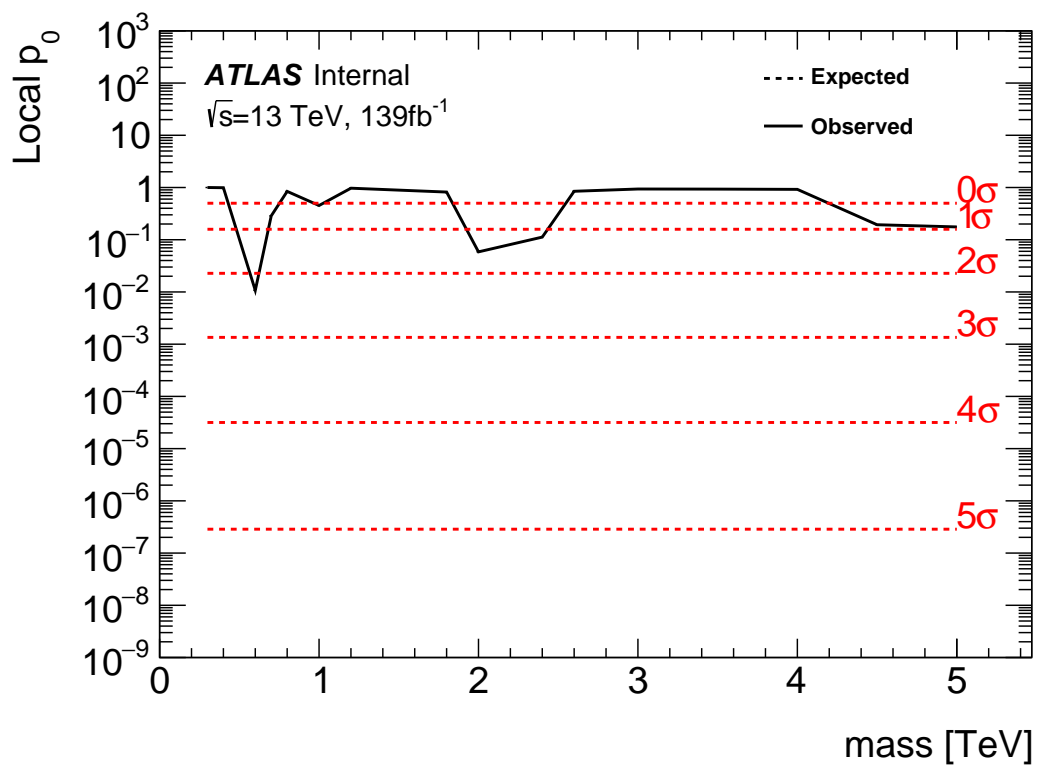


**Figure 12.5:** These plots show the measured  $p_0$  value as a function of resonance mass for the RS Graviton DY production.

## 12.2 Systematic Profiling and Correlations

1270 The ranked systematics and their fitted values are shown for the different anal-  
 1271 ysis regions in Figure 12.6 - 12.8. Note that background normalizations for  $W+jets$   
 1272 and  $t\bar{t}$  are left free to float in the fit. This means the nominal normalization val-  
 1273 ues are at one and the uncertainties are not plotted in the ranked plots. Overall,  
 1274 systematics are not pulled outside their uncertainties, especially for highly ranked  
 1275 nuisance parameters.

1276 The correlation between systematics are shown in Figures ???. Correlations  
 1277 between background normalization are expected. The remaining systematic cor-  
 relations are not very strong or unexpected.

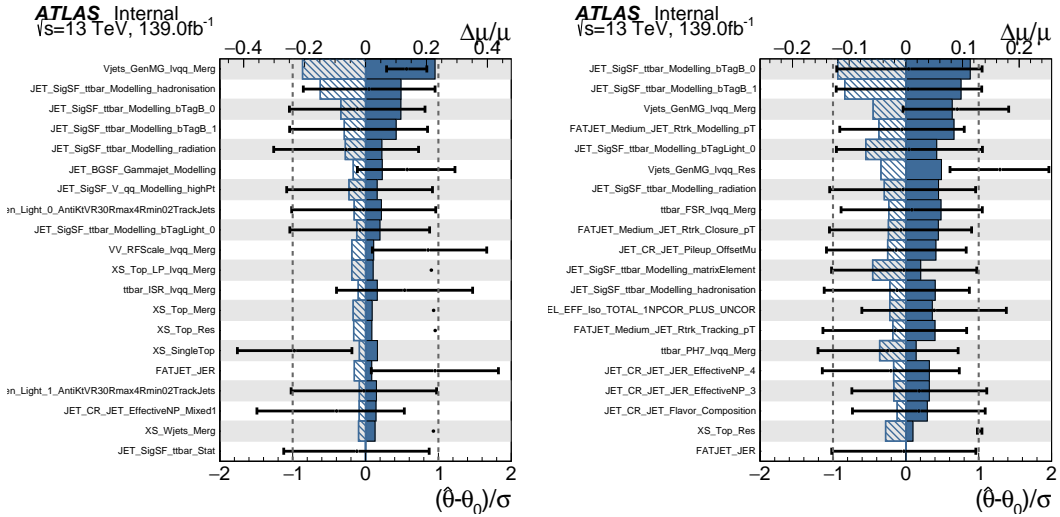


**Figure 12.6:** Ranked systematics and their fitted values for  $WW$  DY (right) and VBF (left) selections.

1278

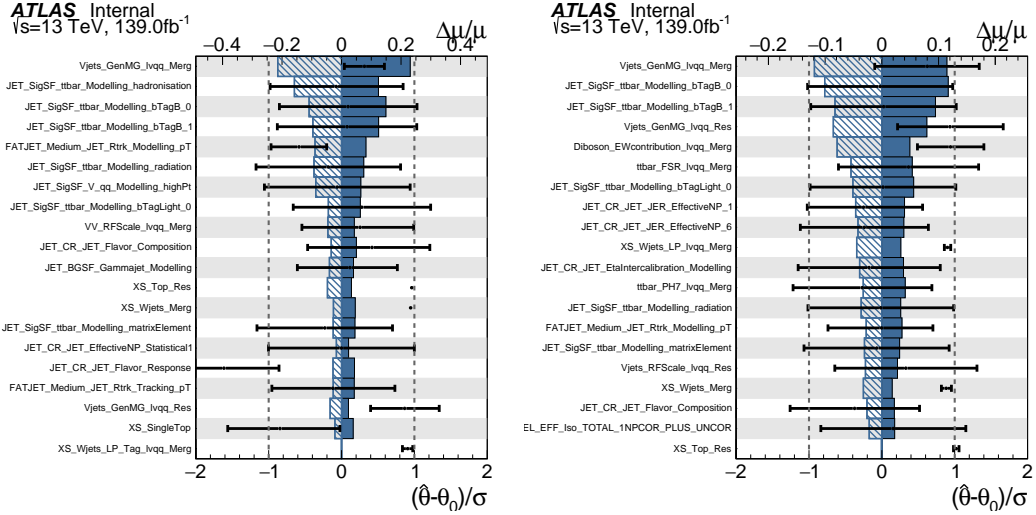


**Figure 12.7:** Ranked systematics and their fitted values for  $WZ$  DY (right) and VBF (left) selections.

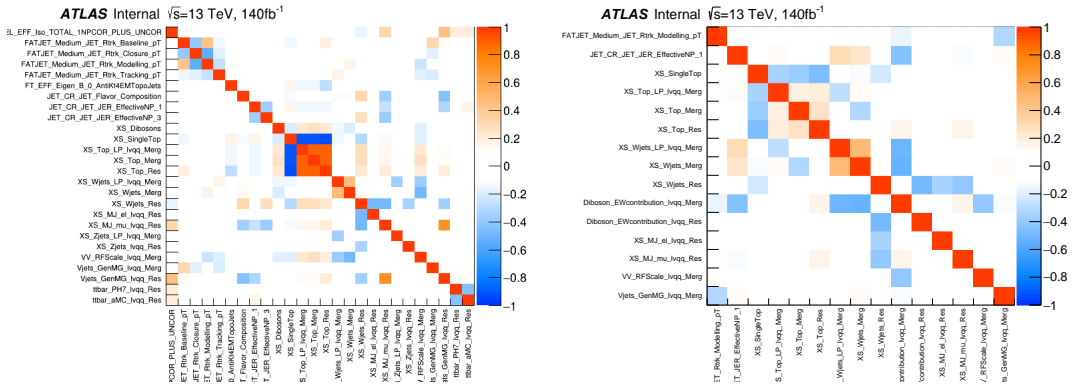


**Figure 12.8:** Correlations between systematics for  $WW$  DY (right) and VBF (left) selections.

## 12.3 Expected and Measured Yields

The yield tables for the four analysis regions are shown in Tables ?? - ???. The fitted background normalizations are shown in Tables ??-???. The control region  $m_{\ell\nu qq}$  distributions are shown in Figures 12.9 - 12.12. The signal region  $m_{\ell\nu qq}$  distributions are shown in Figures 12.13 - ???.

	HP WCR	LP WCR	Resolved WCR
Electron Multi-jet	-	-	$16507.83 \pm 2314.87$
Muon Multi-jet	-	-	$19977.12 \pm 2816.06$
Diboson	$1833.41 \pm 177.78$	$3323.93 \pm 320.92$	$9147.67 \pm 961.63$
Single-top	$2160.62 \pm 402.34$	$3551.09 \pm 660.00$	$20058.36 \pm 3817.26$
$t\bar{t}$	$15518.86 \pm 338.22$	$24069.54 \pm 453.15$	$138866.23 \pm 1989.71$
$W+jets$	$40141.57 \pm 357.79$	$88113.06 \pm 487.87$	$673200.38 \pm 4120.53$
$Z+jets$	$778.83 \pm 78.93$	$1765.54 \pm 179.10$	$16570.50 \pm 1672.71$
Total	$60433.29 \pm 664.92$	$120823.16 \pm 1006.99$	$894328.12 \pm 7247.12$
Data	60264.00	120852.00	895362.00
	HP TCR	LP TCR	Resolved TCR
Electron Multi-jet	-	-	-
Muon Multi-jet	-	-	-
Diboson	$421.11 \pm 37.98$	$550.44 \pm 53.10$	$996.87 \pm 119.63$
Single-top	$4691.44 \pm 846.11$	$3466.26 \pm 631.03$	$16848.71 \pm 3258.26$
$t\bar{t}$	$38945.18 \pm 848.77$	$33836.95 \pm 637.04$	$224226.14 \pm 3212.76$
$W+jets$	$2258.34 \pm 20.13$	$6564.78 \pm 36.35$	$23466.41 \pm 143.63$
$Z+jets$	$66.35 \pm 6.72$	$213.26 \pm 21.63$	$846.66 \pm 85.47$
Total	$46382.43 \pm 1199.25$	$44631.70 \pm 899.23$	$266384.78 \pm 4580.43$
Data	46354.00	44629.00	266443.00
	WW SR	LP SR	Resolved 1-lepton SR
Electron Multi-jet	-	-	$10788.40 \pm 1512.85$
Muon Multi-jet	-	-	$15759.50 \pm 2221.53$
Diboson	$4990.30 \pm 376.50$	$3901.07 \pm 313.22$	$16971.29 \pm 1523.77$
Single-top	$3117.71 \pm 565.07$	$2176.46 \pm 400.52$	$20422.85 \pm 3731.94$
$t\bar{t}$	$13785.77 \pm 302.14$	$11005.12 \pm 207.41$	$126965.25 \pm 1819.66$
$W+jets$	$24718.56 \pm 223.72$	$60080.66 \pm 333.12$	$444133.56 \pm 2719.02$
$Z+jets$	$478.18 \pm 48.46$	$1226.69 \pm 124.44$	$11686.32 \pm 1179.69$
Total	$47090.52 \pm 777.65$	$78389.98 \pm 654.22$	$646727.19 \pm 5963.98$
Data	47330.00	78380.00	645610.00

**Table 12.1:** Expected and Measured for DY  $WW$   $W+jets$ ,  $t\bar{t}$  control regions and signal regions.

	HP Untagged WCR	LP Untagged WCR	Resolved Untagged WCR
Electron Multi-jet	-	-	$15080.03 \pm 2277.99$
Muon Multi-jet	-	-	$27347.10 \pm 2950.07$
Diboson	$1508.48 \pm 154.20$	$2758.24 \pm 284.50$	$9038.55 \pm 728.69$
Single-top	$1756.59 \pm 306.69$	$2913.18 \pm 515.93$	$20511.74 \pm 3523.47$
$t\bar{t}$	$13134.00 \pm 238.30$	$21815.37 \pm 334.98$	$140157.77 \pm 2636.96$
$W+jets$	$40654.84 \pm 333.65$	$87657.76 \pm 501.96$	$665909.12 \pm 4420.62$
$Z+jets$	$768.72 \pm 77.97$	$1759.87 \pm 178.96$	$16512.46 \pm 1673.23$
Total	$57822.63 \pm 540.40$	$116904.42 \pm 862.16$	$894556.75 \pm 7492.20$
Data	57699.00	117306.00	895362.00
	HP Tagged WCR	LP Tagged WCR	Resolved Tagged WCR
Electron Multi-jet	-	-	$384.58 \pm 57.11$
Muon Multi-jet	-	-	$602.93 \pm 190.12$
Diboson	$30.22 \pm 4.69$	$48.95 \pm 7.16$	$264.64 \pm 28.24$
Single-top	$308.44 \pm 56.19$	$371.59 \pm 69.43$	$5752.39 \pm 1029.97$
$t\bar{t}$	$1683.82 \pm 48.73$	$2041.48 \pm 70.00$	$58431.49 \pm 614.30$
$W+jets$	$583.55 \pm 75.37$	$1109.45 \pm 85.78$	$11891.68 \pm 903.01$
$Z+jets$	$13.19 \pm 1.34$	$23.06 \pm 2.34$	$324.74 \pm 32.85$
Total	$2619.22 \pm 106.00$	$3594.53 \pm 130.90$	$77652.45 \pm 1514.89$
Data	2565.00	3546.00	77973.00
	HP Untagged TCR	LP Untagged TCR	Resolved Untagged TCR
Electron Multi-jet	-	-	-
Muon Multi-jet	-	-	-
Diboson	$289.45 \pm 28.45$	$346.78 \pm 35.85$	$650.85 \pm 65.56$
Single-top	$3107.99 \pm 538.03$	$2250.64 \pm 385.41$	$9606.87 \pm 1698.22$
$t\bar{t}$	$30992.40 \pm 562.33$	$26954.21 \pm 413.89$	$91893.59 \pm 1728.91$
$W+jets$	$2236.29 \pm 18.35$	$4874.03 \pm 27.91$	$16122.97 \pm 107.03$
$Z+jets$	$71.54 \pm 7.26$	$155.50 \pm 15.81$	$577.71 \pm 58.54$
Total	$36697.66 \pm 779.03$	$34581.16 \pm 567.59$	$118851.98 \pm 2427.40$
Data	36677.00	34573.00	118928.00
	HP Tagged TCR	LP Tagged TCR	Resolved Tagged TCR
Electron Multi-jet	-	-	-
Muon Multi-jet	-	-	-
Diboson	$9.72 \pm 1.13$	$8.75 \pm 1.16$	$34.06 \pm 4.98$
Single-top	$105.87 \pm 20.65$	$119.66 \pm 22.68$	$656.89 \pm 132.96$
$t\bar{t}$	$1904.75 \pm 50.61$	$1483.86 \pm 47.05$	$17965.33 \pm 188.87$
$W+jets$	$32.36 \pm 4.28$	$85.74 \pm 6.96$	$489.01 \pm 37.13$
$Z+jets$	$1.27 \pm 0.13$	$1.93 \pm 0.20$	$19.14 \pm 1.94$
Total	$2053.98 \pm 54.84$	$1699.93 \pm 52.70$	$19164.43 \pm 234.01$
Data	2047.00	1708.00	19143.00

**Table 12.2:** Expected and Measured for DY  $WZ$   $W+jets$ ,  $t\bar{t}$  tag and untag control regions.

	HP Untagged SR	LP Untagged SR	Resolved Untagged SR
Electron Multi-jet	-	-	$7782.17 \pm 1175.56$
Muon Multi-jet	-	-	$17004.81 \pm 1834.40$
Diboson	$3041.17 \pm 273.77$	$2266.35 \pm 212.79$	$14724.12 \pm 1224.31$
Single-top	$2123.28 \pm 373.83$	$1379.35 \pm 240.92$	$18336.88 \pm 3082.47$
$t\bar{t}$	$11678.86 \pm 213.63$	$8906.34 \pm 136.88$	$112669.24 \pm 2122.46$
$W+jets$	$22741.32 \pm 191.47$	$41726.76 \pm 240.56$	$342934.00 \pm 2280.21$
$Z+jets$	$442.03 \pm 44.84$	$849.79 \pm 86.42$	$9271.83 \pm 939.52$
Total	$40026.65 \pm 546.81$	$55128.59 \pm 432.90$	$522723.03 \pm 5131.71$
Data	40193.00	54735.00	521813.00
	HP Tagged SR	LP Tagged SR	Resolved Tagged SR
Electron Multi-jet	-	-	$199.22 \pm 29.58$
Muon Multi-jet	-	-	$393.43 \pm 124.06$
Diboson	$102.58 \pm 11.59$	$65.44 \pm 8.05$	$624.07 \pm 58.10$
Single-top	$178.21 \pm 33.62$	$155.53 \pm 28.95$	$3470.39 \pm 617.48$
$t\bar{t}$	$1017.93 \pm 31.95$	$706.76 \pm 26.20$	$38189.30 \pm 401.91$
$W+jets$	$325.58 \pm 41.62$	$575.36 \pm 43.29$	$6161.96 \pm 467.71$
$Z+jets$	$7.81 \pm 0.80$	$11.62 \pm 1.19$	$183.36 \pm 18.55$
Total	$1632.11 \pm 63.39$	$1514.70 \pm 58.86$	$49221.74 \pm 884.06$
Data	1699.00	1559.00	48919.00

**Table 12.3:** Expected and Measured for DY  $WZ$   $W+jets$ ,  $t\bar{t}$  tag and untag signal regions.

	HP WCR	LP WCR	Resolved WCR
Electron Multi-jet	-	-	$898.48 \pm 137.82$
Muon Multi-jet	-	-	$601.46 \pm 182.74$
Diboson	$107.45 \pm 45.20$	$166.87 \pm 68.11$	$292.10 \pm 235.29$
Single-top	$78.19 \pm 18.22$	$132.71 \pm 31.93$	$879.82 \pm 216.89$
$t\bar{t}$	$400.71 \pm 28.35$	$569.70 \pm 48.88$	$5067.51 \pm 155.69$
$W+jets$	$864.49 \pm 63.44$	$1940.80 \pm 89.41$	$18563.70 \pm 408.99$
$Z+jets$	$19.51 \pm 2.00$	$46.63 \pm 4.77$	$795.20 \pm 80.89$
Total	$1470.35 \pm 84.89$	$2856.71 \pm 126.74$	$27098.28 \pm 594.01$
Data	1495.00	2898.00	27120.00
	HP TCR	LP TCR	Resolved TCR
Electron Multi-jet	-	-	-
Muon Multi-jet	-	-	-
Diboson	$14.95 \pm 6.61$	$27.57 \pm 14.12$	$24.33 \pm 20.32$
Single-top	$68.31 \pm 16.17$	$58.93 \pm 13.56$	$278.60 \pm 73.04$
$t\bar{t}$	$496.60 \pm 31.72$	$401.23 \pm 32.13$	$3834.49 \pm 104.60$
$W+jets$	$50.68 \pm 4.19$	$144.02 \pm 7.86$	$450.01 \pm 11.87$
$Z+jets$	$1.32 \pm 0.14$	$5.35 \pm 0.55$	$29.96 \pm 3.07$
Total	$631.87 \pm 36.45$	$637.10 \pm 38.44$	$4617.39 \pm 129.77$
Data	636.00	634.00	4615.00
	HP SR	LP SR	Resolved SR
Electron Multi-jet	-	-	$596.34 \pm 91.52$
Muon Multi-jet	-	-	$481.01 \pm 144.48$
Diboson	$148.84 \pm 48.64$	$181.42 \pm 67.30$	$395.52 \pm 318.06$
Single-top	$79.49 \pm 19.80$	$56.82 \pm 14.89$	$782.07 \pm 190.79$
$t\bar{t}$	$338.42 \pm 24.14$	$236.80 \pm 20.88$	$4261.70 \pm 138.98$
$W+jets$	$501.13 \pm 39.36$	$1347.76 \pm 64.50$	$11445.73 \pm 291.49$
$Z+jets$	$9.25 \pm 0.95$	$28.77 \pm 2.95$	$567.66 \pm 57.94$
Total	$1077.13 \pm 69.93$	$1851.57 \pm 96.73$	$18530.03 \pm 523.88$
Data	1096.00	1846.00	18530.00

**Table 12.4:** Expected and Measured for VBF  $WW$   $W+jets$ ,  $t\bar{t}$  control regions and signal regions.

	HP WCR	LP WCR	Resolved WCR
Electron Multi-jet	-	-	$870.00 \pm 132.75$
Muon Multi-jet	-	-	$618.45 \pm 196.90$
Diboson	$92.92 \pm 41.77$	$145.90 \pm 64.26$	$228.62 \pm 114.62$
Single-top	$71.13 \pm 16.29$	$118.82 \pm 27.98$	$1209.87 \pm 281.64$
$t\bar{t}$	$427.80 \pm 29.72$	$509.19 \pm 46.57$	$6860.87 \pm 254.83$
$W+jets$	$871.68 \pm 64.22$	$2020.67 \pm 93.54$	$19088.50 \pm 442.10$
$Z+jets$	$19.58 \pm 2.01$	$47.39 \pm 4.85$	$800.19 \pm 82.02$
Total	$1483.11 \pm 83.79$	$2841.97 \pm 125.92$	$29676.50 \pm 644.96$
Data	1495.00	2898.00	29755.00

	HP TCR	LP TCR	Resolved TCR
Electron Multi-jet	-	-	-
Muon Multi-jet	-	-	-
Diboson	$10.12 \pm 4.51$	$12.73 \pm 6.55$	$14.23 \pm 7.49$
Single-top	$51.57 \pm 12.31$	$35.07 \pm 8.17$	$169.21 \pm 44.54$
$t\bar{t}$	$470.06 \pm 28.97$	$298.99 \pm 25.28$	$2414.75 \pm 75.42$
$W+jets$	$49.64 \pm 4.17$	$109.69 \pm 6.16$	$378.22 \pm 12.05$
$Z+jets$	$1.28 \pm 0.13$	$4.81 \pm 0.50$	$17.62 \pm 1.83$
Total	$582.67 \pm 32.07$	$461.30 \pm 28.05$	$2994.03 \pm 88.75$
Data	584.00	459.00	3001.00

	HP SR	LP SR	Resolved SR
Electron Multi-jet	-	-	$444.65 \pm 67.99$
Muon Multi-jet	-	-	$397.29 \pm 125.59$
Diboson	$109.66 \pm 44.13$	$112.28 \pm 46.45$	$265.75 \pm 139.43$
Single-top	$63.16 \pm 15.20$	$48.02 \pm 11.56$	$872.16 \pm 205.00$
$t\bar{t}$	$348.95 \pm 24.34$	$190.68 \pm 17.75$	$5134.25 \pm 193.57$
$W+jets$	$467.21 \pm 37.12$	$973.73 \pm 47.91$	$10226.83 \pm 254.67$
$Z+jets$	$8.15 \pm 0.84$	$23.62 \pm 2.43$	$558.48 \pm 57.25$
Total	$997.13 \pm 64.42$	$1348.33 \pm 70.06$	$17899.41 \pm 432.98$
Data	1018.00	1313.00	17826.00

**Table 12.5:** Expected and Measured for VBF  $WZ$   $W+jets$ ,  $t\bar{t}$  control regions and signal regions.

Background	Fitted Normalization
XS_Top_LP_lvqq_Merg_binned	$0.905^{+0.0166}_{-0.0166}$
XS_Top_Merg	$0.936^{+0.0199}_{-0.0199}$
XS_Top_Res	$0.957^{+0.0134}_{-0.0134}$
XS_Wjets_LP_lvqq_Merg_binned	$0.884^{+0.00489}_{-0.00489}$
XS_Wjets_Merg	$0.931^{+0.00831}_{-0.00831}$
XS_Wjets_Res	$1.03^{+0.00628}_{-0.00628}$

**Table 12.6:** Fitted background normalizations for  $t\bar{t}$  and  $W+jets$  backgrounds for the DY  $WW$  analysis region.

Background	Fitted Normalization
XS_Top_LP_Tag_lvqq_Merg_binned	$0.973^{+0.0333}_{-0.0333}$
XS_Top_LP_lvqq_Merg_binned	$0.894^{+0.0135}_{-0.0135}$
XS_Top_Merg	$0.893^{+0.016}_{-0.016}$
XS_Top_Res	$0.965^{+0.0179}_{-0.0179}$
XS_Top_Tag_lvqq_Merg_binned	$0.954^{+0.0276}_{-0.0276}$
XS_Top_Tag_lvqq_Res_binned	$0.999^{+0.0105}_{-0.0105}$
XS_Wjets_LP_Tag_lvqq_Merg_binned	$0.912^{+0.0703}_{-0.0703}$
XS_Wjets_LP_lvqq_Merg_binned	$0.876^{+0.00502}_{-0.00502}$
XS_Wjets_Merg	$0.948^{+0.00779}_{-0.00779}$
XS_Wjets_Res	$1.01^{+0.00673}_{-0.00673}$
XS_Wjets_Tag_lvqq_Merg_binned	$0.906^{+0.117}_{-0.117}$
XS_Wjets_Tag_lvqq_Res_binned	$1.2^{+0.0904}_{-0.0904}$

**Table 12.7:** Fitted background normalizations for  $t\bar{t}$  and  $W+jets$  backgrounds for the DY  $WZ$  analysis region.

Background	Fitted Normalization
XS_Top_LP_lvqq_Merg_binned	$0.79^{+0.0673}_{-0.0673}$
XS_Top_Merg	$0.888^{+0.061}_{-0.061}$
XS_Top_Res	$1.01^{+0.0311}_{-0.0311}$
XS_Wjets_LP_lvqq_Merg_binned	$0.88^{+0.0423}_{-0.0423}$
XS_Wjets_Merg	$0.881^{+0.0677}_{-0.0677}$
XS_Wjets_Res	$0.932^{+0.0202}_{-0.0202}$

**Table 12.8:** Fitted background normalizations for  $t\bar{t}$  and  $W+jets$  backgrounds for the VBF  $WW$  analysis region.

Background	Fitted Normalization
XS_Top_LP_lvqq_Merg_binned	$0.708^{+0.064}_{-0.064}$
XS_Top_Merg	$0.958^{+0.0644}_{-0.0644}$
XS_Top_Res	$1.02^{+0.038}_{-0.038}$
XS_Wjets_LP_lvqq_Merg_binned	$0.9^{+0.0438}_{-0.0438}$
XS_Wjets_Merg	$0.883^{+0.0685}_{-0.0685}$
XS_Wjets_Res	$0.945^{+0.0219}_{-0.0219}$

**Table 12.9:** Fitted background normalizations for  $t\bar{t}$  and  $W+jets$  backgrounds for the VBF  $WZ$  analysis region.

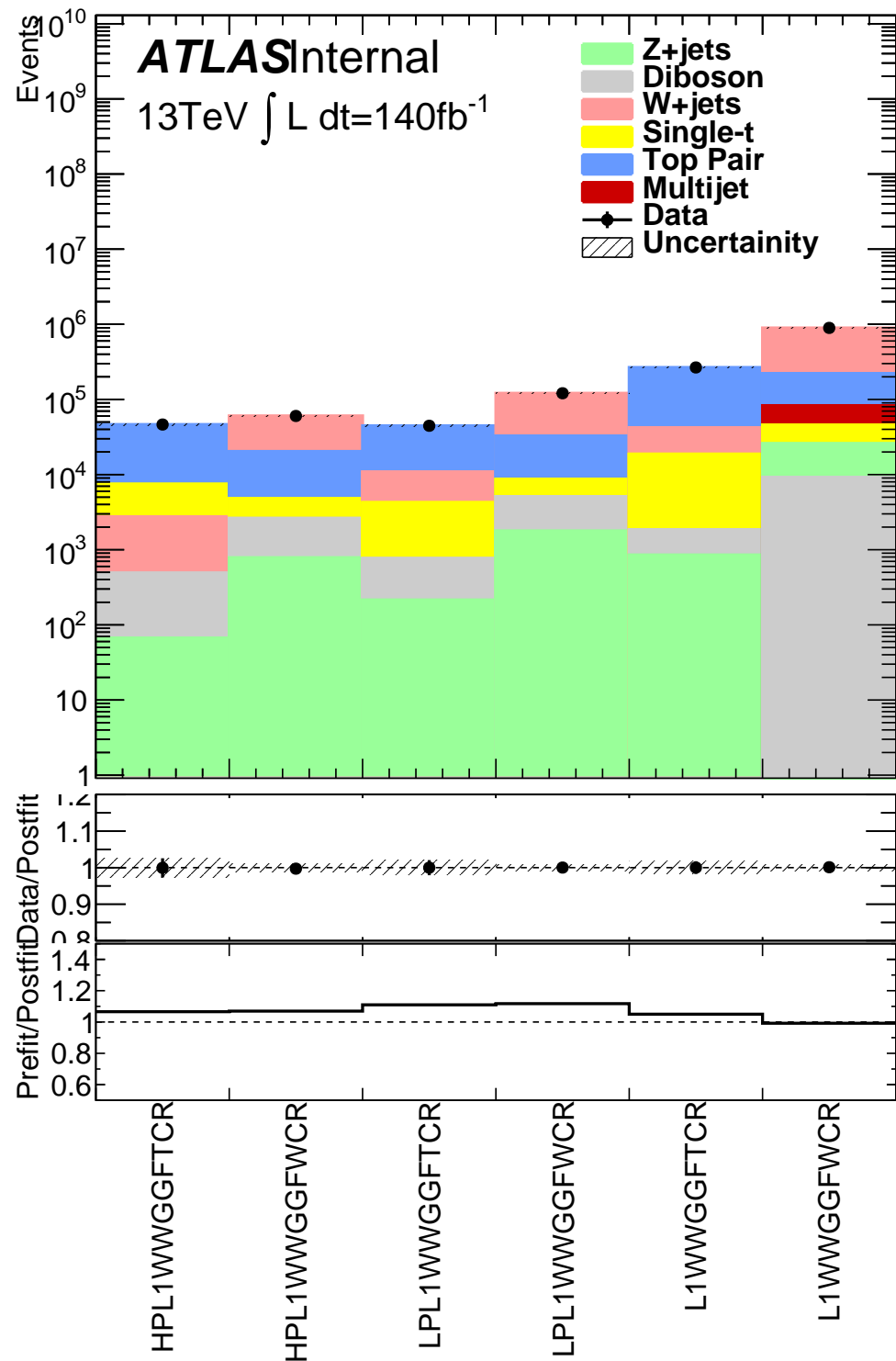


**Figure 12.9:** This figure shows the distribution of  $m_{\ell\nu qq}$  in the DY WW control regions.

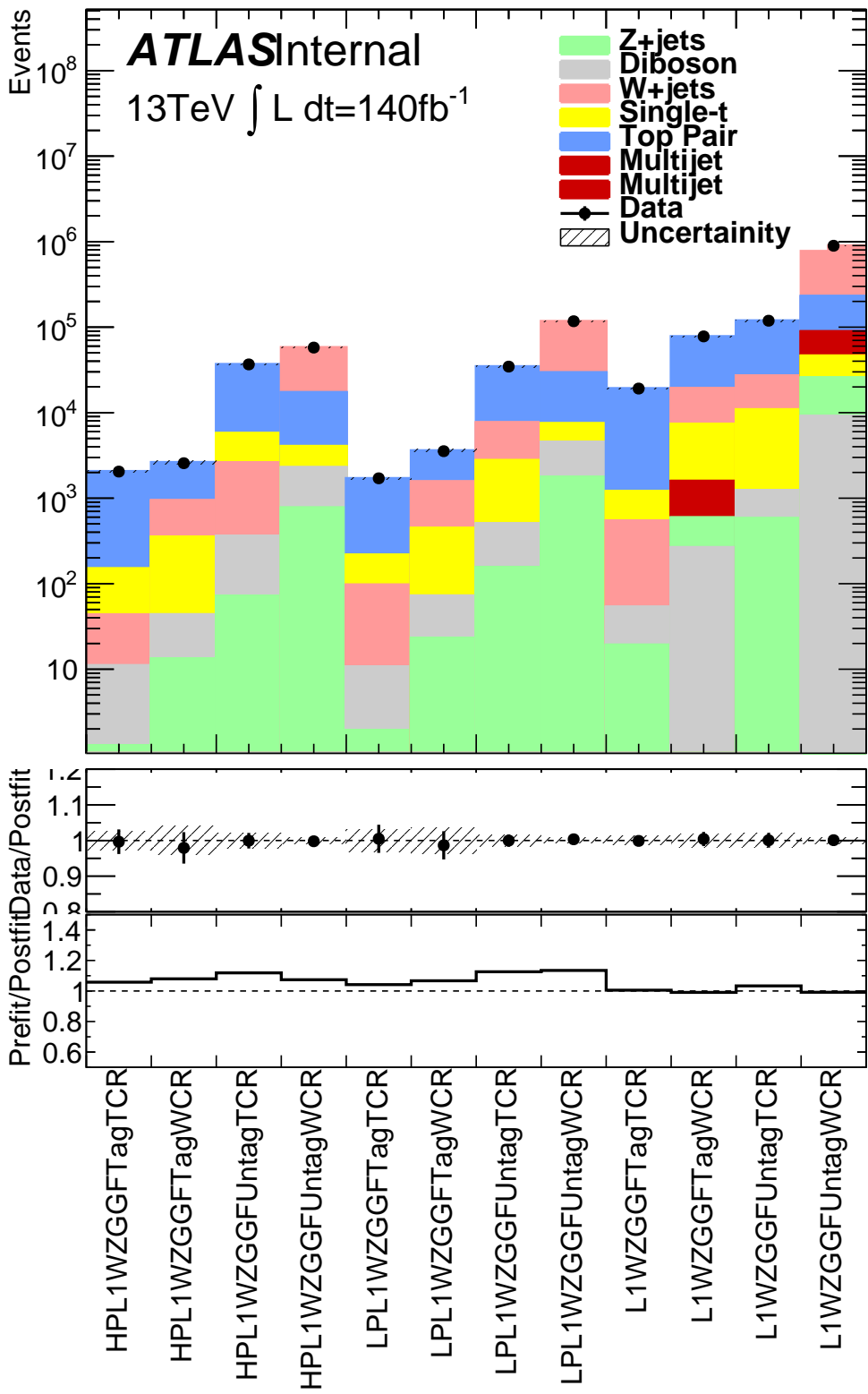


**Figure 12.10:** This figure shows the distribution of  $m_{\ell\nu qq}$  in the DY  $WZ$  control regions.

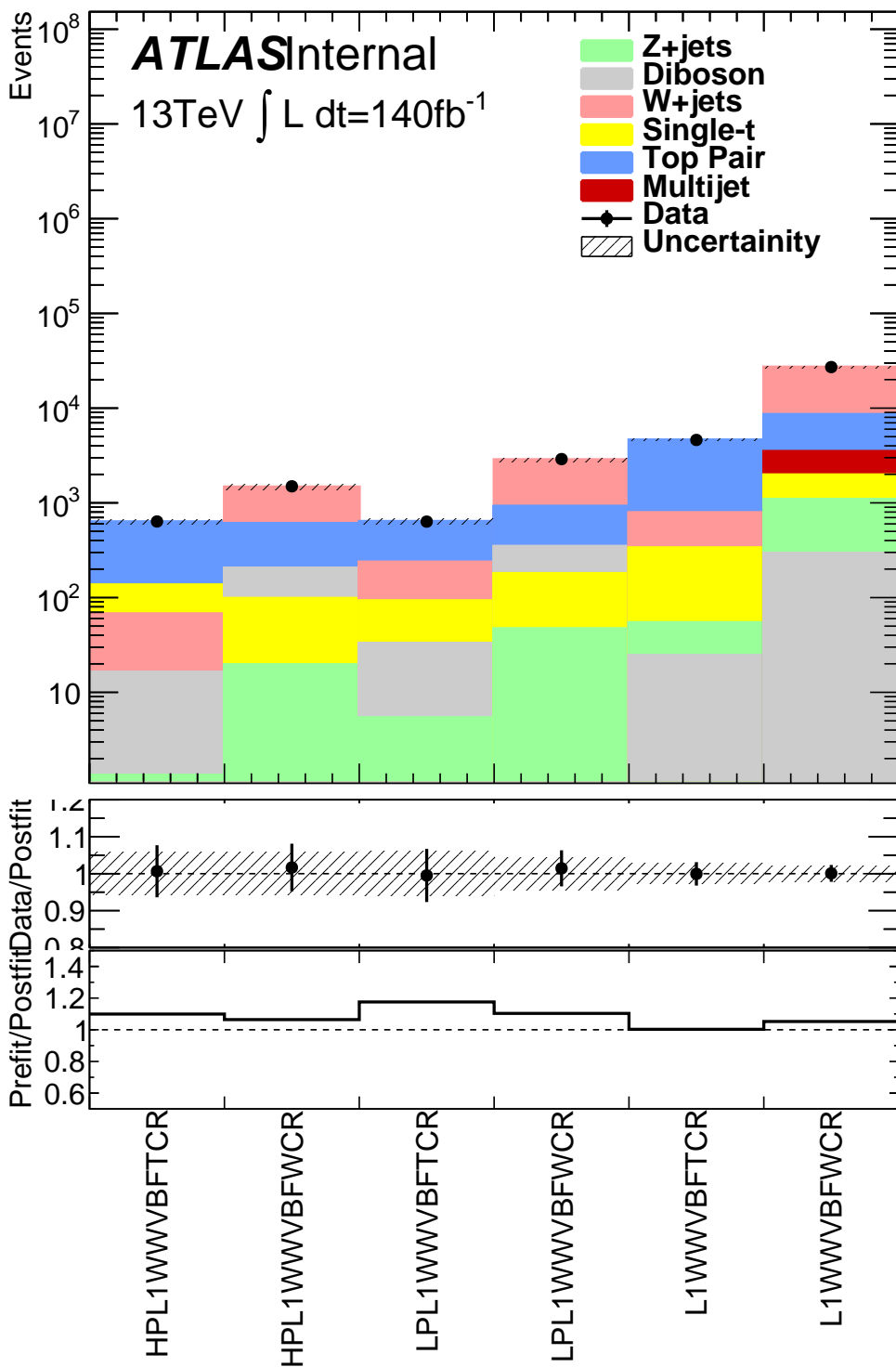


**Figure 12.11:** This figure shows the distribution of  $m_{\ell\nu qq}$  in the VBF  $WW$  control regions.

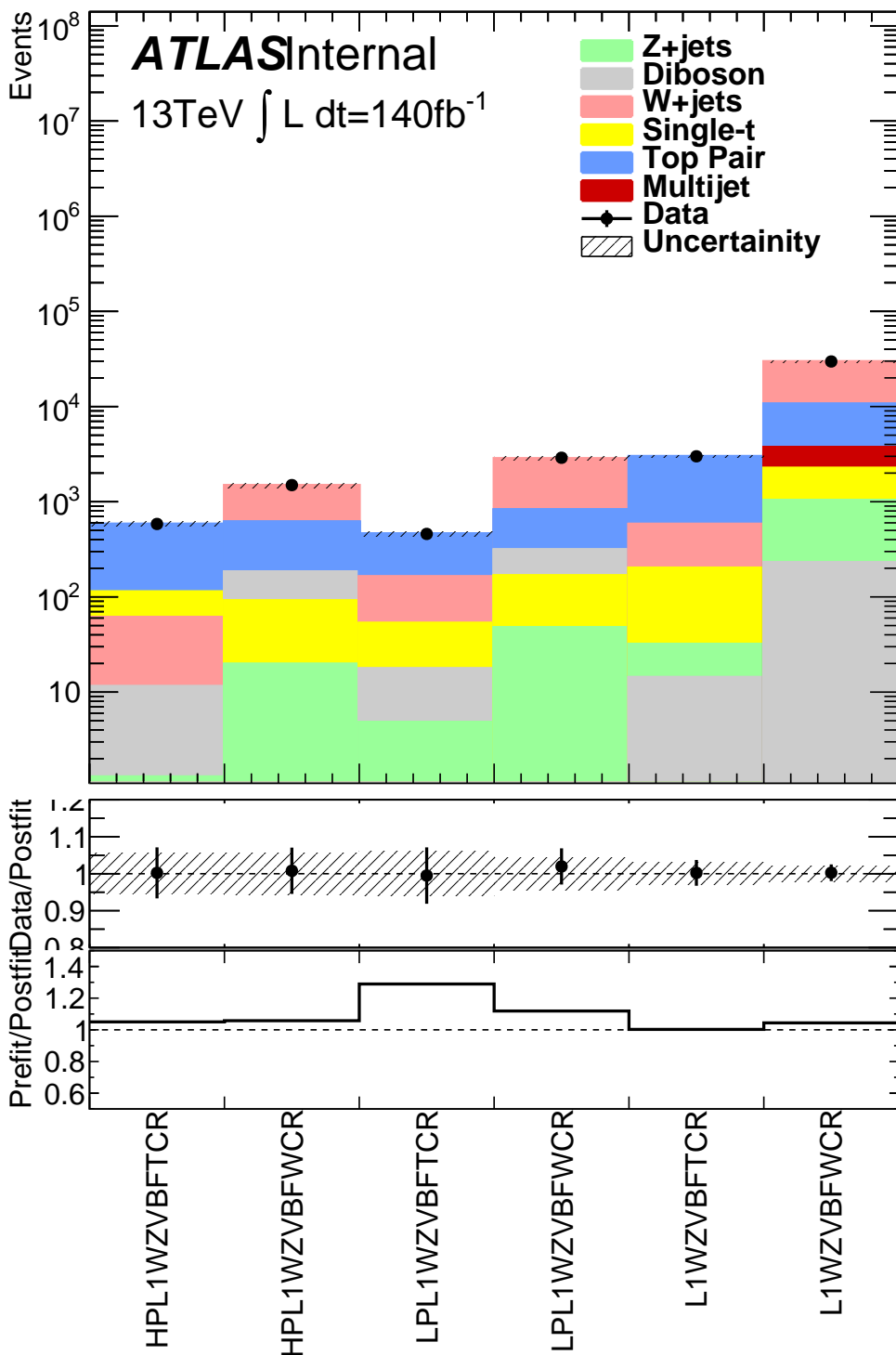


**Figure 12.12:** This figure shows the distribution of  $m_{\ell\nu qq}$  in the VBF  $WZ$  control regions.

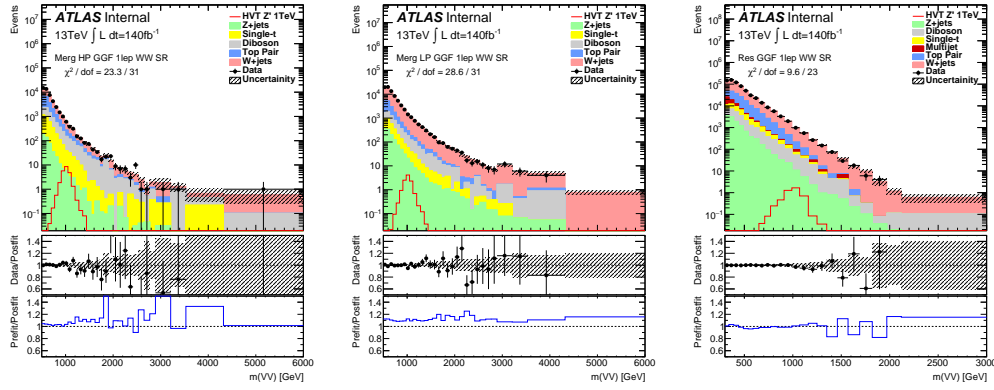


**Figure 12.13:** This figure shows the distribution of  $m_{\ell\nu qq}$  in the GGF  $WW$  signal regions.

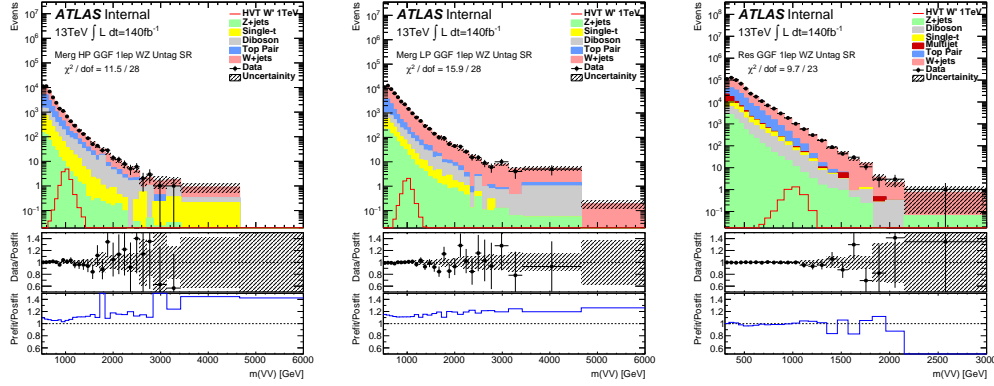


**Figure 12.14:** This figure shows the distribution of  $m_{\ell\nu qq}$  in the GGF  $WZ$  Untag signal regions.

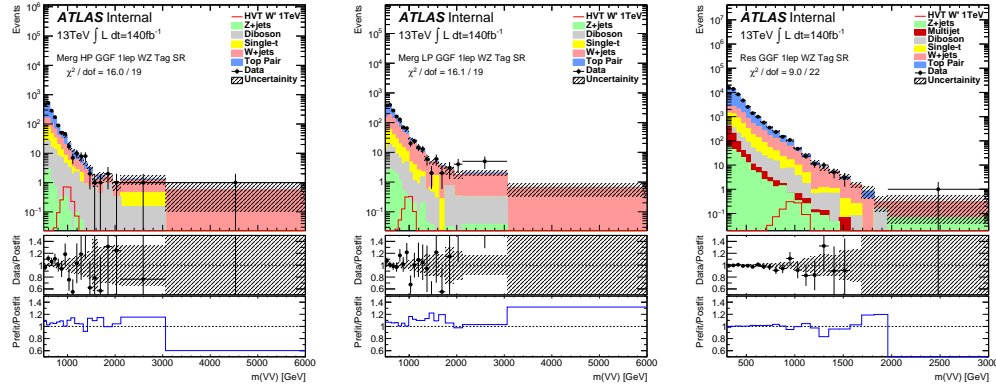


**Figure 12.15:** This figure shows the distribution of  $m_{\ell\nu qq}$  in the GGF  $WZ$  Tag signal regions.

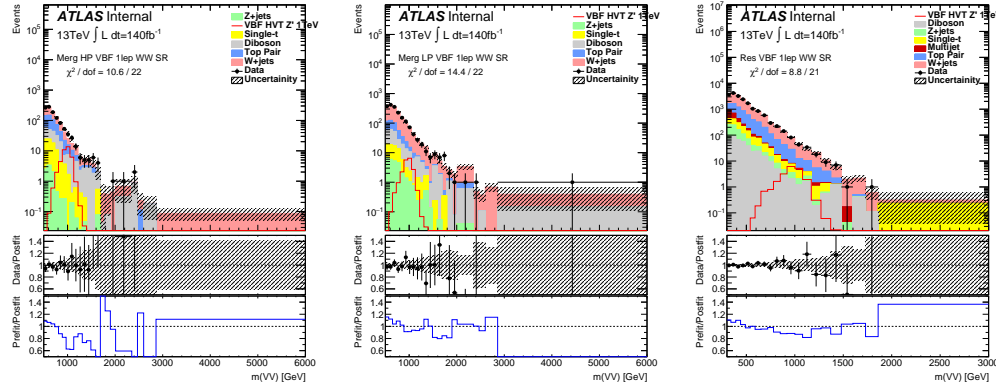


**Figure 12.16:** This figure shows the distribution of  $m_{\ell\nu qq}$  in the VBF  $WZ$  Tag signal regions.

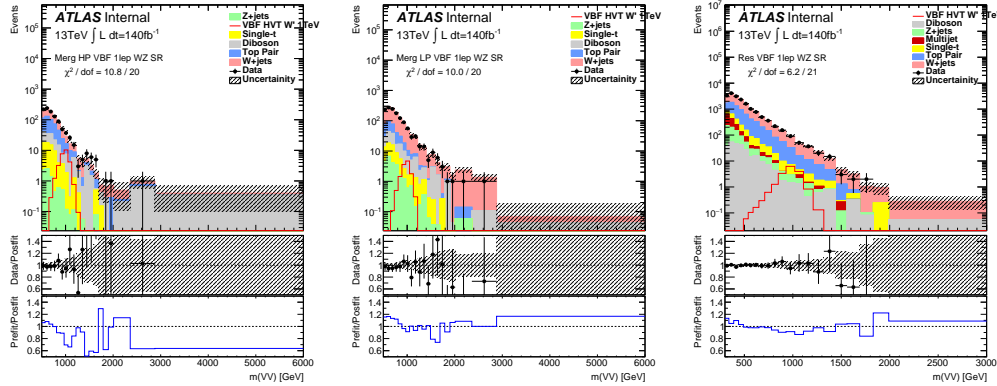


**Figure 12.17:** This figure shows the distribution of  $m_{\ell\nu qq}$  in the VBF  $WZ$  Tag signal regions.

## 12.4 Limits

Using the exclusion limits tests discussed previously, exclusion limits are set on  $\mu$  and consequently cross-sections for different signal models. Exclusion limits for the models considered are shown in Figure 12.18 - 12.20. These limits exclude HVT Model A  $W' < 3.4$  TeV and  $Z' < 3.3$  TeV and Model B  $W' < 3.7$  TeV and  $Z' < 3.7$  TeV. Randall Sundrum Gravitons are excluded for masses below 1.6 TeV .

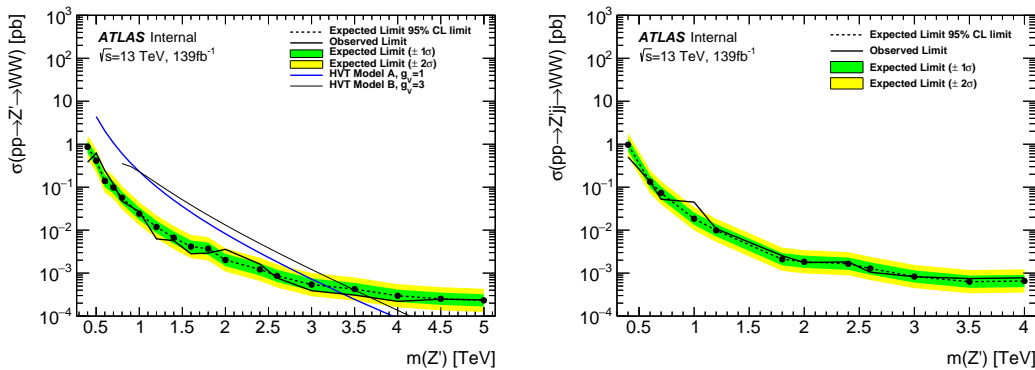


**Figure 12.18:** This figure shows theory, expected and observed limits for HVT  $W'$  DY (left) and VBF (right) production.

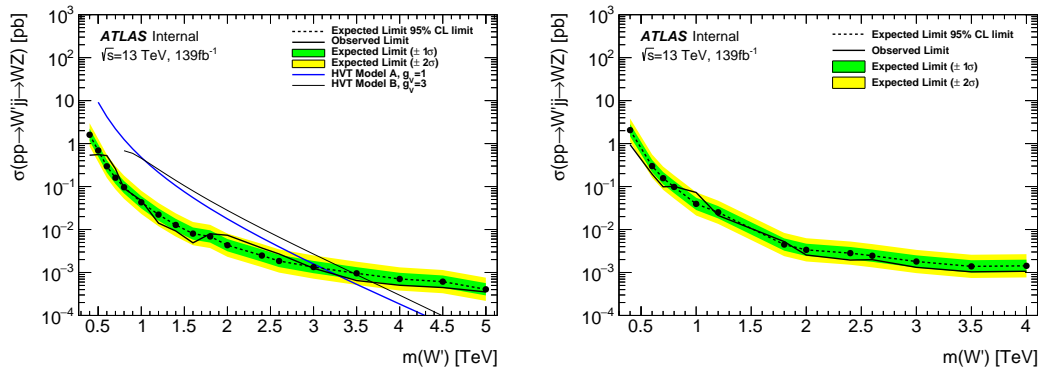


**Figure 12.19:** This figure shows theory, expected and observed limits for HVT  $Z'$  DY (left) and VBF (right) production.

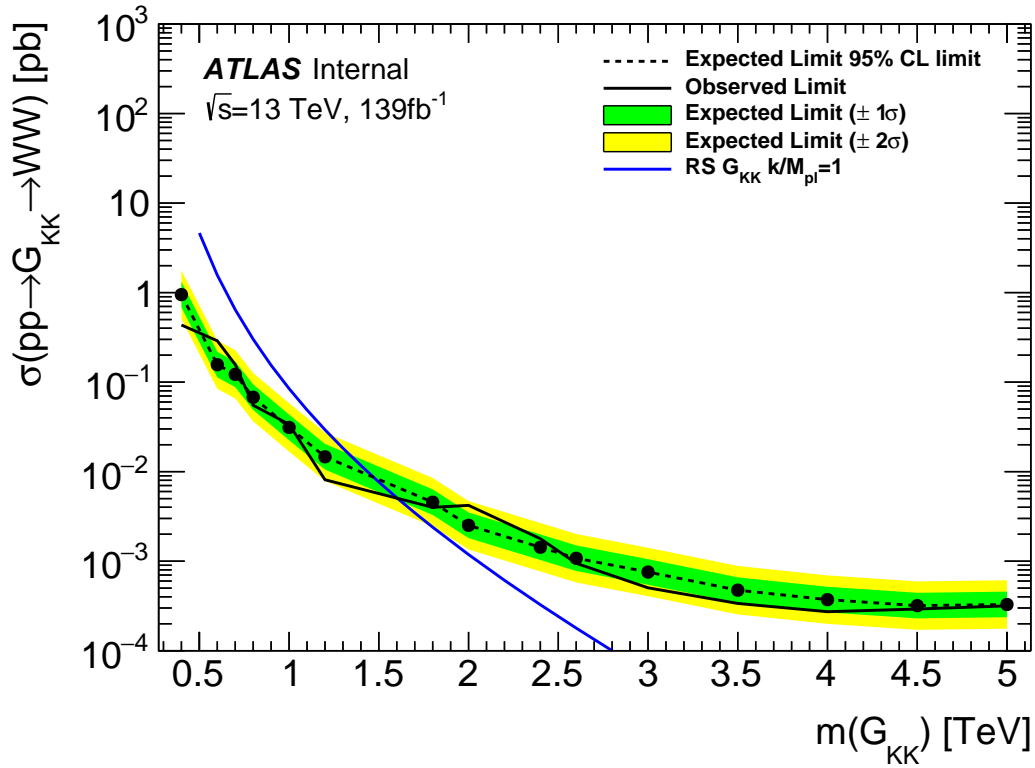


**Figure 12.20:** This figure shows theory, expected and observed limits for RS Gravitons via DY production.

1290

## Part V

1291

## Quark and Gluon Tagging

<sub>1292</sub> **Chapter 13**

<sub>1293</sub> **Prospects**

<sub>1294</sub> For the resolved analysis, signal jets are quark enriched and background jets are  
<sub>1295</sub> gluon dominated. By classifying jets in the event as quark or gluon initiated, less  
<sub>1296</sub> background would contaminate the signal region. Figure 13.1 shows the PDGID  
<sub>1297</sub> for the truth parton matched to the jet (meaning the highest energy parton in  
<sub>1298</sub> the jet catchment area) in events passing the resolved signal region selections.  
<sub>1299</sub> PDGID = -1 corresponds to pileup jets,  $0 < \text{PDGID} < 6$  correspond to quarks  
<sub>1300</sub> and  $\text{PDGID} = 21$  corresponds to gluons. From this Figure, it is evident that a  
<sub>1301</sub> notable fraction of the background that contaminates the signal region contains  
<sub>1302</sub> gluon jets, especially for the sub-leading jet.

<sub>1303</sub> As gluons jets have more constituents and therefore more tracks ( $n_{trk}$ ), the  
<sub>1304</sub> background jets have more tracks than the signal jets. This is shown in Fig-  
<sub>1305</sub> ure 13.2. Therefore, by cutting on the number of tracks in a jet, quark and gluon  
<sub>1306</sub> jets may be distinguished (i.e. jets with less than a given number of tracks are  
<sub>1307</sub> classified as a quark, otherwise the jet is classified as a gluon.) Moreover, as the  
<sub>1308</sub> momentum of the jet increases the number of tracks also increases logarithmically  
<sub>1309</sub> [Cite nachman thesis Natasha]. Therefore by applying a cut on the number of  
<sub>1310</sub> tracks that scales with the  $\ln(p_T)$  is more powerful than a threshold cut on the

1311 number of tracks. Figure 13.3-Figure 13.6 show normalized heat maps of  $\ln(p_T)$   
1312 vs the number of reconstructed tracks for the background and a 300 GeV Z' signal.  
1313 In these plots it is evident that the number of tracks in the background jets grows  
1314 more quickly with  $\ln(p_T)$  than for the signal jets. This is expected given that the  
1315 signal is quark dominated and the background is gluon dominated.

1316 In Figure 13.8 is the ROC Curve for quark gluon tagging with cut on the  
1317 number of tracks in a jet that depends on  $\ln(p_T)$ . The sum of the backgrounds in  
1318 the signal region were used for this curve. Here the quark tagging efficiency is the  
1319 ratio of quarks tagged as quarks to the total number of quarks in the signal region.  
1320 The gluon rejection is calculated as the reciprocal of the gluon tagging efficiency.  
1321 Choosing a 90% efficient working point with a rejection of 1.4 corresponds to a  
1322 slope of 4 and intercept of -5. Tagging both jets in this analysis would yield an  
1323 efficiency of 90% $^{n_{jets}}$ . Focusing on the background in Figure 13.9, this cut helps  
1324 minimize gluon contamination in the signal region. Also, from these heat maps it  
1325 is obvious that the number of tracks in gluon jets grows more quickly than those  
1326 in quark jets.

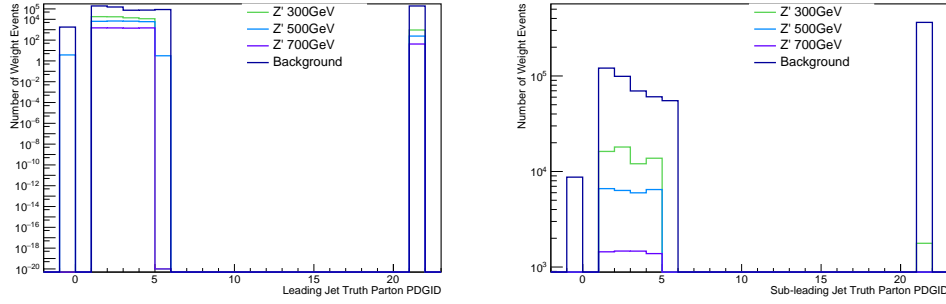


**Figure 13.1:** PDGID of the truth-level parton matched to the small-R jets passing the Resolved GGF WW Signal Region selections for the (a) Leading (b) Sub-Leading jets . These distributions are shown for 300, 500, and 700GeV Z' signals and the background.

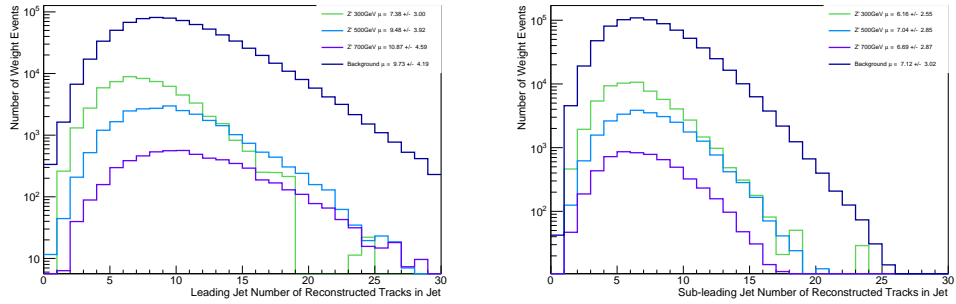


**Figure 13.2:** The number of tracks in small-R jets in events passing the Resolved GGF WW Signal Region selections for the (a) Leading (b) Sub-Leading jets. These distributions are shown for 300, 500, and 700GeV Z' signals and the background.

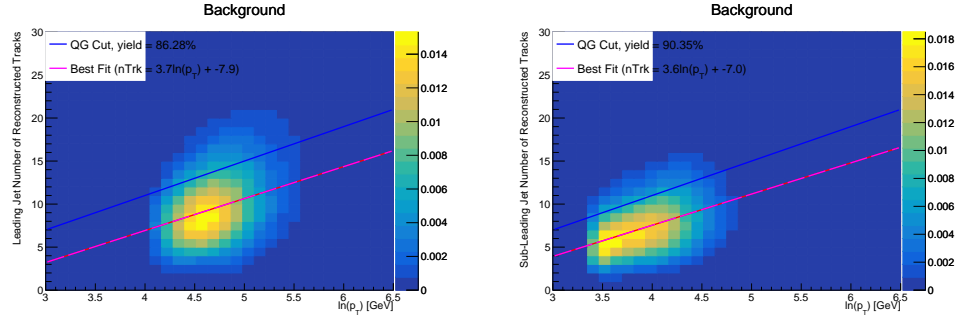


**Figure 13.3:** The number of tracks in background small-R jets in events passing the Resolved GGF WW Signal region selection vs.  $\ln(p_T)$  for (a)Leading (b) Sub-Leading jets. The best fit line for the distribution is also shown, as well as the percentage of jets that pass a cut of number of tracks  $< 4 \times \ln(p_T) - 5$ . Note the number of total entries in these plots has been normalized to one.

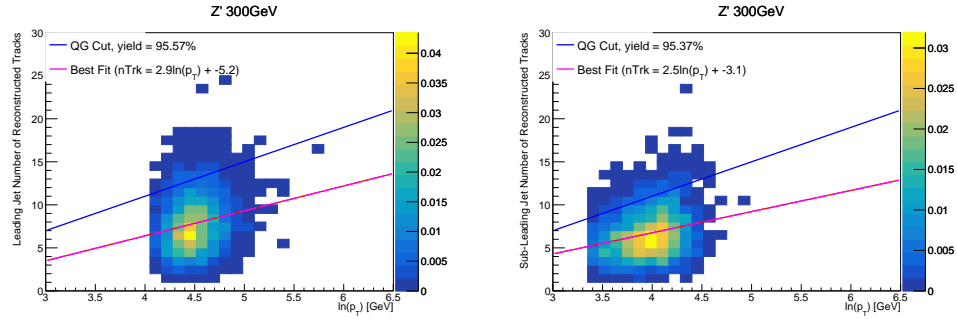


**Figure 13.4:** The number of tracks in small-R jets in 300GeV  $Z'$  events passing the Resolved GGF WW Signal region selection vs.  $\ln(p_T)$  for (a)Leading (b) Sub-Leading jets. The best fit line for the distribution is also shown, as well as the percentage of jets that pass a cut of number of tracks  $< 4 \times \ln(p_T) - 5$ . Note the number of total entries in these plots has been normalized to one.

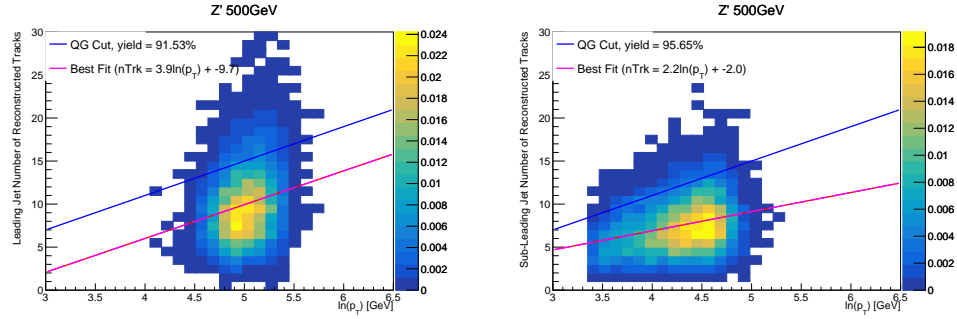


**Figure 13.5:** The number of tracks in small-R jets in 500GeV  $Z'$  events passing the Resolved GGF WW Signal region selection vs.  $\ln(p_T)$  for (a)Leading (b) Sub-Leading jets. The best fit line for the distribution is also shown, as well as the percentage of jets that pass a cut of number of tracks  $< 4 \times \ln(p_T) - 5$ . Note the number of total entries in these plots has been normalized to one.

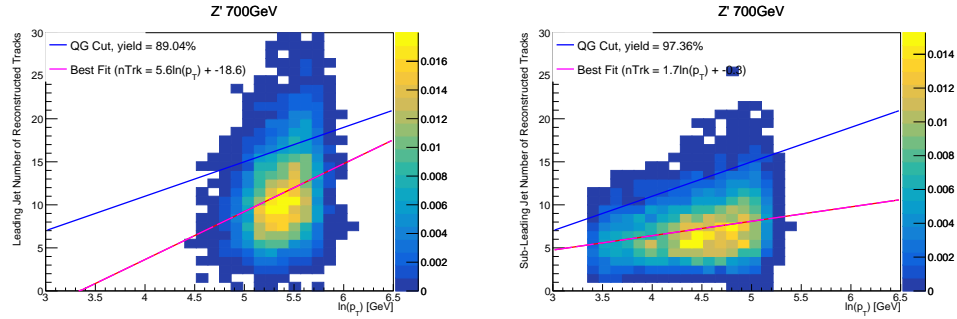


**Figure 13.6:** The number of tracks in small-R jets in 700GeV  $Z'$  events passing the Resolved GGF WW Signal region selection vs.  $\ln(p_T)$  for (a)Leading (b) Sub-Leading jets. The best fit line for the distribution is also shown, as well as the percentage of jets that pass a cut of number of tracks  $< 4 \times \ln(p_T) - 5$ . Note the number of total entries in these plots has been normalized to one.

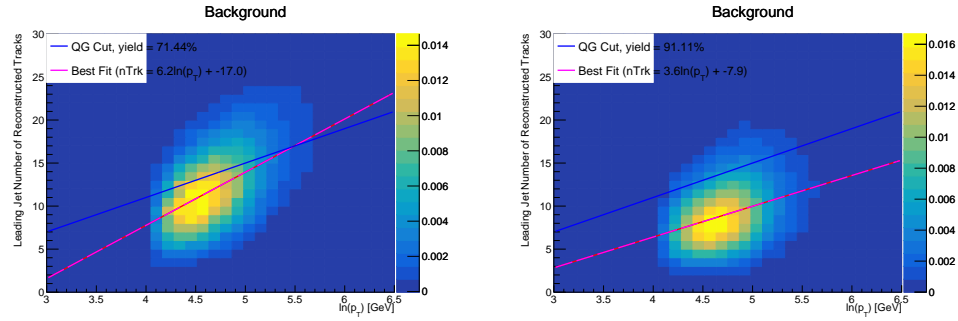


**Figure 13.7:** The number of tracks in leading small-R jets in background events passing the Resolved GGF WW Signal region selection vs.  $\ln(p_T)$  for (a)Gluons (b) Quarks jets. The best fit line for the distribution is also shown, as well as the percentage of jets that pass a cut of number of tracks  $< 4 \times \ln(p_T) - 5$ .Note the number of total entries in these plots has been normalized to one.

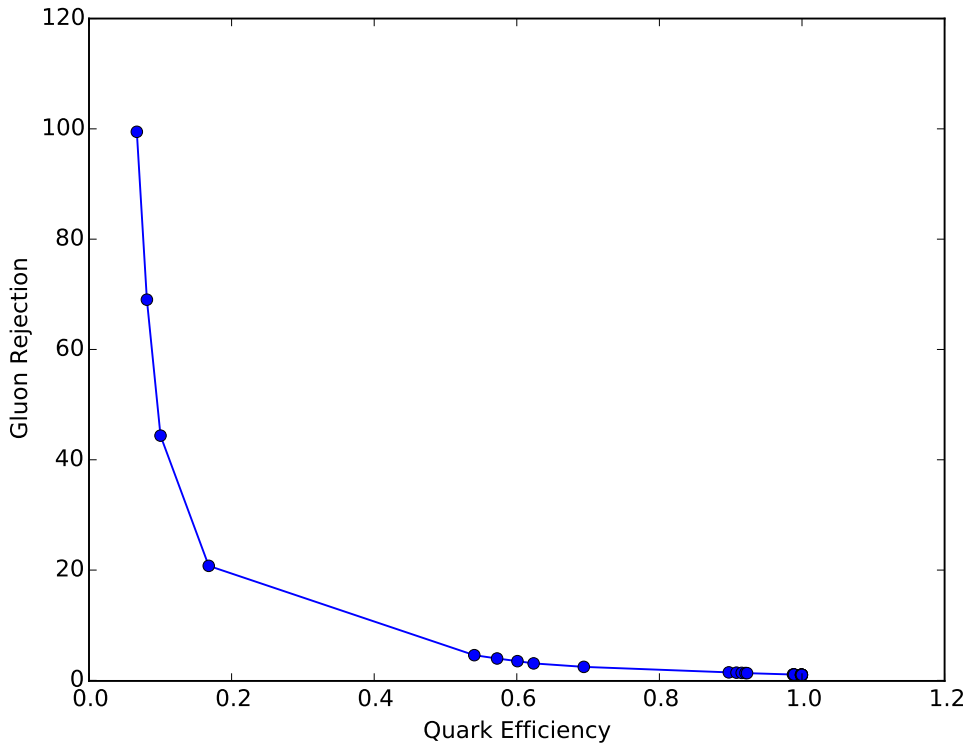


**Figure 13.8:** ROC Curve for Quark and Gluon Tagging with a cut on the number of tracks that depends on the  $\ln(p_T)$ .

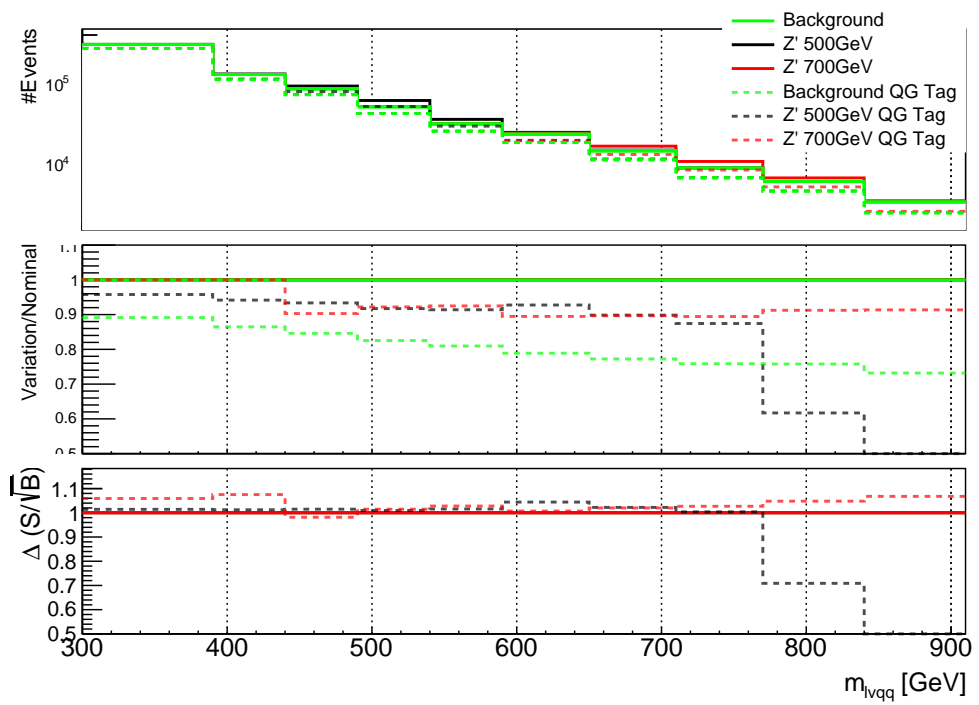


**Figure 13.9:** The top panel shows the distribution of  $m_{lvqq}$  with and without quark gluon tagging. The middle panel shows the ratio of the signals and backgrounds with and without quark gluon tagging. The bottom panel shows the change in  $S/\sqrt{B}$  with quark gluon tagging.

# 1327 Chapter 14

## 1328 $n_{trk}$ Calibration

1329 As tagger based on nTrk cuts on the number of tracks in jets, a quantity that  
1330 is not known with infinite precision, means that relevant systematic uncertainties  
1331 must be evaluated. The sources of uncertainty in  $n_{trk}$  may be split into modeling  
1332 and experimental uncertainties.

1333 Modeling uncertainties are obtained by assessing PDF and ME uncertainties  
1334 on the number of charged particles in particle-level jets in dijet events. The  
1335 number of charged particles as a function of jet  $p_T$  is calculated using an Iterative  
1336 Bayesian (IB) technique [cite paper].

1337 This measurement ([8]) uses the ATLAS 2012 pp collision dataset, correspond-  
1338 ing to  $20.3/\text{fb}$  at center-of-mass energy  $\sqrt{s} = 8\text{TeV}$ . The number of charged con-  
1339 stituents depends on fragmentation modeling and matrix elements, which do not  
1340 depend on  $s$ . For this reason, it is safe to use these uncertainties for  $\text{sqrt}(s)=13\text{TeV}$ .  
1341 Monte Carlo (MC) samples are used to determine the response matrix. The MC  
1342 sample is a dijet sample generated with Pythia 8.175 using CT10 PDF and AU2  
1343 tune. The anti- $k_T$  algorithm is used to cluster jets with a radius parameter  $R$   
1344  $= 0.4$ . Jets are required to have  $|\eta| < 2.1$ . Tracks in jets are required to have  
1345  $p_T > 500\text{MeV}$ ,  $|\eta| < 2.5$ , track-fit  $\chi^2 < 3.0$  and originate from the primary ver-

tex. Matching tracks to jets is accomplished using ghost-association [cite]. In this technique, jets are re-clustered with the track collection augmented with "ghost" versions of tracks. These "ghosts" tracks have the same direction as their parent track, but infinitesimal track  $p_T$ . This insures meta-jet properties (e.g.  $\eta$ ,  $p_T$ , etc) are unchanged. A track is matched to a jet if it's ghost version remains in the jet after re-clustering. Further details of the data, object, and event selection may be found in [cite 35].

To select dijet topologies events are required to have at least two jets with  $p_T > 50GeV$  that are relatively well-balanced ( $p_T^{lead}/p_T^{sub-lead} < 1.5$ ).

In the IB technique, the prior distribution and number of iterations are the inputs [cite Bayesian paper]. The IB response matrix connects number of charged particles to the number of tracks in jets determined using the simulated samples. This response matrix is used to unfold data to extract the  $n_c$ . Before applying the response matrix a fake factor is applied. This accounts for jets that pass detector level selections, but not particle level selections. Following this, the IB method iteratively applies the response matrix using the nominal Pythia 8.175 sample as a prior. The number of IB iterations is chosen to minimize unfolding bias and statistical fluctuations. For this measurement four iterations was found to be optimal by minimizing the unfolding bias from pseudodata simulated with Herwig++ with a prior from Pythia 8 AU2. Finally, the inefficiency factor is applied to account for events passing particle level selection but not detector level, yielding the unfolded nCharged distribution.

This process is prone to three main sources of bias: response matrix, correction factor, and unfolding procedure uncertainties. The response matrix is sensitive to experimental uncertainties impacting jet track reconstruction and calorimeter jet  $p_T$ . Correction factors are also sensitive to experimental uncertainties (e.g. JES)

1372 as such uncertainties modify detector level acceptance. Sensitivity to particle  
 1373 level acceptance is calculated by comparing Pythia and Herwig. Finally, the bias  
 1374 from the IB prior choice is determined by reweighting the particle-level spectrum,  
 1375 so the simulated detector level spectrum more closely matches the uncorrected  
 1376 data. Unfolding this modified detector-level simulation and comparing it to the re-  
 1377 weighted particle-level spectrum indicates bias from the prior distribution choice.  
 1378

A summary of all the systematic uncertainties associated with this unfolding  
 1379 may be found in [ref paper]. Total uncertainties are < 7% for the number of  
 1380 charged particles in jets. The unfolded distribution of the nCharged in jets from  
 1381 data are further analyzed to extract the quark and gluon nCharged distributions.  
 1382 In dijet events, the jet with a larger  $\eta$  is more energetic and therefore more likely  
 1383 to be a quark. This is due to the quarks in protons generally having a larger  
 1384 fraction of the total momentum of the proton constituents. The more central jet  
 1385 is more likely to be a gluon-initiated jet. This correlation between jet  $\eta$  and flavor  
 1386 may then be used to extract nCharged in  $p_T$  bins using:  
 1387

$$\langle n_c^f \rangle = f_q^f \langle n_c^q \rangle + f_g^f \langle n_c^g \rangle \quad (14.1)$$

$$\langle n_c^c \rangle = f_q^c \langle n_c^q \rangle + f_g^c \langle n_c^g \rangle \quad (14.2)$$

1388 In this equation the f and c subscripts denote the more forward and central  
 1389 jets, respectively. The q and g subscripts denote quark and gluon. The fraction  
 1390 of more forward jets that are say gluons is denoted by  $f_g^f$ . The other relevant jet  
 1391 fractions are denoted with the same naming scheme. Finally,  $\langle n_c \rangle$  is the average  
 1392 number of charged particles in a jet in a given  $p_T$  bin. To show that Eq. (??) may  
 1393 be used to extract quark and gluon  $n_c$  distributions the extracted distributions  
 1394 are compared to  $n_c$  distributions determined using the jet flavor in simulation.  
 1395 Figure [add figure natasha] shows that the extracted and true distributions differ

1396 by < 1% over the  $p_T$  range probed for this study. Moreover, this implies that  $n_c$   
1397 depends only on the flavor of the initiating parton and jet  $p_T$ .

1398 These extracted distributions are prone to PDF and ME biases. The bias from  
1399 the choice of the CT10 PDF for the Pythia sample is accounted for by comparing  
1400 quark/gluon fractions for the nominal CT10 sample with its eigenvector variations.  
1401 Comparing the quark/gluon fractions from Pythia 8 and Herwig++ quantify the  
1402 uncertainty from the ME calculation. These uncertainties are added in quadra-  
1403 ture with the unfolding uncertainty to give the total modelling uncertainty on  
1404 the extracted  $n_c$  distribution. This is shown in Figure 15.2.

1405 To apply these uncertainties in  $n_c$  distributions in data, per-jet event weights  
1406 are associated with each uncertainty according to:

$$w_i(n_c) = \frac{P(n_c | n_c > \pm \sigma_{n_c}^i)}{P(n_c | n_c >)} \quad (14.3)$$

1407 In Eq. (??), i denotes the uncertainty considered, P is the Poisson probability,  
1408 and  $\sigma_{n_c}^i$  represents the average impact of the uncertainty on  $n_c$ .

1409 The previous uncertainties described accounted for modeling uncertainty as-  
1410 sociated with the number of charged particles in a jet. However,  $n_c$  is not a  
1411 measurable quantity. Instead the number of tracks in a jet is measured, which is  
1412 a proxy for  $n_c$ . Therefore the uncertainties associated with the measurement of  
1413 nTracks must also be considered ([10]). These uncertainties were calculated using  
1414 a Pythia 8 dijet sample with NNPDF 23 and Run 2 data. Track reconstruction  
1415 efficiency and fake rates are the dominant sources of nTrack uncertainties.

1416 The track reconstruction efficiency is affected by the uncertainty of the de-  
1417 scription of the ID material in simulation and the modeling of charged-particle  
1418 interactions with this material. These uncertainties are accounted for by varying  
1419 the ID material by 5-25% (dependent on the region of the detector considered).

1420 The difference in the tracking efficiency between the nominal and varied simula-  
1421 tion give the uncertainty on the track reconstruction efficiency. Another important  
1422 source of track reconstruction inefficiency arises in the core of jets. The high den-  
1423 sity of tracks in the jet cores can cause ID clusters to merge. The fraction of lost  
1424 tracks due to merging is given by the fraction of tracks that have a charge of two  
1425 minimum ionizing particles. This quantity is compared between data and simu-  
1426 lation resulting in an uncertainty of 0.4% on tracks with  $\Delta R < 0.1$ . Combining  
1427 these effects gives a total uncertainty as a function of  $p_T$  and  $\eta$  that is generally  
1428  $< 2\%$  [references figure 44 from [10]].

1429       Fake tracks are the other dominant source of nTrk uncertainty. Fake tracks  
1430 are tracks that cannot be associated to a single particle. Often these tracks are a  
1431 result of random combinations of hits from charged particles that overlap in space.  
1432 In dense environments, such as the core of jets or high-pileup environments, fake  
1433 tracks are more likely. Fake tracks are estimated with a 'control region method'  
1434 which is briefly summarized here [[9]]. By applying a series of track selections  
1435 to enrich the fraction of fake tracks (e.g.  $|d_0| > 0.1$ , track  $\chi^2 > 1.4$ , etc) in  
1436 simulation, templates for fake track parameters are calculated. These templates  
1437 are then fit to data to determine the fraction of fake tracks. On average the fake  
1438 rate is found to be 30% (independent of  $p_T$  and  $\eta$ ).

1439       To assess the impact of these two detector level uncertainties, tracks are ran-  
1440 domly dropped according to the rates described above. Reconstruction and fake  
1441 uncertainties both lower the number of tracks, hence these uncertainties are one-  
1442 sided. By dropping tracks in this way a varied nTrk distribution is calculated for  
1443 both uncertainties. The associated per-jet event weights are then calculated in  
1444 the same way as the modeling weights as:

$$w_i(n_c) = \frac{P(n_{trk} | < n_{trk} > \pm \sigma_{n_{trk}}^i)}{P(n_{trk} | < n_{trk} >)} \quad (14.4)$$

1445        Adding the modeling and detector level uncertainties in quadrature gives the  
 1446        overall nTrack uncertainty. The effects of the individual uncertainties on the nTrk  
 1447        distributions can be seen in Fig 15.4. Fig 15.3 shows the  $m_{lvqq}$  and nTrk distri-  
 1448        butions for the W and Top control regions before likelihood fitting. In these plots  
 1449        the nTrk uncertainties improve agreement between data and MC. The remaining  
 1450        differences are likely covered by likelihood fitting and improving the analysis itself.

1451 **Chapter 15**

1452 **Application**

1453 Using the 90% WP of the  $n_{trk}$  tagger improves  $S/\sqrt{B}$  is  $\sim 3\%$  as shown in  
1454 Figure 13.9. Although,  $n_{trk}$  is the single most powerful discriminating variable  
1455 for quark and gluon jets, the addition of other jet variables would improve the  
1456 classification efficiency. Figure 15.1 shows the possible improvement of 10%  
1457 in jet classification using the truth label of the jets to classify jets. This type of  
1458 improvement is possible by using variables such as jet width, and energy correlata-  
1459 tors. Figure [add BDT figure/use 1612.01551.pdf] shows for a 90% quark tagging  
1460 efficiency for a 100 GeV jet, a BDT improve the gluon rejection by 0.4. Once this  
1461 tagger is calibrated it would improve the analysis sensitivity of this channel.

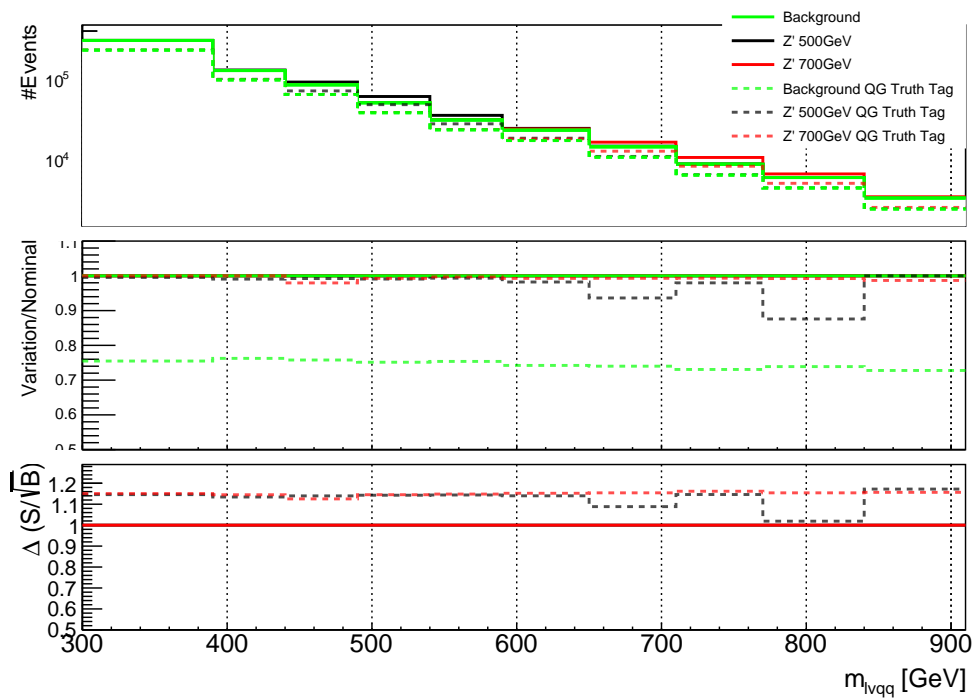


**Figure 15.1:** The top panel shows the distribution of  $m_{lvqq}$  with and without requiring jets to be true quarks. The middle panel shows the ratio of the signals and backgrounds with and without requiring jets to be true quarks. The bottom panel shows the change in  $S/\sqrt{B}$  when requiring jets to be true quarks..

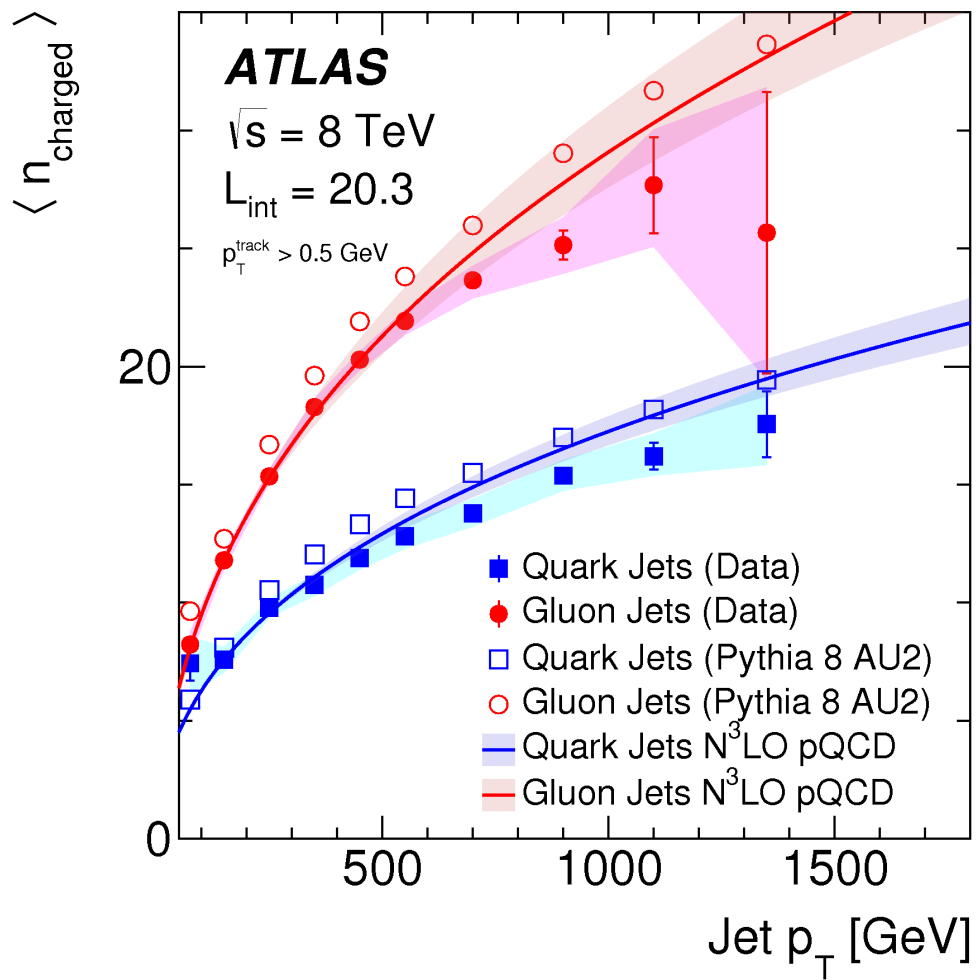


**Figure 15.2:** Unfolded and extracted  $n_C$  qg dstbs..

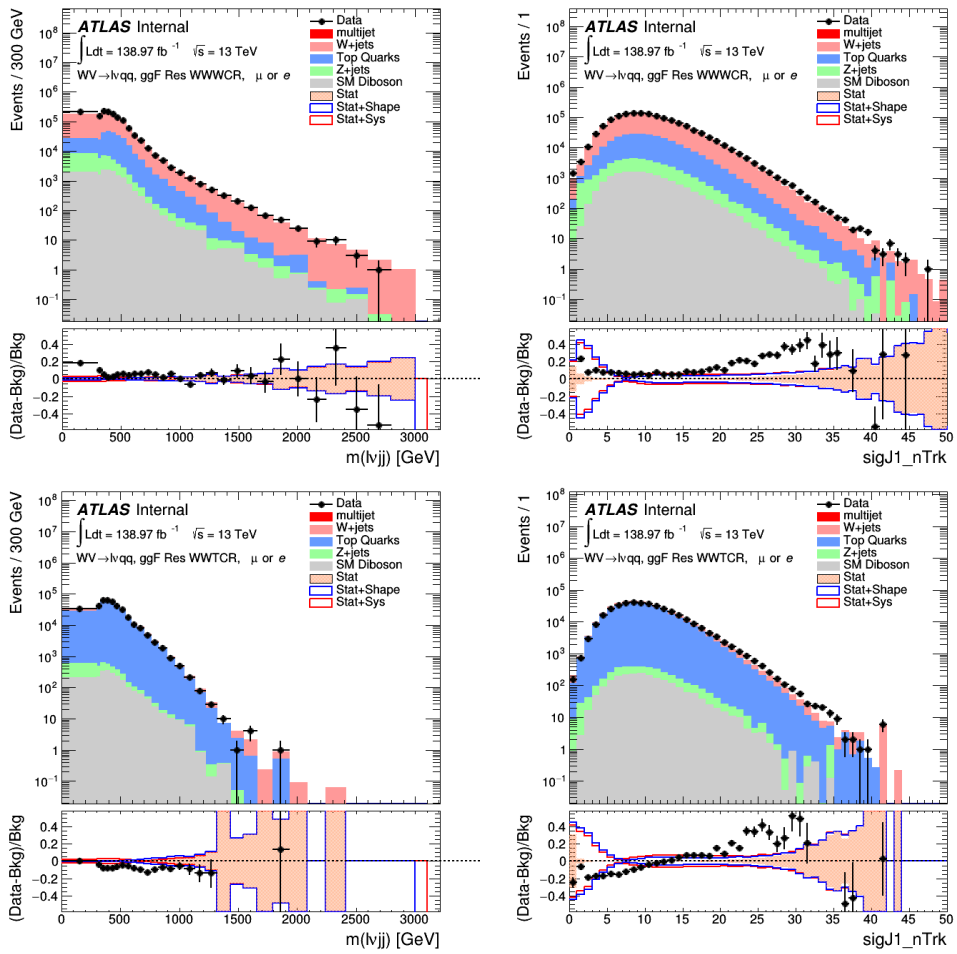


**Figure 15.3:** PDGID of the truth-level parton matched to the small-R jets passing the Resolved GGF WW Signal Region selections for the (a) Leading (b) Sub-Leading jets . These distributions are shown for 300, 500, and 700GeV  $Z'$  signals and the background.

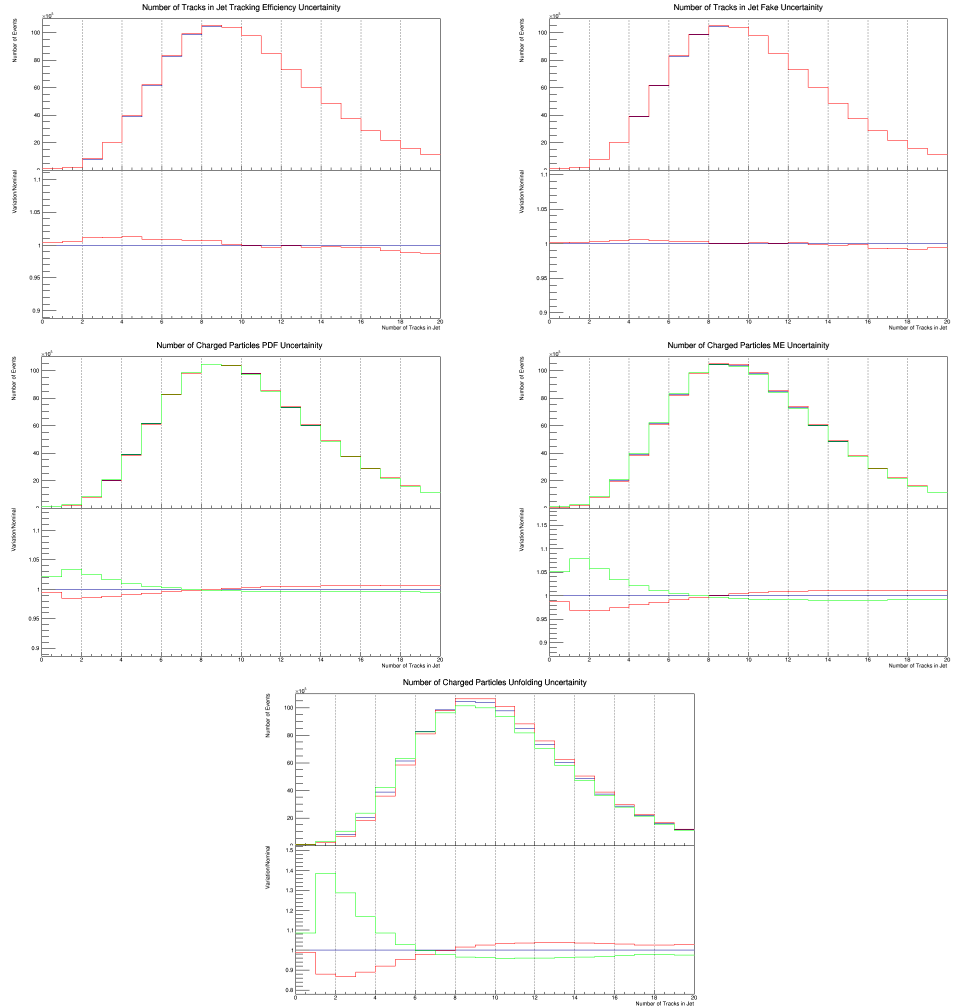


**Figure 15.4:** These figures show the impact of the uncertainties on the number of tracks in the leading jet in the sum of the background sample in the Resolved GGF WW SR (a) tracking efficiency (b) fake (c) PDF (d) ME (e) unfolding uncertainties.

## **Part VI**

1462

## **Conclusion**

1463

1464 **Chapter 16**

1465 **Conclusions**

1466 A search for  $WW$  and  $WZ$  diboson resonance production in  $\ell\nu qq$  final states  
1467 was performed using  $139\text{fb}^{-1}$  of  $pp$  collision data collected at a center-of-mass  
1468 energy of  $\sqrt{s} = 13\text{TeV}$  by that ATLAS detector at the LHC between 2015 and  
1469 2018. No excess of events above the background-only expectation was observed.  
1470 The largest local excess is approximately  $2.7\sigma$ , which is not significant. Limits  
1471 on the production cross section are obtained for the HVT  $W'$  and  $Z'$  and RS  
1472 Gravitons. Signal masses below 3.4 (3.7) TeV are excluded for HVT  $W'$  Model  
1473 A(B). Signal masses below 3.3 (3.7) TeV are excluded for HVT  $Z'$  Model A(B).  
1474 Randall Sundrum Gravitons are excluded for masses below 1.6 TeV. Going forward,  
1475 improving the classification of jets in events would improve analysis sensitivity.  
1476 To distinguish quark from gluon jets a jet tagger based on the number of tracks in  
1477 jets is studied in the context of this search. Finally, the calibration of the number  
1478 of tracks in jets is discussed.

# <sup>1479</sup> Bibliography

- <sup>1480</sup> [1] Lecture notes particle physics ii.
- <sup>1481</sup> [2] Kaustubh Agashe, Hooman Davoudiasl, Gilad Perez, and Amarjit Soni.  
<sup>1482</sup> Warped Gravitons at the LHC and Beyond. *Phys. Rev.*, D76:036006, 2007.
- <sup>1483</sup> [3] G. Altarelli and G. Parisi. Asymptotic freedom in parton language. *Nuclear*  
<sup>1484</sup> *Physics B*, 126(2):298 – 318, 1977.
- <sup>1485</sup> [4] ATLAS Collaboration. Atlas muon reconstruction performance in lhc run 2.
- <sup>1486</sup> [5] ATLAS Collaboration. Summary plots from the atlas standard model physics  
<sup>1487</sup> group.
- <sup>1488</sup> [6] ATLAS Collaboration. Tagging and suppression of pileup jets with the atlas  
<sup>1489</sup> detector.
- <sup>1490</sup> [7] ATLAS Collaboration. Jet energy scale measurements and their systematic  
<sup>1491</sup> uncer- tainties in proton–proton collisions at  $\sqrt{s} = 13$  tev with the atlas  
<sup>1492</sup> detector. arXiv: 1703.09665 [hep-ex].
- <sup>1493</sup> [8] ATLAS Collaboration. Measurement of the charged-particle multiplicity  
<sup>1494</sup> inside jets from  $s=\sqrt{8}$  tev pp collisions with the atlas detector.  
<sup>1495</sup> arXiv:1602.00988 [hep-ex].
- <sup>1496</sup> [9] ATLAS Collaboration. Performance of the atlas track reconstruction algo-  
<sup>1497</sup> rithms in dense environments in lhc run 2. arXiv:1704.07983 [hep-ex].
- <sup>1498</sup> [10] ATLAS Collaboration. Properties of jet fragmentation using charged par-  
<sup>1499</sup> ticles measured with the atlas detector in pp collisions at  $\sqrt{s} = 13$  tev.  
<sup>1500</sup> arXiv:1906.09254 [hep-ex].
- <sup>1501</sup> [11] Alex Dias and V. Pleitez. Grand unification and proton stability near the  
<sup>1502</sup> peccei-quinn scale. *Physical Review D*, 70, 07 2004.
- <sup>1503</sup> [12] Stefan Höche, Frank Krauss, Marek Schönherr, and Frank Siegert. Qcd ma-  
<sup>1504</sup> trix elements + parton showers. the nlo case. *Journal of High Energy Physics*,  
<sup>1505</sup> 2013(4), Apr 2013.

- 1506 [13] Diederik P. Kingma and Jimmy Ba. Adam: A method for stochastic opti-  
1507 mization, 2014.
- 1508 [14] David Krohn, Jesse Thaler, and Lian-Tao Wang. Jets with variable  $r$ . *Journal*  
1509 of High Energy Physics, 2009(06):059–059, Jun 2009.
- 1510 [15] Gregory Soyez Matteo Cacciari, Gavin P. Salam. The anti- $k_T$  jet clustering  
1511 algorithm. arXiv:0802.1189 [hep-ph].
- 1512 [16] Duccio Pappadopulo, Andrea Thamm, Riccardo Torre, and Andrea Wulzer.  
1513 Heavy vector triplets: bridging theory and data. *Journal of High Energy*  
1514 *Physics*, 2014(9), Sep 2014.
- 1515 [17] Antonio Pich. The Standard Model of Electroweak Interactions. In *Proceed-  
1516 ings, High-energy Physics. Proceedings, 18th European School (ESHEP 2010):  
1517 Raseborg, Finland, June 20 - July 3, 2010*, pages 1–50, 2012. [,1(2012)].
- 1518 [18] Lisa Randall and Raman Sundrum. A Large mass hierarchy from a small  
1519 extra dimension. *Phys. Rev. Lett.*, 83:3370–3373, 1999.
- 1520 [19] Sebastian Raschka. Model evaluation, model selection, and algorithm selec-  
1521 tion in machine learning, 2018.
- 1522 [20] Tania Robens and Tim Stefaniak. Lhc benchmark scenarios for the real higgs  
1523 singlet extension of the standard model. *The European Physical Journal C*,  
1524 76(5), May 2016.
- 1525 [21] Alex Sherstinsky. Fundamentals of recurrent neural network (RNN) and long  
1526 short-term memory (LSTM) network. *CoRR*, abs/1808.03314, 2018.
- 1527 [22] Muhammed Ali Sit and Ibrahim Demir. Decentralized flood forecasting using  
1528 deep neural networks. Jun 2019.
- 1529 [23] Wojciech Zaremba, Ilya Sutskever, and Oriol Vinyals. Recurrent neural net-  
1530 work regularization, 2014.